CYRIC

ANNUAL REPORT

2003

(January 2003 - December 2003)

CYCLOTRON AND RADIOISOTOPE CENTER
TOHOKU UNIVERSITY
http://www.cyric.tohoku.ac.jp/

PREFACE

In this twenty-forth issue of the CYRIC Annual Report, we summarize the activities in research and development, and in training of radioisotope safe-treatment at the Cyclotron and Radioisotope Center (CYRIC) during the calendar year 2003.

Research at CYRIC was carried out in the fields of nuclear physics, nuclear chemistry, material sciences, nuclear medicine using PET (oncology, neurology, pharmacology), radiopharmaceutical chemistry, health physics, nuclear instrumentation, nuclear medical engineering (diagnosis and therapy technology), nuclear engineering and elemental analysis using PIXE.

Development and improvement on nuclear instruments and techniques have progressed in acceleration of high intensity negative ion hydrogen beams, which we intend to use for production of a high intensity neutron beam. A total of 2690 hours of beam-time was delivered by the K=110MeV cyclotron for scheduled operation in research work.

New radiopharmaceuticals labeled with ^{18}F and ^{11}C have been developed for PET study. Routine preparations of. [^{18}F]FDG, [^{11}C]methionine, [^{11}C]doxepin, [^{11}C]raclopride, and [^{11}C]donepezil were carried out with the Cyprisl HM-12 cyclotron.

The research program on PIXE analysis has been carried out by using an electrostatic accelerator (4.5 MV Dynamitron) at the Fast Neutron Laboratory (FNL), Graduate School of Engineering, Tohoku University, under the scientific tie up between CYRIC and FNL. A total of 300 hours beam-time was served to this program.

Concerning the education in radioisotope safe-treatment, 576 staff members and students of Tohoku University were trained in the safe handling of radiation and radioisotopes, while 215 staff members and students received training in the " X-ray course". In addition, 82 staff members and students were trained in the safe handling of radiation from a SOR.

This year, we have to announce with deep regret that Emeritus professor Manabu Fujioka has passed away at the age of 67 on 12 Oct. 2003. As mentioned in the preface of CYRIC Annual Report 1999, his contributions to CYRIC and his achievements in scientific

research and education are manifold and admirable. He has been highly regarded in the field of nuclear physics using β-ray spectroscopy and isotope on-line separator. Professor Fujioka will always be remembered for his achievements and for his personality

At the end of March 2003, Professor Orihara retired after 13 fruitful years as director at CYRIC. Prof. Orihara has been active at TOHOKU University for 43 years including his student years and in his long university life, he achieved much in research, education, and management of CYRIC.

He was one of the first staff members at CYRIC, constructed the first cyclotron as a leading member in April 1974 and supported studies at CYRIC as head of the Division of Instrumentations. He accomplished the introduction of a three-dimensional high-resolution positron tomograph (PET) 2400W-S in 1994, the small HM-12 cyclotron in 1998, the new K=110 cyclotron in 1999 and large-scale detection systems for neutrons and γ-rays in 1999. He contributed much to the meetings of directors of National University RI centers as vice-chairman.

Among his accomplishments, the introduction of a beam swinger and neutron time-of-flight system to the cyclotron - a first time in Japan - discovered a new nuclear excitation mode of spin iso-spin interaction by using the (p, n) reaction. He elevated the Cyclotron RI center to among the best in the world and has played an active role as authority in neutron spectrometry. When the cyclotron was renewed in 1998, he developed a new neutron detection system offering high resolution and high efficiency, which ranks among the best in the world. He made considerable contributions to education in Nuclear Radiation Physics in the Graduate School of Science.

We wish to express our deepest gratitude to Prof. Orihara for his devotion to science, technology and education.

National Universities will be corporate entities from April 2004 and in this new situation, CYRIC will continue its efforts to future development in accelerator science.

8We are most grateful to Tohoku University and to the Ministry of Education, Sports, Culture, Science and Technology for continuous support.

March 2004

Keizo ISHII
Director
Cyclotron and Radioisotope Center, Tohoku University

EDITORS:

Keizo ISHII
Tatsuo IDO
Masatoshi ITOH
Mamoru BABA
Ren IWATA
Hiroyuki OKAMURA
Tsutomu SHINOZUKA

WORD PROCESSED BY

Yu-ko YAMASHITA

CONTENTS

I. NUCLEAR PHYSICS

II. NUCLEAR INSTRUMENTATION

V. PIXE ANALYSIS

VI. RADIOCHEMISRTY AND NUCLEAR CHEMISTRY

VII. RADIOPHARMACEUTICAL CHEMISTRY AND BIOLOGY

I. NUCLEAR PHYSICS

I. 1. Search for Gamow-Teller Strengths in ^{14}O via the (*p*,*n*) Reaction

Okamura H., Terakawa A., Suzuki H., Sugimoto N., Shinozaki H., and Hasegawa T.

CYRIC, Tohoku University

The old and well-known feature of the mass A=14 system is the anomalous hindrance of the transition between the ground state of ^{14}N (J^{π}=1^{+}, T=0) and the ground states of ^{14}O and ^{14}C (J^{π}=0^{+}, T=1). Although the quantum numbers involved would permit a Gamow-Teller decay, the log(ft) values are as large as 9.0 and 7.3 for ^{14}C and ^{14}O, respectively, allowing the widely used ^{14}C dating in archaeological studies. A number of theoretical works have been made, but it is interesting to note that none of the widely used empirical effective *p*- or *psd*-shell model interactions can explain this famous suppression. Recently it was suggested that the suppression can be explained if a tensor component of the residual interaction is considered in a large model space[1]. It was also suggested that the main part of the Gamow-Teller strength should be found at higher excitation energies, which, however, has not been established due to the lack of experimental data. Aiming at pursuing this problem, the ^{14}N(p,n)^{14}O reaction has been measured at E_p=70 MeV and θ_n=0°–60° with small contaminants by using a gas target. ^{14}N gas was contained in a cell having 6-μm thick Havar windows at a pressure of 1 atm. The target thickness was 5 cm, which gives an energy loss comparable to other sources of energy spread. Owing to the newly installed beam buncher, the intensity of 20–90 nA was obtained after beam pulse selection by 1/8. A typical excitation energy spectrum is shown in Fig. 1. The l=0 Gamow-Teller strength will be extracted from the angular dependence of the spectra by using the multipole-decomposition analysis.

References

1) Aroua S., Navratil P., Zamick L., Fayache M.S., Barrett B.R., Vary J.P., and Heyde K., Nucl. Phys. **A720** (2003) 71.

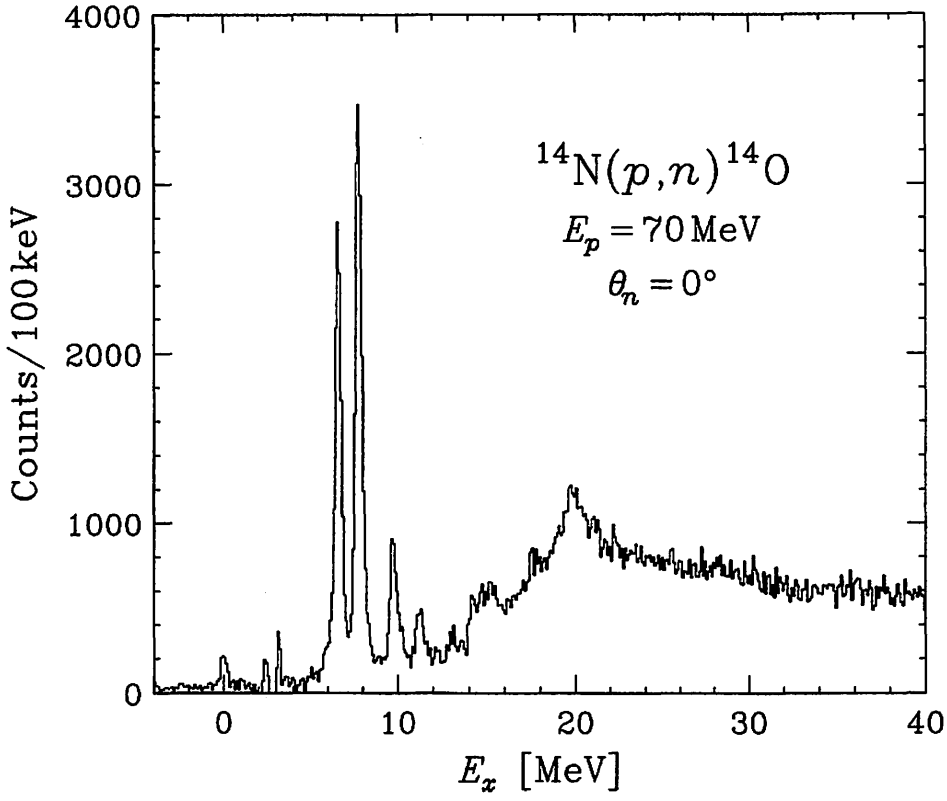

Figure 1. Typical excitation energy spectrum of the $^{14}N(p,n)^{14}O$ reaction at E_x=70 MeV and θ_n=0°, after subtracting the background from the gas-cell window.

I. 2. Reduction of the Gamow-Teller Matrix Element for the β-decay in ^{70}Ga-^{70}Zn by the 35-MeV (*p,n*) Reaction on ^{70}Zn

Orihara H., Terakawa A.[*], *Suzuki H.*[*], *Kikuchi Y.*[*], *Kumagai K.*[*], *G. C. Jon.*[**], *Ishii K.*[***], *and Ohnuma H.*[****]

Tohoku Institute of Technology, Yagiyama-Kasumicho, Sendai 982-8577, Japan
Cyclotron and Radioisotope center, Tohoku University[*]
Institute of Physics, Academia Sinica, Nankang Taipei, Taiwan 11592[**]
Department of Quantum Science and Energy Engineering, Tohoku University[***]
Department of Physics, Chiba Institute of Technology, Chiba 275-0023, Japan[****]

The (*p,n*) reaction has provided us with information about spin-isospin, as well as isospin excitation modes in nuclei. One can selectively excite the spin-flip components in the (*p,n*) reaction at intermediate energies[1] through the relatively strong spin-isospin effective interaction ($V_{\sigma\tau}$). Low energy 35-MeV (*p,n*) reactions, due to the strong spin non-flip isovector effective interaction (V_{τ}), give us equivalent information on both excitation modes. Moreover, it gives us a sufficient energy resolution to discuss (*p,n*) strength for individual nuclear levels[2,3], although exchange contributions are important at low energies. Various problems associated with the distorted-wave (DW) analysis of low-energy (*p,n*) data were discussed in detail by Ohnuma et al[4]. It has been found possible to obtain basically the same information as that at intermediate energies if careful analysis including exchange terms is carried out.

Recently, a simple but reliable linear relation has been found by Orihara et al.[5] to calibrate the 35-MeV (*p,n*) cross section to the corresponding GT matrix element by the aid of the cross section for the IAS transition in the same reaction, and obtained GT-matrix elements have been successfully compared with those at the intermediate energy (*p,n*) reactions. One of the interesting samples for application of this method is prediction of the GT matrix element for the $1^+ \rightarrow 0^+$ transition in the ^{70}Ga – ^{70}Zn system as illustrated in Fig. 1.

As shown in Fig. 1, the parent nucleus ^{70}Ga has two modes of decay occurring simultaneously with a half-life 21.14 minutes[6], and with the percentage p of total decay occurring in the mode under consideration. Beta-decay of the 1^+ ground state of ^{70}Ga is

dominated by the β^- decay to the 0^+ ground state of ^{70}Ge. The contribution of p to the log ft is proportional to log p[7]. The old compilation for the log ft value of electron capture β-decay of ^{70}Ga in Ref. 6 was 5.0 with the branching of 0.2%, and the reported value by Brumster[8] was 4.8 with the percentage 0.24%, while it has been further revised in the recent compilation[9] as 4.7 for the log ft value with 0.41% in Ref. 6 as shown in Fig. 1. As such, it seems significant to study this β-ray strength by other method, for example, with the (p,n) reaction by which we are able to reduce the corresponding B(GT) value. The transition having quite small branching with a large GT matrix element may present a good place to determine an important GT matrix element by the (p,n) reaction.

In this report, we discuss measurements of the weakly populated ground state transition in the ^{70}Zn$(p,n)^{70}$Ga reaction by means of high-resolution 35-MeV experiments. By the aid of the measurements for IAS transition, we suggest a new complementally value of the GT matrix element for $1^+ \rightarrow 0^+$ transition in the ^{70}Ga – ^{70}Zn system, applying the method in Ref. 5.

The experiment was carried out using a 35 MeV proton beam from the AVF cyclotron and the time-of-flight facilities[11,12] at the Cyclotron and Radioisotope Center at Tohoku University. A beam swinger system was used to measure angular distributions of emitted neutrons between 0° and 140° (lab). The target was a 4.04mg/cm^2-thick metallic foil of ^{70}Zn enriched to 85 %. Neutrons were detected by an array of twelve detectors, which were located at 44.3 m from the target and contained a total of 23.2 liters of NE213 scintillator. The detector efficiencies were obtained from Monte Carlo calculations for monoenergetic neutrons with $E \leq 34$ MeV. Absolute detector efficiencies were also measured by counting neutrons from the ^{7}Li$(p,n)^7$Be reaction and comparing its yield with the absolute neutron fluence determined by activation. They were in good agreement with the Monte Carlo calculations. Overall time resolution was typically 1.3 ns corresponding to 174 keV for the most energetic neutrons. Main contributions to this resolution were attributed to the time spread of the beam burst of incident protons. Errors in the absolute scale of the cross sections were estimated to be less than 15%. Further experimental details have been given in a previous report[11,12].

Figure 2 shows an excitation energy neutron spectrum measured at 20-degrees. The weakly populated peak to the ground state in ^{70}Ga is clearly seen. Background-free and high-resolution measurements have been achieved. The over all energy resolutions are 174 keV and 120keV for ground state and IAS transitions, respectively.

Figure 3 shows angular distributions for neutrons leading to the ground state, and to the IAS at E_x = 8.26MeV. The curve for the IAS transition is macroscopic distorted wave predictions calculated by the computer code DWUCK[13]. Optical potential parameters of Becchetti and Greenlees[14] are used for the entrance channel. Those for the exit channel were self-consistent potential parameters derived by Carlson et al[15]. Parameters for the isovector part of the optical potential to generate the IAS transition are taken from Ref. 16. Including cross section magnitudes and their angular distribution, comparison for the IAS transition is quite satisfactory making clear the feature of the L = 0 transition which is common for the IAS and GT transitions. Also illustrated, in Fig. 2, are cross-sections and their angular distribution for the $0^+ \rightarrow 1^+$ transition leading to the ground state in ^{70}Ga. Though cross-section magnitudes for the IAS transition are almost 30 times larger than those for the ground state transition, these angular distributions are quite similar, except the angles at valleys due to the Q-value difference between these two transitions.

The linear relation to calibrate the (p,n) cross section to the corresponding GT matrix element by the aid of the cross section for the IAS transition in the same reaction as described by the following relation as described in Ref. 5:

$$B(\mathrm{GT}: 1^+ \rightarrow 0^+) = \frac{1}{3} < N > \frac{\left(\frac{d\sigma}{d\Omega}\right)_{0^+ \rightarrow 1^+,\, peak}}{\frac{1}{T_0} \cdot \left(\frac{d\sigma}{d\Omega}\right)_{IAS,\, peak}}$$

with <N>= 1.96 ± 0.11 as reported in Ref. 5. T_0 is the target isospin, being not introduced in Ref. 5, where only T_0 = 1 case is discussed. The factor of 1/3 is due to the spin of the initial state.

By taking into accounts the ratio of the cross section described before, we obtain the B(GT) value as 0.109 ± 0.016. We translate the B(GT) into logft values by following relation, assuming the free values for vector and axial-vector coupling constants as $(g_A/g_A)^2$ = $(1.251)^2$.

$$ft = \frac{6170}{B(\mathrm{GT})\left(\frac{g_V}{g_A}\right)^2}$$

Thus, we obtain log ft = 4.56 ± 0.06. The latter may be compared with log ft = 4.7 in Fig.1. The present log ft value yields (0.56 ± 0.07)% for the branching of electron capture β-decay from ^{70}Ga to ^{70}Zn.

In a summary, the weakly populated ground state transition in the ^{70}Zn(p,n) ^{70}Ga reaction was observed successfully by means of high-resolution 35-MeV experiments. By the aid of the measurements for IAS transition, we obtained a new value of the GT matrix element for $1^+ \rightarrow 0^+$ transition in the ^{70}Ga – ^{70}Zn system. The present result suggested that the GT matrix element might be lager than that reported by β-decay experiments.

References

1) Taddeucci T. N. et al., Nucl. Phys. **A469** (1987) 125.
2) Orihara H. et al., Phys. Rev. Lett. **47** (1981) 301.
3) Furukawa K. et al., Phys. Rev. C **36** (1987) 1686.
4) Ohnuma H. et al., Nucl. Phys. **A467** (1987) 61.
5) Orihara H. et al., Phys. Lett. **B539** (2002) 40-44.
6) Table of Isotope Eighth Edition (1998), ed. by Firestone R. B., et al.
7) Moszkowski S. A., Phys. Rev. **82** (1951)35.
8) Table of Isotope Seventh Edition (1978), ed. by Lederer C. M. and Shirley V. S.
9) Brumster U., Z. Physik **A273** (1975) 85.
10) Schrewe U. J. and Schmidt-Ott W.-D., Z. Phys. **A281** (1977) 125.
11) Orihara H. et al., Nucl. Instrum. Methods **188** (1981) 15.
12) Orihara H. et al., Nucl. Instrum. Methods **A257** (1987) 189.
13) Kunz P. D., The code DWUCK-4, unpublished.
14) Becchetti F. D. and Greenlees G. W., Phys. Rev. **182** (1969) 1190.
15) Carlson J. D., Zafiratos C. D. and Lind D. A., Nucl. Phys. **A249** (1975) 29.
16) Jon G. C. et al., Phys. Rev. C **62**, 044609-1~5(2000)

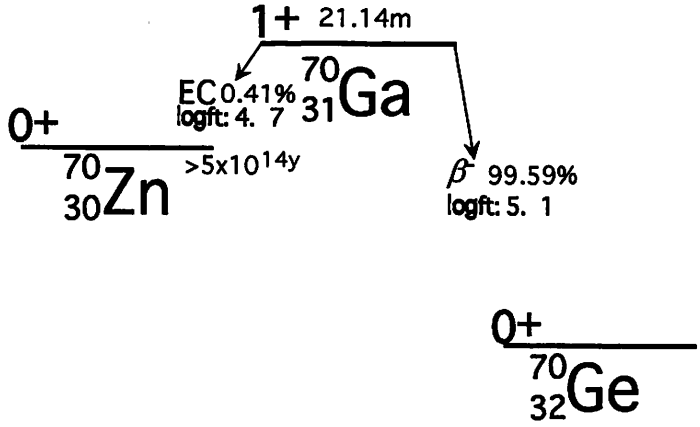

Fig. 1. β-decay scheme for the ^{70}Zn-^{70}Ga-^{70}Ge system.

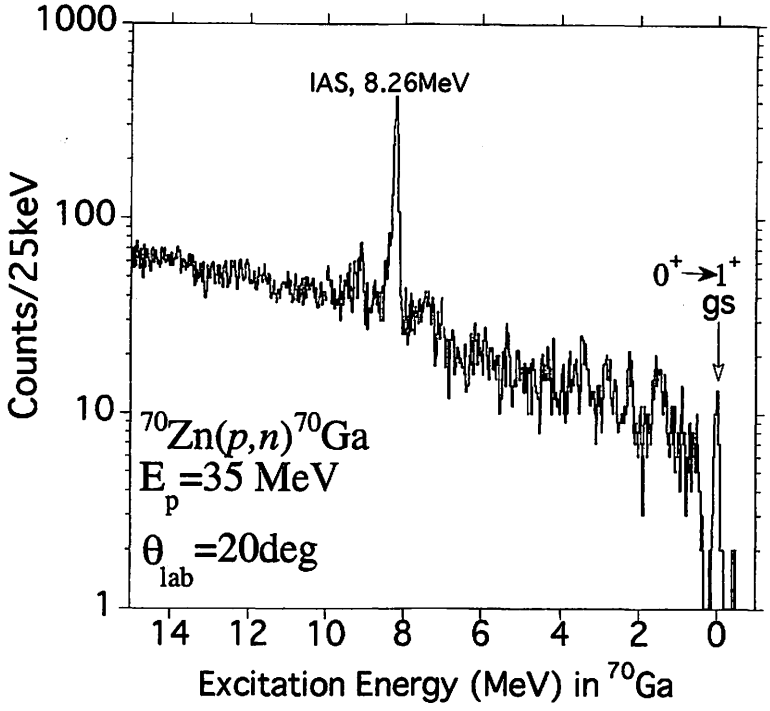

Fig. 2. A sample energy spectrum for the ^{70}Zn(p,n) ^{70}Ga reactions at 20° with a flight path of 44.3m. Energy per channel is 25 keV.

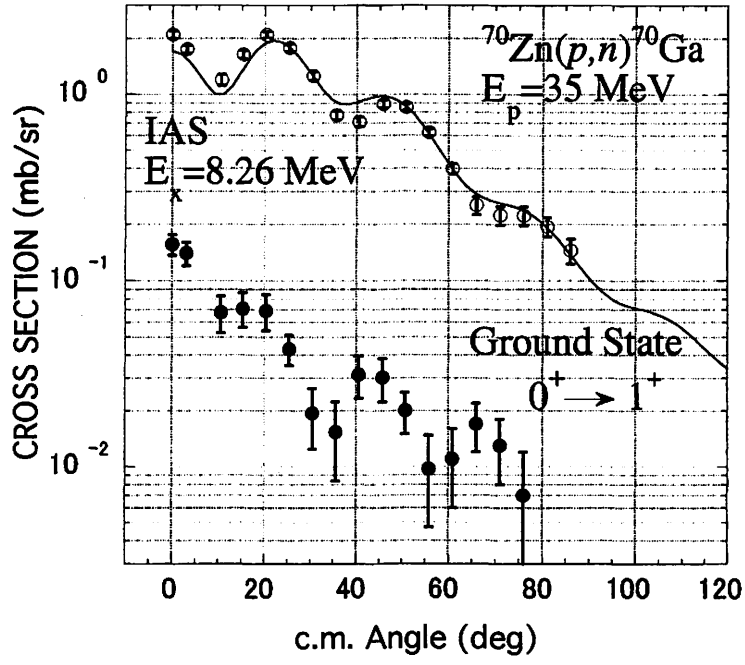

Fig. 3. Differential cross sections for neutrons leading to the IAS and ground state in ^{70}Ga. The curves are macroscopic DWBA results described in text.

I. 3. The $^{16}O(p,n)^{16}F$ Reaction at 50 MeV

Sugimoto N., Orihara H., Terakawa A.*, Suzuki H.*, Kumagai K., Kikuchi Y.,*

Department of Physics, Tohoku University
*Cyclotron and Radioisotope center, Tohoku University**

The isovector $0^+ \rightarrow 0^-$ transition through the (p,n) reaction or inelastic nucleon scattering may provide a good test ground for studies of nuclear pion field. In 1982, Orihara et al. observed[1] the $0^+ \rightarrow 0^-$ transition through the $^{16}O(p,n)^{17}F$ reaction at 35 MeV for the first time and suggested the pion-field effects on the angular distribution of the cross section at the high momentum transfer region (q = 1.0-1.5 fm^{-1}). Although the same attempts to explore the nuclear pion-field effects were made via the the inelastic proton scattering[2] and the (p,n) reaction[3], any anomaly for the cross sections at the high momentum transfer was not observed. The problem of the $0^+ \rightarrow 0^-$ transition is still in controversy.

In order to investigate the nuclear pion-field as well as the discrepancy between the previous results, we have started a systematic study of the isovector $0^+ \rightarrow 0^-$ transition by means of the $^{16}O(p,n)^{17}F$ reaction at the incident energy range from 35 to 80 MeV. In this report preliminary results for the $^{16}O(p,n)^{17}F$ reaction at 50 MeV will be described.

The experiment was performed using a momentum-analyzed 50-MeV proton beam from the AVF cyclotron and the neutron time-of-flight (TOF) facility[4] at CYRIC. The cyclotron beam bursts provided at a frequency of 16 MHz were chopped by the sinusoidal beam chopping system[5] to provide a sufficient dynamic range (493 nsec) for the TOF measurement. A Mylar $(C_{10}H_8O_4)_n$ foil target was bombarded by the chopped beam with a beam intensity of about 5 nA. The target thickness was 11 mg/cm^2. Neutrons emitted from the target were measured using the 16 neutron detectors containing BC501A liquid scintillator located at 43.68 m from the target. Angular distributions of the neutrons were measured with the beam swinger system. The signals from the neutron detectors were processed by the CAMAC-based data acquisition system.

Figure 1 shows a typical neutron spectrum together with the results of the peak-deconvolution analysis for the low-lying states. Neutron energy resolution was about 184 keV (FWHM). In Figs. 2-5 the measured angular distributions of the differential cross section are compared with results of the microscopic Distorted Wave Born Approximation (DWBA) calculations performed with the code DWBA74[6]. We used the global optical potential parameters by Becchetti and Greenlees[7] for the entrance channel, and those by Carlson[8] for the exit channel. In addition, the Michigan 3-range Yukawa (M3Y) potential of Bertsch et al.[9] was used for the nucleon-nucleon (NN) effective interaction. In order to obtain the wave functions for the initial and final states, the shell-model calculations were performed using the shell-model code OXBASH[10] where the 2-particle-2-hole configurations within the $0p1s0d$ shell-model space were assumed while the effective NN interaction by Millener and Kurath[11] was employed.

The comparisons between the experimental and theoretical results have shown that the angular distributions for the 1^-, 2^- and 3^- transitions are reproduced by the DWBA calculations with normalization factors 1.0, 0.5 and 1.0, respectively. However, it is difficult to compare the experimental result for the 0^- transition with that of the calculation at this stage because of the poor statistics and the insufficient energy resolution.

Recently, a beam bunching system was built and installed[12] in the injection line for the AVF cyclotron at CYRIC to increase the beam intensity. Thus, we are planning to improve the statistics for the $0^+ \rightarrow 0^-$ measurements using a higher intensity beam.

References

1) Orihara H. et al., Phys. Rev. Lett. **49** (1982) 1318.
2) Hosono K. et al., Phys. Rev. C **30** (1984) 746.
3) Maday R. et al., Phys. Rev. C **56** (1997) 3210.
4) Terakawa A. et al., Nucl. Instr. and Meth. A491 (2002) 419.
5) Terakawa A. et al., Nucl. Instr. and Meth. A, in press.
6) Schaeffer R. and Raynal J., the computer code DWBA74, unpublished.
7) Becchetti F.D. and Greenlees G.W., Phys. Rev. **192** (1969) 1190.
8) Carlson G.D. et al., Nucl. Phys. A **249** (1975) 29.
9) Bertsch G. et al., Nucl. Phys. A **284** (1977) 399.
10) Etchegoyen et al., the shell-model code OXBASH, unpublished.
11) Millener D.J. and Kurath D., Nucl. Phys. A **255** (1975) 315.
12) Suzuki H. et al., this annual report.

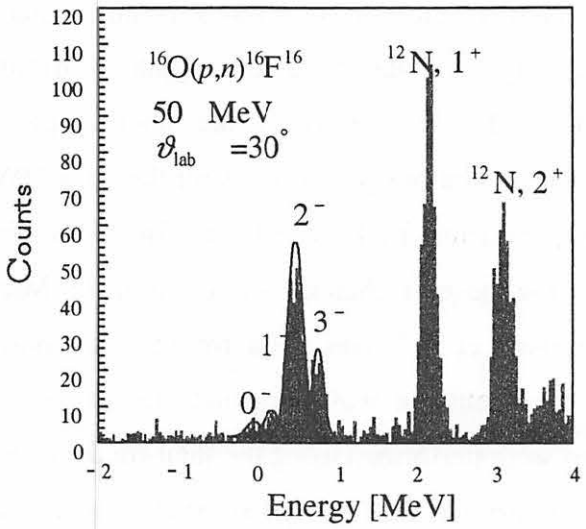

Fig. 1. Excitation energy spectrum of the residual ^{16}F. The solid lines show the results of the peak-deconvolution analysis.

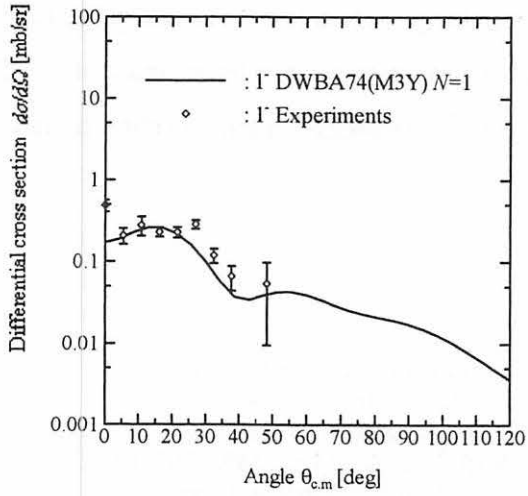

Fig. 2. Angular distribution of the differential cross section for the $0^+ \rightarrow 1^-$ transitions via the $^{16}O(p,n)^{16}F$ reaction (E_x = 0.19 MeV).

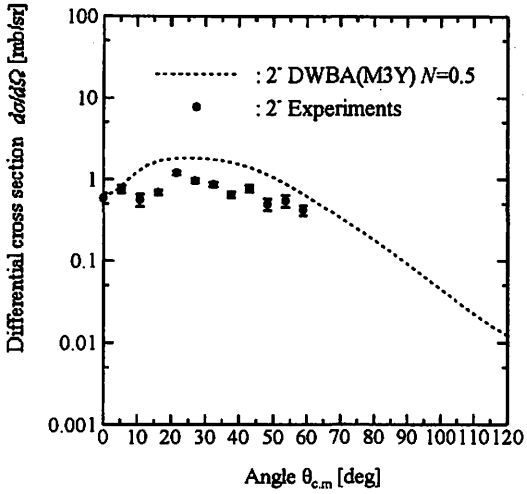

Fig. 3. Angular distribution of the differential cross section for the $0^+ \rightarrow 2^-$ transitions via the $^{16}O(p,n)^{16}F$ reaction ($E_x = 0.42$ MeV).

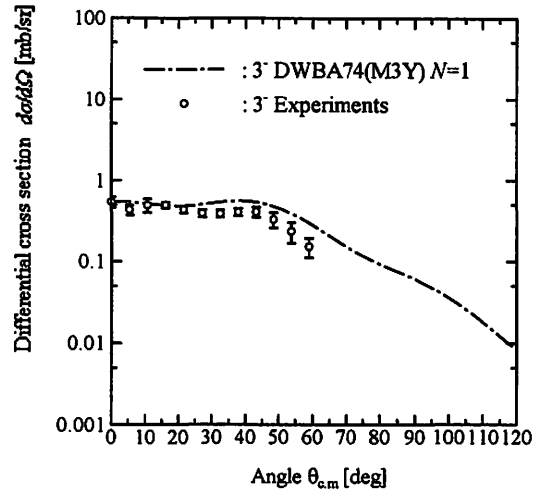

Fig. 4. Angular distribution of the differential cross section for the $0^+ \rightarrow 3^-$ transitions via the $^{16}O(p,n)^{16}F$ reaction ($E_x = 0.72$ MeV).

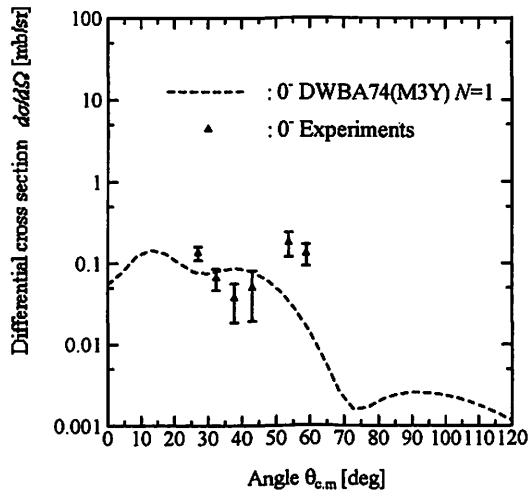

Fig. 5. Angular distribution of the differential cross section for the $0^+ \rightarrow 0^-$ transitions via the $^{16}O(p,n)^{16}F$ reaction ($E_x = 0$ MeV).

I. 4. Nucleon Density Distributions in Nuclei Studied by the Microscopic Lane-model Analysis for the Isobaric-analog-state Transition

Terakawa A., Okamura H., Suzuki H., Sugimoto N. Shinozaki H., Hasegawa T., Fukushima S., Kumagai K., and Orihara H.

Cyclotron and Radioisotope Center, Tohoku University

The isobaric analog state (IAS) is excited by the (*p,n*) reaction via an isovector potential (Lane potential) V_{pn} which can be derived from the Lane model[1] using the following equation:

$$V_{pn} = (T)^{-1/2}(V_n - V_p), \qquad (1)$$

where V_p and V_n are proton-target and neutron-target potentials, respectively. T is the isospin of the target nucleus. When the V_p and V_n are generated from the nucleon-nucleus folding potentials on the basis of both nucleon-nucleon interaction and nucleon densities (ρ_p, ρ_n), the V_{pn} depends on the neutron-proton density difference ($\rho_n - \rho_p$)[2),3)]. Thus, the (p,n_{IAS}) reaction is expected to be affected by the neutron-proton density difference and to provide a good place for studies of the nucleon density distributions in nuclei.

In this work we aim to study the nucleon density distributions in nuclei by comparing the experimental cross sections and angular distributions for the IAS transition through the (*p,n*) reaction as well as the elastic proton scattering at the same incident energy with those for the theoretical calculations including the theoretical or semi-empirical nucleon-densities[4)].

The experiments were performed using a 65 MeV-proton beam from the AVF cyclotron[5)] at CYRIC. The proton beam energy was chosen so that the systematic data[6)] of the elastic proton scattering at 65 MeV performed at RCNP, Osaka University can be employed as the proton data for the above comparison. The proton beam was momentum-analyzed by the analyzing magnet (ANA3)[7)] which has been designed to

provide a momentum resolution of 1/2400. In addition, the sinusoidal beam chopping system[8] was used to obtain a sufficient dynamic range (493 nsec between the beam bursts) for the neutron time-of-flight (TOF) measurements.

The chopped beam was delivered into the neutron TOF facility[9]. The targets used were isotopically enriched ^{42}Ca (99 %) and ^{208}Pb (98 %) metallic foils. The target thicknesses were 5.0 mg/cm^2 for ^{42}Ca and 9.7 mg/cm^2 for ^{208}Pb. Energies of the emitted neutrons were measured by means of a time-of-flight technique using the large-volume neutron-detector system located at a distance of 43 m from the target. Angular distributions of the neutrons were measured in the angular range from $\theta_{lab.} = 0^\circ$ to 60° with the beam swinger system.

Figure 1 shows typical neutron spectra of the ^{42}Ca, ^{208}Pb(p,n) reactions at 65 MeV. The IAS transitions have been observed at the ground state of ^{42}Sc and E_x = 15.18 MeV in ^{208}Bi. In Fig. 2 the measured angular distribution of the differential cross section for the ^{42}Ca, (p,n_{IAS}) reaction is shown. The microscopic Lane-model analysis for the observed angular distributions is now in progress.

References

1) Lane A. M., Nucl. Phys. **35** (1962) 676.
2) Ning P. and Halderson D., J. Phys. G. Nucl. Phys. **11** (1985) 827.
3) Min D. et al., Z. Phys. A **340** (1991) 17.
4) Gambhir Y. K. and Bhagwat A. A., Mod. Phys. Lett. A **17** (2002) 1215.
5) Shinozuka T., et al., CYRIC Annual Report, 2000, p.19.
6) Sakaguchi H. et al., Phys. Rev. C **26** (1982) 944.
7) Terakawa A. et al., CYRIC Annual Report, 2002, p.20.
8) Terakawa A. et al., Nucl. Instrum. Methods A, in press.
9) Terakawa A. et al., Nucl. Instrum. Methods A **491** (2002) 419.

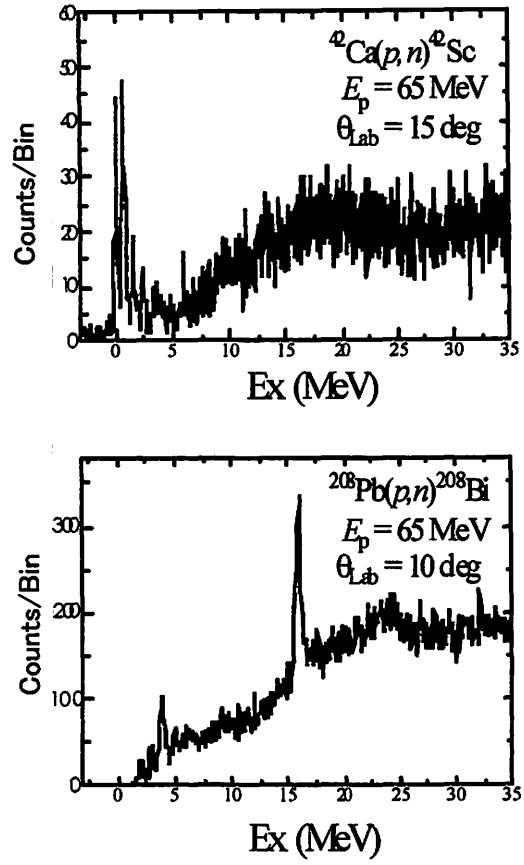

Fig. 1. Typical neutron spectra observed in the ^{42}Ca, ^{208}Pb (p,n) reactions at 65 MeV.

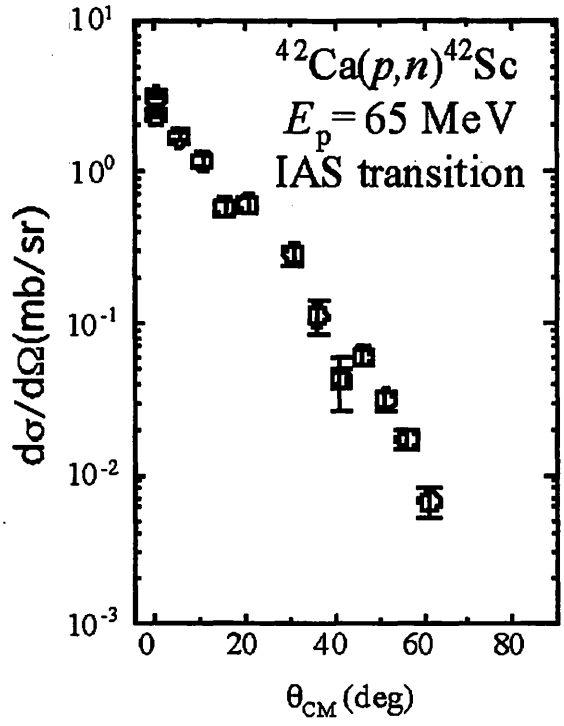

Fig. 2. Angular distribution of the differential cross section for the IAS transition leading to the ground state in ^{42}Sc.

I. 5. Mass Separation of Proton Induced Fission Products by the CYRIC RF-IGISOL

Sonoda T., Fujita M., Yamazaki A.*, Endo T.*, Goto A., Miyashita Y., Sato N., Suzuki T., Tanaka E.*, and Shinozuka T.**

Department of Physics, Tohoku University
*Cyclotron and Radioisotope Center, Tohoku University**

The study of medium-mass neutron rich nuclei far from the valley of beta-stability represents the first important step toward the understanding of nuclear structure and r-process. Unstable radioactive beams of such exotic nuclei can be produced in two complementary ways, the ISOL-method and the in-flight separation method[1]. In the ISOL method that has been used by CERN-ISOLDE[2], University of Jyvaskyla[3], University of Leuven[4], and our group[5], radioactive nuclei are mainly produced by the proton-induced fission reaction with actinide target. Recent progress in this way is largely due to the development of ion-source that is equipped with on-line isotope separator.

A new type of ion-source, RF-Ion Guide[6], has been developed using a large gas cell equipped with dc and rf electric field (Fig.1). A large gas cell has a greater advantage for stopping capability of energetic fission products in gas than the corresponding yields in ordinary small size gas cell ion guide. And additional electric fields can totally control ions in the cell which can reduce the loss by the neutralization and diffusion process. The dc field gives a relatively high velocity in order to quickly guide the ions toward exit the cell and the rf field avoid the loss of ions by impinging on the wall and realize the effective extraction from the exit hall.

The experiments have been performed by using 50 MeV proton-induced fission of ^{238}U at Cyclotron and Radioisotope Center. The targets consist of two 20 mg/cm^2 neutral uranium foils and are surrounded 16 ug/cm^2 Aluminum foils. To avoid neutralization of ions by plasma effect, the target region has been separated by the Aluminum foil to the He gas stopping region. The beam current was typically about 1.0 μA on target. Mass separated ions are collected on an aluminized Mylar tape of the tape transport system. The

optimum electric field in the gas cell and magnetic field of the mass separator was determined by measuring the beta-ray activities of fission products at each mass number. The identification and the determination of radioactivities of fission products were made by the gamma-ray spectrometry using two high pure Ge (HPGe) detectors (Fig.2). Preliminary results show that the yield for the RF-Ion Guide system is about three times larger than that for the ordinary our ion guide system. It is clearly proved that the RF ion guide method with big volume could function well.

Further technical developments have been planned; 1) Gas purification, to reduce the molecular compounds with a cold-trap in the cell, 2) increase the He gas pressure up to 100 Torr from present 30 Torr, 3) modification of the skimmer region to SPIG. It is expected that the yield of fission products will be improved by an order of magnitude greater than the present performance.

References

1) Huyse M. et al., Nucl. Instrum. Methods **B187** (2002) 535.
2) Forkel-Wirth D., Bollen G., Hyperfine Interact.,**129**,1 (2000).
3) Aysto J., Nucl. Phys. **A693** (2001) 477.
4) Van Duppen P. et al., Hyperfine Interact. **127**,401 (2000).
5) Kudo H. et al., Nucl. Instrum. Methods **B126** (1997) 209.
6) Wada M. et al., Nucl. Instrum. Methods **B204** (2003) 570.

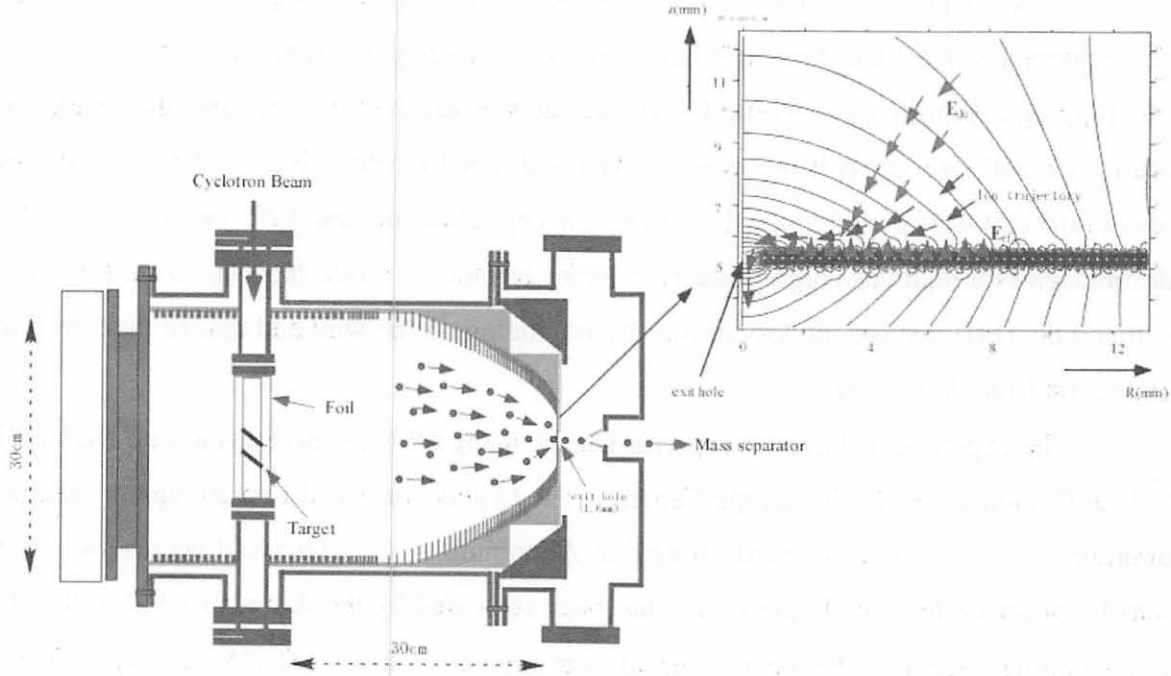

Fig. 1. Cross-sectional view of RF Ion guide gas cell of the on line setup.

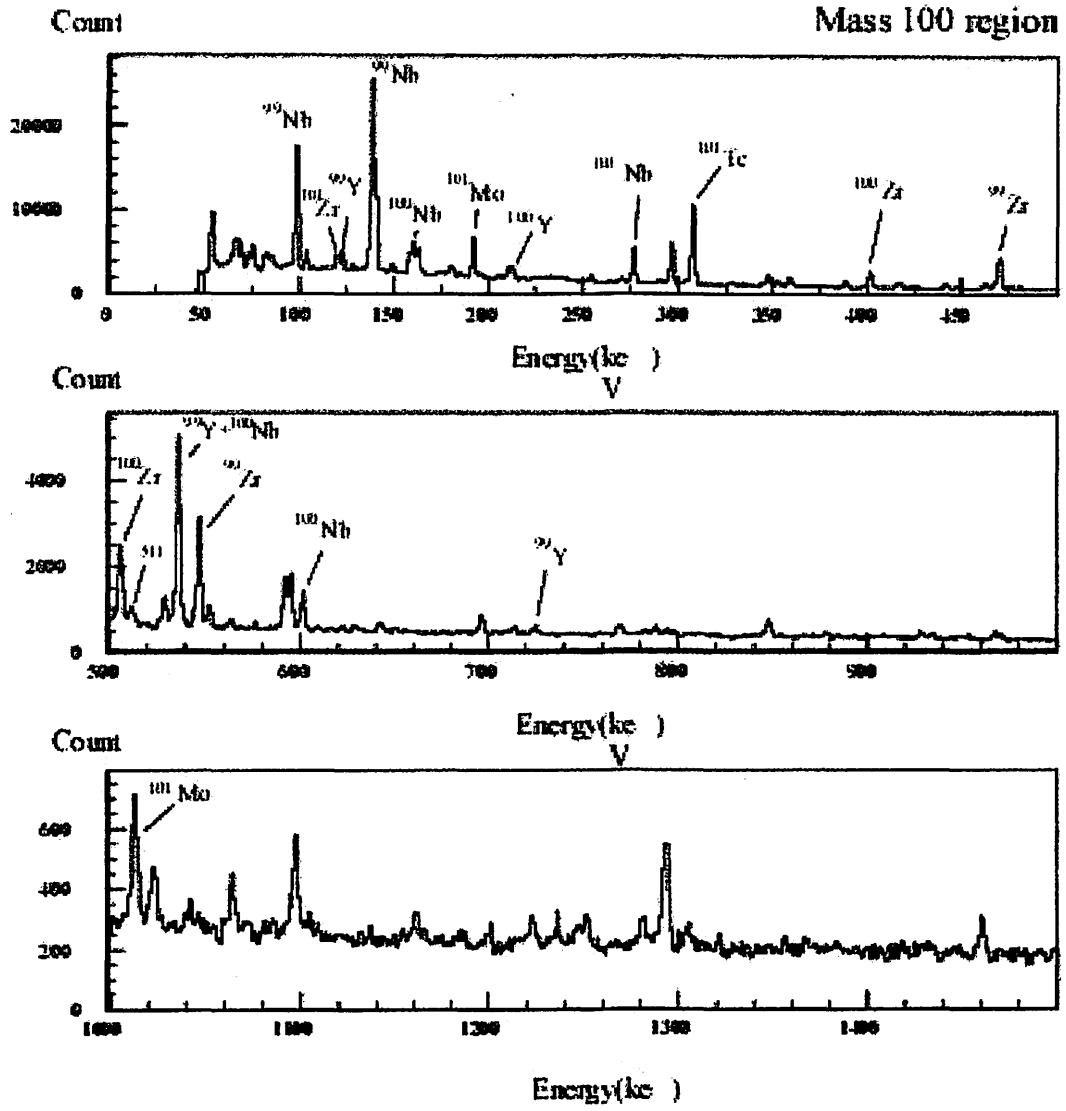

Fig. 2. Gamma spectra measured by Ge detector where is placed at the tape transport system (1 hour measurement).

I. 6. Measurement of the Nuclear G-factor of the 27⁻ High-spin Isomer State of ^{152}Dy

Fujita M., Endo T., Yamazaki A., Miyake T., Tanaka E., Sonoda T., Suzuki T.*, Goto A.*, Miyashita Y.*, Sato N.*, Wakabayashi Y.**, Hokoiwa N.**, Kibe M.**, Fukuchi T.***, Odahara A.****, Gono Y.**, and Shinozuka T.*

Cyclotron and Radioisotope center, Tohoku University
*Department of Physics, Tohoku University**
*Department of Physics, Kyushu University***
*Center for Nuclear Science (CNS), University of Tokyo****
*Faculty of Technology, Nishinippon Institute of Technology*****

The g-factor of the 27⁻ isomer state of ^{152}Dy has been measured using the Time-Integral Perturbed Angular Distribution (TIPAD) method. The high-spin states of ^{152}Dy have been populated by ^{141}Pr(^{16}O,p4n)^{152}Dy reaction at E = 115 MeV from the new AVF cyclotron at CYRIC. An enriched ^{141}Pr target of 6 mg/cm^2 thickness was placed in an external magnetic field (B_{ext}) of 20.3 kG applied perpendicularly to the beam-detector plane. Figure 1 shows the time-integral perturbed angular distributions of γ-rays emitted from the 27⁻ state.

In the case of paramagnetic materials, such as rare earth elements, the effective magnetic field at the nucleus (B_{eff}) is obtained from the relation $B_{eff} = \beta B_{ext}$,where β is called the paramagnetic correction factor, and must be measured independently to obtain the g-factor.

The paramagnetic factor of Dy ions in Pr target has been determined to be 4.2(5) by the Time-Differential Perturbed Angular Distribution (TDPAD) measurement of the 21⁻ state of ^{152}Dy. Because the g-factor of this 21⁻ isomer state has been known to be +0.55(6)[1], we could deduce the effective magnetic field in case of this experimental condition by measuring the Larmor frequency of the nuclear spin precession of this state. Fortunately since both of high-spin isomer states of ^{152}Dy have been populated simultaneously. Figure 2 shows a TDPAD spectrum of this state and the effective magnetic field has been obtained to be 8.50(95) T, which corresponds to $\beta = 4.2$.

As a result, the g-factor of the 27^- isomer state of ^{152}Dy has been obtained to be +0.09(5) and has been found to be much smaller than the expected value of +0.39. It has been deduced from a fully aligned configuration of $\pi(h^2_{11/2}) \otimes \nu(f^2_{7/2}\, h_{9/2}\, i_{13/2})$[2], which is expected as an yrast state as a result of Deformed Independent Particle Model (DIPM)[3] calculation. As seen in Table 1, present data suggest the configuration of $\pi(h_{11/2}\, d_{3/2}) \otimes \nu(i^2_{13/2}\, h_{9/2} f_{7/2})$, however the excitation energy of this configurations has been expected to be more than 2 MeV higher than that of the yrast state in the DIPM calculation. Systematic measurements in the high-spin isomer states of Dy isotope are needed to understand this contradiction, so we are planning to measure the g-factor of the high-spin state in other Dy isotopes.

References

1) Meerdinger J.C. et al., Phys. Rev. Lett. **42** (1979) 23.
2) Cerkaski M. et al., Nucl. Phys. **A315** (1979) 269.
3) Døssing T., Neergård K. and Sagawa H., Phys. Scr. **24** (1981) 258.

Table 1. Expected g-factors for possible configurations.

configuration	g (expected)	*E*x (MeV)	deformation
$\pi(h^2_{11/2}) \otimes \nu(f^2_{7/2}\, h_{9/2}\, i_{13/2})$	+ 0.36 (5)	6.79	–0.097
$\pi(h_{11/2}\, d_{3/2}) \otimes \nu(i^2_{13/2}\, h_{9/2} f_{7/2})$	+ 0.15 (5)	9.02	–0.091

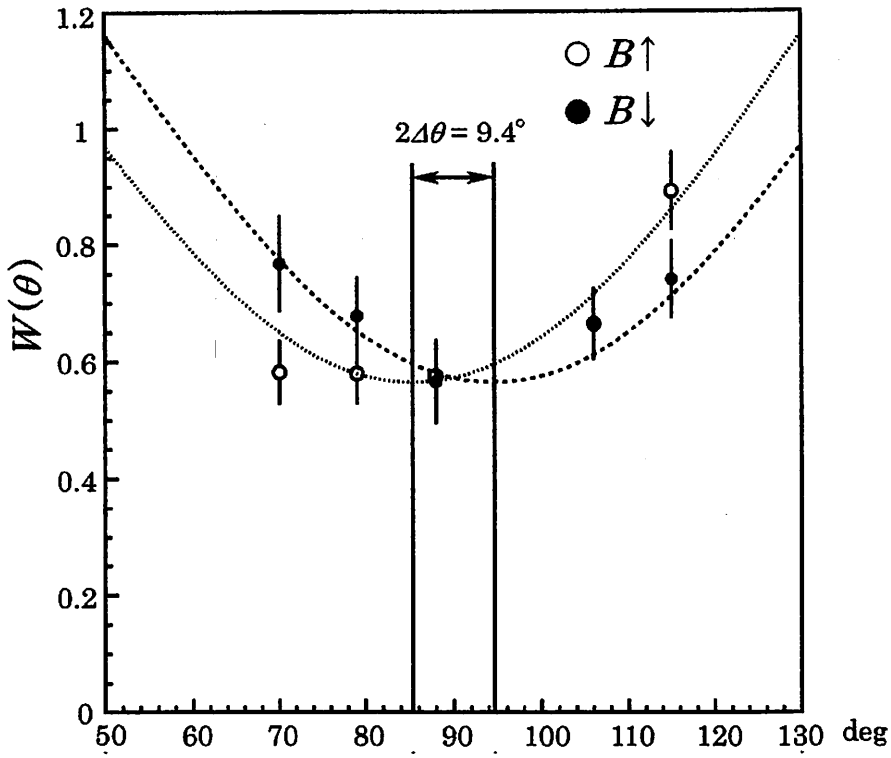

Figure 1. A TIPAD spectrum of 220.6 keV γ-ray emitted from 27^- high-spin isomer state of ^{152}Dy.

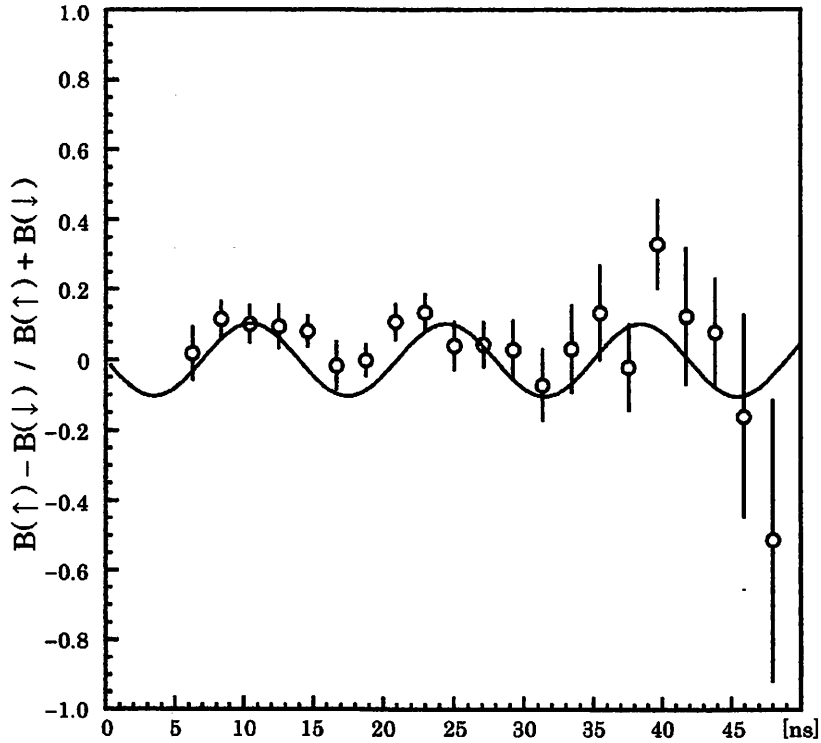

Figure 2. A TDPAD spectrum of 262.4 keV γ-ray emitted from 21^- high-spin isomer state of ^{152}Dy.

I. 7. Half-life Measurement of ^{70}Br and Non-analog Beta Decay

Suzuki T., Miyake T., Endo T., Fujita M., Yamazaki A., Goto A., Miyashita Y., Sato N., Sonoda T., Tanaka E., and Shinozuka T.

Cyclotron and Radioisotope Center, Tohoku University

Precise measurements for the *ft* value of $0^+ \rightarrow 0^+$ superallowed Fermi beta decays are important to test the electro weak standard model[1]. These studies are used to determine the weak vector coupling constant. However in order to extract the precise G_V values from the experimental *ft* values of the beta-decay, we need the small theoretical corrections. In this case, the corrected *ft* value denoted *Ft* is related with effective weak vector coupling constant G_V', as follows:

$$Ft = ft(1+\delta_R)(1-\delta_C) = \frac{K}{2G_R'}$$

where *f* is the statistical rate function, t is the partial half-life, δ_R is the calculated outer radioactive corrections, δ_C is calculated isospin symmetry breaking correction, and K is the known constant value. At the lighter nuclei region, *ft* value has been determined in good precision, however, in the $A \geq 62$ region, only few measurements were exist, i.e. Chiba *et. al.*[2], because of production is the small cross sections and short half-lives. Recently, ^{62}Ga, ^{74}Rb have been measured at ISOLDE[3], TRIUMF[4], and Jyväskylä[5]. But it is not enough to discuss precisely these corrections by the obtained Q-beta values and branching ratios including the non-analog $0^+ \rightarrow 0^+$ transitions[6-9].

The experiments have been done for the beta-decay of ^{70}Br produced by the ^{58}Ni(^{14}N,2n) reaction. A 5.0mg/cm^2-thick natural Nickel target was bombarded by 100-300pnA, 44 MeV Nitrogen 3^+ ions from 930 AVF cyclotron at Tohoku University. The high-speed target transfer system was used[10], which can transport target about50 msec . Nitrogen beam is chopped by pulse-chopper located at the injection line of cyclotron.

After beam irradiation, the beam was stopped and the target was transported to the detector position in 50msec. The emitted beta particles have been detected by counter-telescope which consisted 40mmϕ NE102A with 1mm-thick and 10cm square BC408 plastic scintillators with 10cm-thick mounted on R329-02 Hamamatsu photomultipliers. For gamma rays, the clover type Germanium detector with transistor-reset preamplifiers was placed opposite side of the beta counters. For half-life measurement, 1kHz pulses from synthesizer were counted by CAMAC scalar. The list data of gamma, beta and time gated by beta events have been recorded.

In the half-life analysis, beta particle is discriminated at Am-Be Compton edge. These events were including ^{67}As, ^{70}As and ^{69}Se, which half-lives are 42.5sec, 52.6min, 27.4sec, respectively very longer than ^{70}Br's one. The time spectrum is shown FIG. 1. From this spectrum, we have obtained the half-life of ^{70}Br is 81.19 ± 1.78 msec. This data is good agreement with previous data[11,12].

Figure 2 shows a decay scheme of ^{70}Br [13,14]. Since the ^{70}Br has a long-life isomer[15,16], the transition 945keV of $2^+ \rightarrow 0^+$ on ^{70}Se can be feed from the isomer of ^{70}Br as well as the grand state of ^{70}Br. If non-analog transition from the grand state $^{70}Br(0^+)$ to 945keV 2^+ state of ^{70}Se is exist, the 1066keV gamma ray must be observed. Figure 3 shows the gamma ray spectra coincidenced with beta-rays. In this spectra the 945keV gamma-ray confirmed, but the 1066keV gamma ray is not obviously confirmed.

In Summary, the half-life of ^{70}Br was measured. The result is good agreement with previous data. In the gamma ray analysis with beta-gamma coincidence, the $0^+ \rightarrow 0^+$ transitions from the ^{70}Br is not confirmed.

References

1) Hardy J.C. and Towner I.S., Hyperfine Interactions **132** (2001) 115.
2) Chiba R., Shibasaki S., Numao T., Yokota H., Yamada S., Kotajima K., Itagaki S., Takeda Y., Shinozuka T., Phys. Rev. **C17** (1979) 2219.
3) Oinonen M. et. al., Phys. Lett **B511** (2001) 145.
4) Ball G.C. et. al., Phys. Rev. Lett. **86** (2001) 1454.
5) Blank B., Eur Phys J. **A15** (2002) 121.
6) Delvecchino R.M. and Deahnick W.W., Phys. Rev. Lett. **82** (1999) 488.
7) Zganjar E.F. et. al., Eur. Phys. J. **A15** (2002) 121.
8) Hyman B.C. et. al., Phys. Rev. **C68** (2003) 015501.
9) Hagberg E., Koslowsky V.T., Hardy J.C., Towner I.S., Hykawy, J.G. Savard G., Shinozuka T., Phys. Rev. Lett. **73** (1994) 396.
10) Suzuki T. et. al., CYRIC Ann. Rep. 2002.
11) Alburger D.E., Phys. Rev. **C18** (1978) 1875.

12) Burch Jr. R.H., Galibardi, C.A. Tribble R.E., Phys. Rev. **C38** (1988) 1365.
13) Hees J., Lieb K.P., Raether F., Wormann B., Alber D., Grawe H., Eberth J., Mylaeus T., Z. Phys. **A325** (1986) 45.
14) Mylaeus T. et. al., J. Phys. G: Nucl. Part. Phys. **15** (1989) L135.
15) Piechaczek A., Zganjar E.F., Batchelder J.C., MacDonald B.D., Kulp W.D., Paul S.D., Terry R., Wood J.L., Phys. Rev. **C62** (2000) 054317.
16) Jenkins D.G. et. al., Phys. Rev. **C65** (2002) 064307.

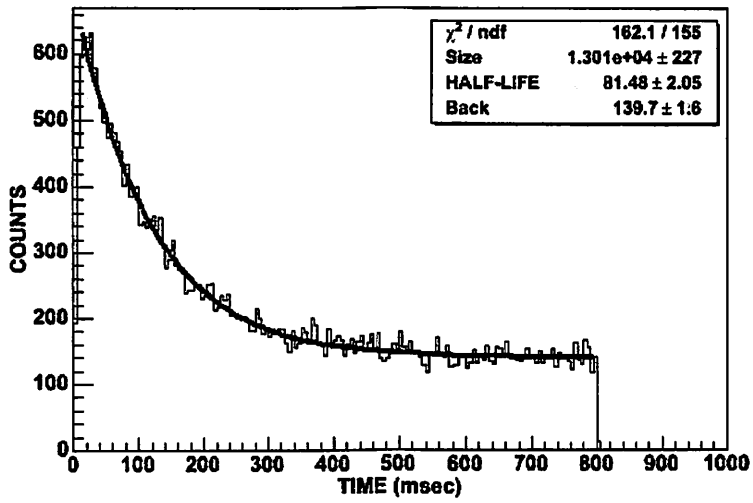

Fig. 1. The time spectrum of ^{70}Br in Mar. 2004 experiments. Adding with data in Jul. 2003, obtained half-life is 81.19 ± 1.78 msec.

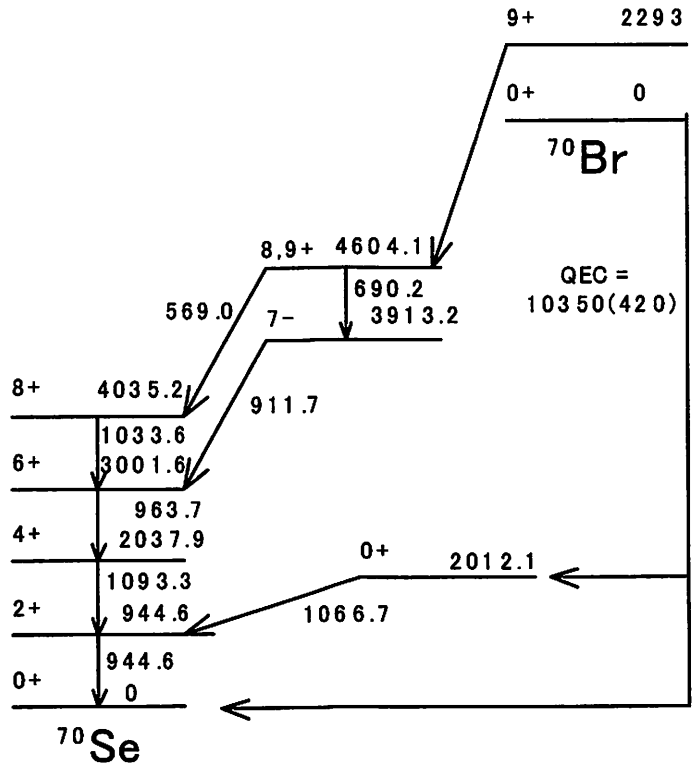

Fig. 2. Level and decay scheme in ^{70}Br from Ref.15 and 16.

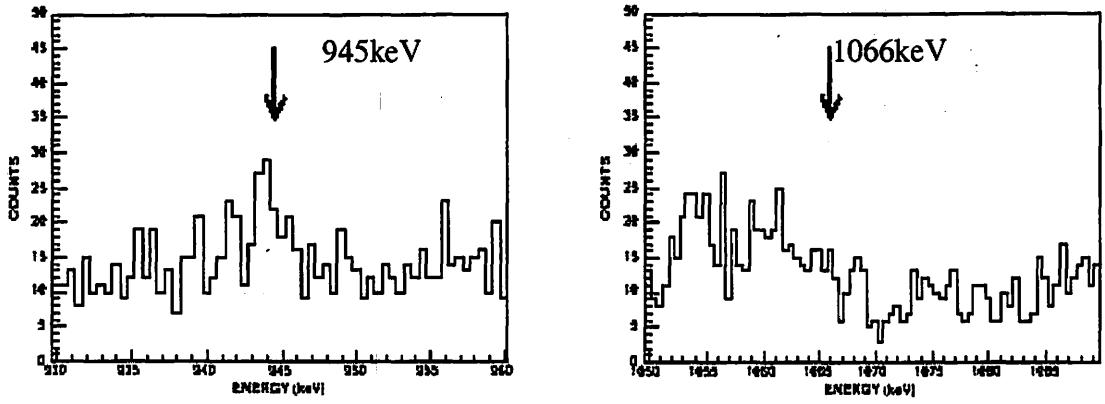

Fig. 3. Gamma spectra with beta-gamma coincidence around 945keV and 1066keV.

II. NUCLEAR INSTRUMENTATION

II. 1. Development of New Data Acquisition Systems

*Okamura H., Terakawa A., Suzuki H., Sugimoto N., Shinozaki H., Hasegawa T., Shinozuka T., Miyake T., Suzuki T., Gotoh A., and Maeda K.**

Cyclotron and Radioisotope center, Tohoku University
*Department of Physics, Graduate School of Sciense, Tohoku University**

Two types of data acquisition (DAQ) systems have been developed for use in experiments at CYRIC. One is a conventional CAMAC-based system but utilizing the FERA bus for improved performance and another is a VME-based system. These platforms are chosen aiming at making the most of existing properties. The considered experiments are medium in scale, typically having an event rate of a few kHz with an event length of several tens of or a hundred words. Experiments being proposed as well as the ones using the facilities recently constructed, e.g., the neutron detector system consisting of 32-set counters and the clover-type Ge-detector array with BaF Compton suppressors, are expected to be covered by these DAQ systems.

The CAMAC/FERA system utilizes a pair of memory modules (LeCroy 4303) in the double-buffer mode; the data are alternately buffered to one module via the FERA bus at a rate of 20 MB/sec while the previously buffered data in another module are transferred to the PC via the CAMAC bus at the same time, so that the slow transfer rate of CAMAC (0.5 MB/sec for TOYO CC/7700-PCI) does not become a bottle neck. The performance is summarized in Fig. 1. The buffer exchange is triggered at a preset size of data by a hand-fabricated module, which takes care of veto logic as well. LeCroy 4303 is also capable of generating LAM at buffer full but only asynchronously with event processing, thus of little use. In the VME system, a similar operation is possible by utilizing multi-functional TDC/ADC modules, CAEN V775/785/792, which incorporate buffer memories, the self-blocking logic, and even the chained block-transfer function for multiple modules. The maximum transfer rate is 26 MB/sec, which is determined by the VME-PCI interface (SBS 617). The overhead of DMA is approximately 100 μs.

Both the systems use personal computers (PC) running a free UNIX clone, Linux, as

host processors for cost-effectiveness. Such a choice is common today and there exist a number of sophisticated systems, yet the UNIDAQ[1], which was developed for the SSC project about 10 years ago, is tentatively employed because it is reasonably versatile and has been familiar to collaborators around CYRIC. The improvement of performance has been realized by developing dedicated device drivers for CAMAC and VME interfaces. For DAQ with a 100% duty factor, which is often the case in cyclotron experiments, a quick response to interrupt is crucial. In the present systems, all the data are collected in the interrupt handler of device driver instead of accessing from user processes, thus allowing access at the highest speed of the hardware. This requires, however, editing the device driver, which is a part of the kernel, depending on the DAQ configuration and accompanies a great danger of freezing the system. For partly relieving this problem, the device drivers are separated into two layers so that the scope of user function is limited as small as possible. For the lower layer of VME device driver, vmehb-2.2.7[2], which was originally developed at NIKHEF, is used by porting to match with Linux kernel-2.4.

References

1) Ball R., Takeuchi Y., Nomachi M. and Timmermans C., UNIDAQ, Software for UNIX-Based Data Acquisition, SDC-93-573 (1993), unpublished.
2) Kruszynska N., vmehb-2.2.7, VME bus Host Bridge (2000), unpublished.

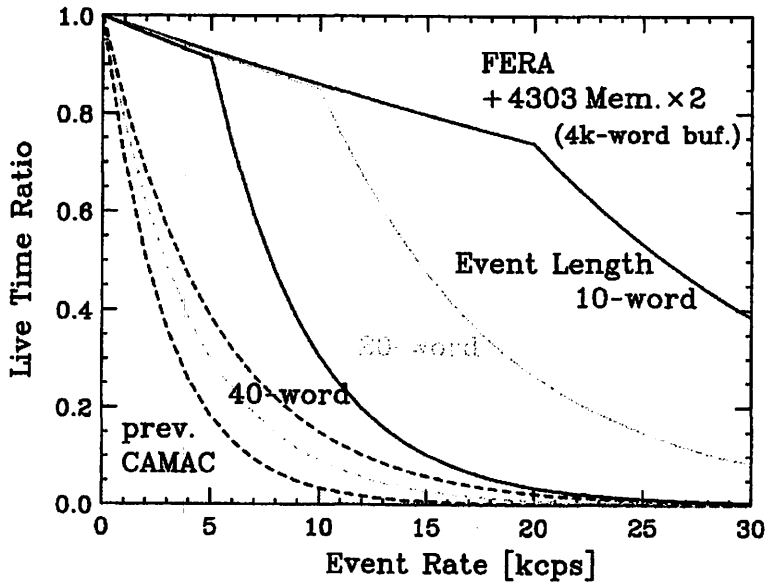

Figure 1. DAQ dead time as a function of event rate and event length is presented compared with the previous system. Practically it is reduced by a factor more than ten, though the transfer rate is not totally increased in the true sense of the word.

II. 2. A New PAC Measurement System Using 6 Clover-type HPGe Detectors

Fujita M., Goto A., Endo T., Yamazaki A., Miyake T., Tanaka E., Sonoda T.*, Suzuki T.*, Miyashita Y.*, Sato N.*, Fujibayashi T.*, Tamura H.*, Maeda K.*, Okamura H., and Shinozuka T.*

Cyclotron and Radioisotope center, Tohoku University
*Department of Physics, Tohoku University**

A new perturbed angular correlation (PAC) measurement system has been installed in combination with the new ion-guide technique at the ISOL facility in CYRIC. The ion-guide is a kind of ion source for the ISOL and has a great advantage of widely applicable to any elements[1]. Recently, a new type of the ion-guide system called "RF ion-guide" have been developed to obtain higher efficiency[2]. The new RF ion-guide system provides us more neutron-rich unstable nuclei produced by proton-induced fission reactions. In addition to a search for double magic ^{78}Ni nuclei and a precise β-γ spectroscopy around this region, the nuclear g-factor measurement for the low lying isomeric states of short-lived isotopes have also been planned. We have already developed 6 sets of clover-type HPGe detectors equipped with 12 pieces of BGO compton suppressors for each clover detector[3]. A new PAC system, which consists of the goniometer for these 6 sets of clover detectors and the permanent magnet with magnetic-flux density of 1.2 T, has been constructed and placed at 2 m higher place than the ISOL beam line (see figure 1). The mass-separated unstable nuclei are transferred to the magnet position from ISOL beam line by the tape transport system.

A VME (Versa Module European) based data acquisition system for this PAC measurement system has been developed as substitute for a CAMAC (Computer Aided Measurement And Control) based one. Since the maximum data transfer rate of a CAMAC system is only ~900 kbyte/sec, it is not suitable for the large scale detector system. On the other hand, the maximum data transfer rate of a VME bus is 40 Mbyte/sec theoretically. In addition, a VME module has high CH density in general, so it can serve to

keep the cost low.

However a VME system is considered to have much noise than a CAMAC system, so it has been kept away from using high-resolution detectors such as HPGe detectors. Therefore we have needed to ascertain whether a VME system can be applied to this PAC measurement system. We have examined a V785 ADC module for the clover-type HPGe detectors, which is multievent peak sensing ADC with 32 CH input and has 12 bit resolution. The Integral Non Linearity (INL) and the Differential Non Linearity (DNL) of this module have been measured and results are listed in table 1 along with the warranted values of a CAMAC ADC module (AD413A). The INL has been found to be in good agreement with the warranted value, however the DNL has a little exceeded the warranted value. Although further efforts to reduce noise must be needed to decrease the DNL, this V785 ADC module has been found to be applicable in our purpose. In regard to the speed of data transfer, it has been found to be 1.5 Mbyte/sec, but it can be much faster by use of the DMA transfer.

References

1) Ärje J., Äystö J., Honkanen J., Valli K. and Hautojärvi A., Nucl. Inst. Methods **186** (1981) 149.
2) Sonoda T. et al., in this volume.
3) Fujita M. et al., CYRIC annual report (2001).

Table 1. A comparative table between a V785 ADC module (VME) and a AD413A module (CAMAC). The warranted values are shown in parentheses.

	V785 (VME)	AD413A (CAMAC)
Input CH number	32	4
resolution	12 bit	13 bit
INL	± 0.049 % (± 0.1 %)	(± 0.025 %)
DNL	3.73±1.57 % (± 1.5 %)	(± 1.0 %)
A/D conversion	Sliding Scale method	Sliding Scale method

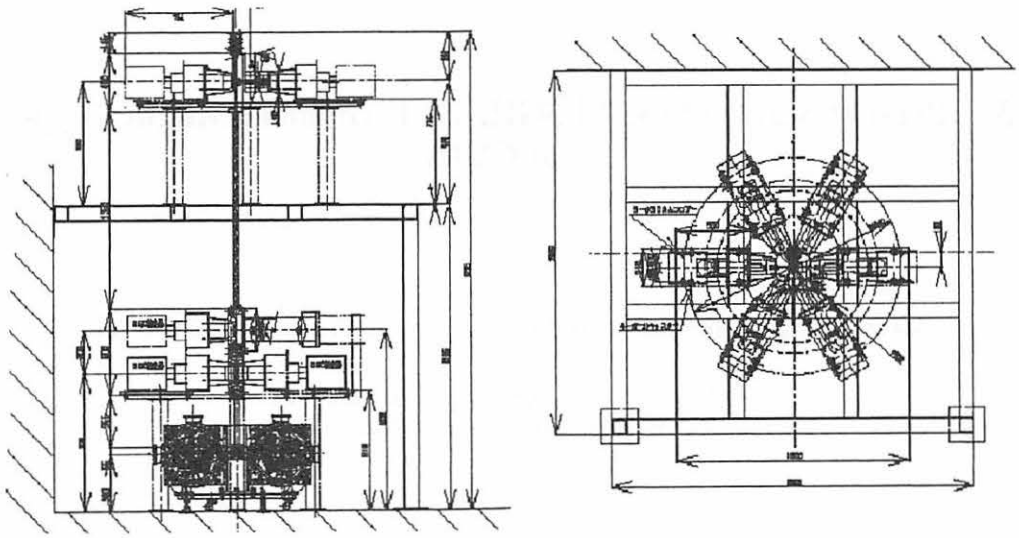

Figure 1. A schematic view of the new PAC measurement system.

II. 3. Present Status of the 14.5GHz all Permanent Magnet Type ECRIS at CYRIC

Miyashita Y., Fujita M., Yamazaki A.*, Tanaka E.*, and Shinozuka T.**

Department of physics, Tohoku University
*Cyclotron and Radioisotope center, Tohoku University**

A 14.5 GHz electron cyclotron resonance ion source (ECRIS) has been installed in February, 2001[1]. This ion source is made of permanent-magnet and has advantages of simple structure and easy handling. The light ions, such as Helium, Carbon, Nitrogen and Oxygen, have been supplied from this ion source and have been accelerated by the K=110MeV cyclotron. But, in the case of light heavy ion, such as Argon, it was not sufficient to obtain the intensities at higher charged ions for the acceleration by the cyclotron. Therefore, several improvements have been performed.

As the first improvement, the plasma chamber has been modified to for adjustable inner length by the movable panel. This made cavity resonator of plasma chamber, and it can effectively optimize these parameters of the resonator to transmit effectively the power of the microwave into the plasma chamber. Figure 1 shows the variation of the extracted ion current to the inner length of plasma chamber. In addition to optimize its length, microwave frequency was optimized at 14.0GHz and 14.5GHz by using a Traveling Wave Tube Amplifier. In comparison with slit current of each frequency, a resonance pattern of cavity resonator was observed in Figure 1. As a result, the extracted ion current has increased by 10~20%, and the reflected power of microwave was decreased. At the same time, the energy of X-ray from ECR chamber was measured by CdZnTe detector. Figure 2 shows the shift of the end-point energy of X-ray and extracted ion current to the plasma chamber length. The end-point energy of X-ray also was affected by cavity resonator, and electron heating in ECR plasma chamber was enlarged. This shows the important properties for the turning of cavity resonator at ECRIS.

The second object of the upgrade is to optimize the magnetic field distribution.

The scaling rule of the magnetic field distribution in ECRIS was proposed by R. Geller[2]. According to this rule, magnetic field should fulfill the following condition[3].

$$\frac{B_{\text{axial(ext)}}}{B_{\text{resonance}}} \geq 2 \quad , \quad \frac{B_{\text{radial}}}{B_{\text{resonance}}} \geq 1.6 \quad \text{and} \quad B_{\text{axial(inj)}} \approx 2B_{\text{axial(ext)}} \qquad (1)$$

Magnetic field intensity of radial direction was increased from 6726G to 8764G by enlarging the diameter of the plasma chamber in 2001[4]. Furthermore, the magnetic field intensity of axial direction at injection side was increased from 9800G to 12461G by inserting the magnetic stainless steel cylinder (SUS 403) in the plasma chamber. Figure 3 shows the calculated magnetic field of axial direction. Magnetic field was calculated using OPERA-3D codes. In calculation, $B_{\text{radial}} / B_{\text{resonance}}$ increased from 1.3 to 1.7, $B_{\text{axial(inj)}} / B_{\text{axial(ext)}}$ increased from 1.1 to 1.3 and $B_{\text{axial(ext)}} / B_{\text{resonance}}$ is 1.7. As a result, the beam intensity of the Ar^{8+} and Ar^{9+} has increased to 15.1eμA and 2.53eμA, the magnetic field distribution has gotten closer to the scaling rule for ECRIS. The extracted ion current is summarized in Table 1. The extracted ion current of ^{12}C and ^{16}O is sufficient, but that of Ne^{7+} and Ar^{9+} is still insufficient. For the improvement of the source performance, it is planed for several ideas. They are the installment of bias electrode in cylinder and the more precise gas flow system.

References

1) Yamazaki A., Fujita M., Tanaka E., Shinozuka T., Yokoi T., Ozawa T., and Tanaka H., Rev. Sci. Instrum. **73** (2002) 589.
2) Geller R., Annu. Rev .Nucl .Part Sci. **40** (1990) 15.
3) Koivisto H., Heikkinen P., Liukkonen E., Arje J., and Vondrasek R., Rev. Sci. Instrum. **73** (2002) 534.
4) Fujita M., Miyashita Y., Yamazaki A., Tanaka E. and Shinozuka T., CYRIC Annual Report (2002).

Table. 1. Extracted ion current for each charge state eμA. Operating conditions for any ions are as follows; microwave power is 200W, extraction voltage is 10kV, no gas mixing method is used.

	1^+	2^+	3^+	4^+	5^+	6^+	7^+	8^+	9^+
^{12}C	46	68		37	4				
^{16}O	94	134	129	125	61	23			
^{20}Ne	77	78	95	78	39	11	2		
^{40}Ar		52	56	54	52	38	24	15	2.5

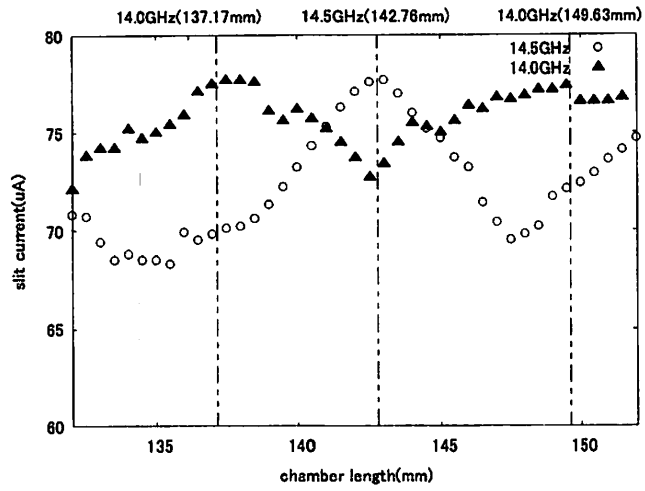

Fig. 1. Plasma chamber length dependence of extracted Ar^{4+} ion current with varying microwave frequency (14.0 and 14.5GHz) of TWTA.

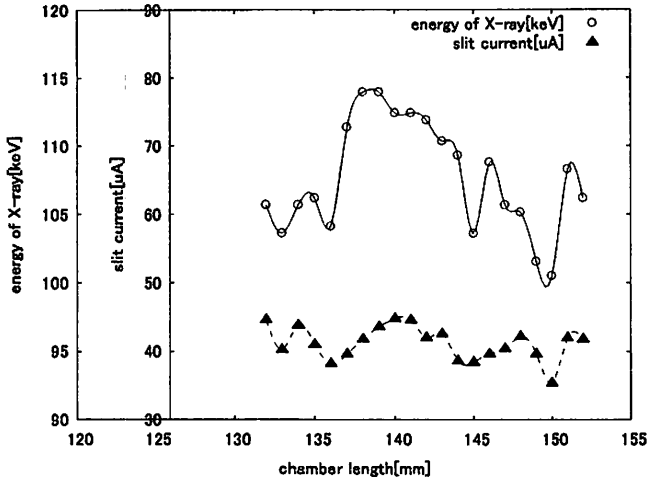

Fig. 2. Plasma chamber length dependence of extracted Ar^{8+} ion current and energy of X-ray. In comparison with Fig. 1., extraction condition is difference with Fig.1. Therefore Fig. 2. was observed many mode of cavity resonator pattern.

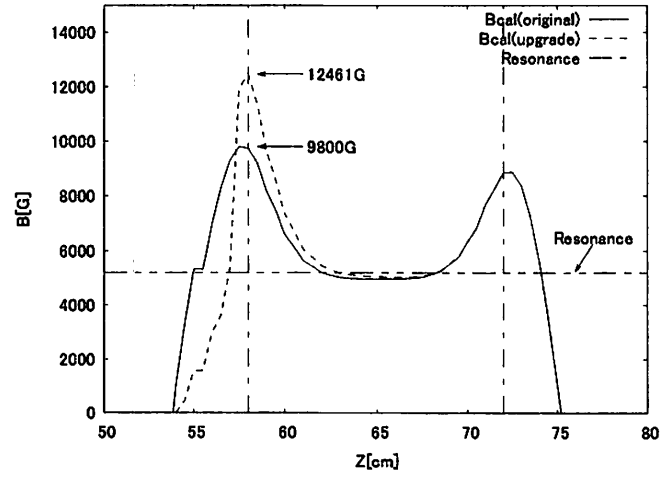

Fig. 3. The calculated magnetic field distribution of axial direction in the plasma chamber using OPERA-3D code.

II. 4. Beam-bunching System for the K=110 AVF Cyclotron at CYRIC

Suzuki H., Terakawa A., Fujita M., Okamura H., Shinozuka T., and Orihara H.[*]

Cyclotron and Radioisotope Center, Tohoku University
Department of Electronic Engineering, Tohoku Institute of Technology[*]

A beam-bunching system has been constructed and installed in the beam injection line of the *K*=110 AVF cyclotron at CYRIC to provide a higher intensity beam for the regular experiments. Before injection of beams into the cyclotron, the beam-buncher generates a pulsed beam from a direct current beam from the external ion source by means of the periodical acceleration and deceleration technique with electric RF field. Beam pulses after the beam-buncher match with the RF phase acceptance of the cyclotron.

Figure 1 shows a schematic drawing of the beam-buncher. It is located at the position of 1.8-m downstream from the median plane of the cyclotron. Acceleration and deceleration gap is a single-type one, consisting of two parallel ring-electrodes made of oxygen-free copper (OFC) sheet. They are insulted with ceramic called Macor. The aperture and gap of the electrodes are 60 mm and 4 mm, respectively. A transversely uniform electric field is generated with hexagonal meshes attached to the ring electrodes. The beam-buncher includes a matching transformer (1:9) and a 450 Ω resister connected to the electrode.

Figure 2 shows the block diagram of the RF voltage for the buncher. One of the two electrodes is excited by a sawtooth-like RF voltage (see Fig. 3) generated from sinusoidal RF signals with the fundamental and higher frequencies up to the third harmonics. The input signal is provided from the low level RF system[1)] for the cyclotron. The amplitude and phase of the fundamental RF are stabilized with a feedback loop. The output signal amplified by a 500 W solid-state amplifier is sent to the beam-buncher. The control system has been built using programmable logic controllers [2)].

Specifications of the bunching system are listed in Table 1. The performance for the beam-buncher is summarized in Table 2. The typical gain in the beam intensity ranges

from 2.3 up to 5.2.

The authors would like to thank Yokoi at NEC TOKIN CO. LTD. and Ohashi at THAMWAY CO. LTD. for technical support during the construction. Thanks are also due to Goto, Ikegami and Kamigaito at RIKEN for fruitful discussions about the design of the beam-buncher.

References

1) Tanigaki M. et al., CYRIC Annual Report 2000, p22.
2) Yokogawa Electric Corporation, Musashino, Tokyo 180-8750, Japan. (http://www.yokogawa.co.jp).

Table 1. Specifications of the beam buncher.

Fundamental input frequency	10.5-22MHz
Fundamental Input level	+10dBm
Output voltage (max).	1200Vp-p
Load impedance	450 Ω
Voltage stability	< 1%
Phase shift	0-400°
Phase stability	<1°

Table 2. Performance of the beam buncher.

Ion	Energy [MeV]	Frequency [MHz]	Harmonics	Gain
$^{1}H^{+}$	65	18.92	1	5.2
$^{2}H^{+}$	40	21.02	2	4.7
$^{4}He^{2+}$	50	16.77	2	3.9
$^{14}N^{3+}$	44	12.80	3	2.3

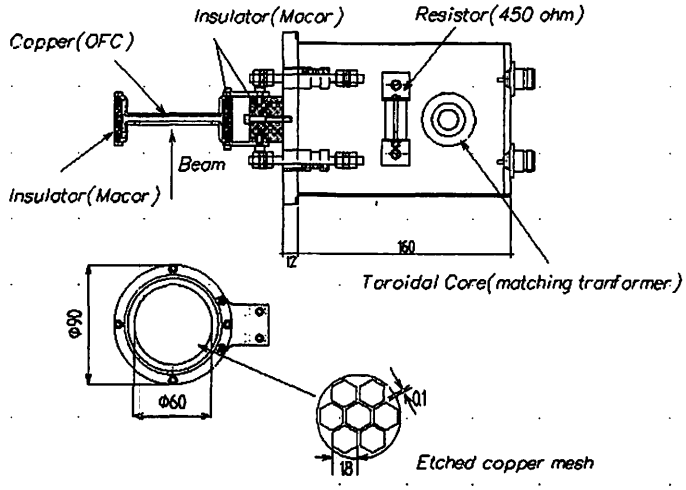

Fig. 1. The design of the beam buncher. The upper electrode (on the side of the cyclotron) is excited by the RF.

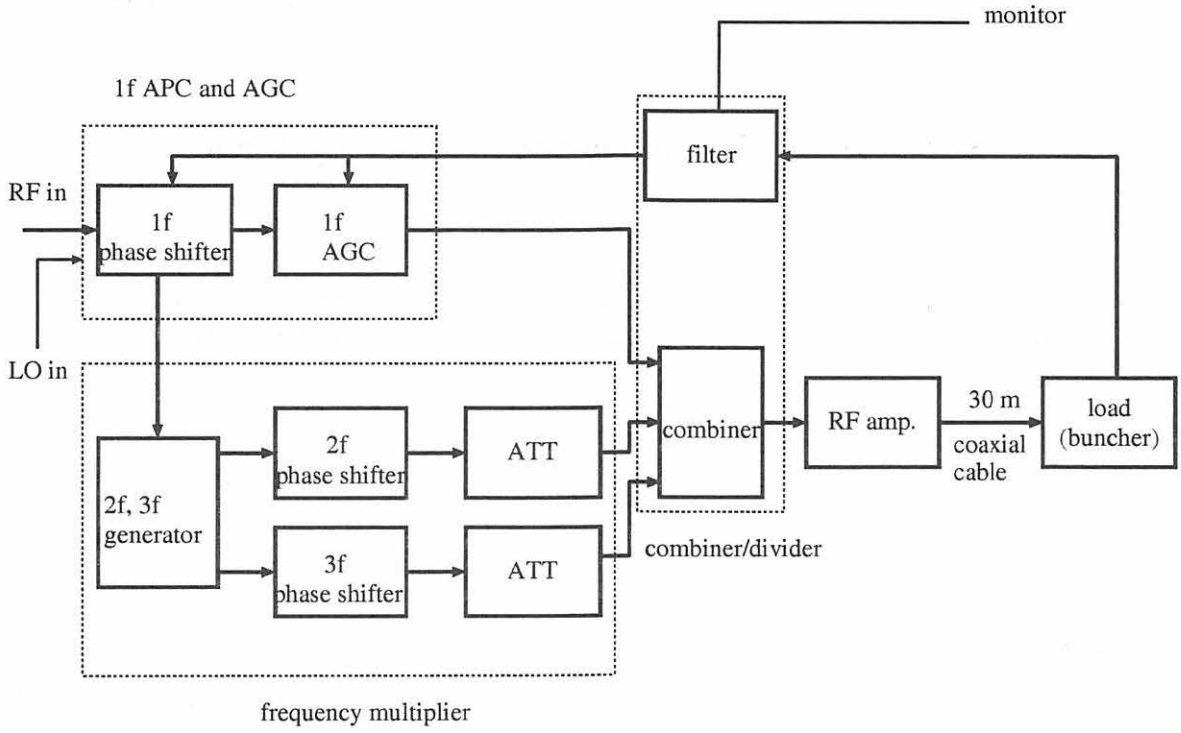

Fig. 2. The block diagram of the RF system for the beam-buncher.

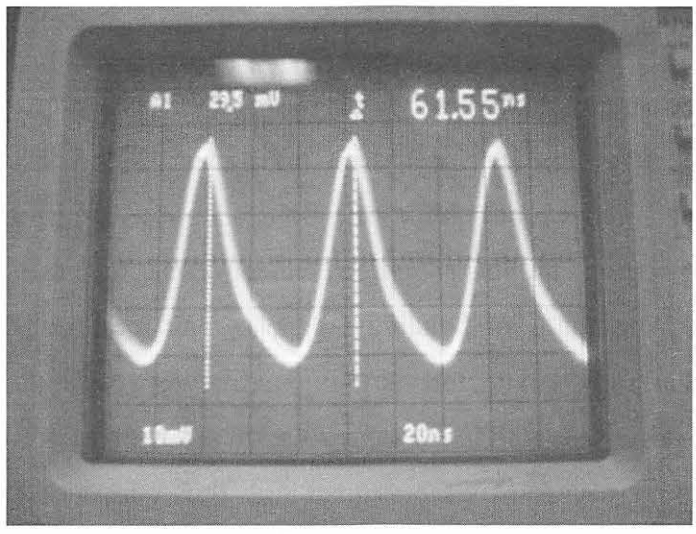

Fig. 3. A monitor signal from the electrode.

II. 5. H^- Acceleration by the 930 AVF Cyclotron

Endo T., Fujita M., Yamazaki A., Miyashita Y., Kan S., Chiba, S.*, Omiya Y.*, Matsumura A.*, Yokokawa S.*, Yokoi T.**, Honma T.***, and Shinozuka T.*

Cyclotron and Radioisotope Center, Tohoku University
*SHI Accelerator Service Ltd.**
*Tokin Machinery***
*National Institute of Radiological Sciences****

Introduction

As one of the projects at CYRIC new cyclotron, high intensity neutron beam has been planned by the negative hydrogen acceleration for various applications. The goal of this project is to supply 300μA proton beam. High intensity neutron beam is expected to be use in nuclear physics, material irradiation and study of BNCT cancer therapy.

Instruments & Methods

Figure 1 illustrates a layout of the new AVF cyclotron and injection- and extraction-lines. Ion sources are located on the under ground level. A negative ion source is installed in another room on the BF1 floor, then ions are injected upward into the central acceleration-region through an inflector electrodes. In negative ion acceleration mode, magnet field directions of bending magnets, main coil and the electric field of inflector electrodes are inverted against these in positive ion acceleration mode. Negative hydrogen (H^-) ions are accelerated in the same rotation direction of positive ion acceleration, then their electrons are stripped by the stripper foil, thus converted into H^+; the H^+ ions after the electron of H^- ions stripping are extracted through the residual magnetic field as shown in the fig.1. The extraction beam line for negative ion acceleration mode consists of one dipole magnet and three quadrupole magnets, then it is connected to the switching magnet at the junction with the beam line for positive acceleration mode.

The multicusp type ion source (BLAKE-V[1]) is used for the negative ion source it can extract 300μA H^- beam. One third of the H^- beam(100 μA) is transported to a faraday

cup at the inlet of the cyclotron and one third of the H^- beam at the cyclotron entrance(30 μA@main probe) is injected into the central region of cyclotron with the aid of the beam buncher[2].

The position of foil stripper, which is thin carbon foil of 50μg/cm^2 is able to move its radial position and azimuthal angle in the cyclotron. These two parameters, which determine the energy and starting point of H^+ ions' trajectory, are adjusted to obtain the optimum extraction trajectory.

Acceleration test & results

Before H^- acceleration test, the preparations of each components have been tuned for the ion source, test of magnet inverting, attaching carbon foil to the moving arm and the test of RF operation under the inverted magnetic field of main coil. Figure 3 shows H^- current profile along the radial direction of acceleration chamber. The beam intensity of H^- doesn't decrease by the gas dissociation or electric stripping[3] of negative ions.

In order to obtain the optimum parameters for the radial position and the azimuthal angle, beam current is measured by the Faraday cup in front of the first Q-magnet in the extraction beam line. Figure 4 shows the position parameters in which H^+ beam after stripping is extracted from cyclotron.

Since the source position of H^+ ion is definitely set at the foil stripping, the beam transport is easily tuned and, finally, 95% of the beam current of accelerated beam is transported to the switching magnet.

Concluding remarks

Now we are making effort to achieve 300μA high intensity H^- beam with the 930 AVF cyclotron. Instruments have already been prepared and acceleration test is now underway. So far, 22μA and 95% extraction efficiency was achieved.

References

1) Mori Y., Rev. Sci. Instrum. **65** (1994) 4.
2) Suzuki H., ibid.
3) Richardson J. R., Progress in Nuclear Techniques and Instrumentation vol.1 (1965) 3.

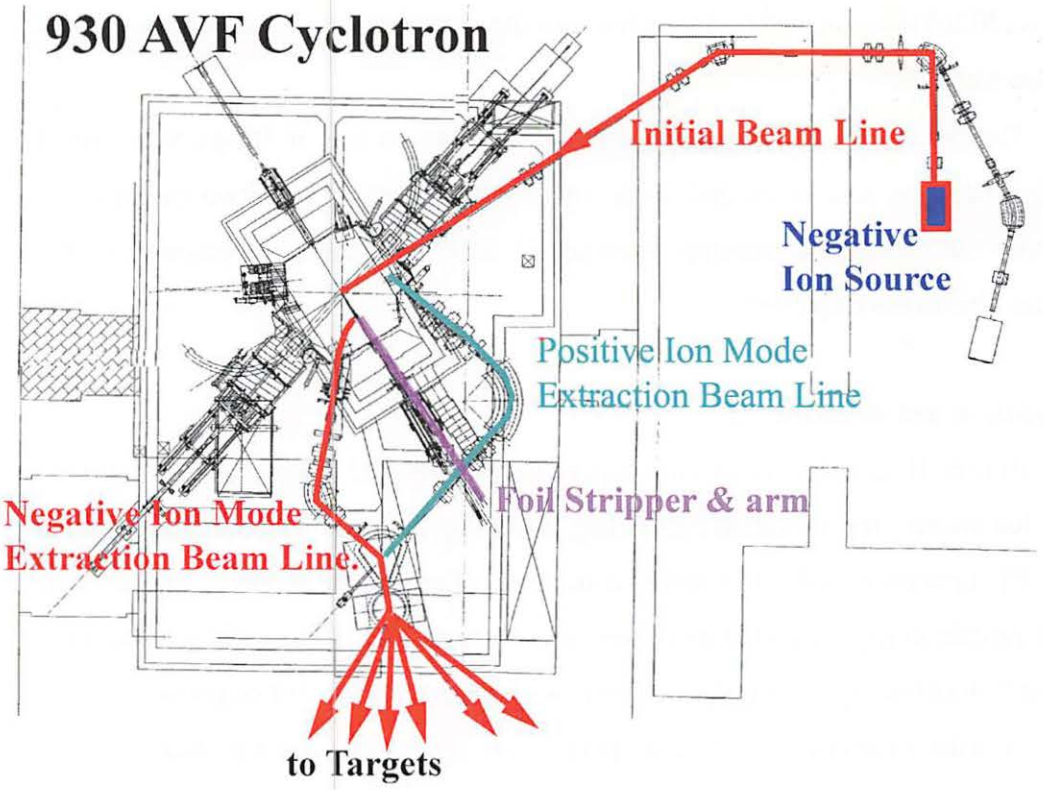

Figure 1. 930 AVF Cyclotron and initial & extraction beam lines.

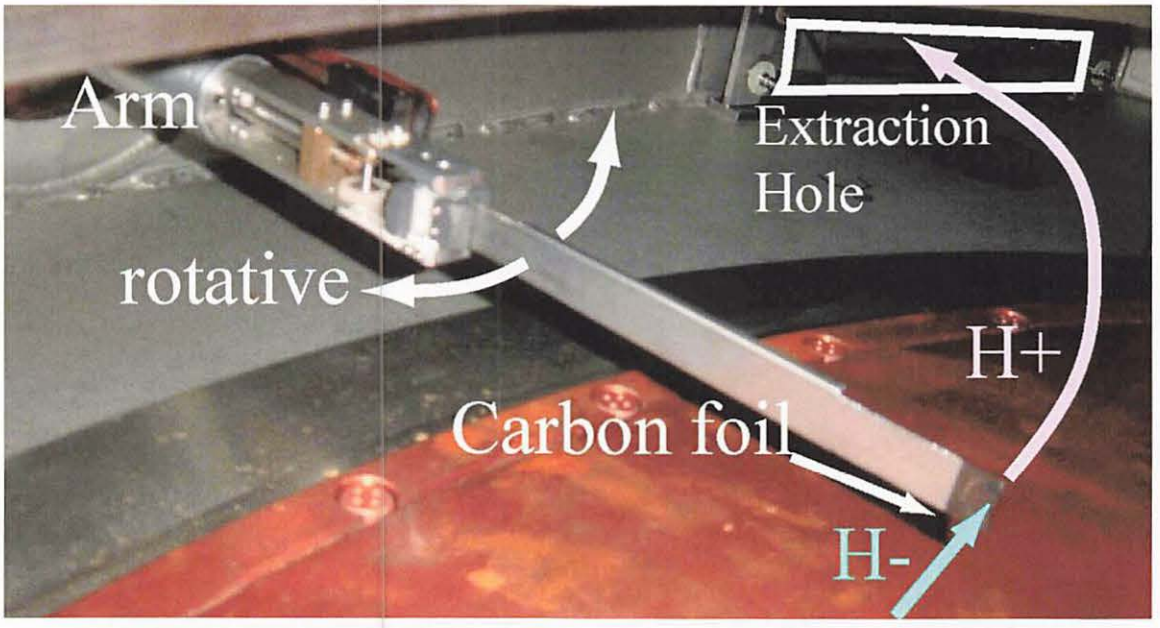

Figure 2. Foil Stripper & arm. A 50μg carbon foil, looks black, put on the tip of the arm.

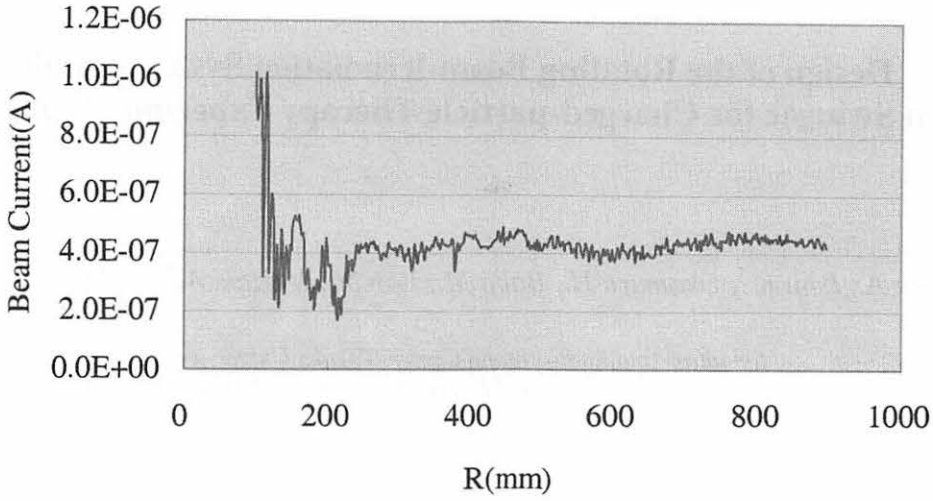

Figure 3. Change of beam current on the R-direction. It is almost flat except for central region.

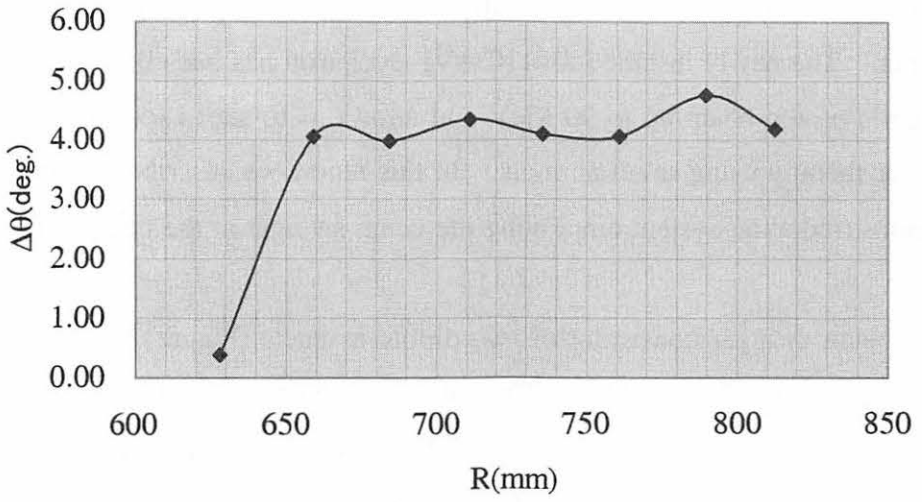

Figure 4. Plot of positions of foil stripper when beam current is observed at the entrance of extraction beam line.

II. 6. Design of the Rotating Beam-irradiation System Employing the Beam Swinger for Charged-particle Therapy Experiments at CYRIC

Terakawa A., Ishii K., Okamura H., Baba M., Itoh M., Ishizaki A.*, and Orihara H.***

Cyclotron and Radioisotope Center, Tohoku University
*Department of Quantum Science and Energy Engineering, Tohoku University**
*Department of Physics, Tohoku Institute of Technology***

In the past more than 20 years the AVF cyclotron facility at Cyclotron and Radioisotope Center (CYRIC), Tohoku University has been used for multipurpose experiments in various fields of research from nuclear physics to nuclear medicine using PET cameras. The newly installed K=110 AVF cyclotron has been designed to provide a more-energetic proton beam up to 90 MeV and allows us to start experimental studies for proton cancer therapy using small animals. In this report we describe a basic design of a rotating beam-irradiation system employing the beam swinger at the neutron time-of-flight facility[1].

The beam swinger consisting of two dipole magnets (Figure 1) changes the beam irradiation angle from 0° to 180°. Thus we are planning to design the therapeutic beam-delivery system on the basis of a broad beam irradiation and construct the rotating gantry by add it to the beam swinger. In the broad beam method the pensile beam form the accelerator is spread so that the irradiation area covers the target tissue size with an uniform fluence using a double scattering system or a beam wobbling system consisting of a pair of wobbling magnets (for horizontal and vertical beam scannings) and a subsequent scatterer.

However, the conventional broad-beam methods cannot be applied to our system because the drift space to install the above instruments for therapeutic-beam delivery is limited between the second dipole magnet and the isocenter of the beam swinger. Thus we will apply a separated irradiation method by shifting the target position. A schematic view of the present irradiation method is shown in Figure 2. The beam is scanned in the

direction of the magnet gap at a frequency of up to 10 – 20 Hz with a wobbling magnet installed between the two dipole magnets. The scanned beam is spread with the scatterer via Coulomb multi-scattering and incident on the target while the separated irradiation in the direction of the rotating axis for the swinger is carried out via the target-position shift. As a result, a uniform irradiation field sufficient for the proton therapy experiments is obtained.

Figure 3 shows the facility planned in the present project. At this stage we are going to design the wobbling magnet, ridge filters, beam-profile and dose monitors, and other related instruments.

References

1) Terakawa A. et al., Nucl. Instrum. Methods A **491** (2002) 419.

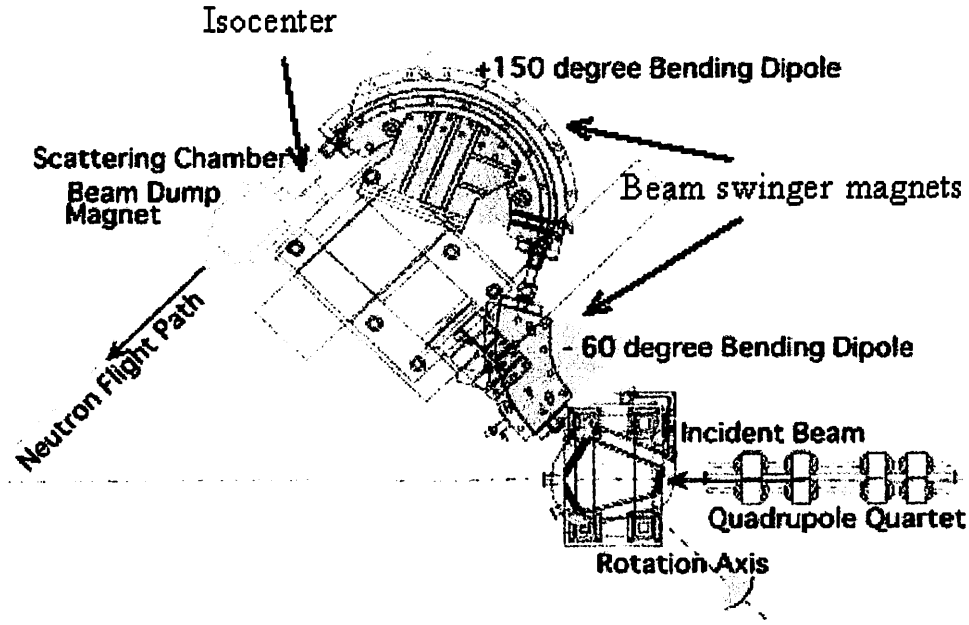

Figure 1. A schematic layout of the beam swinger at CYRIC.

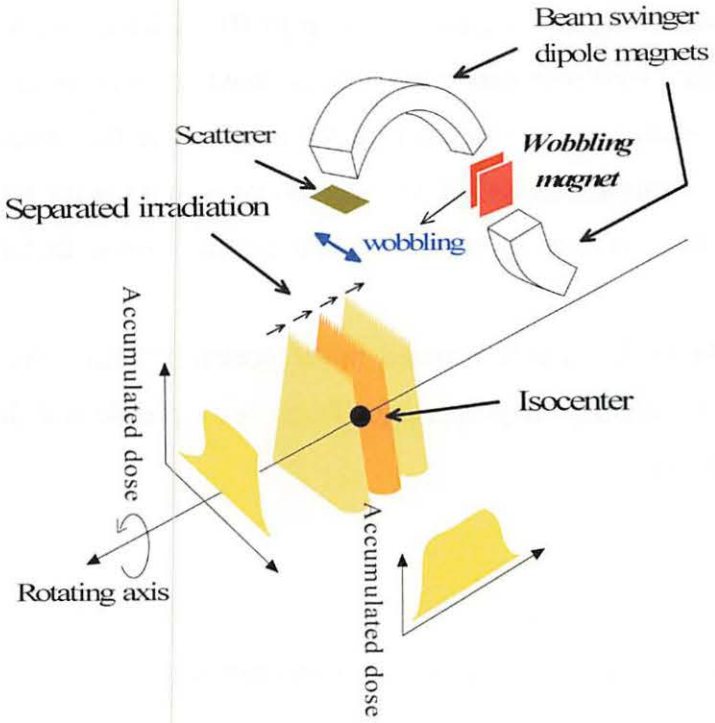

Figure 2. A schematic view for the beam irradiation.

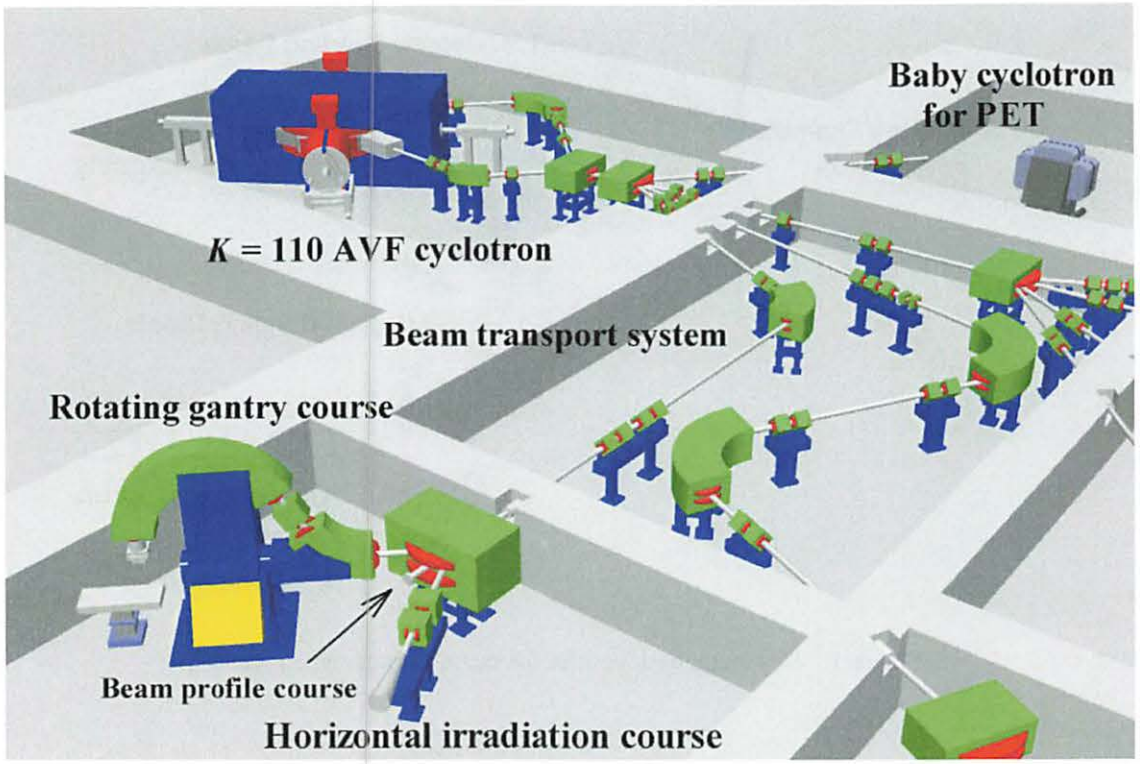

Figure 3. A schematic view of the proton-therapy research project at the K=110 AVF cyclotron facility.

III. NUCLEAR ENGINEERING

III. 1. Experimental Studies on the Neutron Emission Spectra and Activation Cross-section in IFMIF Accelerator Structural Elements

Hagiwara M., Baba M., Uddin M. S. Itoga T., Hirabayashi N., Oishi T., and Yamauchi T.

Cyclotron and Radioisotope Center (CYRIC), Tohoku University

The International Fusion Materials Irradiation Facility (IFMIF) project has been proposed to establish an accelerator-based D-Li neutron source designed to produce an intense fast neutron field for high fluence test irradiations of the fusion reactor candidate materials[1].

To establish the database required for the design of IFMIF, we have been conducting systematic experiments on the neutron emission spectrum and radioactivity accumulation in IFMIF structural elements from 2001[2-5]. In the previous reports (2001, 2002), the results on lithium target for 25, 40 MeV deuterons were reported. The experiments are carried out at the No.5 target room in CYRIC using the AVF cyclotron (K=110 MeV), a beam swinger system and the TOF method, and stack target method.

In the last year, we have carried out new experiments for 40 MeV deuterons with extended techniques and obtained new results for

1) neutron emission spectrum from a thick C, Al target and

2) activation cross-sections of the $^{nat}C(d,x)^{7}Be$, $^{27}Al(d,x)^{7}Be$, ^{22}Na, ^{24}Na reactions using a stacked target technique[6].

The experimental method was almost the same with these in previous experiments[5]. Thirty thin targets of carbon and aluminum with natural composition (200 μm thicknesses) were prepared and stacked to stop the incident beam in the targets to measure not only neutron spectra from a thick C, Al target but also excitation functions of the $^{nat}C(d,x)^{7}Be$, $^{27}Al(d,x)^{7}Be$, ^{22}Na, ^{24}Na reactions concurrently.

The neutron spectra were measured for almost entire range (1-50 MeV) of secondary neutrons at ten laboratory angles between 0- and 110-deg with the two-gain time-of-flight (TOF) method[7] using a beam swinger system. The results are shown in Fig.1 and Fig.2.

The main peaks due to deuteron break-up reaction are observed around 15 MeV having strong angular dependence similar with previous results of Li(d,xn) reactions[2-5]. This yield of the main peak is decreasing with increasing of the mass of target. Such data are very few and will be useful for the model development of the neutron emission.

The number of radioactive nuclides accumulated in the stacked targets was measured by counting the γ-rays from the nuclides of ^{24}Na, ^{22}Na and ^{7}Be using a pure Ge detector. The induced activities were determined with corrections for γ-ray detection efficiency, energy determination and deuteron attenuation using EGS 4[8], TRIM code[9] and Shen's formula[10] respectively. In Figs.3-6, the results of the activation cross-sections are shown, together with other experiments[11], recommended data by the IAEA group and PHITS calculation[13]. No other data are available for carbon but the present values for aluminum are consistent with other data and about two-times as large as the PHITS calculation. To estimate radioactivity induced by deuterons with PHITS, therefore, improvements will be required for cross-section calculation models. Present experimental results will be used as the basic data to check the accuracy of the Monte Carlo simulation and for the shielding design of a medium energy accelerator facility such as IFMIF.

*In collaboration with National Institute for Fusion Science (NIFS).

References

1) IFMIF CDA TEAM, IFMIF Conceptual Design Activity Final Report edited by Marcello Martone, Report 96.11, Enea, Dipartimento Energia, Frascati (1996).
2) Aoki T. et al., CYRIC annual report 2001, p170.
3) Hagiwara M. et al., CYRIC annual report 2002, p141.
4) Baba M., Aoki T., Hagiwara M. et al., J. Nucl. Materials **307-311** (2002) 1715-1718.
5) Aoki T., Hagiwara M., Baba M. et al., J. Nucl. Sci. Tech. **41** (4)(2004) 399-405).
6) Hagiwara M., Itoga T., Baba M., et al., J. Nucl. Materials **329-333** (2004) 218-222.
7) Ibaraki M. et al., Nucl. Sci. Technol., **35** (12) (1998) 843.
8) Nelson W., Hirayama H., Rogers D.W.O., "The EGS4 Code System" SLAC-265, Stanford University, Stanford (1985).
9) Ziegler J.F., Biersack J.P, Littmark U., "The Stopping and Range of Ions in Solids," vol. 1 of series "Stopping and Ranges of Ions in Matter," Pergamon Press, New York (1984).
10) Shen W.Q., Wang B., Feng J., Zhan W.L., Zhu Y.T. and Feng E.P., Nucl. Phys. A **491**, 130 (1989).
11) IAEA, Charged-particle cross section database for medical radioisotope production. http://www-nds.iaea.org/medical/
12) EXFOR system: OECD/NEA http://www.nea.fr.
13) Iwase H., Niita K., Nakamura T., J. Nucl. Sci. Technol. **39** (11) (2002) 1142.

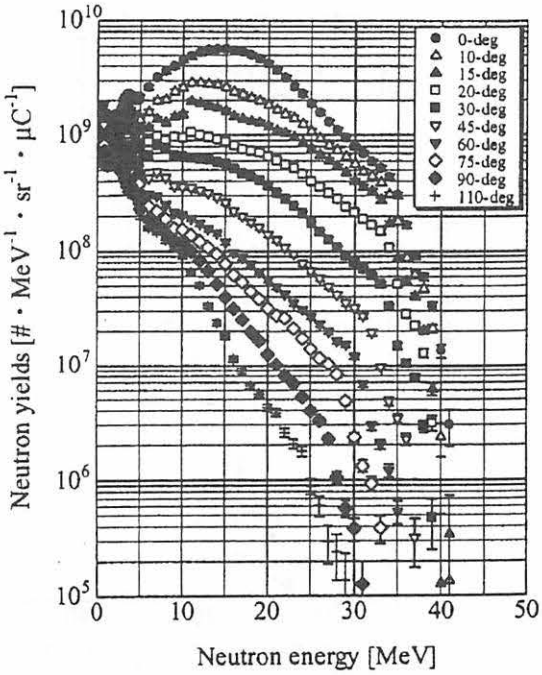

Fig. 1. The neutron spectra from thick carbon target for incident deuteron energy of 40 MeV.

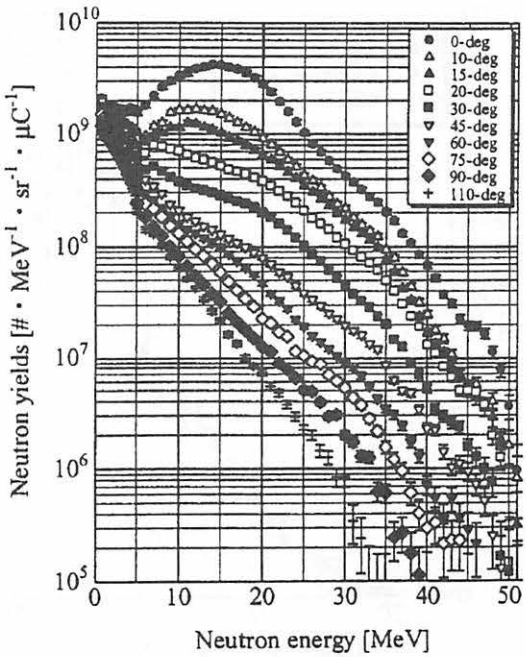

Fig. 2. The neutron spectra from thick aluminum target for incident deuteron energy of 40 MeV.

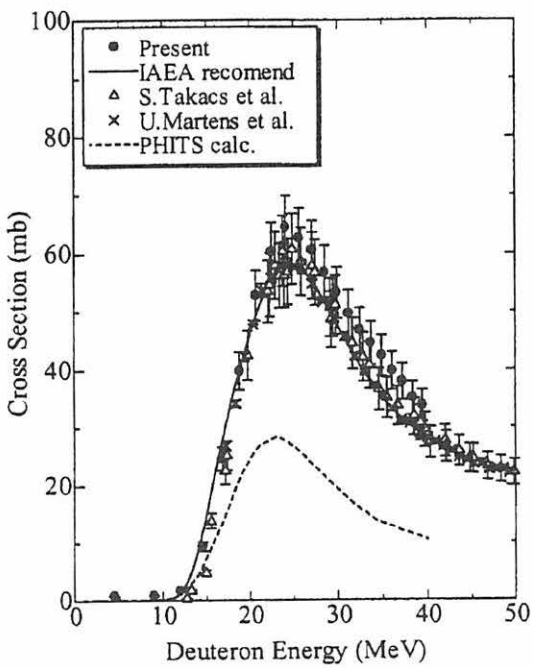

Fig. 3. $Al(d,x)^{24}Na$ cross-sections.

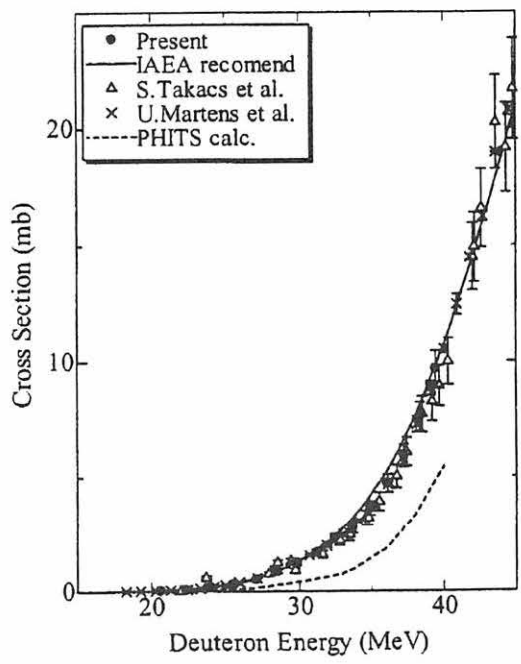

Fig. 4. $Al(d,x)^{22}Na$ cross-sections.

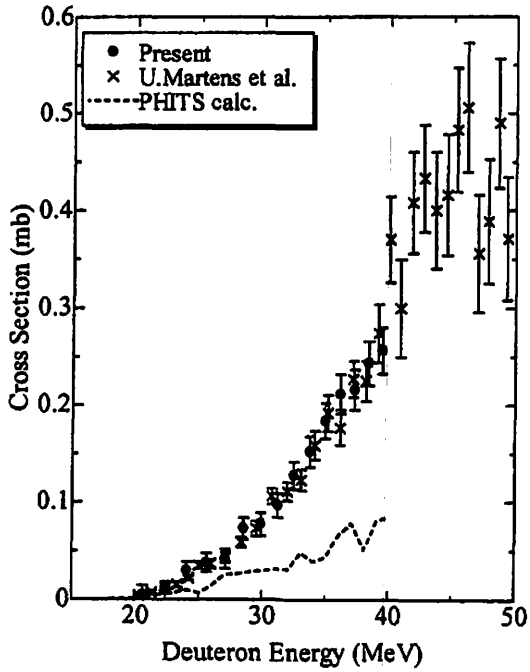

Fig. 5. Al(d,x)^{7}Be cross-sections

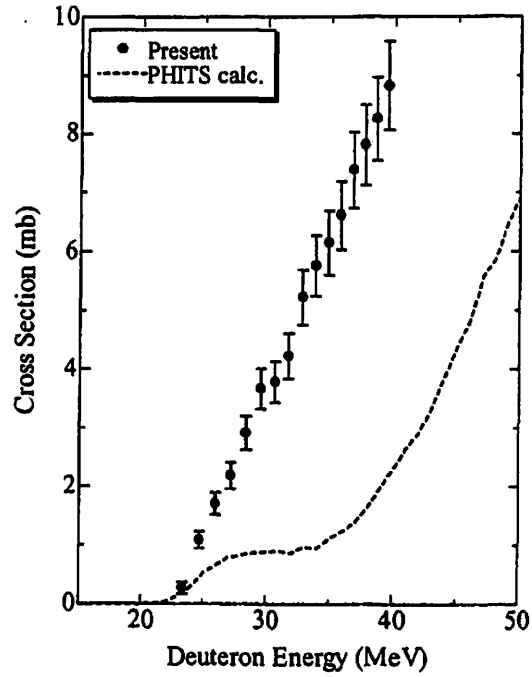

Fig. 6. C(d,x)^{7}Be cross-sections

III. 2. Experimental Studies on the Fragment Productions in Proton- and Neutron- induced Reactions

Hagiwara M., Sanami T., Oishi T., Baba M., Hirabayashi N., Takada M.**, Nakashima H.***, and Tanaka S.****

Cyclotron and Radioisotope Center (CYRIC), Tohoku University
*High Energy Accelerator Research Organization (KEK)**
*National Institute of Radiological Sciences***
*Japan Atomic Energy Research Institute****

Energy and angular doubly differential cross-section data of fragments (secondary charged particles heavier than α particle) production for proton- and neutron- induced reactions are of importance for dosimetry and the evaluation of radiation effect such as single event upset (SEU) by cosmic ray because of their large local ionization. However, experimental data on the fragment production are very scarce due to experimental difficulties of fragment detection, i.e., low yield, and large energy loss in samples. For the reason, almost all of past experimental data were obtained by the activation method that does not provide energy and angle information. Furthermore, theoretical calculation treating fragment production is very few and uncertain. Therefore, it is important to obtain reliable experimental data of differential cross section of fragment production.

Typical methods for the charged-particle production cross-section measurement are 1) the activation method and 2) the counter telescope method (ΔE-E method). The activation method can be applied only to some reactions that result in radioactive residual nuclei and does not provide the energy and angle information. The method of 2) has been applied for the secondary light charged-particle measurement generally. In the case of fragment measurements in ten's of MeV energy region, the application of the method is very difficult due to the energy loss in the ΔE detector and the small detector solid angle. Therefore, an experimental method adequate for fragment measurement is required.

For fragment detection, we adopted 1) a Bragg curve spectrometer (BCS) providing almost all information on the particle with a single counter and 2) an energy-time of fight (E-TOF) method having the capability of mass identification in almost whole energy region

for fragments.

BCS is a gridded-ionization chamber[1-3] as shown in Fig.1. The fragments can be identified on the basis of the difference of Bragg peak value[4,5] and the energy information can be obtained from the total charge produced. BCS has been mainly used for fragment measurement by charged particle induced reactions but not applied to neutron-induced reaction. We designed the BCS with special care to apply to a neutron beam in addition to a charged particle beam, and resulted in success to identify the fragments by proton- and neutron-induced reactions[7] as shown in Figs. 2, 3, 4 and 5. BCS proved very promising for fragments detection in neutron-induced reaction, while there are still some problems that should be solved[6].

For 2), we fabricated a special chamber as shown in Fig.6 and installed at No.2 target room in CYRIC to conduct the fragment measurement for proton-induced reactions using the E-TOF method[8]. In this method, the energy and TOF of the fragment is measured by SSD (silicon solid state detector) and MCP (micro-channel plate) with a thin carbon foil (50 $\mu g/cm^2$), respectively, and the mass number is derived by combing the energy, TOF and the energy loss information. Though this method is restricted only in charged particle-induced reactions due to the small detector solid angle, the dynamic range of fragment energy will be higher than in BCS, and much higher counting rate will be obtained. We conducted the test experiment by using the system and resulted in success to identify the fragments from polyethylene (4 μm) by 70 MeV proton-induced reactions as shown in Fig.7.

References

1) Bunemann O. et al., Can. J. Res. **A27** (1949) 373.
2) Ito N., Baba M. et al., Nucl. Instrum. Methods **A337** (1994) 474.
3) Sanami T. et al., Nucl. Instrum. Methods **A440** (2000) 403.
4) Gruhn C.R. et al., Nucl. Instrum. Methods **196** (1982) 33.
5) Shenhav N.J.and Stelzer H., Nucl. Instrm. Methods **228** (1985) 359.
6) Sanami T. et al., J. Nucl. Sci. and Tech. **Suppl. 4** (2004) 502.
7) Baba M.et al., Nucl. Instrum. Methods **A428** (1999) 454.
8) Roche C.T. et al., Phys. Rev. C **14** (1976) 410.

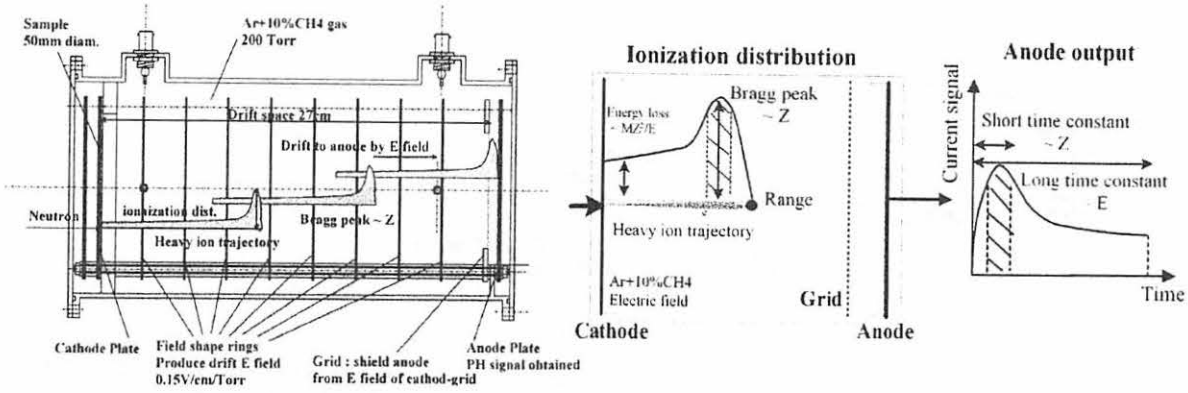

Fig. 1. Schematic diagram of the Bragg curve spectrometer.

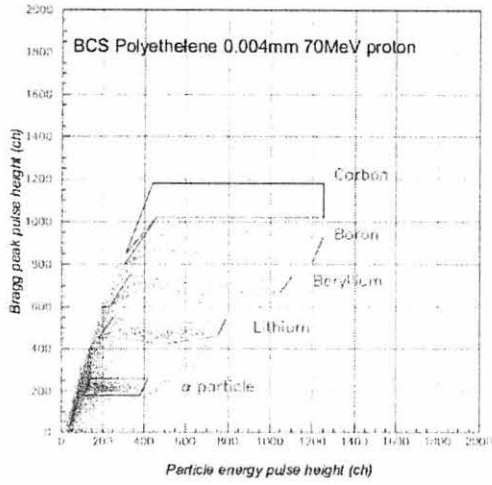

Fig. 2 Energy *vs* Bragg peak two-dimensional spectra for polypropylene (4 μm) induced by 70 MeV protons.

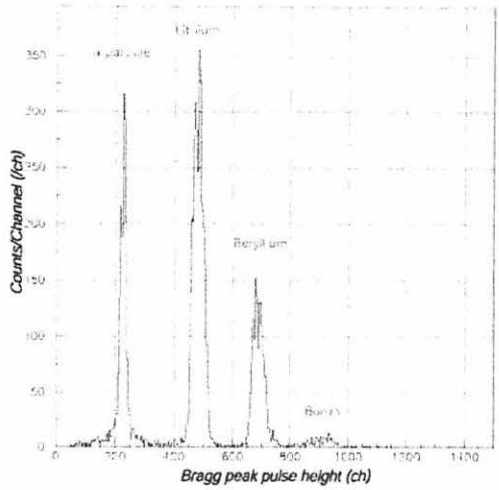

Fig. 3 Bragg peak spectrum over separation limits for polypropylene (4 μm) induced by 70 MeV protons.

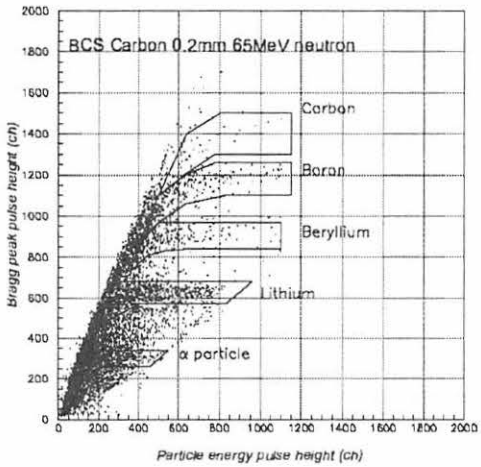

Fig. 4 Energy *vs* Bragg peak two-dimensional spectra for carbon (200 μm) induced by 65 MeV quasi-monoenergetic neutron[7].

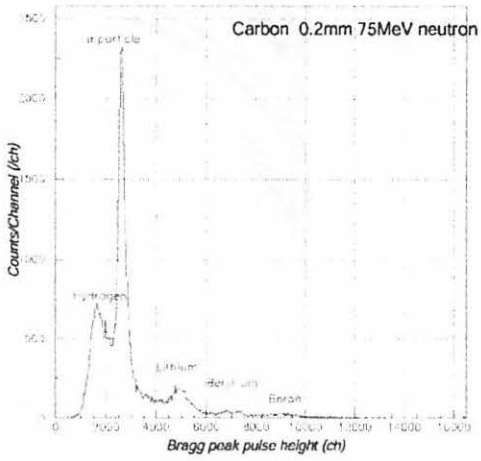

Fig. 5 Bragg peak spectrum over separation limits for carbon (200 μm) by 65 MeV quasi-monoenergetic neutron[7].

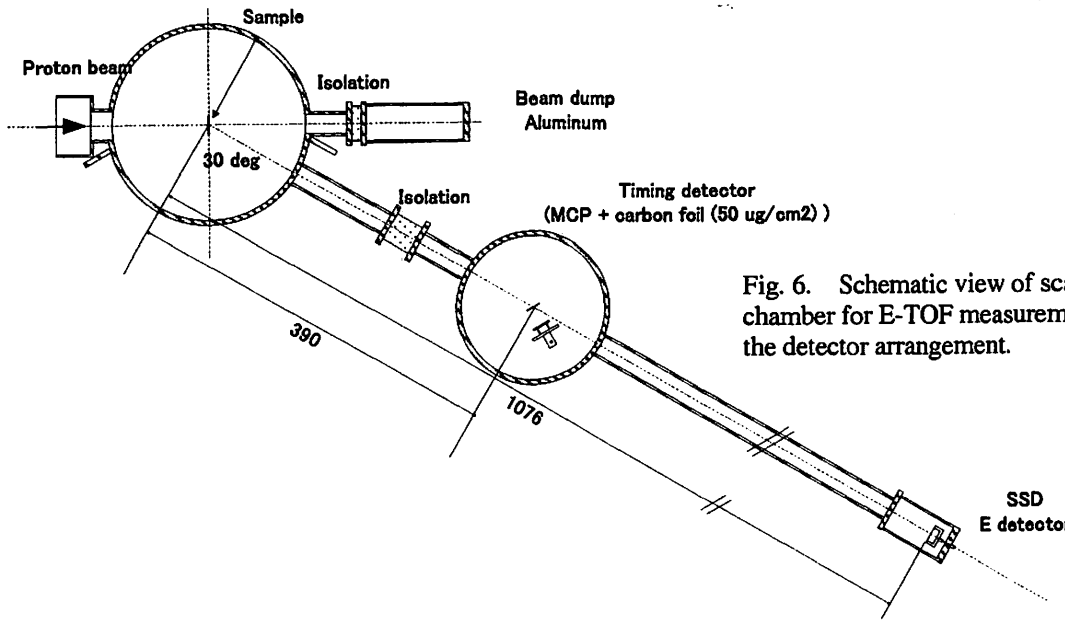

Fig. 6. Schematic view of scattering chamber for E-TOF measurement and the detector arrangement.

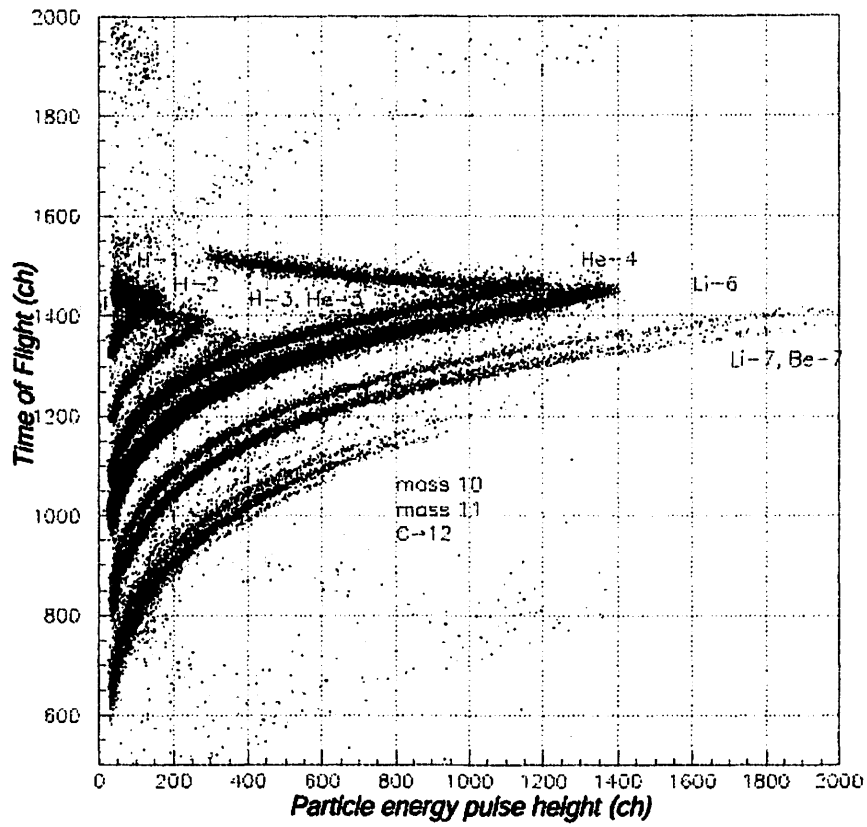

Fig. 7. Energy *vs* TOF two-dimensional spectra for polypropylene (4 μm) induced by 70 MeV protons.

III. 3. Measurements of Differential Thick Target Neutron Yield for Fe, Cu(p,xn) Reactions at 35, 50 and 70 MeV

Itoga T., Hagiwara M., Yamauchi T., Ohishi T., Kawata N., Hirabayashi N., and Baba M.

Cyclotron and Radioisotope Center, Tohoku University,

Introduction

By the development of accelerator technology, high intensity and high energy accelerators are now available. Now some accelerators with high energy and intensity are under construction or in plan e.g., Japan Proton Accelerator Research Complex (J-PARC, by the corporation of JAERI and KEK) and Spallation Neutron Source (SNS, United States) and so on. For the design of accelerator shielding and the accelerator-based neutron sources, differential thick target neutron yields (TTY) data are required. Data are required with high energy resolution over a wide energy and angle range. However, the experimental data covering wide range of secondary neutron energies are very few, and such the nuclear data files are not good enough in quality for high energy accelerators. We are considering series of TTY measurement for (p,xn) and (d,xn) reactions in ten's MeV region.

In the present experiments, we obtained the TTY data for the ^{nat}Fe, ^{nat}Cu(p,xn) reaction at 35, 50 and 70 MeV. These elements are used for beam-lines and beam-dumps in accelerators. Therefore, it is important to know secondary neutron spectra from these elements bombarded by accelerated charged particles. The experiment was carried out as a part of the series of TTY measurements using a time-of-flight (TOF) technique at the Cyclotron and Radioisotope Center (CYRIC), Tohoku University with the K = 110 AVF cyclotron and the beam-swinger system[5].

Experiment and analysis

The experimental setup and the technique are same as in the past experiments[2-4]. The targets of Fe and Cu were plate of natural elements with full stop thickness (Table. 1).

The pulse width of the proton beam was generally less than 2 ns in FWHM. The repetition rate was 2.3 MHz and the average beam current on the target was around 5 ~ 10 nA. The TOF data were obtained at five laboratory angles (0, 30, 60, 90 and 110 deg.). The efficiency *vs.* energy curves of the detectors were obtained by the calculation with a SCINFUL-R[6], which is revised version of the Monte Carlo code SCINFUL[7] and was verified to be accurate within ± 5 % up to 80 MeV[6]. The spectra were normalized by the integrated beam current.

Results and discussion

Figures 1 ~ 4 show the present results of TTY from the ^{nat}Fe, ^{nat}Cu(p,xn) reactions at 35, 50 and 70 MeV. The data have not been corrected yet for the effect of neutron attenuation in the target and air. As shown fig. 3 and fig. 4, both spectra show similar feature with no marked structures. Figure 1 shows pronounced increase in lowest energy region because of evaporation neutrons and the total neutron yields are larger than light nuclide like ^{nat}C and ^{nat}Al[1]. The angular dependence of the spectra becomes stronger with increasing neutron energy.

In fig. 2, the present results are compared with the data by Nakamura et al., at E_p = 52 MeV obtained by the unfolding technique[8]. The data by Nakamura et al. are limited in energy range but in fair agreement with the present one in the overlapping energy region. Figure 3 show the comparison with the data by S. Meigo, at E_p = 68 MeV using TOF method[9] indicating very good agreement in the highest energy end.

In the following, experimental data are compared with the TTY data calculated by the Monte Carlo code MCNPX which employs the LA150 data[10), 11)] and takes account of the particle transport. LA150. Figure 1 and 4 show the comparisons with the present results and the LA150 data. Both data for ^{nat}Cu show marked disagreements with LA150 in higher energy region. Such disagreement with LA150 was observed also in the case of heavy nuclide as tungsten and tantalum[1].

We are conducting to measure net of the thin target neutron yield from same reaction to clarify the causes of such difference of experimental results and LA150 data.

References

1) Aoki T., Hagiwara M., Baba M., Yonai S., Kawata N., Hagiwara M., Miura T. and Nakamura T., Nucl. Sci. Eng. **146** (2004) 200.
2) Aoki T., Hagiwara M., Baba M., Sugimoto M., Miura T., Kawata N. and Yamadera A., J. Nucl. Sci. Tech. **41(2004)** 399.

3) Hagiwara M., Itoga T., Baba M., Uddin M.S., Hirabayashi N., Ohishi T. and Yamauchi T., J. Nucl. Materials **329-333** (2004) 218.
4) Ibaraki M. et al., Nucl. Sci. Technol. **35** (1998) 843.
5) Kumagai K., Kikuchi Y., Uekusa T., Uemori T., Fujisawa H., Sugimoto N., Itoh K., Baba M. et al., Nucl. Instrum. Methods **491** (2002) 419.
6) Meigo S., Nucl. Instrum. Methods **A401** (1997) 365.
7) Dickens J.K., ORNL-6436. Oak Ridge National Laboratory, 1988.
8) Nakamura T., Yoshida M., Shin K., Nucl. Instrum Methods **151** (1978) 493.
9) Private communication
10) Chadwick M.B., Young P.G., MacFarlane R.E., Moller P., Hale G.M., Little R.C., Koning A. J., Chiba S., LA150 Documentation of Cross Sections, Heating, and Damage: Part A (Incident Neutrons). LANL Accelerator Production of Tritium Program, 1999.
11) Chadwick M.B., Young P.G., MacFarlane R.E., Moller P., Hale G.M., Little R.C., Koning A. J., Chiba S., LA150 Documentation of Cross Sections, Heating, and Damage: Part B (Incident Protons). LANL Accelerator Production of Tritium Program, 1999.

Table 1. The thickness of targets and proton stopping range.

Proton Energy [MeV]	Nuclide	Stopping range [mm]	Thickness [mm]
35	Fe	2.26	3
	Cu	2.11	3
50	Fe	4.24	5
	Cu	3.93	5
70	Fe	7.66	10
	Cu	7.09	10

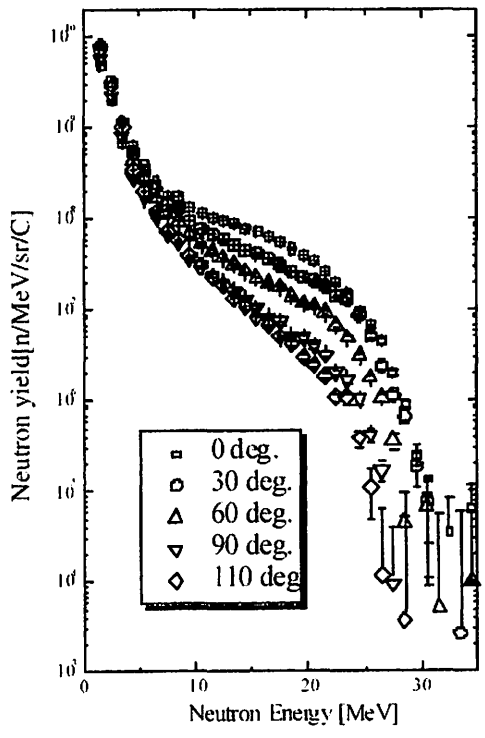

Fig. 1. Neutron yield for the ^{nat}Fe(p,xn) at 35 MeV.

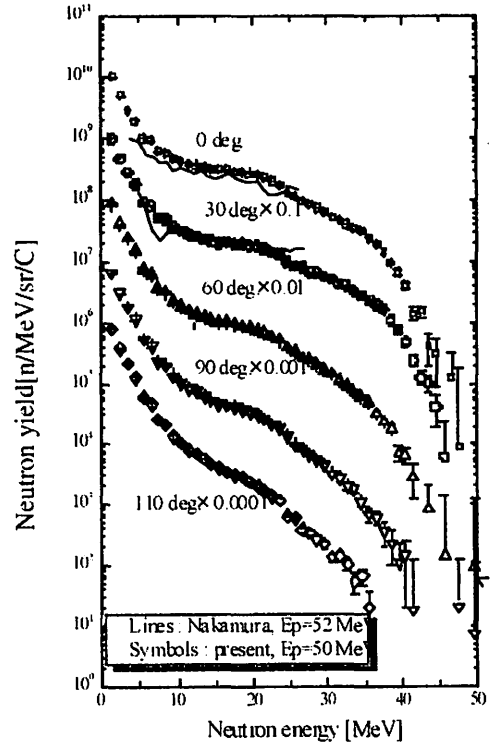

Fig. 2. Neutron yield for the natCu(p,xn) at 50 MeV in comparison with Nakamura's data at 52 MeV[8].

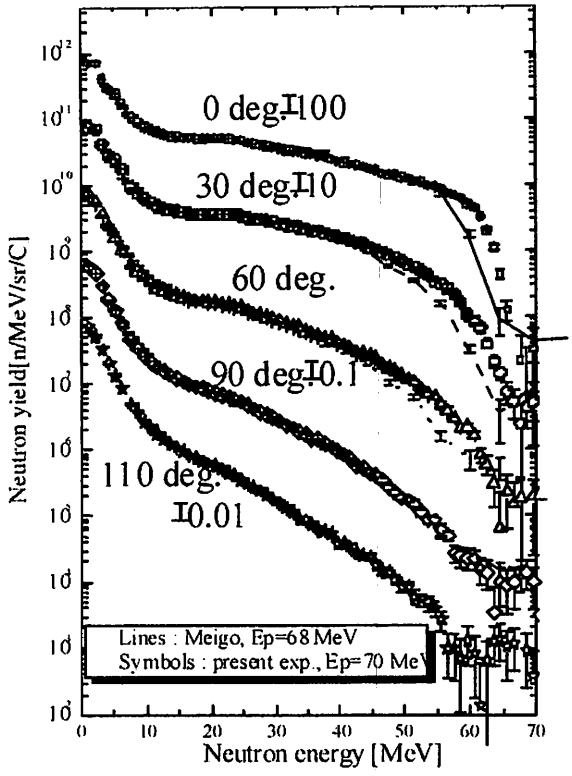

Fig. 3. Neutron yield for the ^{nat}Fe(p,xn) at 70 MeV in comparison with Meigo's data at 68 MeV[6].

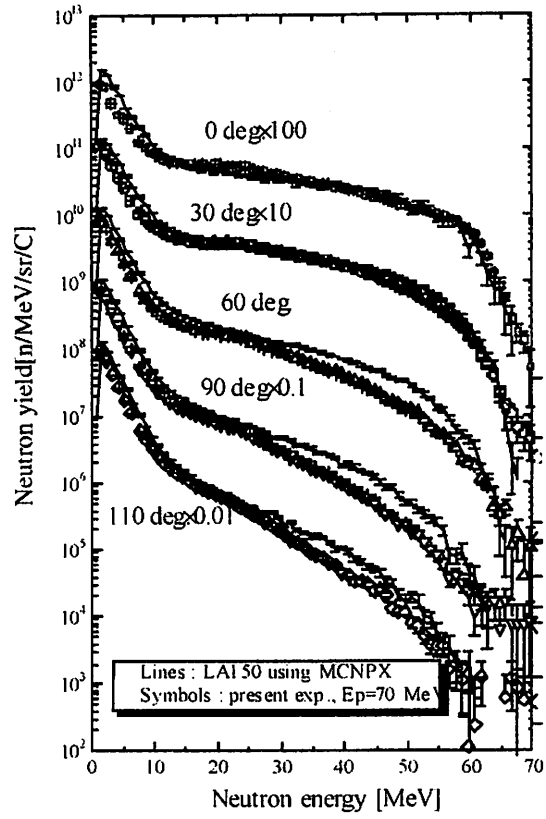

Fig. 4. Neutron yield for the ^{nat}Cu(p,xn) at 70 MeV in comparison with LA150.

III. 4. Experimental Investigations on the Proton-induced Activation Reactions on Tantalum and Molybdenum

Uddin M.S, Baba M., and Hagiwara M.

Cyclotron and Radioisotope Center, Tohoku University, Sendai, Japan

Introduction

Tantalum and molybdenum are the important structural materials that are used in various parts of accelerator. Tantalum is important as target for the production of medically important radioisotopes such as $^{178}W/^{178}Ta$, $^{172}Hf/^{172}Lu$, ^{177}Lu etc. Tantalum is a monoisotopic element, so it has special interest to test model calculations.

Molybdenum is used as target material for the production of medical radioisotopes like as $^{99m}Tc/^{99}Mo$, ^{96}Tc etc. ^{99}Mo is the parent nuclide of the daughter ^{99m}Tc, which is widely used in diagnostic nuclear medicine. Due to their nuclear decay properties, this radioactive pair is well suited for the production and distribution of the $^{99}Mo \rightarrow {}^{99m}Tc$ generator over the world. The amount of ^{99}Mo consumed for radiopharmaceuticals increases year by year. The ^{99}Mo is produced commercially by using nuclear reactors and these are based on the (n,γ) and (n,fission) nuclear reactions. Currently, there is no supply of accelerator-made ^{99m}Tc or ^{99}Mo anywhere. But it is possible to make production of ^{99m}Tc and ^{99}Mo by the proton bombardment *via* the most suitable reactions $^{100}Mo(p,2n)^{99m}Tc$ and $^{100}Mo(p,pn)^{99}Mo$ respectively. Molybdenum is also useful as a refractory and corrosion resistant material in accelerator applications.

Activation cross-section for Ta+p and Mo+p reactions are of interest in various fields, like accelerator technology, charged particle activation analysis, thin layer activation, medical isotope production, model calculations etc. The present work was undertaken to give new and reliable excitation functions and thick target yields for Ta+p and Mo+p reactions in the energy range 20-70 MeV.

Experimental techniques

The excitation functions of the proton-induced activation reactions on tantalum and molybdenum were measured using a conventional stacked foil technique. The stacked samples were irradiated with 70 MeV collimated proton beam of 100 nA and 200 nA using a k= 90 MeV AVF Cyclotron at Cyclotron and Radioisotope Center (CYRIC) of Tohoku University. Cu and Al foils were inserted into stack as monitor, beam energy degraders and to check the beam parameters. We have to mention that separate irradiations were performed for tantalum and molybdenum.

The activity of the residual nuclei was measured nondestructively by HPGe gamma-ray detector. For short-lived radionuclides, measurements were done about 10 minutes after end of irradiation. To minimize the relative errors of the calibration curve, several gamma lines were used to determine the activity for a given radionuclides, where it was possible. The detector efficiency *versus* energy curve was determined experimentally using the standard gamma-ray point sources, ^{152}Eu, ^{133}Ba, ^{241}Am, ^{60}Co , ^{137}Cs etc.

The proton energy degradation along the stack was determined using the computer program SRIM-2003[1]. The proton beam intensity was determined *via* the monitor reactions[2], ^{27}Al(p,x)^{22,24}Na and ^{nat}Cu(p,x)^{62,63}Zn taken place at the front radioactive monitor foils of the stack considering that the monitor foils were irradiated simultaneously and measured with the same detector and in a comparable geometry as the targets. From the decay rates of the radioactive products and the measured beam current, the cross-sections were deduced for the productions of the radionuclides. It has been observed that two or more radionuclides emitted gamma-rays having very close energies, which cannot be resolved by HPGe-detector. We have separated the contribution to the peak area from different processes using their another independent gamma-rays and by establishing decay curve. The data were corrected for the sum-coincidence effect caused by the coincidental detection of two or more gamma-rays in cascade by using the SUMECC code[3].

Results and discussion

Activation cross-sections were measured for the production of ^{90,93m,99}Mo, ^{93m,93,94m,94,95m,95,96}Tc, ^{89,89m,90,92m,95,96,97}Nb, ^{86,88,89}Zr and ^{86,87,88}Y from molybdenum target and ^{174,175,176,177,178,180}Ta, ^{173,174,175,176,177,178}W, ^{173,175}Hf and ^{179}Lu from tantalum target. The thick target integral yields were derived by using measured excitation functions. This work has given new data for all of the investigated radionuclides. We have also remeasured the excitation functions for monitor reactions and obtained good consistency

with recommendation. Although, it has been found that the recommended cross-section data for $^{27}Al(p,x)^{22}Na$ reaction are not in agreement with this work below 50 MeV.

The main problem in the stacked foil technique is energy degradation calculation along sample layers. We observed that the reliability of SRIM calculation decreases with the increasing depth of stack. It has been corrected by comparing with recommendation data of monitors.

The efficiencies obtained by using ^{133}Ba standard source were deviated from the common trend of other sources. The established efficiency *versus* energy curve was consistent with EGS4 Monte Carlo Code[4].

We observed that two or more radionuclides emitted gamma-rays having very close energies which were difficult to separate by the graphical analysis of the multicomponent decay curve. We analyzed data using the difference in half life of the nuclides by plotting the photon emission rate as a function of time. An example on the radioactive decay curve for 140.5 keV peak energy is shown in Fig.1. From Fig.1, we see that the daughter, ^{99m}Tc activity grows to a maximum and then decreases at a constant rate which depends on the decay rate of the parent, ^{99}Mo and that fact indicates the parent-daughter transient equilibrium, $^{99}Mo \rightarrow {}^{99m}Tc$. Actually the directly produced ^{99m}Tc completely decayed out before the measurement. The measured activity was the sum of 140.5 keV gamma from the daughter, ^{99m}Tc and 141.2 keV from ^{90}Nb, because these gamma lines could not be resolved by the HPGe-detector. We deduced the activities of 140.5 keV and 141.2 keV gamma lines from the independent gamma lines of ^{99}Mo and ^{90}Nb respectively and compared with the results of radioactive decay curve and obtained excellent agreement.

The cross-sections and integral yields obtained in the present work would be useful to upgrade theoretical codes, for estimation of the activity for future accelerator developments and other radiation safety problems, for thin layer activation technique and for checking the yield on enriched target for medical isotope production. The results of this work have been submitted to publish in the J. Nucl. Scien. and Tech.[5] and in the J. Appl. Radiat. and Isotopes[6].

References

1) Ziegler J.F., Biersack J.P. and Littmark U., " The stopping and range of ions in solids", Pergamon, New York (1984).

2) Tarkanyi F., Takacs S., Hermanne A., Mustafa M.G., Nortier M., Oblozinsky P., Qaim S.M., Scholten B., Shubin Yu.N. and Youxiang Z., Beam monitor reactions (Chapter 4). "Charged particle cross-section database for medical radioisotope production: diagnostic radioisotopes and monitor reactions". IAEA-TECDOC-1211, IAEA, Vienna. < www-nds.iaea.or.at/medical>, p.49 (2001).
3) Torii A., UwaminoY. and Nakamura T., INS-T-468, Institute for Nuclear Study, University of Tokyo (1987).
4) Nelson W.R., Hirayama H. and Regers D.W.O., EGS4 code system, SLAC-265, Standford Linear Accelerator Laboratory (1985).
5) Uddin M.S., Hagiwara M., Tarkanyi F., Ditroi F. and Baba M., Appl. Radiat. and Isot. (submitted 2003).
6) Uddin M.S., Hagiwara M., Kawata N., Itoga T., Hirabayashi N., Baba M., Tarkanyi F., Ditroi F. and Csikai J., J. Nucl. Scien. Tech. (submitted 2003).

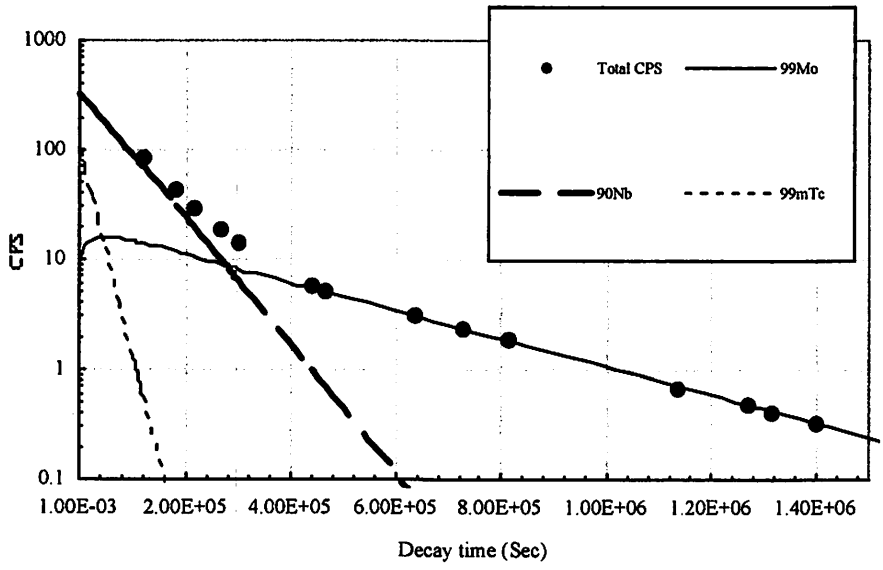

Fig. 1. Separation of complex decay of a mixture of activities for 140 keV gamma line.

III. 5. Application of Digital Signal Processing for Radiation Detectors Using Digital Storage Oscilloscope

Oishi T., Sanamil T., Hagiwara M., Itoga T., Yamauchil T., and Baba M.*

Cyclotron and Radioisotope Center, Tohoku University
*High energy accelerator research organization**

Introduction

In recent years, progress of a digital storage oscilloscope (DSO) enables raw waveform acquisition from a radiation detector. In this method digital storage oscilloscope is connected just after a radiation detector, a raw signal data is saved in it as digital waveform outs. By using this method, there are many advantage compared with the method using electronic circuits as follows,

- Because the whole raw data is saved, a complicated and flexible analysis is possible such as smoothing and noise reduction.
- Fine parameter adjustment in signal processing
- Easy to setup

On the other hand, there are some disadvantages to overcome.

In this study, the method was adopted to the measurement of secondary fragments from neutron induced reaction for Bragg carve spectrometer (BCS)

Application

Figure 1 shows a schematic view of the BCS which is a cylindrical gridded ionization chamber[1,2]. A target was mounted on cathode plate and irradiation by neutron. Fragment from the target produced by neutron induced reaction ionize the gas in the BCS. Electrons drift toward the anode by the electric field keeping a shape of ionization distribution Bragg curve. Therefore, the time distribution of the anode signal is just to the reversed. Thus, the fast part of anode signal is proportional to the Bragg peak that provides the information on the atomic number of the fragment. The integration of the whole anode signal represents the total charge that is proportional to the fragment energy.

By using anode signal, we distinguish the energy and the charge of fragments event by event.

Signals from the BCS were digitized b a Lecroy WAVEPRO7000 digital oscilloscope with a sampling frequency of 100 MHz after charge –sensitive preamplifier. Digitized signals were transmitted to a personal computer by Ethernet.

Figure 2 shows one of a transmitted signal which is integrated Bragg curve by a preamplifier. The pulse height is equal to particle energy and the maximum differentiation value, (the steepest slope), corresponding to Bragg peak. When we determine the steepest slope, there was a problem of high frequency noise, however, pulse height was obtained exactly. In the noise elimination process, Fourier analysis was adopted to determine frequency of signals originated fragments. The components with other frequencies were remove as noise components by "the finite impulse response (FIR) filter". FIR filter is one of the frequency selective digital filters. Figure 3 shows example of the suppression of high frequency noise component.

After the procedure, pulse height and the steepest slope were obtained for each waveform. Figure 4 shows scatter plot of pulse height and the steepest slope. A result by analog electronic circuit is also shown in Figure 5. "H", "He", and "Li" denote the hydrogen, helium, and lithium particle respectively. In order to show the ability of particle discrimination quantitatively, the portion except the former was projected on the vertical axis. Figure 6 and figure 7 show Bragg peak pulse height spectra by the digital waveform analysis and the analog electronic circuit, respectively. It was observed that the result by the digital waveform analysis had the better ability of particle discrimination than by the analog electronic circuit.

This method has much possibility. Application and improvement of this technique for various detectors is in progress.

References

1) Ito N., Baba M. et al., Nucl. Instrum. Methods **A337** (1994) 474.
2) Hagiwara M. et al., CYRIC annual report 2003, to be published.

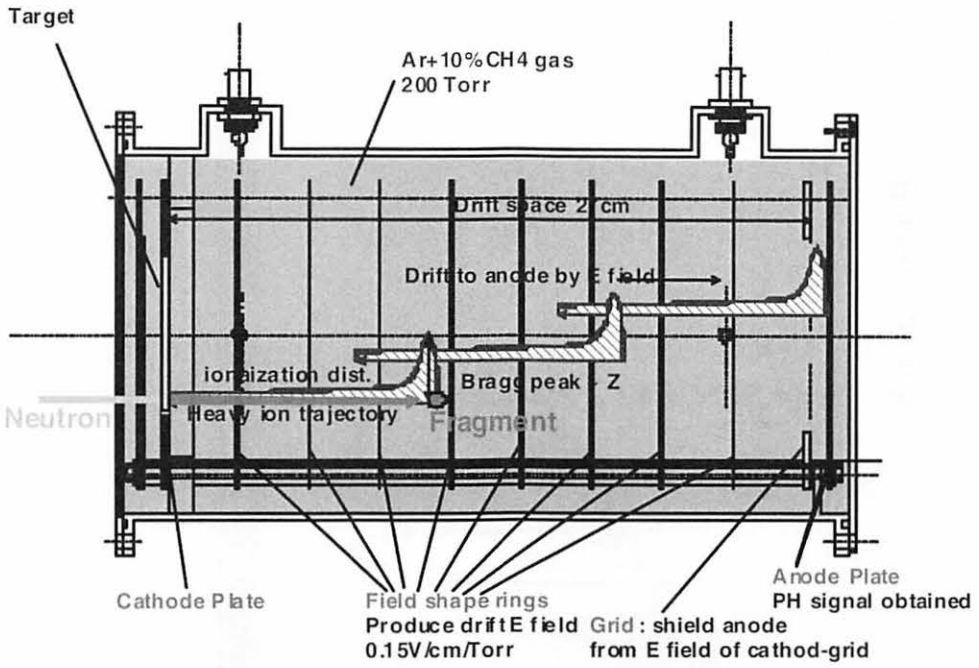

Fig. 1. Schematic view of the Bragg curve spectrometer.

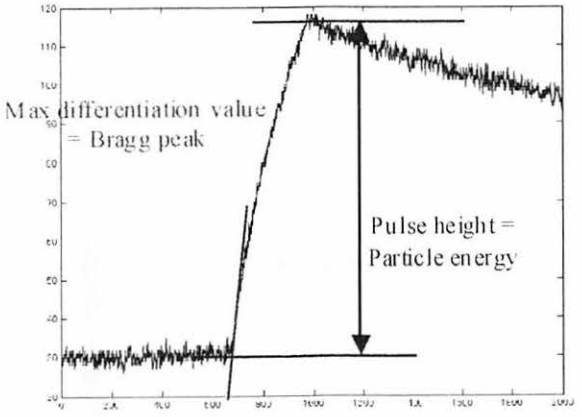

Fig. 2. One of raw data

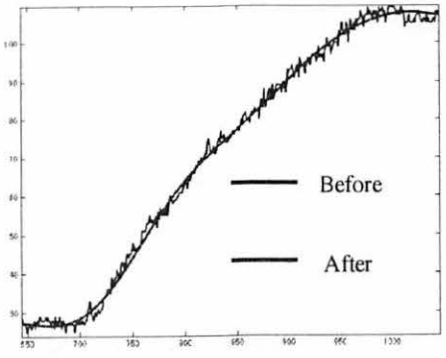

Fig. 3. Suppression of high frequency.

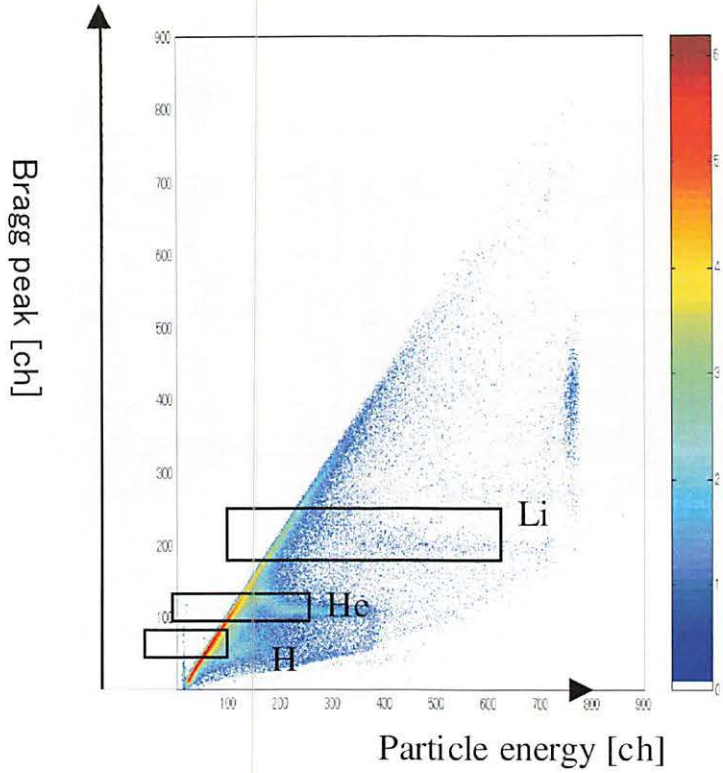

Fig. 4. Scatter plot by digital waveform analysis.

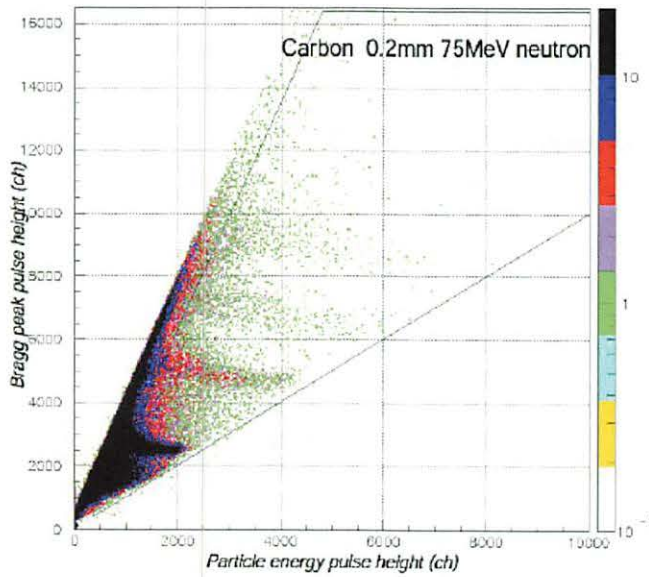

Fig. 5. Scatter plot by analog electronic circuit.

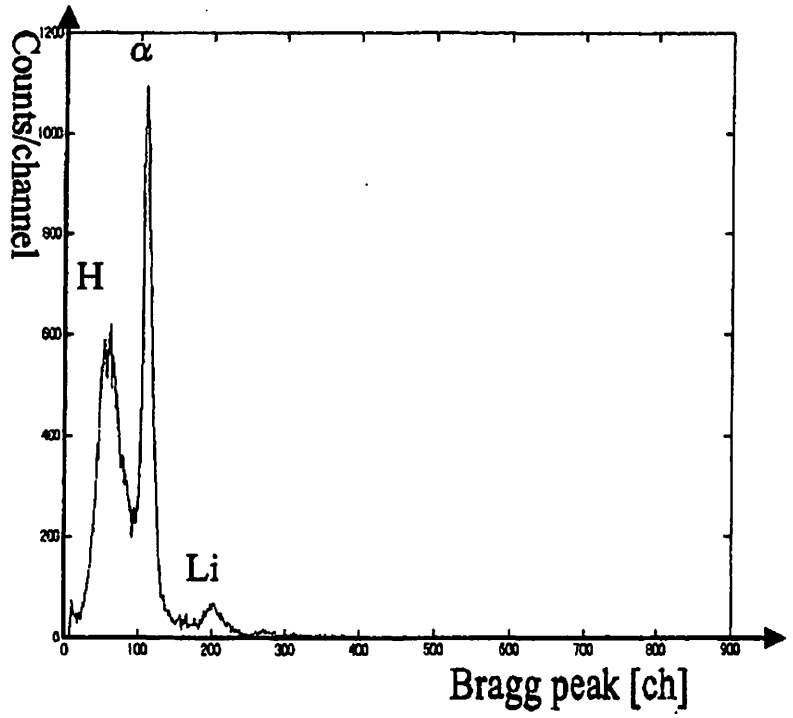

Fig. 6. Bragg peak pulse height spectra by digital waveform analysis.

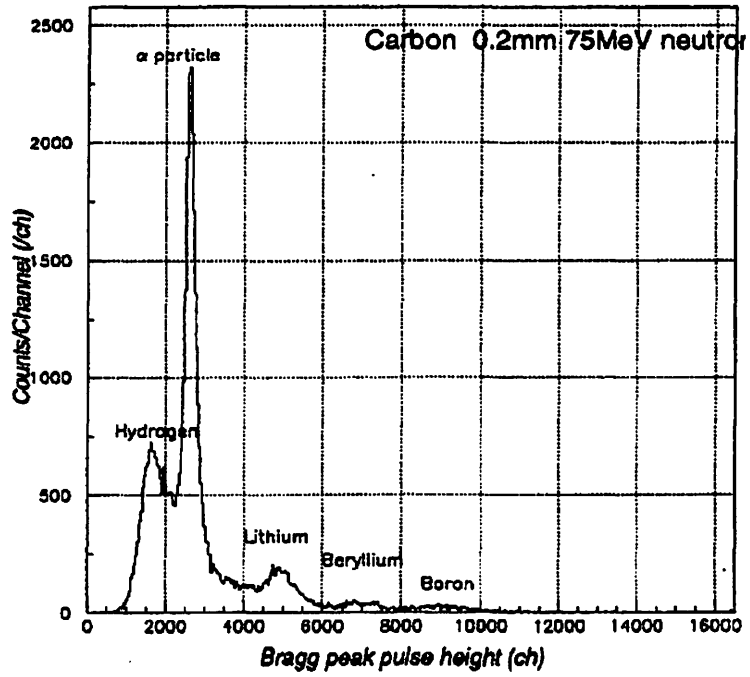

Fig. 7. Bragg peak pulse height spectra by analog electronic circuit.

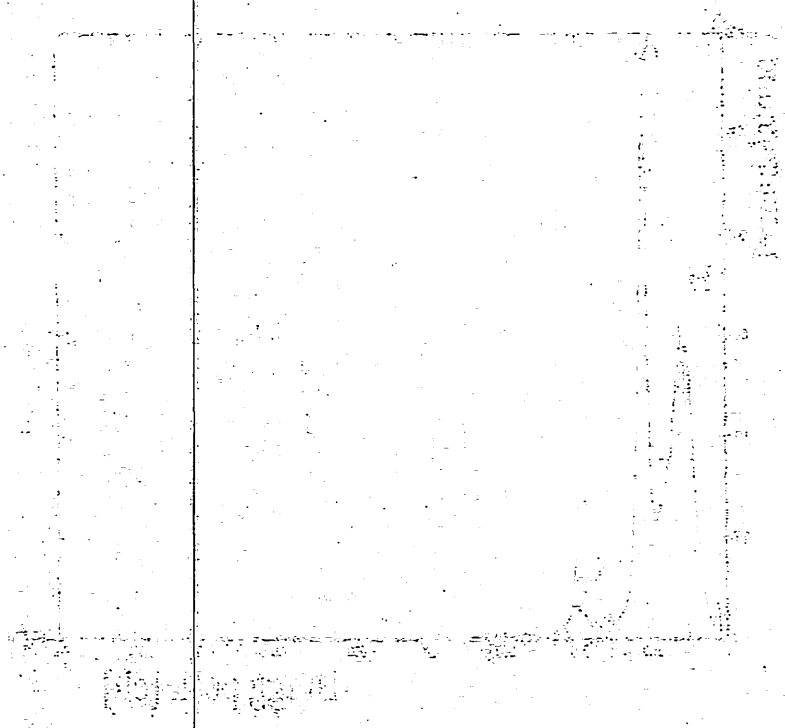

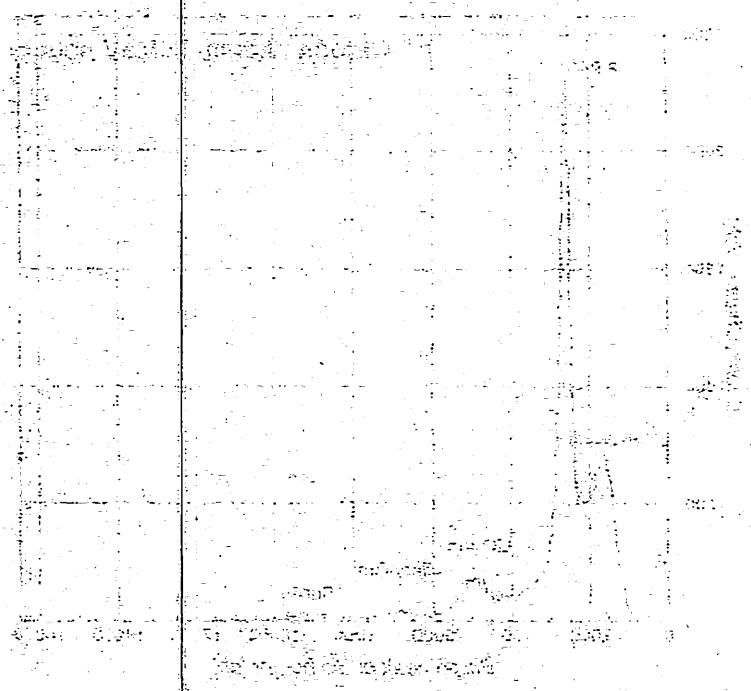

IV. NUCLEAR MEDICAL ENGINEERING

IV. 1. Relationship Between Transmission Scan Duration and Object Size in PET

*Watanuki S., Kumagai K., Itoh M., and Ishii K**

Cyclotron and Radioisotope center, Tohoku University
*Department of Quantum Science and Energy Engineering, Tohoku University**

Introduction

In positron emission tomography (PET), a transmission scan is required to correct for attenuation in emission scan data in quantitative PET imaging. The statistical accuracy of transmission data is determined by the number of events in projection data those passed through a scanned object. Therefore, attenuation correction with insufficient transmission events causes problematic noise and bias for a corrected emission image[1-2]. Our previous work investigated sufficient transmission scan durations, but it was not conditioned on different size of objects[3]. In this work, we defined the scan durations related to object sizes.

Materials and methods

A relative variance of emission projection data, which is corrected for attenuation by a noisy transmission and a noise free blank data can be described as follows.

$$(\sigma_c/m_c)^2 = (\sigma_c'/ m_c')^2 + (\sigma_t/m_t)^2 \quad - (1)$$

Where σ is the variance, m is the expected value, and c, c' and t indicate an emission data corrected by a noisy transmission, that by a noise free transmission and a noisy transmission data respectively. We assumed that an average variance of projection data is proportional to an average variance of emission image value. Here, a difference of square of a coefficient of variation (CV) in emission image between an image corrected by a noisy transmission and that by noise free transmission is defined as a square of X. The X^2 is in proportion to square of a relative variance of noisy transmission data.

$$(\sigma_t/m_t)^2 \propto X^2 = CVc^2 - CVc'^2 \quad - (2)$$

This relation is a function of a scanning object diameter D when emission and transmission sources activity and scan duration are constant.

In this work, we decided that 5% is the upper limit of the CV increase (CVc^2/CVc'^2 = 1.05) that results from a increasing the phantom diameter. Here, the equation (2) can be rewrite at the same transmission scan duration as below.

$$X^2_{(D)} / CVc'^2_{(D)} = (CVc^2_{(D)} - CVc'^2_{(D)}) / CVc'^2_{(D)}$$
$$= (1.05)^2 - 1 = 0.1025 \quad - (3)$$

On this premise, we expect the object size ($D_{5\%}$) in which $CVc_{(D)}/CVc'_{(D)}$ equal to 1.05 from experimental data in fixed transmission scan duration and equation (3).

Experiments were carried out with a SET-2400W (Shimadzu Co, Kyoto, Japan) PET system. Transmission and emission data were made with four different sizes (10.5, 16, 21 and 30 cm outer diameter) of water-filled cylindrical phantoms. Transmission and blank scans were acquired with an external line sources (^{68}Ge-^{68}Ga). The external source activity varied from 96 to 351 MBq. Transmission scan duration also varied from 1, 2, 3, 5, 7, 10 and 60 min at each size of the phantom and activity of the external source. Count rate of blank scans were obtained from total events of a frame without dead time correction. Attenuation correction factors (ACFs) were obtained from the transmission and the blank data by using non-linear smoothing process[4]. Emission scans were acquired during 20 min in 2D mode at all phantoms that filled with ^{18}F solution (5kBq/ml).

Emission data were corrected for attenuation by the set of ACFs that varied in activity of the external source, and were reconstructed by using OS-EM method. A circular region of interest (ROI) was placed at center of a phantom image, and a size of the ROI was set to90% of the inner diameter of phantom. CV values were obtained from pixels inside of the ROI. The differences of square of the CV ($X^2_{(D)}$) were calculated to subtract a square of CV at 60 min transmission ($CV_{(D)60} = CVc'_{(D)}$) from that at shorter time transmissions ($CV_{(D)}$) on a same object size (D). The logarithm of $X_{(D)}/CV_{(D)60}$ were calculated for linearizing of the relationship with phantom size. In each scan duration, $\log(X_{(D)}/CV_{(D)60})$ were plotted as a function of D, and the object size of $D_{5\%}$ were expected from the results of linear regression of the plotted data. Transmission scan durations with different source activity were normalized against the blank scan count rate at the maximum activity, and it was obtained that the relationship between $D_{5\%}$ and transmission scan time.

Results and discussion

The figure - 1 shows the relative blank scan count rate as a function of the external source activity. The solid line represents the fitting curve of the measured data to a quadratic polynomial. The fitted result was used to convert the scan duration at a decayed external source into the duration at initial activity (351 MBq) to compensate a decline of count rate. The logarithm of $X_{(D)}/CVc'_{(D)}$ are plotted as a function of object size for several scan durations (figure - 2). The logarithm of $X_{(D)}/CV_{(D)}c'$ has a good linear relation with the phantom size. The solid lines represent the results of the linear regression (R^2=0. 965 on average). The $D_{5\%}$ with a 351 MBq external source as a function of the corrected transmission duration is represented in figure - 3. The scan durations at decayed source were converted into the duration with a 351 MBq external source by using the curve in figure - 1. However, the data points distant from the range of the measured size are eliminated from figure - 3, because those data will probably have a larger error. The continuous representation of $D_{5\%}$ was obtained by fitting an involution function ($y = ax^b$) to the data in figure - 3 and is shown as the solid line. The plotted data are very close to the curve (R^2=0. 968). The $D_{5\%}$ with a 138 MBq external source was expected from the solid curve and the curve in figure - 1 and represents as a dashed line in figure - 3. The $D_{5\%}$ durations with a 351 and 138 MBq source indicates 3.6 and 5. 5 min transmission scan respectively at 30 cm phantom diameter.

We evaluated transmission scan duration as a function of object size. At fixed scan duration, the size of $D_{5\%}$ is varied with external source activity. However, it can be compensated simply by extending scan duration according to a decline of blank scan count rate. Therefore, the $D_{5\%}$ will not need to measure every external source activity. Some articles reported in term of the fraction of transmission duration for total (emission plus transmission) scan time to minimize a noise in emission image[5,6]. We consider that a minimum transmission scan time should be determined to limit the absolute error cause from a transmission data in an emission image. Then we believe that the $D_{5\%}$ will be index of minimum transmission scan duration. In our results, the minimum transmission scan duration in a whole body scan was recommended about 3.6 min with the initial source activity and 5.5 min with the external source passed one year. However, these values are obtained from pre injection transmission data. In actual PET study, a transmission scan is measured after injection of radiotracer. Therefore, the proper transmission scan duration will be somewhat longer than the result of this study. In our institute, emission scan duration is performed from 3 to 5 min per bed position for a normal body and an injection

dose. Then about 10 min is required for total scan time per bed position with the external source passed one year. The ten minutes is the upper limit of total scan duration per bed position, since a number of bed positions are from 5 to 7 in whole body scan. Therefore, the lifetime of the external sources will be estimated about one year.

In conclusion, we evaluated transmission scan duration as a function of object size. The result recommends that transmission scan duration for a whole body study is more than 3.6 min at the initial activity of external source and the external source lifetime is one year.

References

1) Dahlbom M. and Hoffman E.J., IEEE Trans. Nucl. Sci. **34** (1987) 288.
2) Visvikis D., Cheze-LeRest C., Costa D.C, et al., Eur. J. Nucl. Med. **28** (2001) 1326.
3) Watanuki S., Ishii K., Itoh M., CYRIC Ann. Rep. (2002) 59.
4) Kitamura K., Iida H., Shidahara M. et al., IEEE Trans. Nucl. Sci. **47** (2000) 994.
5) Stearns C.W., Wack D.C., IEEE Trans. Med. Imag. **12** (1993) 287.
6) Beyer T., Kinahan P.E. and Townsend D.W., IEEE Trans. Nucl. Sci. **44** (1997) 2400.

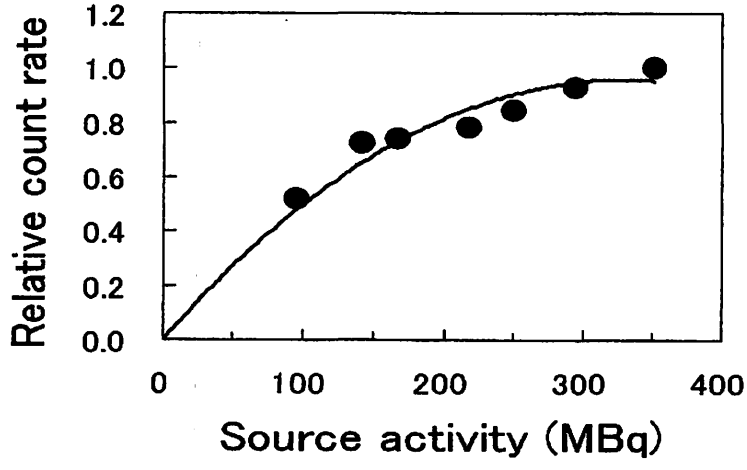

Fig. 1. Relative blank scan count rate of the SET-2400W as a function of external source activity. The solid line represents the fitting curve of measured data to a quadratic polynomial. The count rates were normalized against the count rate at initial source activity (351 MBq).

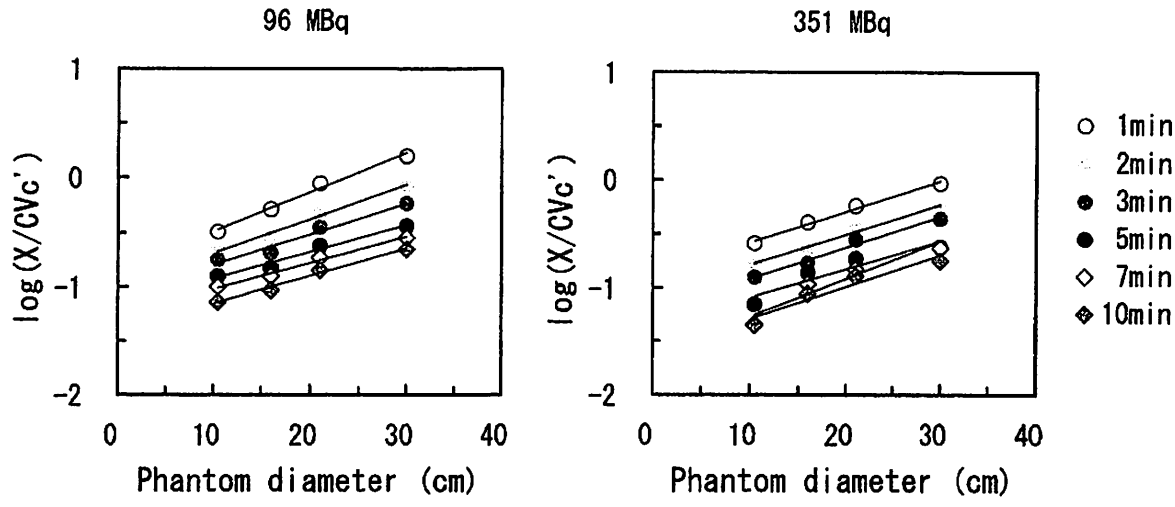

Fig. 2. Logarithm of X(D)/CV(D)c' as a function of phantom size for several scans duration. The graphs are in case of (right) 96 and (left) 351MBq external source respectively. The solid line represents the result of linear regression of the data.

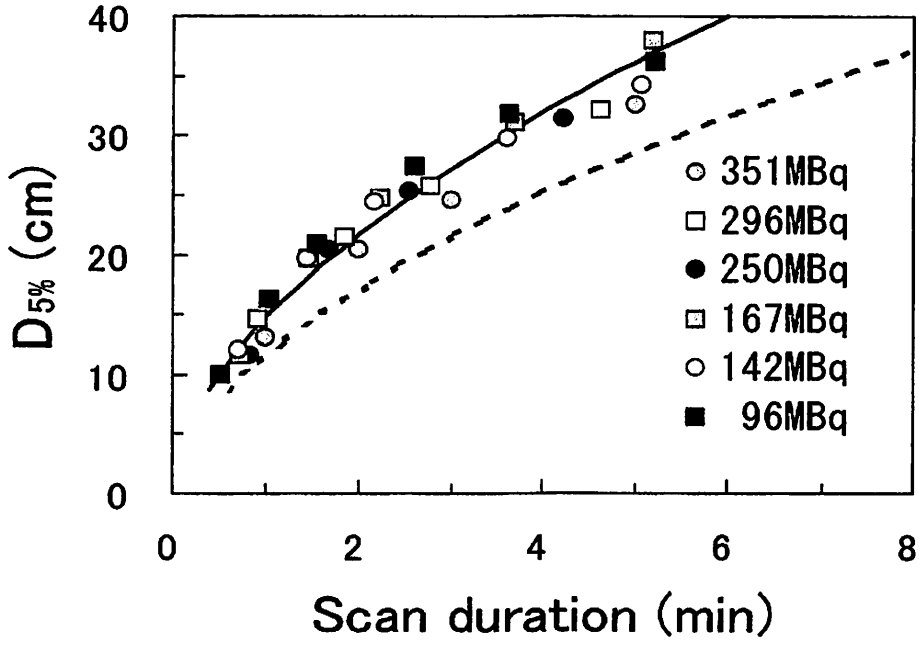

Fig. 3. The phantom diameter of $D_{5\%}$ with a 351 MBq external source as function of corrected transmission duration. The solid line represented the fitting curve of measured data to an involution function. The dashed line represents the expected $D_{5\%}$ phantom diameter with a 96 MBq external source.

IV. 2. Improvement in the Quantitative Accuracy and Quality of PET Images by Iterative Method

Oishi Y., Ishii K., Yamazaki H., Matsuyama S., Kikuchi Y., Rodriguez M., Suzuki A., Yamaguchi T., Itoh M., and Watanuki S**

Accelerator Science and Engineering Lab., Dept. of Quantum Science and Energy Engineering, Graduate School of Engineering, Tohoku University,
*Division of Cyclotron Nuclear Medicine, Cyclotron and Radioisotope Center Tohoku University**

Introduction

There are two distinct reconstruction methods in PET imaging, one is the analytical reconstruction and the other is the iterative reconstruction method. The most common analytical reconstruction is the Filtered Back-Projection (FBP) algorithm[1]. More recently many different iterative reconstruction algorithms are used and a representative example is the Maximum-Likelihood Expectation-Maximization (ML-EM) algorithm[2]. Nowadays the ML-EM algorithm is frequently used in PET facilities instead of the FBP algorithm. The reasoning is that the ML-EM algorithm provides better quality images compared to the FBP algorithm. However, the ML-EM algorithm does not guarantee quantitative accuracy of radioactivity estimations. The poor quantitative accuracy of ML-EM algorithms is strongly related to the lack of a suitable stopping rule for the iteration procedure; it is necessary to reliably estimate how many iterations are required to guarantee quantitative accuracy. In this paper, a new approach of stopping rule is proposed using the images reconstructed by FBP algorithm. It is well known that FBP algorithm provides reliable quantitative accuracy for the chosen ROIs. If a stopping rule is derived by referring to images reconstructed by FBP algorithm, concurrent images reconstructed by ML-EM algorithm are expected to possess the quantitative accuracy characterized by FBP algorithm as well as the good graphic quality inherent in the ML-EM algorithm. This stopping rule is incorporated into the reconstruction of 2-D simulated data in order to evaluate the quantitative accuracy.

New Stopping Rule

A stopping rule for ML-EM algorithm by referring to an image reconstructed by FBP algorithm are proposed, which is the stopping rule algorithm of the ROI manual setting.

At first, images are reconstructed by FBP algorithm from data sets and the ROIs are manually set around an area with similar pixel values. Secondly, ML-EM algorithm process is applied to same data sets. After each iteration, a transient image is compared to the image reconstructed by FBP algorithm until the square of difference of the mean values at a ROI set on the images reconstructed by the two methods is minimum. This process is repeated until image update is finished for all ROIs set on the image. This comparison algorithm results in images with reliable quantitative accuracy, when images by ML-EM algorithm have closest mean values at all ROIs to the images by FBP algorithm.

Method

Data sets were acquired by a Monte Carlo simulation of a one ring PET scanner. Figure 1 shows used phantoms in this simulation. Phantom1 was composed by 7 regions. The radioactivity ratio of each region (A:B~G) is 1:5 and diameter ratio is 100:4:6:8:10:12:14.

The stopping rule algorithm was applied to data sets for each phantom and its validity was examined; that was the quantitative accuracy was compared between the true image and the images obtained by using the stopping rule algorithm.

In the case of 3-D simulation, data sets were acquired with a 32 ring PET scanner whose diameter is 85cm and axial length is 20cm. Phantom2 is shown in figure 1. Radioactivity ratio of A, B, C and D were 1:3:4:5. Acquired data sets were processed by Fourier rebinning algorithm in order to transform 3-D data sets to 2-D and the rebinned data were reconstructed by ML-EM algorithm with the stopping rule. Finally, a scatter correction was applied based on a realistic estimate of the scatter fraction from reconstructed images.

Results

Result 1; 2D~Phantom1

When the stopping rule was applied to this phantom, image update was stopped at 32 iterations. Figure 2 shows the image obtained by applying this stopping rule algorithm and reconstructed by FBP and ML-EM algorithm. The images in a warm region show the

big difference between this stopping rule and normal ML-EM algorithm. Figure 3 shows the profile through the warm region. The pixel value at a warm region converges earlier than one at hot regions. Hence, after the mean value at a hot region in the image reconstructed by ML-EM algorithm arrives at one in the image reconstructed by FBP algorithm, the emphasis of noise because of over iteration arise for a warm region in the case of normal ML-EM algorithm. However, this effect was suppressed when applying this stopping rule because image update in the converged ROI was halted. This result indicates the advantage of this stopping rule.

Table 1 shows the ratio between true value and mean value in applying stopping rule and normal ML-EM algorithm at 6 hot regions. From ROI 1 to ROI 5, the quantitative accuracy of the stopping rule was achieved 98%~103%.

Result 2; 3D~Phantom2

Figure 4 shows images reconstructed by FBP and ML-EM algorithm applied the stopping rule before and after scatter correction. Before scatter correction, the reconstructed images exhibit higher radioactivity in the center region than on the edges because of the fraction of scattered photons. However, after scatter correction, the counts are quite uniform in the warm region.

Table 2 shows the ratio of mean value between each ROI and ROI 4 shown in figure 5. Input ratio of ROI 1~6 was 3:4:5:1:1:1. Before scatter correction, the ratio was not correct because of scatter fraction. However, after scatter correction, the ratio was close to input ratio. This shows that when stopping rule and scatter correction are applied to 3-D PET, images with good quantitative accuracy are obtained.

Conclusion

The new stopping rule algorithm was proposed based on ML-EM algorithm enhanced with the quantitative merit of FBP algorithm and the validity of the algorithm were evaluated by Monte Carlo simulation. The stopping rule algorithm was highly successful in all cases with quantitative accuracy close to 100% for all ROIs, excluding hot regions smaller than $0.8cm^2$. In such small hot regions, the stopping rule algorithm is still effective if standard images reconstructed by FBP algorithm are corrected for the partial volume effect. Finally, the usefulness of the reconstructed images for performing reliable quantitative research in 3-D PET was evaluated and the main concluding remark was that improvement on quantitative accuracy was achieved by combining scatter corrections and

this new stopping rule.

References

1) Townsend D.W., Bailey D.L., Defrise M. and Kinahan P.E., IEEE NSS/MIC Short Course, p1-54, 1994.
2) Shepp L.A. and Vardi Y., IEEE Trans. Med. Imag., Vol.MI-1, No.2, pp.113-121, October 1982.

Table 1. Ratio between mean value and true value.

	ML-EM (32 iterations)	Stopping Rule
ROI 1 (14pixel)	99.8%	98.9%
ROI 2 (12pixel)	104.0%	102.7%
ROI 3 (10pixel)	99.6%	99.2%
ROI 4 (8pixel)	103.3%	101.3%
ROI 5 (6pixel)	106.2%	100.1%

Table 2. Ratio between ROI 4 and each ROI.

	FBP before S.C.	after S.C.	Stopping Rule before S.C.	after S.C.
ROI 1	161.7%	283.8%	170.5%	301.2%
ROI 2	190.1%	371.0%	205.4%	407.1%
ROI 3	234.1%	465.7%	254.8%	519.6%
ROI 4	100.0%	100.0%	100.0%	100.0%
ROI 5	82.6%	112.7%	85.0%	114.6%
ROI 6	50.6%	99.4%	49.8%	98.7%

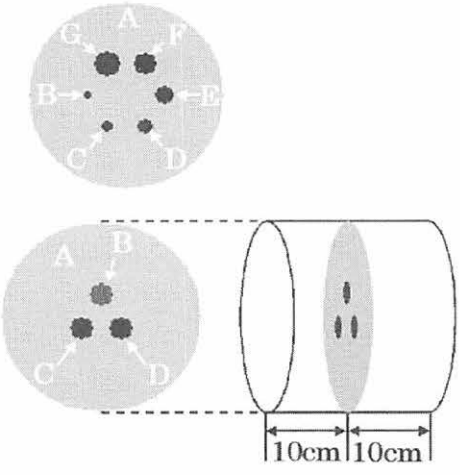

Fig. 1 Phantom (top: phantom 1, bottom: phantom2 for 3D simulation).

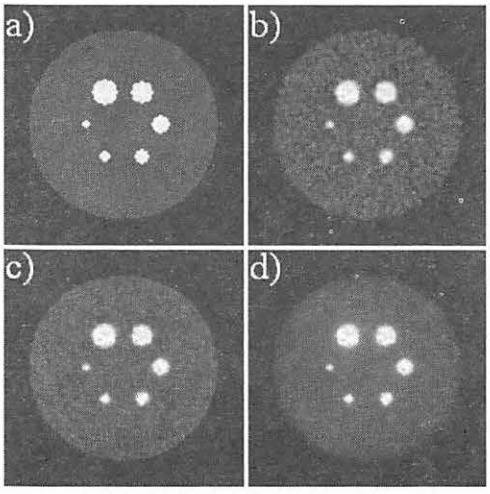

Fig. 2 a) true image, b) image of FBP, reconstruction c)image of ML-EM reconstruction~ 32 iterations, d) image of stopping rule applying.

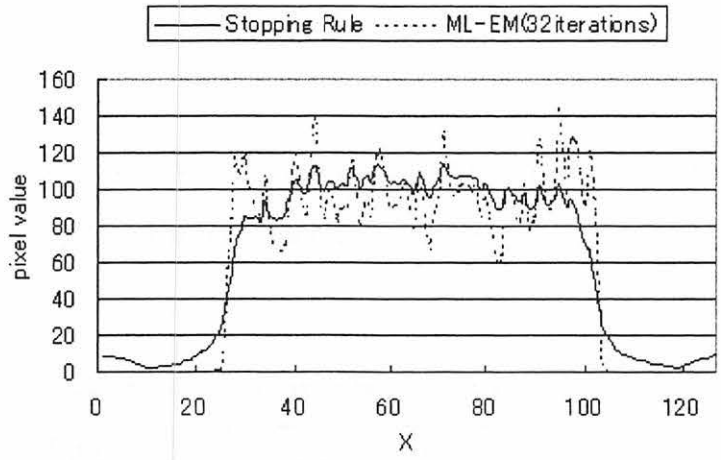

Fig. 3 Profile

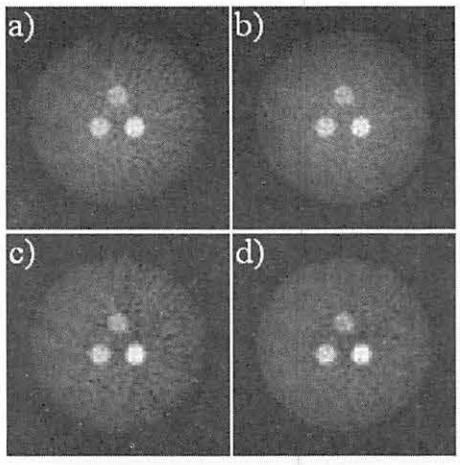

Fig. 4. a, c) FBP reconstruction, b, d) ML-EM reconstruction, a, b) before scatter correction, c, d) after scatter correction.

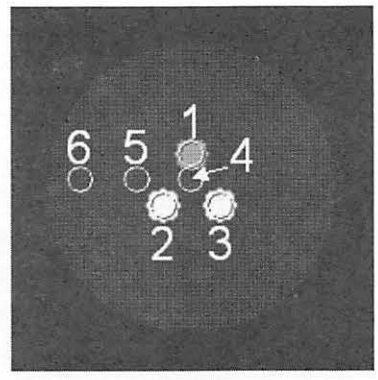

Fig. 5. ROI position

IV. 3. Improvement of PET Image Reconstruction by Using the Single Events Spectrum

Rodriguez M., Ishii K., Yamazaki H., Matsuyama S., Kikuchi Y., Oishi Y., Suzuki A, Yamaguchi T., Itoh M., and Watanuki S.**

Department of Quantum Science and Energy Engineering, Tohoku University
*Cyclotron and Radioisotope Center, Tohoku University**

INTRODUCTION

Positron Emission Tomography is based on detecting in coincidence two γ rays originated from the annihilation positron-electron[1]. The probability that one of these γ will undergo either photoelectric effect or Compton scattering out of the gantry is very high [2]. In this case only one photon will be detected, thus producing a non-coincidence event. Therefore, each individual detector in a PET scanner will count photons that will be assigned to coincidence and non-coincidence events. This total amount of photons is known as single events. Nowadays, single events are used to precorrect the measured coincidence data for random coincidences[3]. Since the positron activity distribution $\lambda(x,y)$ generates both coincidence and single events, it is reasonable to think that single events carry out useful information about the images reconstructed from coincidence events. This is the hypothesis that originates this work where the objective is directed to utilize single events for improvements of the PET images. The approach is to use single events for avoiding noisy images due to overiteration and for evaluating image degradation due to Partial Volume Effects (PVE)[4]. A large amount of research is addressed for improving the noise characteristics of iteratively reconstructed PET images. Improvements in computing technology encourage the utilization of iterative reconstruction techniques for clinical applications. Despite this, there is still a drawback when the choice to reconstruct the image is an iterative algorithm. It is the noise propagation on the reconstructed images with the increment of iterations used for the reconstruction process. It is thus well known that the image becomes very noisy if the iterative process is kept running much longer than what it is really needed[5]. There are three main approaches to solve this problem:

penalizing the likelihood objective function, post-smoothing and stopping rules[5]. In this work we concentrate on the third. The stopping rules deal with the problem by utilizing a determined criterion that allows estimating the optimum number of iterations necessary to reconstruct a coincidence data set in such a way that degradation caused by overiteration is minimized, meanwhile image convergence is guaranteed. Therefore, the reconstruction process is halted at that optimum point. The major drawback for using stopping rules is that objects of different sizes within the images converge at different rates[5]. Specifically, larger objects converge faster that the smaller ones. Hence, an optimum estimation of the number of iterations is still a trade among different convergence rates. Among the iterative reconstruction techniques, the Maximum Likelihood-Expectation Maximization algorithm[6,7] was soon adopted by the PET and it has surely become the most popular iterative reconstruction technique, which has lead to a strong interest dedicated to improve its performance. Several research groups have dedicated a great deal of their research to the development of suitable stopping criteria for the ML-EM algorithm[8-17]. Probably the most popular stopping criterion nowadays is the cross-validation rule[11] which is based on splitting the coincidence data set into two or more data subsets with similar statistical properties[12]. However, this technique suffers the strong dependence on the total coincidence counts present on each subset. The feasibility criterion[15] suggests stopping the reconstruction process when the image reaches the range of feasibility. This range of feasibility is evaluated through a chi-square analysis. The method proposed by G. Kontaxakis and G. Tzanakos[16] proposes to follow the updating factors of the ML-EM algorithm which eventually converge to one. From this point, the new activity estimations do not change significantly compared to the previous ones while the images become very noisy. Therefore, the reconstruction process should be halted. A problem with this technique is the need to draw several regions within the image in order to obtain the average value of the updating factor for each region. The single events data set represents a measurement independent of the coincidence detection. Therefore, it is attractive to restrict the iteratively reconstructed image to satisfy not only the coincidences measurement but also the singles measurement, thus the reconstructed image can reproduce two independent measurements. This point is very important since the already developed stopping rules are based only on the coincidence events and some special properties of the reconstruction process. It appears that the usefulness of single events is underestimated since the utilization of single events in PET imaging has been limited to corrections for random coincidences[3]. It is worth to note that collimated single events measurement have

also been used to estimate attenuation coefficients[17]. Another image degrading problem, which is a direct effect of the finite spatial resolution of PET detectors, is the Partial Volume Effect (PVE)[5]. The main degradation associated with PVE is the underestimation of the radioactivity for objects whose size is less than three times the spatial resolution of the scanner. It will be demonstrated later that the single event spectrum provides useful information about PVE. The objective of this work is to use single events to (1) develop simple new stopping rule for the ML-EM algorithm and (2) evaluate the image degradation due to PVE.

MATERIALS AND EXPERIMENTAL PROCEDURE

A. PET scanner, coincidence and single events measurement

The measurements of single and coincidence events are performed with the ECAT 931 located at the Cyclotron and Radioisotope Center (CYRIC) at Tohoku University. The coincidence measurements last 10 *min* and the single measurements last 640 *s*. A ^{22}Na point source is located at the center of the gantry in order to measure the single events spectrum for 30 minutes. This data is used to determine the multiplicative normalization coefficients used to correct the single events measurements. In this work a measurements is equivalent to obtaining the coincidence and the single data sets.

B. Estimation of Single Events from the reconstructed and a new stopping rule

In order to evaluate the agreement between the measured single data and the single events calculated from the reconstructed images, we assume to have a ring surrounded by a total of D individual radiation detectors and the image is reconstructed into a grid composed of B pixels. Therefore, the number of photons emitted from the pixel b that are counted by the detector d within the time interval Δt, after each iteration n of the ML-EM algorithm, is written as:

$$N_n^{db} = \lambda_n^b p_{db} \varepsilon_{db} A_{db} \Delta t \qquad (1)$$

where λ^{β}_n represents the estimated activity inside the pixel b after the ML-EM iteration n, $p_{\delta\beta}$ is the solid angle that the pixel b forms with the detector d, $\varepsilon_{\delta b}$ accounts for the intrinsic efficiency of BGO scintillators to detect 511 keV photons and $A_{\delta b}$ is the probability that the photon will not be scattered or absorbed in it way from b to d. Ignoring dead time effects, the calculated amount of photons acquired by detector d after n is expressed as:

$$N_n^d = \sum_{b=1}^{B} N_n^{db} \tag{2}$$

The measured single counts for each detector d are symbolized as M^d. Thus, a chi-square figure is defined in order to evaluate quantitatively the differences between the measured and the calculated set after each iteration n. Assuming the single counting process as Poisson distributed, the chi-square is calculated as:

$$\chi_n^2 = \sum_{d=1}^{D} \frac{(N_n^d - M^d)^2}{N_n^d} \tag{3}$$

It is tempting to suggest that the reconstruction process should be halted when the chi-square reach a minimum value, but the results will show later that this value does not reach a minimum and instead it converges to a constant value. Therefore, the reconstruction process should be halted when the chi-square does not show meaningful variation for consecutive iterations. For the purpose of evaluating the variation of the chi-square, we define the following parameter:

$$C_n = \left| \frac{\chi_n^2 - \chi_{n-1}^2}{\chi_{n-1}^2} \right| \tag{4}$$

The parameter C_n is calculated after each iteration and this value represents the medullar point of the stopping rule sketched in Fig. 1. This figure shows that after each iteration, C_n is compared to the constant value α and the reconstruction process is stopped when C_n is smaller than α. The constant α represents how much we consider negligible the variation of the chi-square parameter through consecutive iterations. Thus, it can be argued that it is an observer dependent value and due to the convergence properties of the ML-EM algorithm, this constant should also be object dependent.

C Estimation of the uncertainty associated with C_n

It is very important to determine the significance of the parameter C_n because it represents the core in the implementation of the stopping rule studied here. Therefore, it is essential to know the error associated to the calculation of C_n. For this purpose, the basic theory of statistical error propagation[18] is used. Basically, the error of a multivariable function $f(x_1, x_2, x_3, ...)$ is given in terms of the error for each variable, as follows:

$$\sigma_f^2 = \left(\frac{\partial f}{\partial x_1}\right)^2 \sigma_{x_1}^2 + \left(\frac{\partial f}{\partial x_2}\right)^2 \sigma_{x_2}^2 + \left(\frac{\partial f}{\partial x_3}\right)^2 \sigma_{x_3}^2 + ... \tag{5}$$

Hence, applying the equation (5) to equation (4), the square of C_n's error is given by:

$$\sigma_{C_n}^2 = \left(\frac{\chi_n^2}{(\chi_{n-1}^2)^2}\right)^2 \sigma_{\chi_{n-1}^2}^2 + \left(\frac{1}{\chi_{n-1}^2}\right)^2 \sigma_{\chi_n^2}^2 \tag{6}$$

This mathematical expression reduces the problem in hands to estimating the uncertainty of the chi-square parameter. It is possible to express the chi-square factor as follows:

$$\chi_n^2 = \sum_{d=1}^{D} (f_n^d)^2 \tag{7}$$

thus that

$$\sigma_{\chi_n^2}^2 = 2\sum_{d=1}^{D} f_n^d \sigma_{f_n^d}^2 \tag{8}$$

Again, using equation (5), the error of f_n^d is written as

$$\sigma_{f_n^d}^2 = \sigma_{M^d}^2 + \sigma_{N_n^d}^2 \tag{9}$$

Since M^d are the measured single counts, assuming that this counting process is Poisson distributed, its variance is itself. It is written as:

$$\sigma_{M^d}^2 = M^d \tag{10}$$

In order to estimate $\sigma_{N_n^d}^2$, it is necessary to apply (5) to (1). The variance of the calculated single events is expressed as

$$\sigma_{N_n^d}^2 = \sum_{b=1}^{B} (\varepsilon_{db} s_{db} A_{db})^2 \sigma_{\lambda_b^n}^2 \tag{11}$$

It is also assumed that the coincidence emission is a Poisson process, therefore it is possible to express that

$$\sigma_{\lambda_b^n}^2 = \lambda_b^n \tag{12}$$

Connecting the previous results, the squared of the error on the estimation of the chi-square factor for iteration n is expressed by the following equation

$$\sigma_{\chi_n^2}^2 = 2\sum_{d=1}^{D} (M^d - N_n^d)(M^d + \sum_{b=1}^{B} (\varepsilon_{db} s_{db} A_{db})^2 \lambda_b^n) \tag{13}$$

The variance of the chi-square parameter can be easily inserted into (5) to obtain the variance of C_n.

D Three different positron activity distributions

The performance of the stopping rule illustrated in Fig. 1 is studied by using two

different activity distributions (DA and DB) of positron emitters. The relationship between PVE and the single events spectrum is studied by measuring the activity distribution DC. These three activity distributions are illustrated in Fig. 2. The different objects in these activity distributions have the same activity concentration. In the case of DA and DB the different spot sizes aim to study the trades of the stopping rule among objects of different sizes. Six independent measurements are carried out for DA. The main purpose is to study the stability of the stopping rule when the total number of coincidence counts decreases. These six measurements are consecutives. For the same purpose DB is measured two times, but the variation of coincidence events is larger because the second scan is performed 770 minutes after the first one. In the case of DC, it has been used three spots (represented by d_1, d_2 and d_6) that will surely undergo PVE and one spot (d_4) that at worse will slightly suffer PVE. DC is measured two times separated by a 180 min interval.

E Evaluation of image convergence

In order to evaluate the convergence of the reconstructed image, two, six and four regions of interest (ROI) are drawn in the images reconstructed for DA, DB and DC, respectively. Fig. 3 illustrates the locations of the ROIs on each reconstructed image. These ROIs attempt to cover the hot spots on each reconstructed image.

RESULTS AND DISCUSSION

A. Stopping rule

The data sets obtained from DA and DB are reconstructed by the ML-EM algorithm restricted with the stopping rule. For the first measurement of DA, called DA 1, the behavior of χ_n^2 and C_n is illustrated in Fig. 4. The chi-square (Fig. 4 a) converges very fast (around $n = 5$). Therefore, it is necessary to decide what will be considered as its negligible variation. C_n varies rapidly for the first iterations and around $n = 14$ it starts to converge. At this point $C_n = 0.0259 \pm 0.0024$, hence we set $\alpha = 0.0300$. This α value is used to run the reconstruction process illustrated in Fig. 1 for the data sets obtained from DA and DB. The optimum numbers of iterations estimated for each data set are summarized in Table I. The estimations for DA's reconstructions do not change which means that the stopping rule is independent of the measured coincidence counts which ranged from 3×10^6 to 1×10^6 counts. The variation of the mean value of ROI 1 and ROI 2

in the images of the first data set measured for DA (DA 1) is shown in Fig. 5. From the point of view of the mean value, it is possible to see that at n = 14, both ROIs have already converged. ROI 1 converges faster that ROI 2, nevertheless it is still not degraded due to overiteration. The behavior of the mean value for the other five measurements of DA is similar to the behavior illustrated in Fig. 5, therefore the same conclusion holds for all data sets of DA. In the case of the data sets measured from DB, the variation of the mean value for six ROIs is illustrated in Fig. 6 and Fig. 7. For DB 1, at n= 20, the larger hot spots (ROI 1-ROI 4) have already converged and the smaller spots (ROI 5 and ROI 6) exhibit estimated that are around 90% of the convergence value. Therefore, 20 iterations appear to represent a good trade between the converged and the non-converged ROIs. In general, DB 2 slightly faster than DB and it is possible to see the same tradeoff in ROIs convergence, if the reconstruction is halted at n = 15. The total amount of coincidence counts measured for DB 1 is 3.5×10^6 and for DB 2 is 1.7×10^3. Thus, the stability of the stopping rule using single events is evident from the measurements of the activity distribution DB.

B. Partial Volume Effect

The comparison between measured and calculated single events shows that this type of measurement provides with useful information on image degradation due to PVE. To begin discussing this topic, let's take a look to Fig. 8. This figure compares the measured single events spectrum with the one calculated from the reconstructed image for the second scan of DC, without PVE corrections. It is important to see that the activity distribution DC is composed of four hot spots, so that four peaks would be expected in the single events spectrum. However, there is only one broad peak which means that the single spectrum cannot resolve the amount of hot spots in the reconstructed image, at least in the measurements designed for this work. However, it is interesting to see that the calculated single spectrum does not show good agreement with the measurements by the tails of the broad peak. Comparing DC (Fig. 2) with its reconstructed image (Fig. 3) it is clear that the smallest hot spot is not recovered in the reconstruction process due to PVE. Therefore, this non-recovered spot does not contribute to the calculated single events while it contributes to the measured singles. Correction for PVE is carried out. For this purpose, it is obtained the variation of the count recovery coefficient (RC) [5] for the ECAT 931 with respect to the known hot spot size. The RCs are obtained as the ration between estimated and true maximum count for each ROI.

$$RC_{ROI} = \frac{Estimated \quad Maximum \quad ROI \quad Count}{True \quad Maximum \quad ROI \quad Count} \tag{14}$$

It is important to remember that each ROI aims to cover the respective hot spot. Therefore, the RCs are determined for different hot spot sizes. This information is illustrated in Fig. 9. The hot spots whose size is larger than 16 mm do not suffer significant degradation due to PVE. The information provided by Fig. 9 allows correcting the estimated activity of a ROI by taking the horizontal activity profile, assuming the ROI size to be the FWHM of its profile, determine the RC corresponding to this size and finally multiply this RC by the activity estimates of each image element within the ROI. This correction method is applied to the images reconstructed for DC and the improvement is remarkable, as shown in Fig. 10. The smallest hot spot is almost non-recovered without PVE correction, but after applying the count recovery coefficient technique it is perfectly visible in the reconstructed image. Now it is necessary to evaluate how effective is the PVE correction. This evaluation is carried out by comparing the measured single events with the calculated singles from the PVE corrected-image. This comparison is illustrated in Fig. 11. In this figure, the measured single spectrum is compared to the calculated one, after PVE correction. The tails region exhibits a good agreement between measured and calculated single events. This suggests that the single event spectrum can be a very useful tool to study the degradation of reconstructed images due to PVE. Furthermore, a comparison between measured and calculated singles after PVE would indicate the effectiveness of the PVE correction method.

CONCLUSION

This work has shown that iterative image reconstruction by ML-EM could be monitored through the single events and good agreement between measured and calculated singles from the reconstructed image was useful to halt the reconstruction process at a point where the image was not excessively iterated. This halting point is characterized by a reasonable tradeoff among different convergence rate, i.e. different object sizes. The main drawback for implementing this technique is to decide the α value, which represents what will be considered as negligible variation of the calculated single event spectrum. In this work, α = 0.0300 provided reliable estimation of the optimum number of iterations necessary to reconstruct different data sets. However, it is not possible to conclude that this value is independent of the positron activity distribution. The stopping rule introduced

in this work has shown to be independent of the total amount of coincidence counts, at least for the range of counts measured in this work. This work also shows that comparison between measured and calculated singles provides information on image degradation due to PVE. The disagreement in this comparison arises when the size of imaged objects are comparable to twice the image resolution. This is witnessed by the fact that disagreement between measured and calculated singles was seen only for DC. After PVE correction is carried out, the comparison between calculated and measured singles provided information on the quality of the reconstructed image.

REFERENCES

1) Turkington T.T., J. Nucl. Med. Technol. **29** (2001) 1.
2) http://oden.nuc.ucla.edu/rs200b/lecture_notes/lecture7/pet9.html
3) Budinger T.F., Brennan K.M., Moses, W.W. Derenzo S.E., Nucl. Med. Biol. **23** (1996) 659.
4) Phelps M., Mazziotta J., Schelbert H., Raven Press, 1986.
5) Barrett H.H., Wilson D.W., Tsui B.M.W., Phys. Med. Biol. **39** (1994) 833.
6) Shepp L.A., Vardi Y., IEEE Trans. Med. Imag. **MI-1** (1982) 113.
7) Lange K., Carson R., JCAT **8** (1984) 306.
8) Veklerov E., Llacer J., Hoffman E.J., IEEE Trans Nucl. Sci. **35** (1988) 603.
9) Herbert T., Leahy R., Singh M., IEEE Trans. Nucl. Sci. **35** (1988) 615.
10) Coakley K.J., IEEE Trans. Nucl. Sci. **38** (1991) 9.
11) Coakley K.J., Llacer J., SPIE Proc. Image Phys: Med. Imaging **1443** (1991) 226.
12) Johnson V.E., IEEE Trans. Med. Imag. **13** (1994) 569.
13) Selivanov V.V., Lapointe D., Bentourkia M., Lecomte R., IEEE Trans. Nucl. Sci. **48** (2001)883.
14) Veklerov E., Llacer J., IEEE Trans. Med. Imag. **MI-6** (1987) 313.
15) Llacer J., Veklerov E., IEEE Trans. Med. Imag. **8** (1989) 186.
16) Kontaxakis G., Tzanakos G., "Study of the convergence properties of the EM algorithm: A new stopping rule", Conference Record of the IEEE Nuclear Science Symposium and Medical Imaging Conference, Vol. 2, pp. 1163-1165,1992.
17) Laymon C.M., Turkington T.G., IEEE Trans. Med. Imag. **18** (1999) 1194
18) Knoll G.F., "Radiation Detection and Measurement", 2nd Edition, New York, Wiley, 1989.

Table 1. Optimum number of iterations estimated for each data set obtained from the activity distribution DA.

Data set	DA 1	DA 2	DA 3	DA 4	DA 5	DA 6	DB 1	DB 2
Optimum *n*	14	14	14	14	14	14	20	15

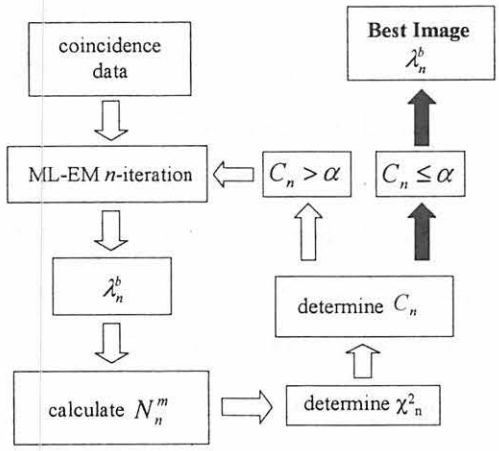

Fig. 1. Schematic of the procedure followed on the implementation of the stopping rule using the single events.

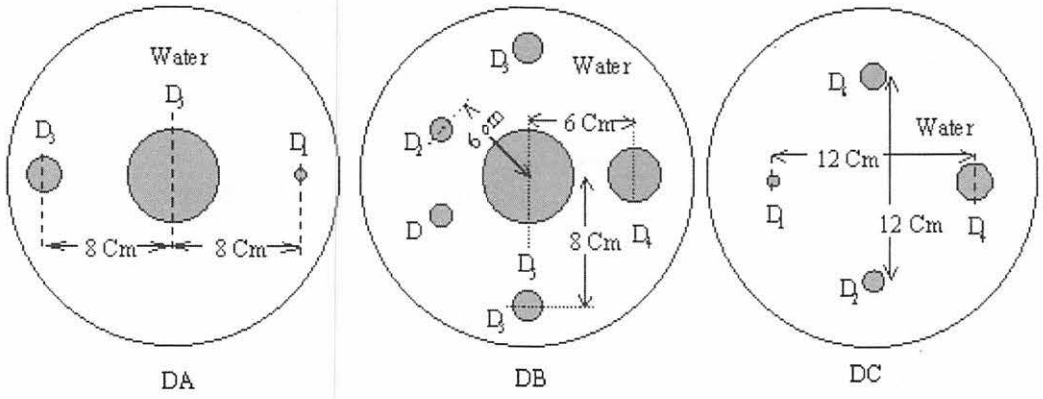

Fig. 2. Schematic of two activity distributions (DA and DB) used to study the stopping rule and one activity distribution (DC) utilized to study PVE. The activity concentration is the same for all hot spots. The positron emitter is ^{18}F. There are different diameters. Their value in mm is: d_1=7.5, d_2=17.4, d_3=22.7, d_4=40.0, d_5=70.0, d_6=13.4

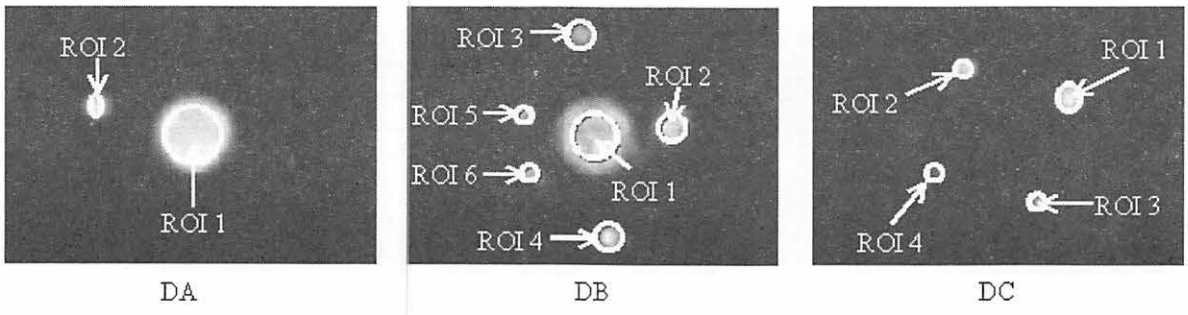

Fig. 3. Illustration of the location of the regions of interest (ROIs) drawn on the reconstructed images for DA, DB, DC aiming to study the convergence of the positron activity estimations.

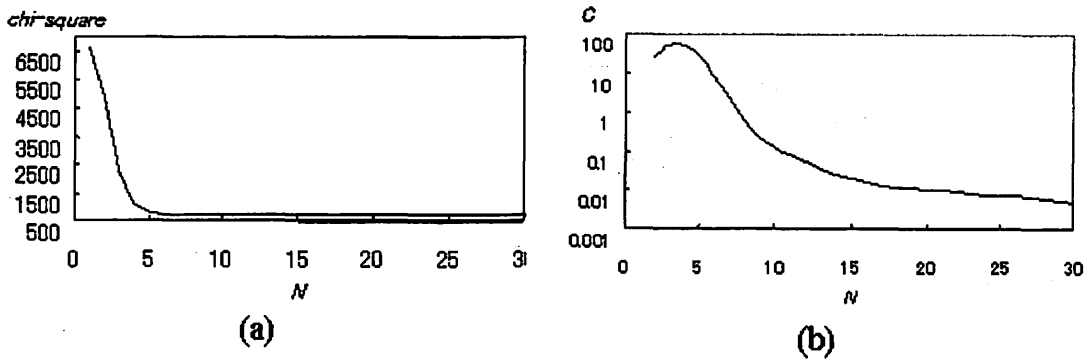

Fig. 4. Behavior of (a) chi-square and (b) C_n values obtained from the ML-EM image reconstruction of the first data set measured for DA.

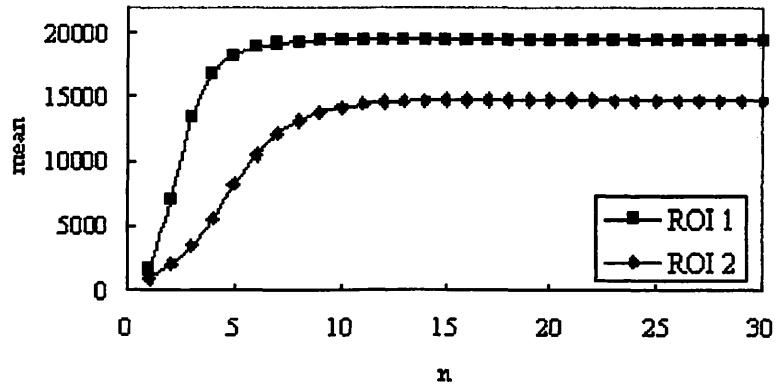

Fig. 5. Variation of the mean value for two regions of interest drawn in the reconstructed images for the first data set of DA

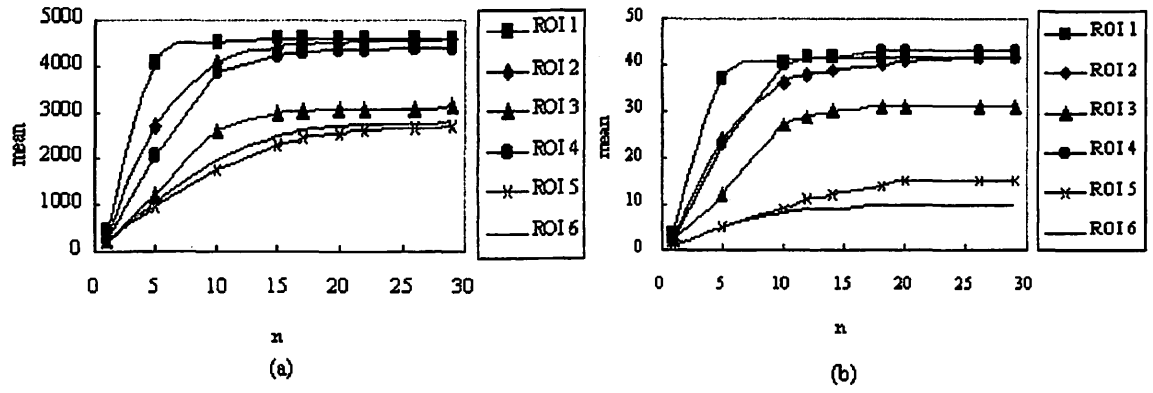

Fig. 6. Variation of the mean value for six regions of interest drawn in the reconstructed images for the first data set (a) and the second data set (b) of DB.

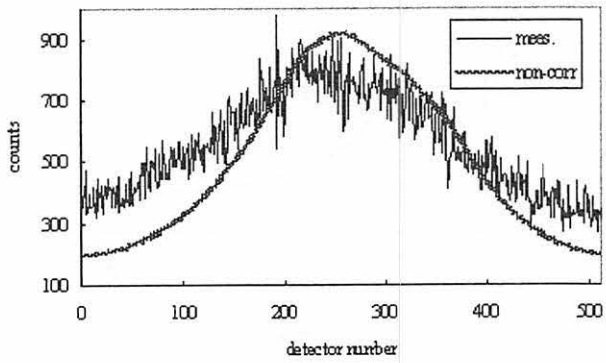

Fig. 7. Comparison between the measured (meas) and the calculated (non-corr), after 16 iterations, single events spectrum for the second data set measured for the distribution DC.

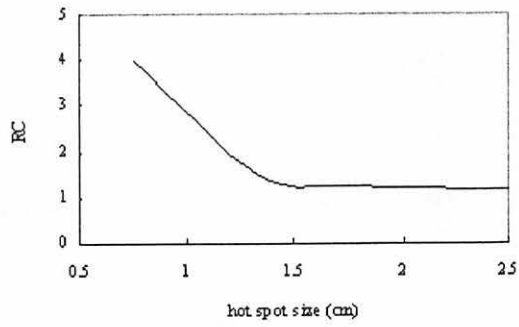

Fig. 8. Recovery coefficient in the ECAT 931 scanner with respect to the size of the hot spot. The true sizes of the hot spots are taken from the phantoms described for DB and DC

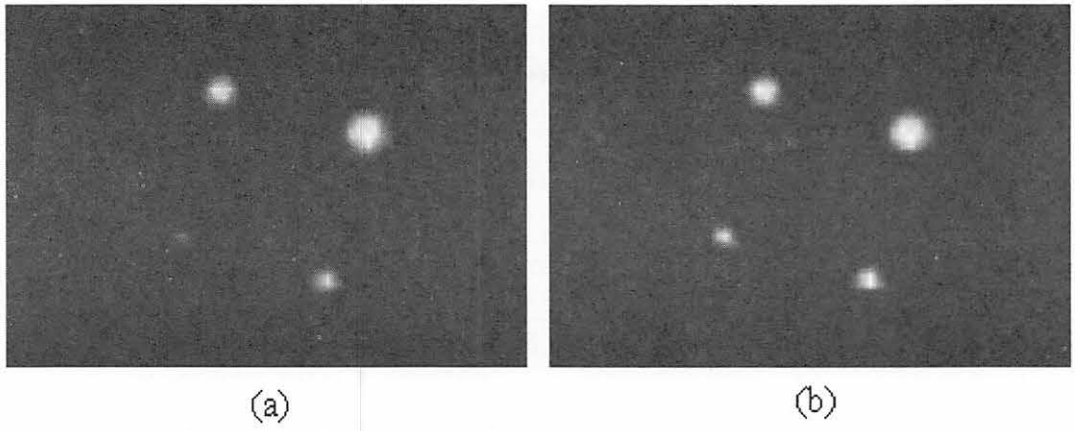

Fig. 9. Comparison of reconstructed images for data set DC 2 (a) without and (b) with PVE correction by using a count recovery coefficient technique.

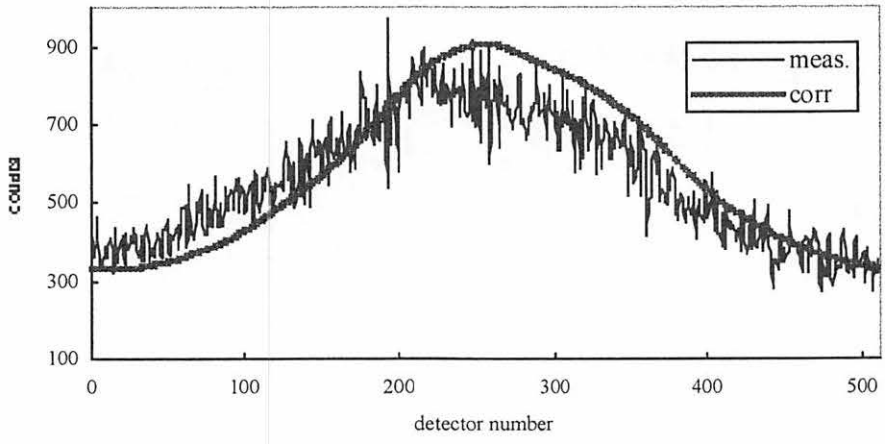

Fig. 10. Comparison between the measured (meas) and the calculated (corr), after 16 iterations, single events spectrum after PVE correction for the second data set measured for the distribution DC.

IV. 4. Benchmark Experiments for Cyclotron-based Neutron Source for BNCT

Yonai S., Itoga T., Nakamura T., BabaM., Yashima H. Yokobori H., and Tahara Y.***,

Cyclotron and Radioisotope Center, Tohoku University
*Advanced Reactor Technology Co., Ltd., Japan**
*Mitsubishi Heavy Industries, Ltd., Japan***

Introduction

Boron Neutron Capture Therapy (BNCT) is promising treatment for brain tumors such as glioblastoma multiforme, which are at present considered to be inoperable. BNCT relies on two components, ^{10}B-doped pharmaceuticals and neutrons for irradiation. The ^{10}B component, which is delivered preferentially to the tumor cells, is administered to the patient, who is subsequently irradiated with an external neutron beam. The ^{10}B (n,α) ^{7}Li reaction, on which BNCT is based, has a large cross section of ~3800 barn for thermal neutrons and produces two particles, α and ^{7}Li, with high linear energy transfer (LET) and relative biological effectiveness (RBE). The mean free path of the particles in cells is about 10 μm and 5 μm for α particles and for ^{7}Li, respectively. Considering that the mean cellular diameter is of the order of 10 μm, it is possible that BNCT may act selectively in killing cells.

The use of epithermal neutrons in BNCT has recently been of increasing interest, taking into account that incident neutrons are moderated in the human body. The accelerator-based neutron sources are also required for the ease of use and the establishment with hospitals. Many groups have been investigating the accelerator-based neutron sources. However they have not been realized yet in practical applications, mainly because of a very high beam current required for accelerators which introduces a serious difficulty in target cooling. In the previous study[1], we found the feasibility of a cyclotron-based BNCT using the Ta(p, n) neutrons at 90° bombarded by 50 MeV protons, and the iron, AlF_3, Al and ^{6}LiF moderators through measurements of angular distributions of neutron energy spectra from Ta(p, n) reaction and simulations using the MCNPX code[2]. This

cyclotron-based BNCT which requires comparatively low beam power gives similar dose distribution with the other accelerator-based BNCT, and provides a realistic solution to the realization of the accelerator-based BNCT.

In order to realize the cyclotron-based BNCT, it is required to validate the accuracy of the simulations by the measurements. Here in this study, we measured the neutron energy spectra behind the moderator and the distribution of thermal neutrons in an acrylic phantom by using the gold activation foils through the $^{197}Au(n,\gamma)^{198}Au$ reaction at the Cyclotron and Radioisotope Center (CYRIC) of Tohoku University. The method for measuring the intensity of neutrons irradiated to the patient has not been established yet in the BNCT treatment using the epithermal neutrons, and most facilities use the computer code for the treatment planning. Because the neutron energy spectrum behind the moderator is the neutron source in the code, the validation is essential for accelerator-based BNCT. The measurement of distribution of thermal neutrons in a phantom is also very important, because the thermal neutrons directly interact with ^{10}B and dominate the tumor dose.

Experimental method

The experimental arrangement is shown in Fig. 1. The measurements of the epithermal neutron energy spectrum and the thermal neutron distribution in an acrylic phantom were performed at the TOF (Time-Of-Flight) room at CYRIC, which is connected to the 5th target room and has very low background. The experimental arrangements for neutron spectrometry and thermal neutron distribution in a phantom are both shown in Fig. 1. The neutrons were produced from the 3mm thick (stopping-length) Ta target bombarded at an angle of 90° by 50 MeV protons, and extracted to the TOF room through the first and second collimators. The first collimator made of 150 cm thick concrete has a hole shown in Fig. 1. The moderators were set in the second collimator with a hole of 100 cm wide by 50 cm high in a concrete wall of 283 cm thickness between the 5th target room and the TOF room. The front surface of the moderator is 1048 cm distant from the neutron production target. Since this geometrical arrangement is a little different from that in our previous feasibility study[1] due to a space limitation, the shape of the neutron energy spectrum behind the moderator may be slightly different from simulations. However, its difference is not very serious for validation of simulation. The number of beam particles incident on the target was measured from the current of the target itself which was surrounded by a biased-copper mesh to suppress secondary electrons escaping from the target.

The measurement of the epithermal neutron spectrum was performed with our new multi-moderator spectrometer[3] and a bare ^{3}He counter with/without the Cd absorber and a conventional Bonner Sphere of 11.6 cm radius moderator developed by Uwamino et al.[4]). The neutron energy spectrum was obtained by unfolding the measured counts with the SAND-II code[5]. Two initial guesses of the neutron energy spectrum were used in the unfolding procedure. One is calculated spectrum under this experimental geometry with the MCNPX code, the other is the 1/E spectrum.

The measurement of the thermal neutron flux distribution was performed in an acrylic phantom of 30 cm × 30 cm × 30 cm (density: 0.944 g/cm^3) by the gold activation technique. The phantom was set at 15 cm behind the moderators. The gold foils of 1 cm diameter by 100 μm thickness were set at 0, 1, 3, 5, 8, 10 and 12 cm depth in a phantom on the beam line. The ^{198}Au gamma ray activities through the ^{197}Au(n,γ) reaction were measured with a HP-Ge detector, whose efficiency was calculated with the EGS4 code[6].

Result and Discussion

Figure 2 shows the comparison of measured and calculated neutron energy spectra behind the moderator. Good agreement between the calculation and the measurements could be obtained. The energy spectrum gives two peaks at thermal energy of ~0.1 eV and at epithermal energy of ~10 keV. The former peak component mainly comes from the neutrons scattered down to thermal energy by the surrounding bulky concrete and the latter peak component is the neutrons moderated through the moderator assembly which can be used for BNCT.

Figure 3 shows the comparison of the depth distribution of measured and calculated reaction rates of ^{197}Au(n,γ)^{198}Au in an acrylic phantom. The calculations agree with the measurements within ~20 % over the depth of 16 cm. The calculations at the depth shallower than 8 cm underestimate the measurements, which is the similar as the result for measuring the neutron energy spectrum. We consider that these underestimations may come from underestimation of the neutron-production yield from the Ta(p,n) reaction. The calculation using the LA150 cross-section data[7] underestimates the measurement in the energy range lower than ~5 MeV[1]. This underestimation may give a strong influence on the results in this study. While at the deeper position, the calculations of the reaction rates overestimate the measurements. This may be because the measurements of gamma rays emitted from ^{198}Au have the large uncertainties due to the insufficient radioactivities. We

could not get the higher neutron flux at the irradiation points in this experimental arrangement.

Because the discrepancy between the measurement and calculation was found for the thermal neutron flux distribution in the phantom as the above, we performed the measurement using the mono-energetic neutrons at Fast Neutron Laboratory (FNL) of Tohoku University. Figure 4 shows the comparison of measured and calculated reaction rates of $^{197}Au(n,\gamma)^{198}Au$ in an acrylic phantom by 8 keV neutrons. As shown in the figure, the result is the same as those using the continuous energy neutrons at CYRIC. From these the results, the above mentioned discrepancy may be arising from the problem in the MCNPX code or the cross section data. We will need to investigate further the cause.

Reference

1) Yonai S., Aoki T., Nakamura T., Yashima H., Baba M., Yokobori H. and Y. Tahara, Med. Phys. **30** (2003)2021.
2) "MCNPX user's manual," edited by L. S. Waters, TPO-E83-G-UG-X-00001 Rev. 0, Los Alamos Natl. Lab., 14 November 1999.
3) Yonai S., J. Nucl. Sci. Tech. Supplement **4** (2004) 415.
4) Uwamino Y., Nakamura T. and Hara A., Nucl. Instrum. Methods **A239** (1985) 299.
5) McElroy W.N., Berg S., Crockett T. and Hawkins R.G., "A Computer-Automated Iterative Method for Neutron Flux Spectra Determination by Foil Activation - Vol. I: A Study of the Iterative Method." AFWL-TR-67-41, Air Force Weapons Lab. (1967).
6) Hirayama H., Nelson W.R. and Rogers D.W.O., "The EGS4 Code System." SLAC-265, Stanford Linear Accelerator Center, Stanford University, (1985).
7) Young P.G., Chiba S., Frankle S.C., Hale G.M., Hughes H.G., Koning A.J., Little R.C., MacFarlane R.E., Prael R.E. and Waters L.S., Nucl. Sci. Eng. **131** (1999) 293.

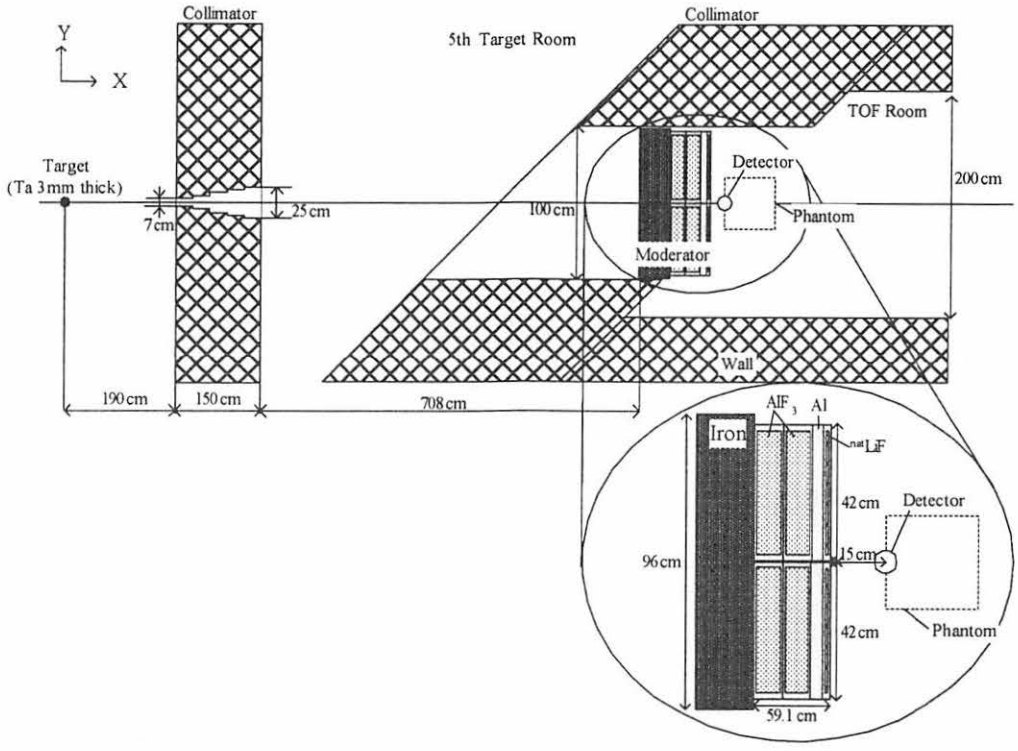

Fig. 1 Cross-sectional view of the experimental setup.

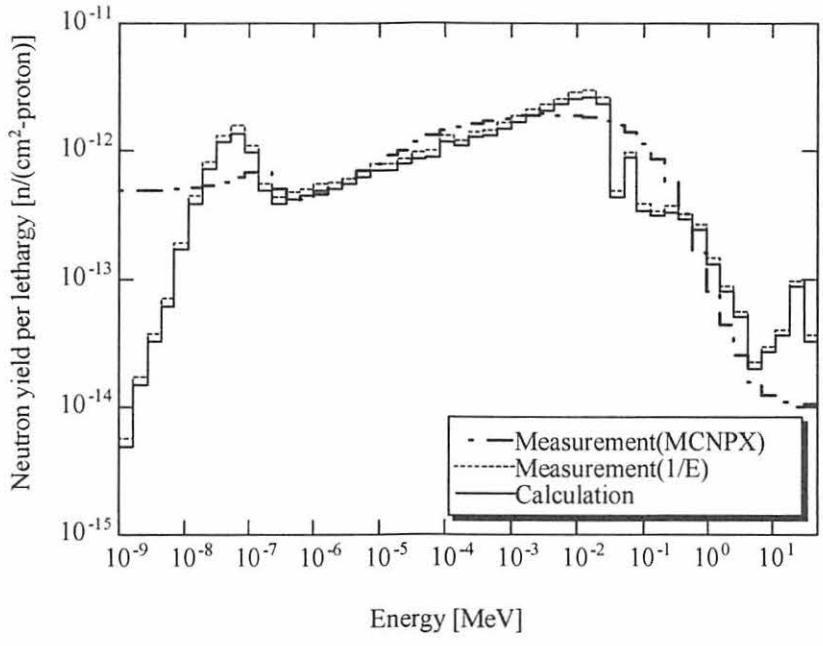

Fig. 2 Comparison of measured and calculated neutron energy spectra behind the moderator.

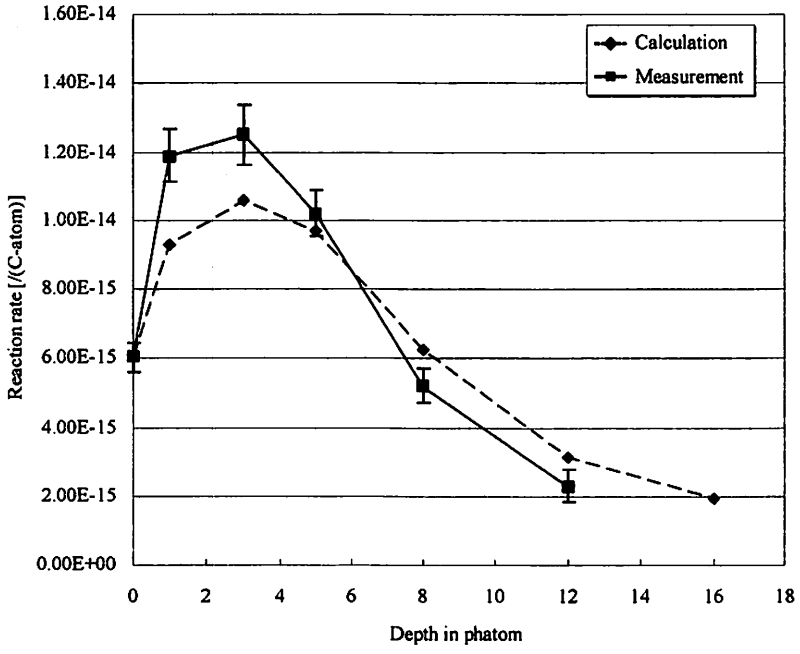

Fig. 3. Comparison of measured and calculated reaction rates of $^{197}Au(n,\gamma)^{198}Au$ in an acrylic phantom put behind the moderator at CYRIC.

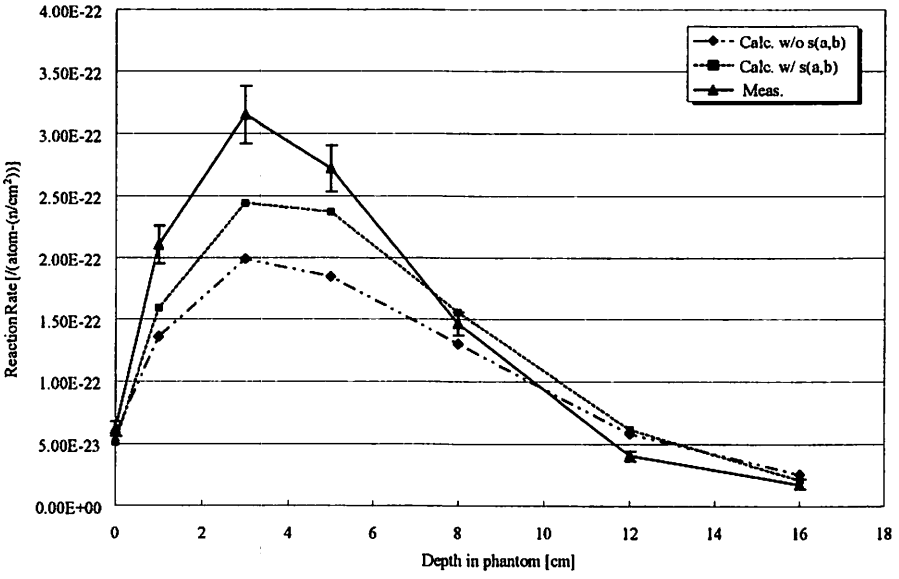

Fig. 4. Comparison of measured and calculated reaction rates of $^{197}Au(n,\gamma)^{198}Au$ in an acrylic phantom by 8 keV neutrons at FNL.

IV. 5. An Approach of Dose Mapping Using Imaging Plates in Interventional Radiology Procedures

Ohuchi H., Satoh T., Eguchi Y.*, and Yamadera A.***

Graduate School of Pharmaceutical Sciences, Tohoku University
*Department of Radiology, Yamagata University Hospital, 2-2-2 Iidanishi, Yamagata 990-9585, Japan**
*School of Health Sciences, Hirosaki University, 66-1 Hon-cho, Hirosaki 036-8564, Japan***

Introduction

The use of interventional radiology (IR) in diagnostic and therapeutic procedures has seen a vast increase in recent years, primarily because of its numerous significant benefits. Prolonged fluoroscopy times and large numbers of radiographs delivered to limited areas of the patient, however, can cause deterministic effects ranging from transient erythema and dermatitis to skin necrosis[1,2]. Mapping skin doses in complex fluoroscopy interventions is useful to determine the probability of a possible injury, to detect areas of overlapping irradiation fields, and to obtain a permanent register of the patient's most exposed skin areas.

In this work, a new method for mapping skin doses in IR using an imaging plate (IP) has been developed. IPs are made of photostimulated luminescence (PSL) materials, are highly sensitive two-dimensional radiation sensors, can be reused repeatedly. Although the IP has already been applied for use as a passive dosemeter[3], there is an issue for applying IP to measure cumulative doses in IR. In the X-rays energies range, IP has a strong dependence on photon energy. By combining the sensitivity data measured with filters of three different metals (aluminum, copper, and cadmium), flat sensitivity of an IP to the dose equivalent (Hp(0.07)) within 8% for X-rays with effective energies of 30 to 120 keV can obtained[4]. However, in X-ray diagnosis, since a shadow of the filter appears on the image and interferes with clinical examination, IPs should be used without filters. Variation of sensitivity without filters for effective energy range in IR procedures was measured by obtaining ratio of the weighted sum of the sensitivities with these three different metal filters to the sensitivities obtained values without filters by irradiation, simulating actual fluoroscopy and radiography procedures. Direct measurement of the

entrance skin dose (ESD) by wrapping a large piece of IPs around the back of a water phantom was attempted and the ESD obtained by IPs was compared with the results obtained by Dose Ace, which was commercially available a photoluminescent glass dosemeter.

Methods

Imaging plate and readout technique

The BAS-TR type IP of 12.7 cm × 12.7 cm in size, manufactured by Fuji Photo Film Co., Ltd. was used. It has a 50-μm-thick photostimulable phosphor ($BaBrF:Eu^{2+}$) and has no protective surface layer. For measuring the ESD using a water phantom, a large piece of IPs of 38.1 cm × 50.8 cm, which was made by coupling 12 sheets of BAS-TR together, was used. The IPs were wrapped in black polyethylene to shield them from sunlight during irradiation. IPs were scanned with a 200 × 200-μm BAS-1000 readout system (Fuji Photo Film Co., Ltd.) 3 - 4 hours after irradiation by the cellophane technique[5], and then, IPs were rescanned after annealing at 100°C for 70 hours.

X-ray irradiation

The IPs were irradiated by using X-ray beams from the X-rays generator (KXO-2050, Toshiba Medical Co.) at Yamagata University Hospital. To generate the data needed to compare the PSL values obtained by combining results with metal filters with the PSL values obtained without filters, the IP, which was in contact with three different metal filters, was placed on the tabletop just under an acrylic phantom and the X-ray beam was provided from under the table. The acrylic phantom was 20 cm thick and had a 33 × 33 cm front face. Figure 1 shows that the IP and the set of filters used in these experiments, which were made of 0.5 mm thick aluminum, 0.1 mm thick copper, and 1.0 mm thick cadmium. Two IPs with filter set were irradiated at every irradiation. Two typical IR procedures were performed, varying tube potential between 60 kV and 120 kV and varying tube current between 1.6 mA and 3.2 mA for fluoroscopy and 250 mA and 400 mA for radiography. To know the dose on a real-time during the procedure, a Skin Dose Monitor (SDM104-101, McMahon Medical Co.) was placed beside IPs.

The relation between PSL density (PSL/mm^2) and absorbed dose (Gy) in the range from 1 mGy to 2 Gy was evaluated by placing IPs under an acrylic phantom. The IP was also in contact with metal filters as shown in Fig.1. Two IPs with filter set were irradiated

at every irradiation. The tube voltage was fixed at 100 kV and the tube currents of 200 and 400 mA were used. The absorbed dose was measured by an ionization chamber (model1015, RADCAL Co.,).

For mapping the ESD, the large piece of IPs was wrapped around the back of a water phantom, which mimicked a human body and had cylindrical shape 20 cm × 30 cm × 45.5 cm, and a typical IR procedure simulating percutaneous transluminal coronary angioplasties (PTCAs) was performed, varying tube potential between 60 kV and 120 kV and using tube current 200 mA for radiography. In this procedure, the IP surface faced toward the X-rays generator, so that the IP could automatically correct for radiation backscattered from the water phantom. The image intnsifier had a field of view (FOV) with a square area of 10 × 10 cm cm on the surface of the water phantom.

Dose Ace

Dose Ace (Asahi Techno Glass Co.,) consists of a silver-activated photoluminescence glass dosemeter (PLD) chip and 0.76 mm thick tin filter for energy compensation (GD-352M). 48 PLD chips were used to measure the ESD. Each PLD chip was placed at intervals of 5 cm in a grid of 8 lines and 6 rows on the reverse of the IP sheet. PLD chips were read out by a PL reader (FGD-1000) by using pulsed UV laser stimulation[6].

Results

Irradiation simulating actual medical practice for fluoroscopy and radiography showed that ratio of values obtained with three different metal filters to values without filters remained constant to within 5% in two typical IR procedures. This indicates that metal filters are not necessary when IPs are used for estimating skin dose distributions in typical IR procedures.

The correlations between PSL density (PSL/mm^2) and the absorbed dose (mGy) are exhibited in Figure 2, showing excellent linearity. The results by the annealing technique showed better linearity than those by the cellophane technique. Because the former can decrease the effects of fading and give a more precise estimate of quantitative dose, though the latter does not account for the effects of fading[5].

Images of dose distributions obtained by scanning of the large piece of IPs with the annealing technique are shown in Figure 3. Peak skin dose (PSD) area, which is marked

with a white line, can be easily recognized visually by variations of PSL density. The higher level of ESD in this area is due to overlapping of irradiation fields with two views; LAO 45° - CRA 25 ° and LAO 60- ° CRA 0 ° , which are frequently used projection in PTCAs. The result of mapping of ESD, which was calculated from the PSL values with the annealing technique using an equation obtained from the regression line in Fig.2, are exhibited in Figure 4. The PSD was estimated to be 1.62 Gy (±4.3%) with the annealing technique and 1.16 Gy (±8.5%) with the cellophane technique. The results by PLD chips were also mapped and shown in Figure 5, giving 1.41 Gy as the highest dose. Both mapped dose distribution by using IPs (Fig.4) and PLD chips (Fig.5) show an excellent agreement, however, the PSD area cannot be recognized in mapped ESD obtained by PLD chips.

Discussion

The easiest way to determine the ESD is by direct measurement with special detectors such as TL dosemeters. Incorrect positioning of dosemeters, however, can easily result in underestimation of the ESD. An important issue on the measurement in IR is to know the extent of the irradiation field and the intensity of dose. In order not to miss hot spots, we have to increase the number of monitoring points and dosemeters. At this point of view, mapping skin doses in IR by using two-dimensional radiation sensors is the best way. Since most installations avoid high dose rates in the vicinity of the patient and staff by using fluoroscopy equipment configured with an over-couch image intensifier and an under-couch X-ray tube, the patient's skin dose can be mapped by placing a large piece of film relatively insensitive to X-rays on the tabletop just under the patient. Guibelalde reported that Kodak EDR2 film could be used this way to estimate maximum skin doses up to 1400 mGy but that the linear range for accurate dose measurements was only from 50 mGy to 500 mGy[7]. According to ICRP Publication 85[8], all patients with estimated skin doses of 3 Gy or above should be followed up after exposure. They are thus not adequate for indicating the likely onset of deterministic effects. Furthermore, films like EDR2 cannot be reused. The IP of BAS-TR can estimate skin doses ranging from 1 μGy to 100 Gy and has linearity up to about 10 Gy[4,5]. This, along with the possibility of reusing IPs repeatedly by irradiating them with visible light between uses, supports the usefulness of IPs for estimating and mapping skin dose distributions in high-dose IR procedures.

References

1) Vano E., Arranz L., Sastre J.M., Moro C., Ledo A., Garate M.T. and Minguez, I., Br. J. Radiol.,**71** (1998) 510.
2) Faulkner K. and Vano E., Radiat. Prot. Dosim. **94** (2001) 95.
3) Ohuchi H., Yamadera A. and Baba M., Radiat. Prot. Dosim. **107** (2003) 239.
4) Ohuchi H., Yamadera A., Satoh T. and Eguchi Y., FULL PAPERS of the 11th International Congress of the International Radiation Protection Association (2004)
5) Ohuchi H., and Yamadera A., Nucl. Sci Technol. (Suppl.) **4** (2004) 140.
6) Tsuda M., Japan. J. Med. Phys. **20** (2000) 131.
7) Guibelalde E., Vano E.,Gonzalez L., Prieto C.,Fernandez J.M. and Ten J.I., Br. J. Radiol. **76** (2003) 332.
8) International Commission on Radiological Protection (ICRP). ICRP Publication 85.(Ann. ICRP **30** (2))(Oxford: Pergamon Press) (2000).

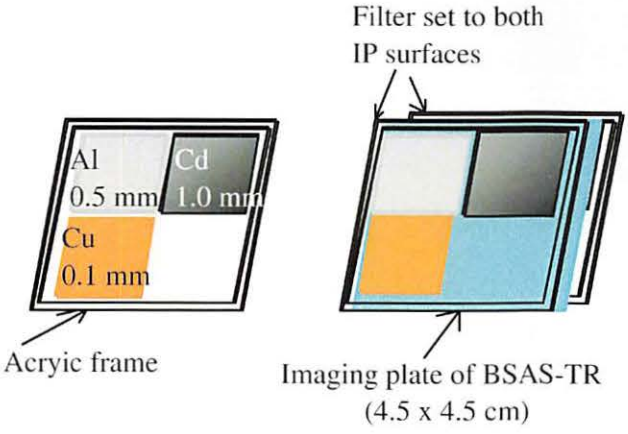

Fig. 1. IP and the set of filters.

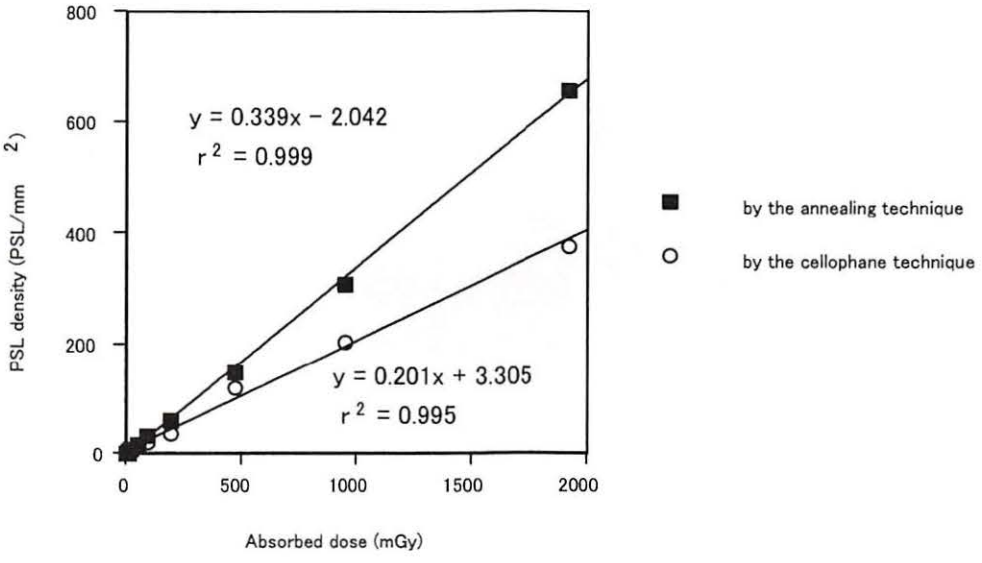

Fig. 2. Correlation between PSL density and the absorbed dose (mGy). IPs are scanned by the cellophane technique, and then, after annealing at 100°C for 70 hours, they are rescanned.

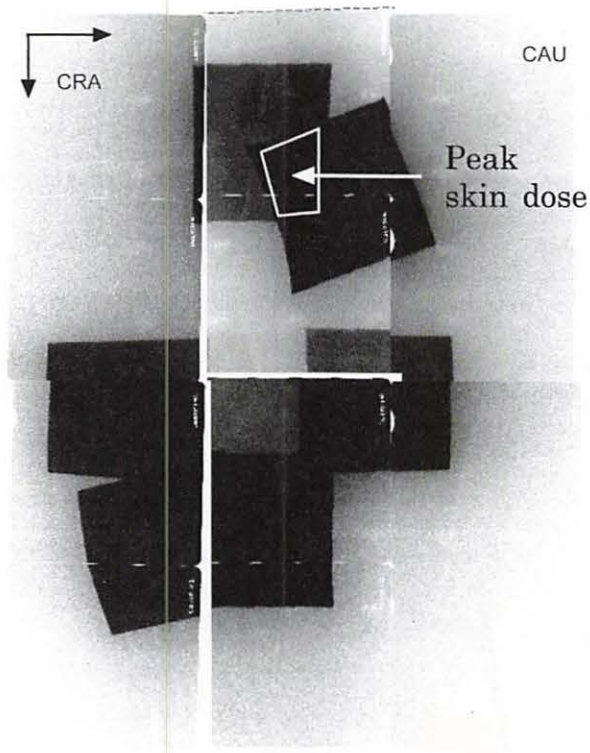

Fig. 3. Images of dose distributions obtained by scanning of the large piece of IPs with the annealing technique. Peak skin dose (PSD) area is marked with a white line.

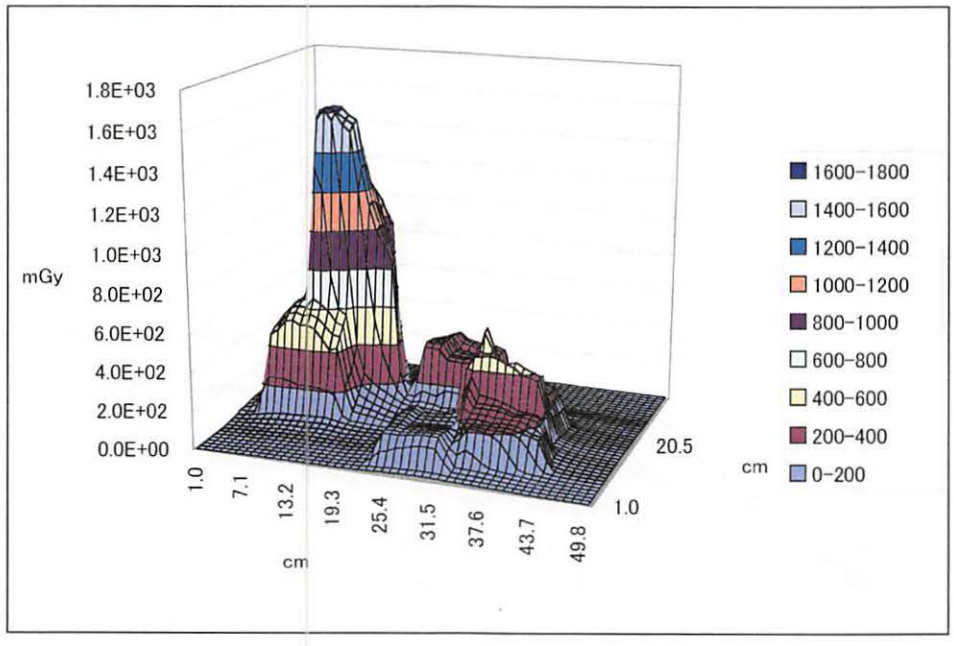

Fig. 4. Mapped ESD obtained by IPs. IPs are read out after annealing at 100°C for 70 hours.

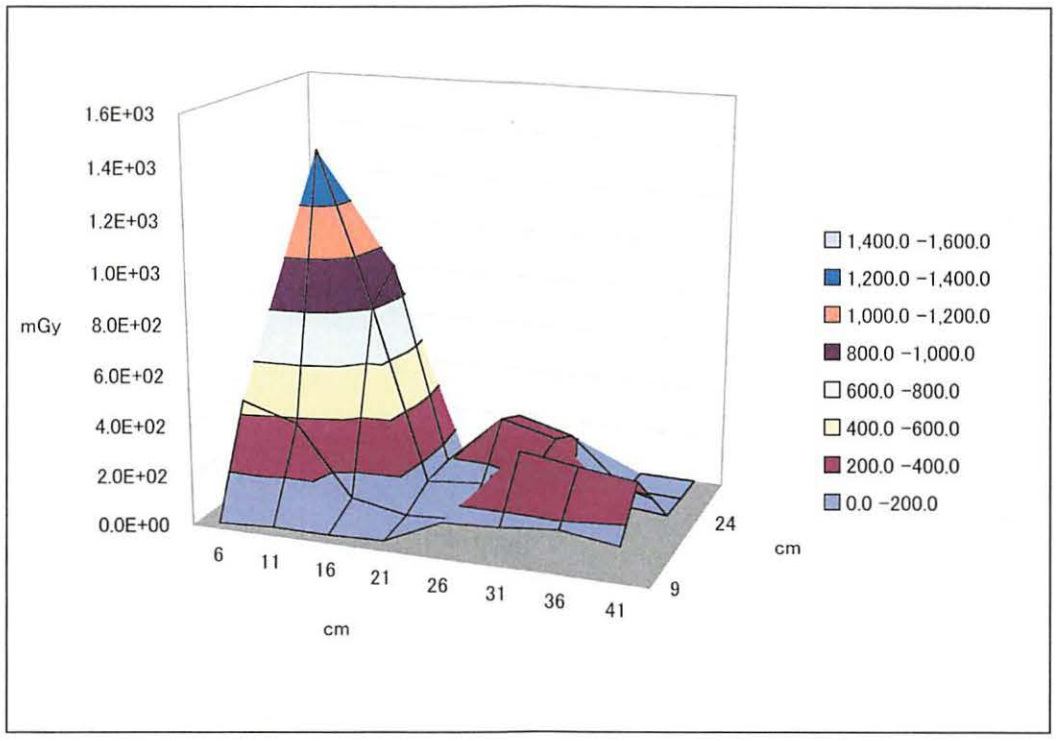

Fig. 5. Mapped ESD obtained by PLD chips.

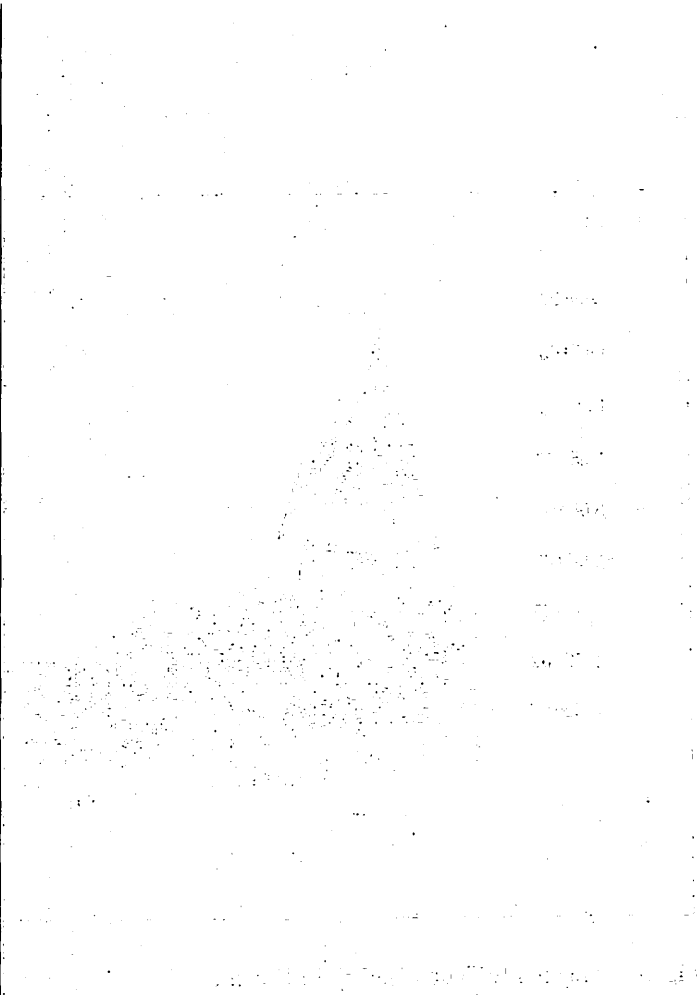

V. PIXE ANALYSIS

V. 1. Applicability of Carbon Ions in PIXE Analysis

Amartaivan T., Ishii K., Yamazaki H., Matsuyama S., Suzuki A., Yamaguchi T., Abe S., Inomata K., and Watanabe Y.

Department of Quantum Science and Energy Engineering, Graduate School of Engineering, Tohoku University

INTRODUCTION

The heavier elements, like As, Cd, Pb, Hg are highly toxic to the human body even at trace level. Therefore, high sensitivity of trace heavy element analysis is of great importance for environmental monitoring. Particle induced X-ray emission (PIXE) is a powerful technique for quantitative analysis because it is non-destructive, multi-elemental (from Na to U), highly sensitive and requires no special sample preparation. Usually proton beams with an energy around 3 MeV, are used in PIXE offering high sensitivity. Since the sensitivity of PIXE strongly depends on the X-ray production cross-sections, which are proportional to the square of the projectile charge, it can be expected that the use of heavy ion beams improves the sensitivity of the analysis considerably. However, extensive systematic applications to elemental analysis using heavy ion beams are lacking due to a number of problems such as the determination of fluorescence yield, line shifts and peak broadening due to multiple ionization[1]. In addition, continuous X-ray backgrounds, which determine the detection limit of PIXE, are created by the same ionization process as the characteristic X-ray signal and increase in the same ratio, thus there seems to be no significant advantage in using heavy ions compared to proton beams. However, the lower detection limit (LDL) of an element is given by $3\sqrt{N_B}/N_X$, where N_X is the net counts of a characteristic X-ray line and N_B is the background counts covered by the full width at half maximum (FWHM) of the characteristic X-ray line, namely it is proportional to $1/Z_P$ at the same projectile velocity, where Z_P is a projectile charge[2]. Consequently, using of heavy ion beams may improve LDL by Z_P times.

Carbon ion beams are applied to PIXE analysis of trace heavy elements in samples deposited on a thin organic film consisting mainly of C, H and O, because nuclear

bremsstrahlung vanishes in the case of symmetric collisions such as ^{12}C-^{12}C or ^{12}C-^{16}O[3]. In this study, we have measured continuous X-ray backgrounds in the energy region 5 keV<E_x<32 keV emitted from polypropylene film and X-ray production cross-sections of several elements (Cr, Fe, Ge, Ag, In, Pb) using 70 MeV $^{12}C^{6+}$ ions. The measured backgrounds are compared with theoretical calculations. We have estimated the LDL of heavy metal elements to investigate the applicability of 70 MeV carbon ions to PIXE analysis of heavy elements.

On the other hand, the elements will be toxic depending on the atomic valence as well as chemical environment. For example, most Cr in nature occurs with tri-valent and six-valent, and the latter is very toxic and carcinogenic. Therefore, it is suggested that the environmental pollution monitoring is not only for elemental concentrations but also for its chemical environment.

It is already well known that, X-ray spectra are sensitive to the chemical environment of the target atom and can yield information on the atomic and electronic structure of materials[4]. Baun[5] classifies the changes occurring in the X-ray emission spectra in four categories: changes in wavelength, presence or absence of band or lines, changes in bandshapes and changes in band intensity. Among them changes in band intensity or changes in K_β/K_α X-ray intensity ratio is relatively easily and most precisely measurable. The change of K X-ray intensity ratio has been studied extensively by many workers and well known experimentally and theoretically that the intensity ratio specially for 3d elements depends on the its oxidation state[6,7] and on the crystal symmetry in which the atom interest is located[8] as well as on the number of 3d electrons[9]. In almost all case, the X-ray intensity ratio was studied by using X-ray as an excitation source where the ionization of L and higher shell nearly not occur. But, in case of heavy ion projectiles, K-shell vacancy production is typically accompanied with the creation of multiple vacancies in the L and higher shells of the target atoms. In this study, we have measured Kb/Ka intensity ratio for Cr compounds using carbon ions at some different energies to study the possibility of discrimination of chemical environments.

EXPERIMENTAL

The targets for the measurement of X-ray production cross sections were prepared by vacuum evaporation on a thin polypropylene film. The thicknesses of the evaporated layer were determined by Rutherford backscattering (RBS) measurement to be less than 100 μ g/cm^2, thus self-absorption of characteristic X-rays and energy loss of the incident ion in

the targets can be neglected. The thickness was determined within the error ±5%. A polypropylene film ($(C_3H_6)_n$) of 4.25 μm thickness was used as a target for continuous X-ray background measurement for both 70 MeV carbon ion and 3 MeV proton bombardment. Targets for K_β/K_α intensity ratio measurement were prepared by dropping 40 μl of 1000 ppm Cr solution ($K_2Cr_2O_7$ and $CrCl_3$) on polypropylene film and drying at 60°C. In all measurement, the targets were placed at an angle of 45° with respect to the beam direction. X-rays emitted from the target were measured at an angle of 90° with respect to the beam direction, by a Si(Li) detector with an energy resolution of 160 eV at 5.9 keV and an effective area of 80 mm^2. 1 mm Mylar film was placed in front of the Si(Li) detector to absorb the intense yield of low energy X-rays. The solid angle was 0.0071 sr. The energy calibration was obtained with characteristic X-rays from a ^{241}Am source.

RESULTS AND DISCUSSION

Continuous X-ray backgrounds

The experimental cross sections of continuous X-ray background calculated from the measured PIXE spectra for both carbon ions and protons are presented in Fig.1, where detector efficiency and X-ray absorption in the Mylar absorber in front of the detector were not corrected. The calculations of cross-sections for each component of bremsstrahlung (QFEB-Quasi Free Electron Bremsstrahlung, SEB-Secondary Electron Bremsstrahlung, AB-Atomic Bremsstrahlung, NB-Nuclear Bremsstrahlung) were carried out as described elsewhere[10], and bremsstrahlung component and their sum are also shown in Fig.1. Cross-sections of radiative electron capture (REC) for carbon ion bombardment are not included in this calculation. The experimental cross-sections of continuous X-ray for carbon ions in the lower X-ray energy region (5-20 keV) are about 3 orders of magnitude higher than for proton bombardment. At higher X-ray energies (20-30 keV), the difference between the two cross sections is about 2 orders of magnitude. For proton bombardment, the calculated cross sections are in excellent agreement with experimental ones in a wide X-ray energy region, but they underestimate the experimental values in the region >10 keV in the case of carbon bombardment. The backgrounds at energies <13 keV can be estimated by SEB, whereas the backgrounds at energies >13 keV cannot be explained by SEB nor AB. In case of proton bombardment, the background at higher X-ray energies is well reproduced by NB. For carbon bombardment, the contribution of NB with carbon nuclei in the target (polypropylene film which consists C and H) is negligibly small because of symmetric

collisions, however the contribution from hydrogen ones in the target can be considered the same order as the NB contribution of carbon nuclei in the target during proton bombardment. Therefore, the backgrounds at the energies >20 keV are considered to be due to the Compton scattering tail of nuclear γ-rays, but the excess in the 13 to 20 keV region cannot be theoretically explained at present.

X-ray production cross section

The procedure of the evaluation of X-ray production cross sections was identical as described elsewhere[11]. Fig.2 shows the measured X-ray production cross sections σ_K (K-line) and σ_L (L-line) of 70 MeV carbon ions for several elements (K line-● and L line-■) and experimental data of another group[11] (K line-O L-line-□), which are in good agreement with our results. The total errors of experimental data are <±10 %. Since experimental cross-sections are up to one order of magnitude lower as ECPSSR calculations[11], calculated cross-sections will not be used in the LDL estimation.

K_β/K_α intensity ratio

K_β/K_α intensity ratios of several elements (Cr, Fe, Ge, Ag and In) were measured for carbon ions. From the results (Table 1), one sees that the difference between the measured intensity ratio for 70 MeV carbons and the theoretical value[12] diminishes with increasing atomic number Z of the target. This implies that for higher Z-targets, the degree of multiple ionization is lower compared to medium Z-targets, because the K_β/K_α intensity ratio increases with the number of L-shell vacancies[13]. Here, we can use theoretical K_β/K_α intensity ratio for higher Z-targets in LDL estimations.

Chemical effect on K_β/K_α intensity ratio

K_β/K_α intensity ratios for tri-valent and six-valent Cr compounds ($CrCl_3$ and $K_2Cr_2O_7$, respectively) were measured at 13, 22, 35, 70 MeV energies of carbon ions. The results and the intensity ratio for Cr metal[13] are shown in Fig. 4. Since the number of L-shell vacancies increases with decreasing projectile energy, the intensity ratio increases. But the clear difference between the intensity ratios for Cr compounds compared to for X-ray excitation is not observed in this study. From the BEA calculation[14] for 13 and 70 MeV carbon ions, the contribution of higher level of multiple ionization is small in both cases (Fig. 4) and contribution of 2 L-shell vacancies increased at 13 MeV carbon energy

compared to 70 MeV energy. Consequently, a few L-shell vacancies do not affect the K X-ray intensity ratio considerably.

Lower detection limit (LDL) estimation

PIXE spectra from the same target for both 70 MeV carbon ion (0.8 μC) and 3 MeV proton (8.1 μC) irradiation are shown in Fig. 4. The target was prepared by dropping 40 μl of the 1ppm solution of Cu, Pb, and Cd on the polypropylene film. From the spectra, it is clearly seen that peak-to-background ratio enhances at higher X-ray energy region. Since the deposited target is not uniform within the beam spot, we prefer to estimate the LDL from the continuous X-ray background spectra in Fig.1 using the equation[2)]

$$LDL[g/cm^2] = \frac{3\sqrt{N_B} \cdot A_Z}{N_Q \cdot \sigma_X \cdot eff \cdot ab \cdot b_\alpha \cdot d\Omega \cdot N_{Av}} \qquad (1)$$

where, N_B is background counts at the FWHM of the characteristic X-ray line, A_Z is atom mass of the target element, N_Q is the number of the incident particles, σ_Ξ is X-ray production cross section, *eff* is detector efficiency, *ab* is absorption of X-ray lines prior to detection, b_α is the fraction of K or L X-rays that appears in the K_α or L_α line, $d\Omega$ is solid angle of the detector and $N_{A\varpi}$ is Avogadro's number. The obtained LDL of Cu-K_α, Cd-K_α and Pb-L_α for 1μC irradiation were 2, 6 and 68 ng/cm^2 respectively. Compared to proton bombardment, the LDL of Cu-K_α (8.04 keV) for carbon bombardment is estimated to be 2 times lower for the same number of incident particles. Moreover, in the higher X-ray energy region, LDL for Cd-K_α (23.1 keV) is about 4 times lower than for proton bombardment.

CONCLUSIONS

Continuous X-ray backgrounds were measured for 70 MeV carbon ions and 3 MeV protons, and compared to theoretical calculations. The calculations for protons are in excellent agreement with experiments. But calculations for carbon ions underestimate the experiment by up to 2 orders of magnitude at X-ray energies from 13 keV to 20 keV. This difference cannot be explained by bremsstrahlung theory at present.

The X-ray production cross-sections of several elements were measured for 70 MeV carbon ions and confirmed to be much higher than for 3 MeV protons. For example, the X-ray production cross-section of Ag K X-rays was about 200 times larger than in the case of

3 MeV proton bombardment. Using the results of this study, the LDL of a few elements were estimated for 70 MeV carbon ions. The LDL for 70 MeV carbon ions at higher X-ray energies was 4 times lower than for 3 MeV protons. The results show that heavy elements such as Ag, Cd can be analyzed by 70 MeV carbon ion with higher sensitivity and on a much shorter time compared to 3 MeV protons. In addition, higher sensitivity will be obtained when thinner (<4 μm) organic film is used as a backing.

K_β/K_α intensity ratios for Cr compounds are measured by using carbon ions at different energies. The intensity ratio increases with increasing with the degree of multiple ionization. But the difference of intensity ratios between the Cr compounds do not vary significantly at these energies, because the degree of multiple ionization at 13 and 70 MeV energies differs not too much.

ACKNOWLEDGEMENTS

The authors thank the working group of the Cyclotron Radioisotope Center, Tohoku University for the operation and maintenance of the accelerator and Prof. W. Galster for helpful discussions.

REFERENCES

1) Johansson S.A.E. and Campbell, J.L., PIXE A Novel Technique for Elemental Analysis, John Wiley & Sons Ltd., 1988, pp 32-33
2) Ishii K., Orihara H., Iwata Y., Bessho K., Int. J. PIXE **4** (1994) 1.
3) Alder K., Bohr A., Huus T., Mottelson B. and Winther A., Rev. Mod. Phys. **28** (1956) 432.
4) Ishii K. and Morita S., Int. J. PIXE **1** (1990) 1.
5) Meisel A. et al., X-Ray Spectra and Chemical Binding, Springer-Verlag: Berlin Heidelberg, 1989, 458p
6) Baun W.L., Electron Probe Microanalyses, Academic Press: New York, 1969, 155p
7) Küçükönder A. et al., J. Radioanal. Nucl. Chem. **170** (1993) 125.
8) Küçükönder A. et al., J. Phys. B: At. Mol. Opt. Phys. **26** (1993) 101.
9) Mukoyama T. et al., Phys. Rev. B **34** (1986) 3710.
10) Mukoyama T., Taniguchi K., Adachi H., X-ray Spectrom. **29** (2000) 426.
11) Schmelmer O., Dollinger G., Datzmann G., Hauptner A., Körner A.J., Maier-Komor P., Reichart P., Nucl. Instrum. Methods **B 179** (2001) 469.
12) Scofield J.H., Phys. Rev. **A9** (1974) 1041.
13) Li T. and Watson R.L., Phys. Rev. **A9** (1974) 1574.
14) Hansen J.S., Phys. Rev. **A8** (1973) 822.

Table 1. K_β/K_α intensity ratios for 70 MeV carbon and theoretical value[12].

Element (Atomic number)	70 MeV carbon ions	Theoretical value
Cr (24)	0.1637±0.0015	0.1336
Fe (26)	0.1608±0.0010	0.1391
Ge (32)	0.1764±0.0010	0.1504
Ag (47)	0.2061±0.0012	0.2130
In (49)	0.2154±0.0032	0.2195

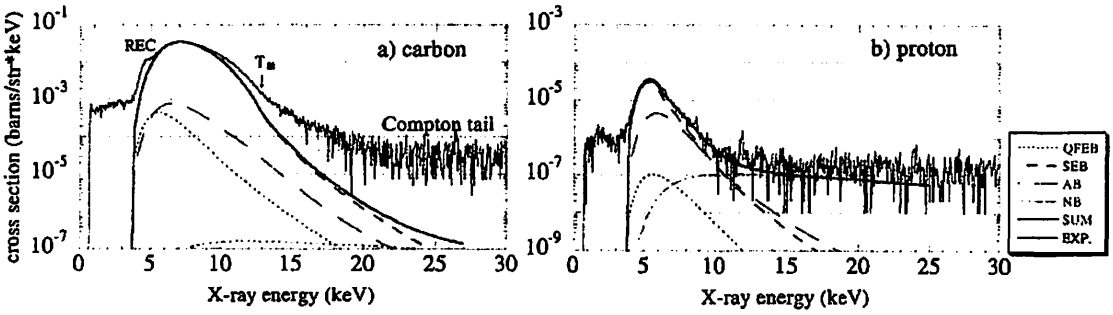

Figure 1. Continuous X-ray background from polypropylene film for 70 MeV carbon ions (a) and for 3 MeV protons (b).

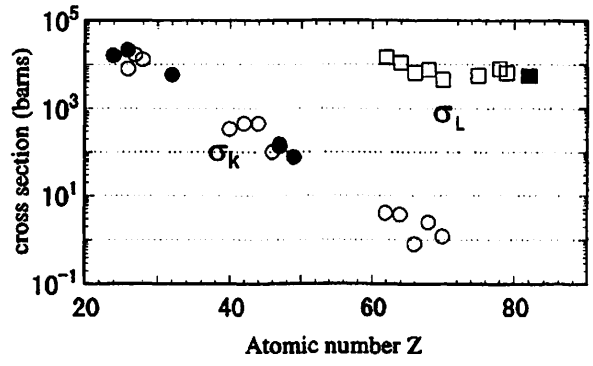

Figure 2. X-ray production cross-sections for 70 MeV carbon ions. (●-σ_K, ■-σ_L) - this study, (○-σ_K, □-σ_L) – the results of another group[11].

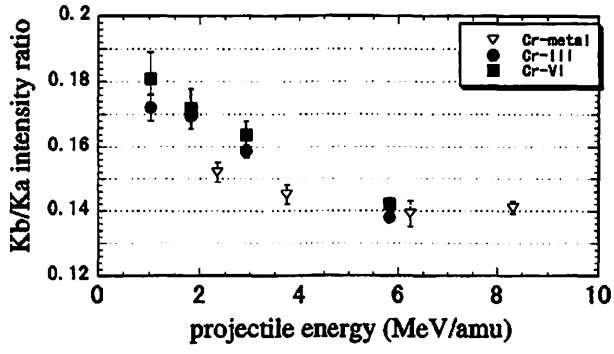

Figure 3. K_β/K_α intensity ratio for Cr compounds: CrIII-$CrCl_3$, CrVI- $K_2Cr_2O_7$.

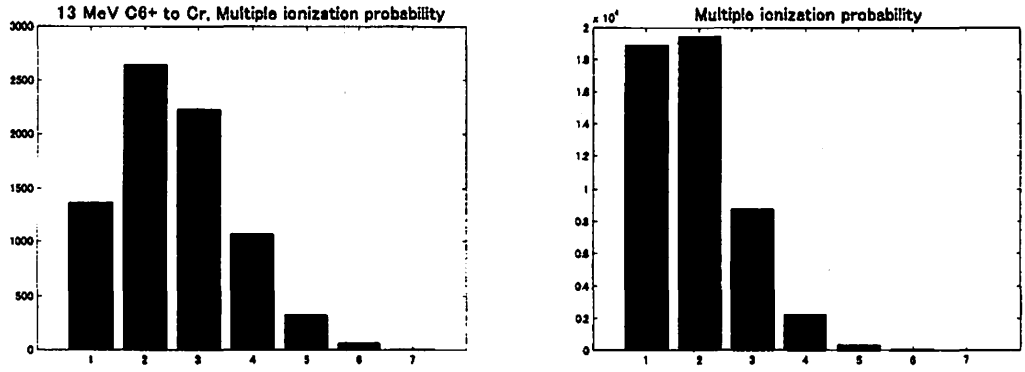

Figure 4. BEA calculation of multiple ionization probability for 13 and 70 MeV carbon energies on Cr target. (abscissa: 1-one K-shell vacancy and no L-shell vacancy KL^0, 2-KL^1, 3-KL^2 ...).

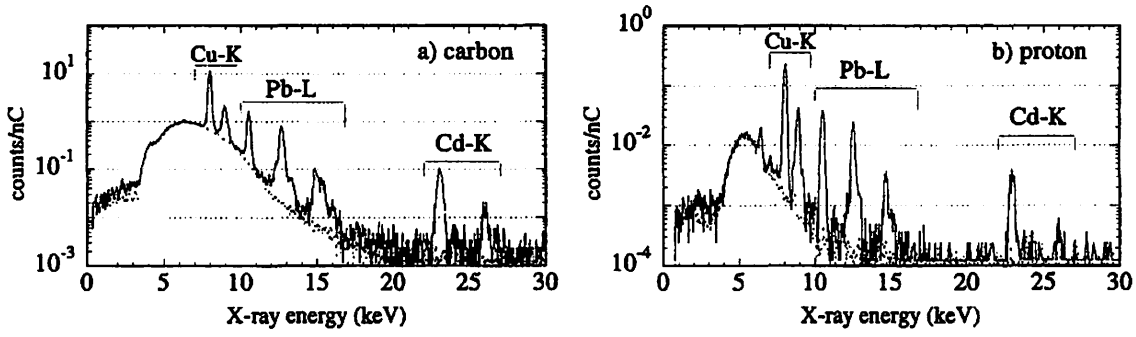

Figure 5. PIXE spectra from the target which contains Cu, Pb and Cd in the same amount (~40 ng). 0.8 μC and 8.1 μC irradiation for carbon ions (a) and protons (b), respectively. (straigth line- from the target, dashed line- from the backing film)

V. 2. Development of Monitoring System of Aqueous Environment by PIXE V: Elemental Analysis of Water Leakage from a Landfill Site of Industrial Waste Generating Hydrogen Sulfide

Yamazaki H., Ishii K., Matsuyama S., Takahashi Y., Amartaivan Ts., Suzuki A., Yamaguchi T., Momose G., and Abe S.

Department of Quantum Science and Energy Engineering, Graduate School of Engineering, Tohoku University

INTRODUCTION

The underground disposal of industrial waste is only done in remote regions away from a city, where population density is low, but industrial waste is different from household garbage because it may include various toxic elements. Designated disposal sites have been strictly limited recently, and possible health problems originating from the diffusion of harmful elements often heat up to the debate between residents in the site surroundings and the local administration. Water pollution caused by drain from a landfill site of industrial waste not only poses a problem for the neighborhood's health but is also a source of environmental pollution including the generation of foul smell. Complaints are frequent from residents about high hydrogen sulfide levels from the landfill site of industrial waste, *Takenouchi*, which lies to the southwest 25 km of Sendai City. The concentration of hydrogen sulfide is legally limited to low permissible levels in the gas and liquid effluents from disposal sites in Japan, since a high concentration of hydrogen sulfide, > 50 ppm, may cause problems to person's respiratory system and brain apart from the occurrence of foul smell. For example, the concentration of hydrogen sulfide is restricted to below 0.3 ppm in a site's water leakage depending on the rate of effluent. However, the residents also worry about water pollution because the disposal site is located close to the river, from which they are drawing agricultural water for cultivating rice fields.

Ultramicro amounts of sulfide in aqueous samples can be detected spectrophotometrically as methylene-blue, where sulfide is allowed to react with *p*-phenylenediamine and ferric ion to form the dye[1,2]. However, this method is sensitive to the presence of traces of heavy metals and to air-oxidation, and hence cannot be applied to analysis of water

leakage from waste disposal without pretreatment by complex chemical separation. Particle Induced X-ray Emission (PIXE) has been proven to be a very useful technique for the study of trace element distribution in ecosystems due to its multielement analysis capability and high sensitivity[3]. Additional advantage is the high speed of analysis of a wide variety of samples. However, it should be stressed that adequate sample preparation is required in order to make full use of PIXE capabilities.

In this study, we examine the method of converting sulfide ions dissolved in aqueous samples into copper sulfide of low solubility for enhancing target preparation of PIXE analysis. This method is then applied to the sample preparation of water leakage from a landfill site, where the question of water pollution by dissolved sulfides has been raised. The applicability of PIXE is discussed to the monitoring of water pollution by hydrogen sulfide and heavy metals discharged from landfill sites of industrial waste.

EXPERIMENTAL

Sample preparation of dissolved sulfide

Very low concentrations of < 0.3 ppm sulfide ions dissolved in aqueous samples should be analyzed to assess the permissible concentration in drainage discharged from the disposal site to the environment. Hence an enhanced sample preparation method for PIXE analysis was adopted where dissolved sulfide ions are converted to an insoluble compound and then collected on a thin organic filter suitable as a sample backing material. It is reported that a compound of sulfide with heavy metals such as Ni^{2+}, Zn^{2+}, Sn^{2+}, Cd^{2+}, Pb^{2+}, Cu^{2+}, Ag^{+} and Hg^{2+} has very low solubility[4,5]. As for the precipitation reaction of sulfide with silver or mercury, a side reaction leading to the formation of silver chloride or hydrolysis of mercury is feared[6], since a relatively high concentration of chloride ions and a little bit alkaline condition are often observed in water leakage from a waste disposal site. On the other hand, the solubility product is much lower for CuS (K_{sp}=6 x 10^{-36}) than for ZnS (K_{sp}=3 x 10^{-24}) and compounds with other divalent metals. Hence, Cu^{2+} ion was selected as a scavenger of sulfide ions dissolved in water leakage from a disposal site.

The standard method for collecting CuS precipitates on Nuclepore filter is tested on an investigation of the pH-dependence of the recovery of dissolved sulfides and the obtained calibration curve covers the concentration range from 10 to 1000 ppb for sulfide ions. The sample preparation procedure is as follows. A chosen amount of Cu^{2+} is added to a 25-ml solution containing a given amount of sulfide ions, and its pH is adjusted to an

appropriate value. After stirring 2 min, the solution is filtered under suction (~250 mmHg) through a Nuclepore filter of 0.4 μm pores. Test solutions containing $Cu(NO_3)_2$ and K_2S in appropriate concentrations were used after serial dilution of the standard solution of the certified concentration (1.00 mg/ml). The standard solution of K_2S had been made immediately before use in order to avoid the air oxidation.

Sample preparation of water leakage from an industrial waste disposal site

We collected 250 ml of three kinds of samples of water-leakage from a side ditch in the "*Takenouchi*" landfill site of industrial waste; water in a side ditch pit away from the disposal place (S1) and drain leaching from the protective barrier banking the disposal site (S2 and S3). For comparison, we also bottled samples of water flowing out from the rice cropland located upstream (R1) and downstream (R2) of the disposal site along with water supplied to the rice cropland downstream of the disposal site (R3). The values of pH in the water samples collected at the side ditch were a little bit higher (7.47-7.94) compared to the reference water of agricultural use (7.24-7.42).

After pH measurement, 30 ml of each sample were filtered under suction (~250 mmHg) with a Nuclepore filter of 0.4μm pores; the residue on the filter accounted for the insoluble fraction, and the filtrate contained the soluble components. The filter, on which insoluble components were collected, was mounted on a Mylar target frame and kept in a desiccator for PIXE measurement. In order to determine the concentration of the soluble component of sulfide in each sample, a filtration target was separately prepared after copper was added to the solution with a concentration of 3 ppm and the pH of the sample was adjusted to 7.50 ± 0.01. This procedure converts the soluble component of sulfide in a sample solution into insoluble copper sulfide that can be scavenged on filter. Hence, the increase in sulfur content in the filtration target with addition of 3-ppm Cu^{2+} indicates the concentration of soluble sulfides in a sample. The targets for the soluble components including oxidized species of sulfur were also prepared by depositing 30 μl of sample solution on an user-made polycarbonate film of around 0.3 mg/cm^2 thickness; the sample solution was prepared by adding 10 μl of 1000 ppm Ga in 1M HNO_3 to 4 ml of filtrate beforehand[7,8]. After drying at 60 °C, the procedure was repeated four times to give a total of 150 μl dried onto the film. The filtration targets with and without adding 3-ppm Cu^{2+} and the deposit target were separately prepared three times for each same sample.

PIXE analysis

The targets prepared from test solutions and drainage samples were irradiated for 5 to 10 minutes in a vacuum chamber by 3 MeV protons (5-7 nA beam currents, 2 mm beam diameter) from the single-ended type 4.5 MV Dynamitron accelerator at Tohoku University, Japan. X-rays from targets were measured with two Si(Li) detectors; No.1 detector (0.012 mm thick Be window) with a low geometric efficiency is well suited for the detection of elements of low atomic number $Z \leq 20$, and No.2 detector (0.025 mm thick Be window) with a 500-μm Mylar absorber and high geometric efficiency allows the detection of X-rays > 4 keV[9]. Targets containing Fe^{3+} and Cu^{2+} of a known amount, which corresponded to 25ml of solution in concentrations from 10 to 100 ppb, were prepared by a DBDTC-DBS pre-concentration technique[7], and used as an external standard for normalization of PIXE spectra for the filtration targets. For PIXE-spectrum analysis, we used a least-squares fitting computer program, which has been developed in our laboratory based on the pattern analysis method[10,11]. The lower detection limit was obtained based on the statistics 3σ error of the background counts integrated over the width of detector resolution (FWHM) at the position of the X-ray energy characteristic of the element of interest in the PIXE spectrum for a sample.

RESULTS AND DISCUSSION

The highest concentration of sulfide ions in test solutions for producing PIXE targets was set to 1ppm as the permissible concentration of hydrogen sulfide in drains is legally limited to be 0.3ppm or less. Figure 1 shows the PIXE spectra for precipitates collected on Nuclepore filter of 0.4 μm pores. The precipitates formed at pH 8.01 from a solution containing sulfide ions in 100 ppb and divalent copper ions in 2.5 ppm. It is understood that the precipitation of an almost pure copper sulfide is collected, though iron impurity may be detected at the trace level. Figure 2 shows the pH dependence of the recovery factor of filtration scavenging of copper sulfide, examined in a 25 ml solution containing divalent copper ions of 2.5 ppm (39 μM) and sulfide ions of 1 ppm (31μM). The pH of samples was adjusted by using nitric acid and ammonia. Both sulfide and copper ions are collected appreciably once the pH of the solution exceeds 7, and the recovery factor of both ions increases almost correspondingly up to pH=8. Since the solutions initially contained copper and sulfide ions in similar concentrations, an equimolar compound of copper and sulfide like CuS precipitates in the region of pH from 7 to 8.

However, when the pH exceeds eight, the collection of the equimolar precipitation is not approved. That is, the recovery factor of sulfide ions decreases beyond the maximum value of around 0.5 at pH 8. On the other hand, the recovery of copper ions increased further up to about pH=8.5 and then decreases in the more alkaline region. It is considered that the strong pH-dependence of the recovery factor of CuS-precipitate is ascribed to the influences of the hydrolysis reaction of divalent copper ions and of the stability of the hydrogen sulfide as a very weak acid. That is, sulfide ions are stable as a weak acid such as H_2S in a solution of pH < 7, and in an alkaline condition over pH 8 the hydrolysis reaction of divalent copper ions occurs in preference to the generation of copper sulfide[6]. It is well known that the hydrolysis reaction of metals is irreversible and the generated hydroxide colloids have various physicochemical properties. Therefore, it is necessary to avoid the coexistence with the hydrolysis reaction of copper as much as possible to ensure the steady collection of copper sulfide. From this viewpoint, the pH at precipitation was selected to be 7.5, and six experiments were carried out at pH=7.5 as seen in Fig. 2. The average of recovery factors was 0.27 ± 0.03 when the pH values were adjusted to 7.50 within the accuracy of the measuring instrument (± 0.01). It is understood that the fixed fraction of dissolved sulfide ions is converted to a target for the PIXE analysis when divalent copper ions are added to the solution in 2.5 ppm concentration and the pH is adjusted strictly to be 7.50 ± 0.01. However, judging from the standard deviation of the recovery factor, we expect the uncertainty of ±11 % in the analyzed quantity.

The concentration of copper ions as the scavenger for 1 ppm sulfide was changed from 1 to 12 ppm and the recovery factors of both sulfide and copper ions were examined at pH 7.50 ± 0.01. The recovery factors ranging from 0.25 to 0.31 for both ions were obtained in six test-samples by adding Cu^{2+} ions in either almost equal amount to the sulfide ions (2 ppm Cu^{2+}) or with a little bit excess amount (3 ppm Cu^{2+}). The recovery factor was quite small and did not satisfy the relation of equimolar precipitation like CuS when copper ions were added in underdose (< 2ppm). When copper ions were added at 6 ppm or more, an excessive amount of copper ions was collected on the target due to the hydrolysis reaction. The pileup of Cu K_α X ray signals occurred in PIXE sample spectra with the excessive recovery of copper, leaving an adverse effect on the spectrum region from 8 to 16 keV at 5 nA beam current. Therefore, it is appropriate to restrict the concentration of copper ions to be 3 ppm as the scavenger for sulfide ions of 1ppm or less in order to enable a prompt PIXE analysis that uses beam currents of a few nA. As for

other compounds which might interfere with the scavenging of sulfide ions by divalent copper ions, we tested the recovery factor of sulfide ions at pH 7.50 in solutions containing sulfide and phosphate ions, as $Cu_3(PO_4)_2$ is a poor solubility compound as well as CuS. At the coexistence level of phosphate ions three times exceeding the concentration of sulfide ions, a decrease in the recovery factor of sulfide ions of 17% was observed, but the coexistence of phosphate ions less equal twice the sulfide concentration did not influence the recovery of CuS.

In order to evaluate the reliability of the quantitative PIXE analysis for dissolved sulfide ions, a calibration curve was measured using targets, which were prepared by adding 3 ppm Cu^{2+} to a 25 ml of K_2S solution in concentrations of sulfide ranging from 10 to 1000 ppb, as shown in Fig.3. The quantification limit in the present PIXE measurement setup is around 10 ppb, where the yields of characteristics X-ray peaks are close to the statistics 3σ error of the background counts. In a wide dynamic range from the lower detection limit to a high concentration of 1000 ppb, a linear relationship is observed between the initial concentrations of sulfide ions in the solutions and the concentrations converted from the PIXE analysis values of sulfide ions scavenged on the filter. It is concluded that a constant fraction of copper sulfides generated in the solutions was collected on the filter regardless of the molar ratio of sulfide to copper ions in solutions. In fact, the recovery factors were concentrated in the range of 0.25 to 0.30. Therefore, concentrations of dissolved sulfides can be determined based on the PIXE results of copper sulfides scavenged on the filtration targets using the recovery factor 0.27 ± 0.03 at pH 7.50.

Figure 4 shows the PIXE spectra for both insoluble and soluble fractions of drain leaching from the protective barrier of the banking disposal site (S2). It was clarified by the PIXE analysis that 16 elements existed as either insoluble or soluble components at a different soluble/insoluble ratios. Sulfur existed dominantly in the soluble fraction, whereas heavy metals such as Mn, Fe, Cu, and Zn, which form compounds of low solubility with sulfide ions, were detected in much lower concentrations.

In Fig.5, the elemental concentrations in both insoluble and soluble fractions of water leakage samples from the disposal site are compared with those in the reference samples of water used for agriculture around the landfill site. As for the insoluble components, elements of soil origin such as Al, Si and Fe were predominantly detected in the reference water and the concentrations are near the values generally detected in samples of river water[8,9,12]. On the other hand, Ca, Mn and Fe were the main constituents in the

insoluble fraction of the water leakage, and P, S and heavy metals such as Cr, Cu, and Zn occurred at comparatively high concentrations, whereas the same elements in the reference water samples were detected at trace level close to the detection limits. The insoluble component of sulfur was not detected in the reference water samples; the detection limit in agricultural water is around 10 ppb. On the other hand, the samples of the leakage water contained around 150 ppb of insoluble sulfur component together with Mn and Fe to form the sulfide of the poor solubility from several times to a few tens of times higher concentration. A big difference in elemental concentrations in the soluble fraction was observed among pit water (S1), the water leakage samples from the protective wall of disposal place (S2, S3), and the reference water used for agriculture around the disposal place (R1-3). In S2 and S3 samples, many different elements like Mg, K, Ca, Sr, S, Cl, Br, Mn, Fe, and Ni were detected at several times to tens of times higher concentrations than in the samples of water for agricultural use. That is, it is found that many different elements included in industrial waste stored underground dissolved into rain water and flowed out from the protective wall of the disposal. In the agricultural water, many elements except Ca, Mn and Fe, which existed in high concentrations, were detected at concentration levels reported for river water in Japan[12]. The concentration of the dissolved sulfur component was 30 to 40 ppm for water leakage samples, which is considerably higher than 11-15 ppm observed in agricultural water. Judging from 2 ppm or less concentrations of heavy metals such as Mn and Fe, which form compounds of poor solubility with sulfide, it is suggested that the dissolution ratio of sulfur into metal sulfide is low.

Table 1 shows concentrations of sulfide ions dissolved in the sample solutions. These concentrations were determined based on the difference in PIXE analyses of sulfur between the filtration-targets prepared separately from a 30 ml sample with or without the addition of 3 ppm copper ions. Here, the average value of analytical values of three each targets are shown. In the samples of agricultural water (R1, R2), the amount of sulfur corresponding to 30-40 ppb in the solution was collected as CuS precipitation by adding copper ions. The concentration of dissolved sulfide ions in the reference solution is120-130 ppb based on the recovery of CuS. In samples of water leakage from the disposal site, the amount of sulfur collected on the filter appreciably increased. The concentration of dissolved sulfide in the water leakage, which was calculated at the increment of sulfur content, is evaluated to be 3 to 4 times higher than concentrations in agricultural water samples. From the comparison of total concentrations of sulfur in the solutions as shown in the third column of Table 1, the analytical results of all samples

suggest that about 1% of sulfur detected in the solutions is most likely sulfide of the lowest oxidation number, which is most dangerous to health. This means that higher oxidized species of sulfur are predominant in all kinds of sample solutions. Since Fe and Mn were detected in both the insoluble fraction and the soluble one of both the reference solution and the water leakage from the disposal site, the oxidation potential of these elements stabilized the oxidized species of sulfur like SO_4^{2-}: The oxidant of these elements such as Fe^{3+} and Mn^{4+} is highly hydrolysable in a neutral or slightly alkaline solution and is more easily detected in the insoluble fraction compared to the reductants such as Fe^{2+} and Mn^{2+}. The oxidation-reduction potential between HS^- reductant and SO_4^{2-} oxidant is –0.22 V in a solution at pH 7.5. The potentials of redox reactions at pH 7.5 are –0.26 V for Fe^{3+}/Fe^{2+} and 0.41 V for Mn^{4+}/Mn^{2+}, respectively. It is thought that the redox potential of manganese largely contributes to the stabilization of the oxidant of sulfur. Therefore, PIXE analysis reveals that water leakage from the disposal site contains hydrogen sulfide in slightly higher concentrations than the legally permissible level, though sulfur is dissolved in much higher concentrations compared to water for agricultural use. At the present, the water pollution problem due to hydrogen sulfide is acceptable to the risk of health injury of residents in the surroundings and concerning foul smell. However, the situation needs to be monitored carefully concerning the impact of disposal site leakage on agriculture.

CONCLUSION

We developed a method for preparing targets of dissolved sulfide ions for PIXE analysis. Sulfide ions dissolved in an aqueous sample were converted to the insoluble compound CuS and a constant fraction of CuS was collected on a thin organic filter suitable as backing for PIXE measurement, in spite of the strong pH-dependence of the recovery factors. This method was applied to the sample preparation of water leakage from a landfill site of industrial waste. The increase of sulfur content in targets scavenged on Nuclepore filter with the addition of divalent copper ions clearly revealed a very low dissolution ratio of sulfide in samples of both water leakage from the disposal site and in agricultural water. Leakage from the disposal site at *Takenouchi* does not pose a health risk at present but its impact on the surrounding agriculture needs to be investigated further. The PIXE method is advantage as for multielement detection and has high sensitivity, making it very effective to analyze and discuss the low fraction of dissolved sulfides in terms of the oxidation condition of soluble and insoluble components detected in samples.

REFERENCES

1) Gustafsson L., *Talanta* 4 (1960) 227.
2) Golterman H.L. and Clymo R.S., "Methods for Chemical Analysis of Fresh Waters", Blackwell Scientific Publications, Oxford, pp.53-57 (1969).
3) Ghermandi G., Cecchi R. and Laj P., Nucl. Instrum. Methods **B109/110** (1996) 63.
4) Japan Industrial Standard, K 0101, p.169 (1991).
5) Japan Industrial Standard, K 0102, p.136 (1993).
6) Base C.F. and Mesmer R.E., "The Hydrolysis of Cations", John Wiley & Sons, New York (1976), 268-273; 274-278; 287-294; 301-312.
7) Yamazaki H. et al., Int. J. PIXE 7 (1997) 31.
8) Yamazaki H., Tsutsumi K., Ishii K. et al., Int. J. PIXE **9** (1999) 83.
9) Yamazaki H., Ishii K., Amartaivan Ts. et al., Int. J. PIXE, **11** (2001) 79.
10) Murozono K., Ishii K., Yamazaki H. et al., Nucl. Instrum. Methods **B150** (1999) 76.
11) Ishii K. and Morita S., Nucl. In strum. Methods **B3** (1984) 57.
12) "Water Analysis", The Japan Society for Analytical Chemistry, Hokkaido Branch (1994), 6-24.

Table 1. Analysis of soluble sulfide fraction in reference water and in leakage from the industrial disposal site at *Takenouchi*.

Sample	Insoluble (I) Sulfur Concn. ppm	Soluble Sulfur Concn. ppm	Insoluble (II) Sulfur Concn. ppm	Soluble Sulfide Concn. ppm	Fraction of soluble sulfides
R1	ND	13.15±0.24	0.04 ± 0.01	0.13± 0.03	0.010
R3	ND	10.97±0.24	0.03 ± 0.02	0.12± 0.04	0.011
S2	0.14±0.01	29.18±0.54	0.24 ± 0.02	0.35± 0.10	0.012
S3	0.15±0.02	40.84±0.60	0.30 ± 0.01	0.54± 0.08	0.013

The samples are described in Experimental. Insoluble (I) sulfur concentration: Analyzed value for the filtration-target without 3-ppm Cu^{2+}addition. Insoluble (II) sulfur concentration: Analyzed value for the filtration-target with 3-ppm Cu^{2+} addition. Soluble sulfide concentrations were determined based on the CuS recovery factor (0.27±0.03) at pH 7.50.

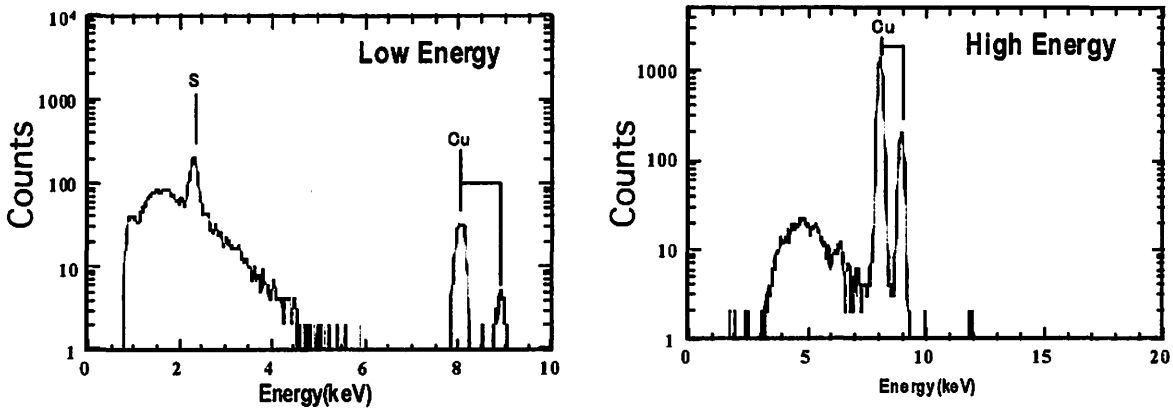

Fig. 1. PIXE spectra for precipitates formed at pH 8.01 in a solution containing 100 ppbof sulfide ions and 2.5 ppm of divalent copper ions. Irradiation: 3 μC of 3MeV protons.

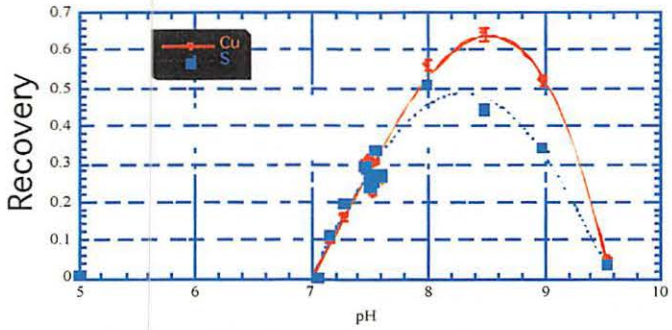

Fig. 2. The pH-dependence of filtration scavenging for sulfide and divalent copper ions. A 25 ml solution contained sulfide ions in 1 ppm and copper ions in 2.5 ppm. The precipitates were filtered under suction (~ 250 mmHg) with a Nuclepore filter of 0.4μm pores.

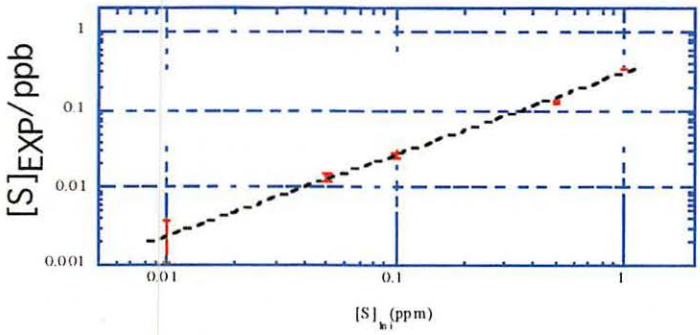

Fig. 3. Experimental results ($[S]_{Exp}$/ppb) versus nominal concentrations ($[S]_{Ini}$/ppb) for calibration measurements of dissolved sulfides. 3 ppm of Cu^{2+} scavenger, filtration at pH 7.50 ± 0.02, 1.5-3 μC irradiation.

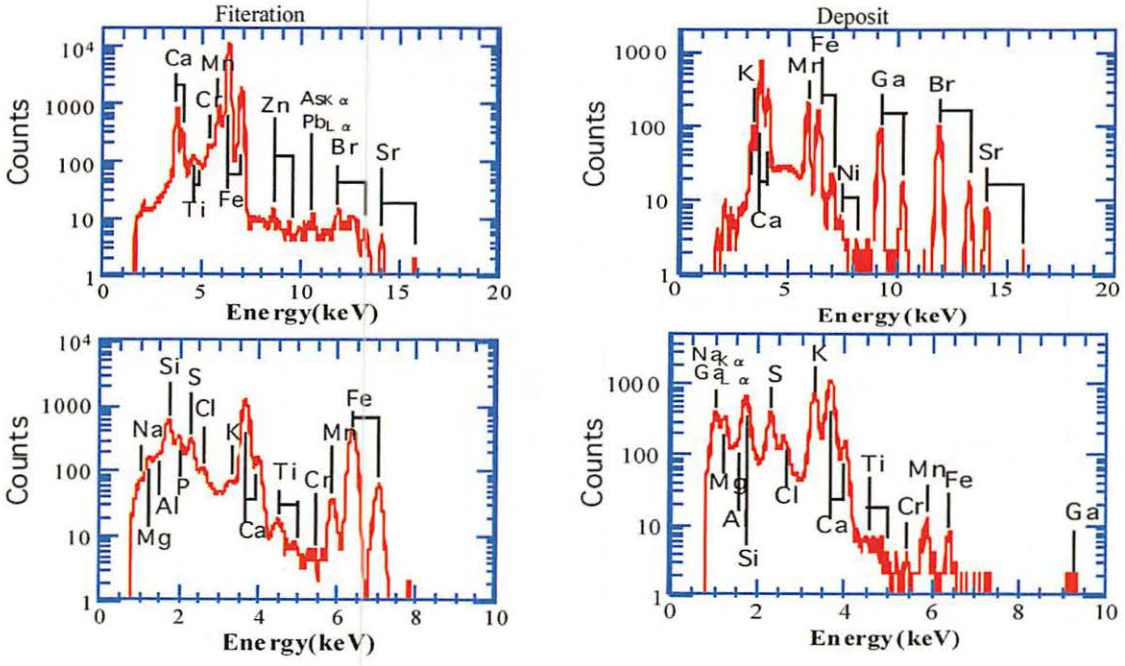

Fig. 4. PIXE spectra of insoluble and soluble fractions of water leakage from the landfill site of industrial waste(S2). Irradiation: 1.5 μC of 3 MeV protons. The lower spectra were obtained by No.1 detector (low energy X-rays), and the upper spectra were obtained by No.2 detector (high energy X-rays).

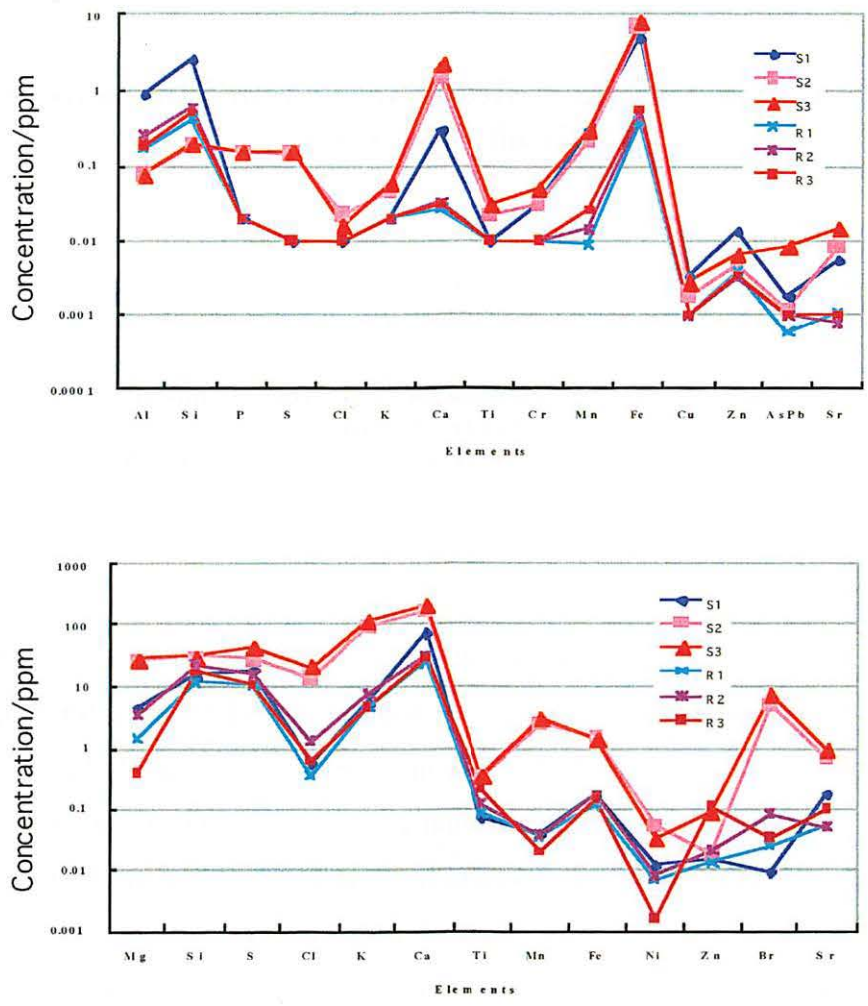

Fig. 5. Elemental distribution in the insoluble and the soluble fractions of water leakage samples and of reference water samples. The samples are described in Experimental.

V. 3. Mapping of Heavy Metals Accumulated Implants Using a Submili-PIXE Camera

Watanabe R., Hara J.[*], *Inoue C.*[*], *Chida T.*[*], *Amartaivan Ts.*[**], *Matsuyama S.*[**], *Yamazaki H.*[**], *and Ishii K.*[**]

Department of Geoscience and Technology, Tohoku University
Graduate School of Environmental Studies, Tohoku University[*]
Department of Quantum Science and Energy Engineering, Tohoku University[**]

Introduction

Heavy metal contamination in the subsurface environment is a major problem for human health and environmental quality. A number of technologies for remediation of soils contaminated by heavy metals have been developed. Most of these technologies, however, are expensive, and they occasionally produce secondary waste[1]. Recently, environmentally friendly, low-input approaches such as phytoremediation have been proposed to cleanup soils contaminated with heavy metals and metalloids[2]. Phytoremediation is a technology for cleaning environments using the metabolism of plants, and interaction between plants and microorganisms in the rhizosphere. To develop practical applications of this technology, it is necessary to explicate effective accumulation mechanisms for heavy metals. In general, contaminated soil and plant samples are chemically analyzed using atomic absorption spectrometry (AAS) and inductively coupled plasma-mass spectrometry (ICP-MS), after oxidizing pre-treatment. However, these methods are laborious and provide only average metal concentrations in each plant organ. For this reason, Particle-induced X-ray Emission (PIXE) analysis is an attractive analytical tool. PIXE analysis has high sensitivity and multi-elemental capability[3,4], does not require sample pretreatment, and can be performed quickly and simply.

The purpose of this work is to investigate the localization and speciation of heavy metals in plants using a submilli-PIXE camera and to establish fundamental information about the mechanism of heavy metal accumulation in plants.

Materials and methods

Plant and soil samples were obtained on 23 April 2003, from a shooting range in Japan. Whole bodies of *Polygonum cuspidatum* were sampled. The ground part of this plant was about 10cm tall. The following pretreatment was conducted for the plant and soil samples: firstly, the plant samples were rinsed with tap water, then deionized water, prior to PIXE analysis. In contrast, the subterranean stems were oven-dried at 105 ℃ and decomposed with concentrated HNO_3 to measure their heavy metal content.

The soil sample was air-dried and sieved using a 2 mm mesh sieve. For PIXE analysis, the soil sample was oven-dried at 105, ground and stuck on to a tape. In addition, the sample was chemically analyzed. The total contents of heavy metals were determined by dissolution with a mixture of concentrated H_2SO_4, HNO_3 and $HClO_4$ (1:5:20). Different chemical and physical forms were analyzed by a sequential extraction procedure (following the Community Bureau of Reference (BCR)[5], which is the Standard Measurement and Testing Program of the European Community (STM) [6], which identified the following forms: Fraction 1: water soluble, exchangeable and carbonate bound; Fraction 2: Fe-Mn oxide bound; Fraction 3: organic matter and sulfide bound.

Heavy metals in the plant and soil extracts were analyzed by ICP-MS. The soil components and distribution of elements in the leaf and subterranean stem were analyzed by submill- PIXE camera of Tohoku University[7].

This PIXE analysis system provides spatial distribution images of elements in a region several cm^2 with a resolution of < 0.5 mm. 3 MeV proton beam (10 nA beam current, <0.5 mm beam diameter) from a 4.5-MV single-ended Dynamitron accelerator was extracted to open air through a thin polyimid (Kapton) film of 12.5 μm. In usual manner, beam was scanned mm^2 on a surface of samples. Plant samples were fixed to the target frame and set up just after the beam exit window. The distance from the beam exit window and a sample is around 5mm. Fig. 1 shows experimental set-up. The X-ray energy and the beam position were simultaneously measured in order to obtain spatial distribution of elements. The X- rays from a target passed through the exit window and a 110-μm Mylar absorber and were measured with a Si (Li) detector (10-mm diam. x4-mm thick crystal with 25-μm Be window) which viewed a target at a distance of 45 mm with an angle of 135 degree with respect to the beam axis. The absorber in front of the detector removed recoil protons and low-energy X-ray components. This resulted in a decrease of the dead time of the signal processing and pile-up. The list mode data acquisition system can sort the data for a

selected element/ energy region and generate an elemental image even while the data are accumulated.

Results and Discussion

Table 1 shows the different forms of Cu and Pb metals in the soil samples. The total concentrations of Cu and Pb were 7000 and 5000 mg/kg, respectively, which are two-orders of magnitude greater than in common soils (Cu 30mg/kg, Pb 35mg/kg)[8]. The metals have mobility in the soil, since the proportion of water-soluble fraction is large (Fraction 1, Table 1). Plants readily absorb these metals, although the spread of contamination is a problem. In common soils, K, Ca, Ti, Mn and Fe occur in relatively high concentrations, but Cu, Pb and Zn occur at lower levels. The characteristic X-ray spectrum of each element in the soil samples is shown in Fig. 2. K, Ca, Ti, Mn, Fe, Cu, Zn and Pb are detected in the soil by PIXE analysis (Fig. 2), which proves the effectiveness of PIXE analysis for rapid determination of heavy metal contamination in soils.

Fig. 3 shows the characteristic X-ray spectrum of each element in the leaf sample of *P. cuspidatum*. Some toxic heavy metals, i.e. Cu, Pb and Zn were detected. Also, essential plant elements K, Ca and Fe, were detected. The elemental distribution images of K, Ca, Cu and Pb are shown in Fig. 4. Potassium is uniformly distributed, whereas Cu and Pb occur mainly in the vein. Calcium mostly occurs in the vein, but also at a low level in the lamina.

The average concentrations of Cu, Pb in the subterranean stem are 200 and 400mg/kg, respectively, which are very low compared with typical values in soil. The characteristic X-ray spectrum for subterranean stems is shown in Fig. 5 and elemental distribution images are shown in Fig. 6, with similar patterns for Cu and Pb that accumulated in the epidermis of subterranean stems. However, the distribution patterns are not strongly developed inside the plant. These results lead to the speculation that *P. cuspidatum* acquires tolerance for heavy metals by accumulating them on the epidermis. In Figs. 4 and 6, K and Ca are distributed over the entire plant. In contrast, Cu and Pb are translocated from the subterranean stem to leaves, but into the vein rather than tissue, as they are unnecessary and possibly toxic. The fixing of Cu and Pb into the vein is a feature revealed by PIXE mapping.

Plants grown in contaminated soil are harvested and disposed when phytoremediation is adapted, so it is desirable to accumulate most of the heavy metal component in the ground part of plants. Cu and Pb mostly accumulated in roots and are not translocated to the ground part[9,10]. Therefore, phytoremediation is regarded as being a difficult technique to put into

practical use for remediation of Cu and Pb. However, *P. cuspidatum* analyzed in this study has a tolerance to heavy metals and tends to accumulate Cu and Pb in the ground part, so it can be potentially utilized to cleanup soil that is contaminated by heavy metals.

Conclusion

In this study, PIXE was used to analyze *P. cuspidatum* that inhabited soil contaminated by heavy metals (mainly Cu and Pb). The submilli-scale distribution of Cu, Pb and other elements in leaves and subterranean stems was investigated. The images lead to the clarification of an accumulation mechanism, such as the route of absorption and correlation of each element. PIXE analysis can be used to investigate components in soils, and very useful for phytoremediation research.

References

1) Lombi E., Zhao F-J., Fuhrmann M., Ma L.Q. and McGrath, S.P., New Phytologist **156** (2002) 195.
2) McGrath S.P., Zhao F-J. and Lombi E., Advances in Agronomy **75** (2002) 1.
3) Yamazaki H., Tanaka M., Tsutsumi K., Ishii K., Iwasaki S., Matsuyama S., Inoue J., Murozono K. and Orihara H., Int. J. PIXE **6** (1996) 483.
4) Yamazaki H., Ishii K., Amartaivan Ts., Takahashi Y., Matsuyama S., Satoh T. and Sugihara S., Int. J. PIXE **11** (2001) 79.
5) Ure A.M., Quevauviller Ph., Muntau H. and Griepink B, Analyt. Chem. **51** (1993) 135.
6) Wang Z., Shan X.Q.S. Zhang S., Chemosphere **46** (2002) 1163.
7) Matsuyama S., Gotoh K., Ishii. K., Yamazaki H., Satoh T., Yamamoto K., Sugimoto A., Tokai Y. and Orihara H., Int. J. PIXE **8** (1998) 209.
8) Bowen H.J.M., Environmental Chemistry of the Elements, pp.333, Academic Press, London, New York, Toronto, Sydney, San Francisco (1979).
9) Blaylock M.J. and Huang J.W., Phytoextraction of metals. In: Ilya Raskin, Burt D. Ensley (eds.), Phytoremediation of toxic metals, John Wiley & Sons, Inc, 53-70, (2000).
10) Wang C.X., Mo Z., Wang H., Wang Z.J., Cao Z.H., Chemosphere **50** (2003) 717.

Table 1. Total and different chemical and physical forms of heavy metals in soils.

Element	Total (mg/kg)	Fraction 1 (%)	Fraction 2 (%)	Fraction 3 (%)
Cu	7000	63	32	3
Pb	5000	87	11	1

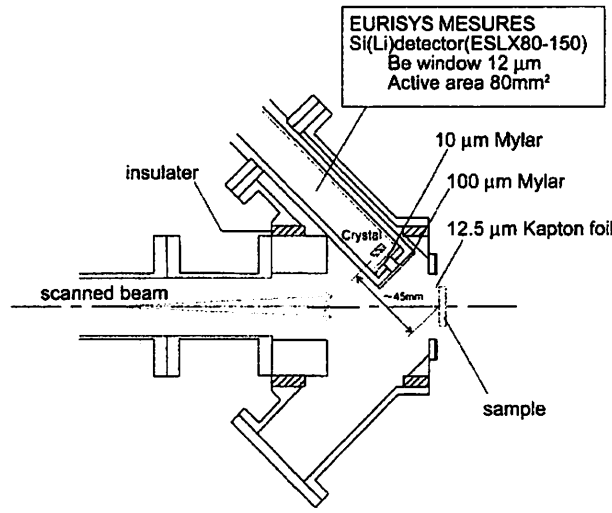

Fig. 1 Layout of the submilli-PIXE analysis system at the Dynamitron laboratory in Tohoku University.

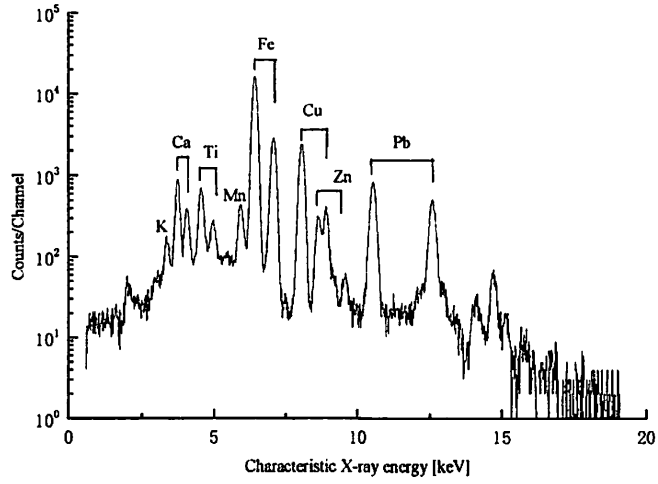

Fig. 2 X-ray spectrum of heavy metal contaminated soil analyzed by PIXE.

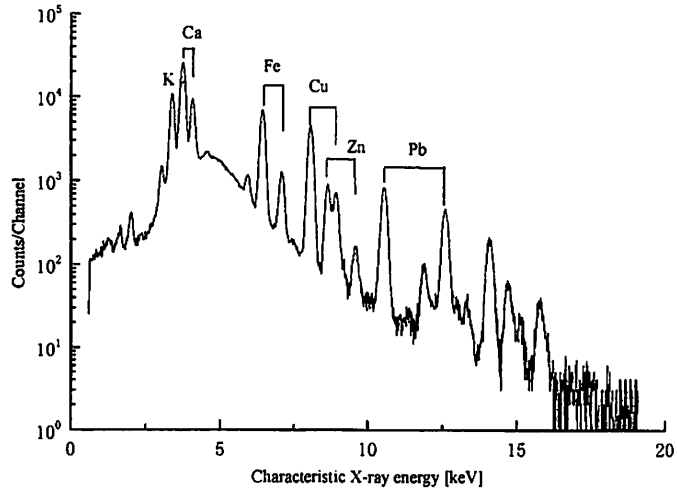

Fig. 3 X-ray spectrum of leaf of *P. cuspidatum* analyzed by PIXE

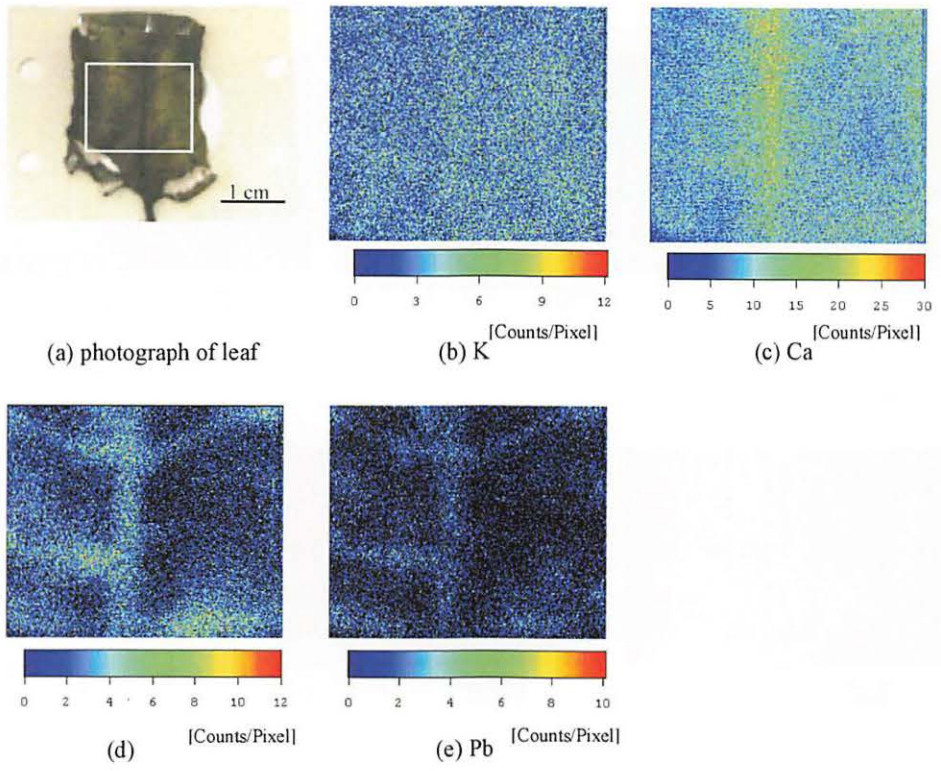

Fig. 4 Photograph of leaf (a), the corresponding to PIXE dot-maps of K, Ca, Cu and Pb (b, c, d and e, respectively).

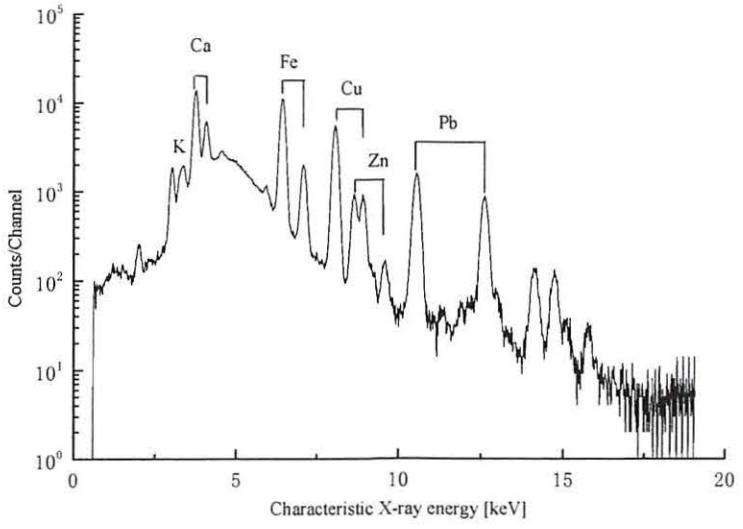

Fig. 5 X-ray spectrum of subterranean stems of *P. cuspidatum* analyzed by PIXE.

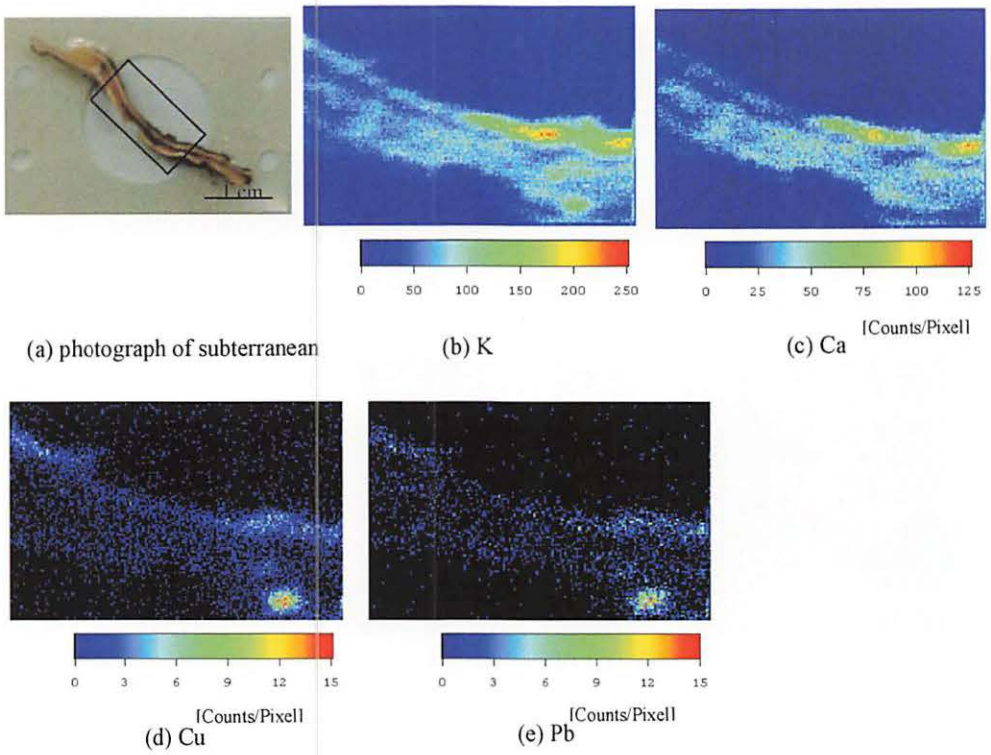

Fig. 6. Photograph of subterranean stems cut perpendicularly (a), the corresponding to PIXE dot-maps of K, Ca, Cu and Pb (b, c, d and e, respectively).

VI. RADIOCHEMISRTY AND NUCLEAR CHEMISTRY

VI. 1. Measurement of the Cross Section of the $^{40}Ar(\alpha,2p)^{42}Ar$ Reaction

Sato N., Yuki H., Ohtsuki T.*, Shinozuka T.**, Baba M.**, Ido T.**, and Morinaga H****.

Department of Physics, Tohoku University
*Laboratory of Nuclear Science, Tohoku University**
*Cyclotron and Radioisotope Center, Tohoku University***
*Munchen University****

The accurate value of the formation cross section of radionuclides is important for several applications of radioactivities. In the case of ^{42}K, an importance is mainly in medical applications and educational tool as a demonstration of radioactivities. One of the generators of radioactivities, ^{42}Ar-^{42}K, is firstly proposed by Morinaga et al. as for the educational tool of radioactivities, where ^{42}Ar was produced by the $^{40}Ar(t,p)^{42}Ar$ reaction. The half lives of ^{42}Ar (parent) and ^{42}K(daughter) are 33 years and 12 hours, respectively, and they are in correlation of a secular equilibrium, therefore one can use for long time as a ^{42}K generator (in Fig.1). However, no tritium accelerator is available in nowadays. Therefore, the $^{40}Ar(\alpha,2p)^{42}Ar$ reaction should be used to produce the ^{42}Ar-^{42}K generator even though the reaction cross section might be smaller than that of the $^{40}Ar(t,p)^{42}Ar$ reaction.

^{40}Ar gas was filled in the target chamber of 118m*l* in volume with 1 atom in order to irradiate as a gas-target. The target was irradiated by using 45MeV α-beam from cyclotron. After the irradiation, the target chamber was left during a few months for cooling the radioactivities of byproducts. Then, the gas was transferred to the generator chamber with passing through two babbling bottles filled by water for removing the ^{42}K radionuclides produced directly by the $^{40}Ar(\alpha,pn)^{42}K$ reaction. After leaving a few days for considering the half life of ^{42}K (12 h) and the secular equilibrium, a few m*l* of water was injected in the generator chamber and shaken for trapping the ^{42}K in water. Then water removed from the generator was dried in a paper filter to measure the characteristic γ-ray of ^{42}K. The γ-ray activities of 1524 keV from the ^{42}K radionuclide (in the filter) were measured with a Ge-detector coupled to a 2048-channel pulse-height analyzer.

From the amount of radioactivities of 1524 keV γ-ray, the counting rate in secular equilibrium C_0 is as follows;

$$C_0 = I_\gamma \varepsilon V \lambda_{Ar} N_0 \sigma L \rho$$

where, I_γ (intensity of 1524keV gamma rays) = 18%, ε (efficiency of Ge detector at 1524keV) = $(0.38 \pm 0.03)\%$, V(volume difference between target chamber and glass buffer) = 41%, λ_{Ar} (decay constant of ^{42}Ar) = 6.66×10^{-6} decay/sec., N_0 (number of incident α ions) = 2.82×10^{17} ions, L(length of target chamber) = 16.5 cm, ρ (density of target ^{40}Ar) = 2.51×10^{19} atoms/cm^3. Finally, we obtained the value of C_0 as $C_0 = C\exp(\lambda_K t) = (3.28 \pm 0.23) \times 10^{-2}$ counts/sec. Substituting these parameters, we find that cross section of ^{40}Ar(α,2p)^{42}Ar reaction at $E_\alpha = (41.6 \pm 1.8)$ MeV is $\sigma = (1.5 \pm 0.2)$ mb. Further studies will focus on measurement of excitation function of ^{40}Ar(α,2p)^{42}Ar reaction in order to increase the yield of ^{42}Ar.

References

1) Fenyvesi A., et al., Appl. Radiat. Isot. **46** (1995) 1413.
2) Tarkanyi F., et al., Radiochem. Acta **54** (1991) 165.
3) Tanaka S. et al., J. Phys. Soc. Japan **15** (1960) 952.

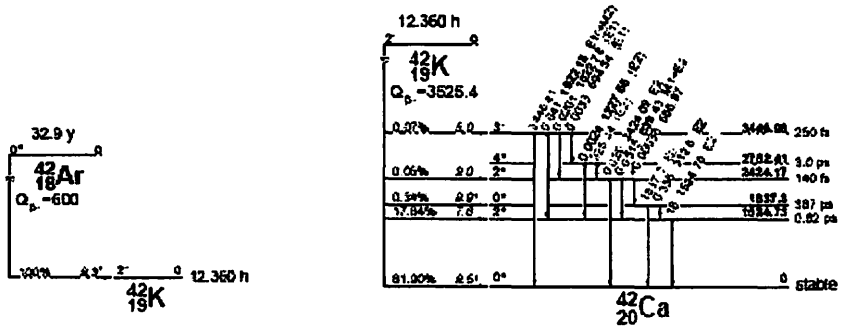

Fig. 1. Decay schemes of ^{42}Ar and ^{42}K.

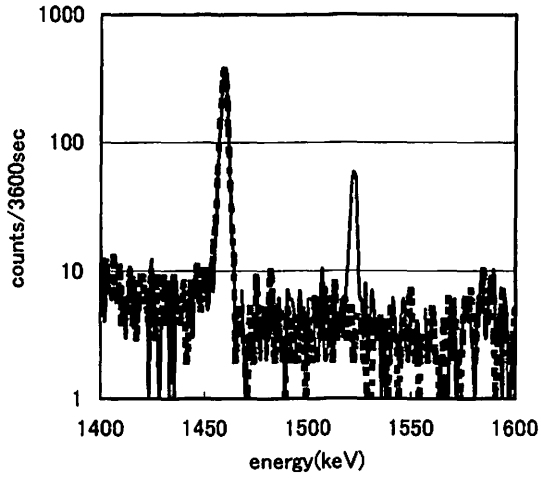

Fig. 2. Energy spectrum of ^{42}K in the generator chamber (solid line) and of background (dashed line). A 1524 keV γ -ray from ^{42}K (daughter of ^{42}Ar)was observed at one month later after the irradiation.

VI. 2. Collection of the Potassium-42 from $^{40}Ar(\alpha,pn)^{42}K$ Reaction

Yuki H., Satoh N., Ohtsuki T., Shinozuka T.*, Baba M.*, Ido T.*, and Morinaga H.***

Laboratory of Nuclear Science, Tohoku University
*CYRIC, Tohoku University**
*Technische Universitat Munchen***

Radiation sources are great important not only for research in basic science, material science, medical and radiopharmaceutical use but also for education in those area, and even in that in a high school. A ^{42}Ar-^{42}K generator is one of the convenient sources for β- and/or γ-rays as proposed by Morinaga. However, no value for the cross section of the $^{40}Ar(\alpha, 2p)^{42}Ar$ reaction experimentally measured have been reported so far. We have measured the excitation function of $^{40}Ar(\alpha, 2p)^{42}Ar$ reaction for investigating a possibility of the ^{42}Ar-^{42}K generator. The value measured at the incident energy of 41.6 MeV was estimated to be 1.5 ± 0.5 mb, however, which was lesser than that calculated value, 8.3 mb, using ALICE code[1]. In order to investigate another methods by means of chemical treatment, the ^{42}K produced by the $^{40}Ar(\alpha, pn)^{42}K$ reaction was separated chemically and measured, further compared with an amount estimated from the experimental value of the cross section reported by Tanaka *et. al.* [2]

A target of ^{40}Ar-gas sealed by 1 atm in aluminum chamber (165mm in length, 40mm in diameter) was irradiated by α-particles of 41.6 MeV with 1 electric-μA at CYRIC. The irradiation time was about 14 hours. Fig. 1 shows a schematic view of the target chamber and the generator chamber. Two bubbling bottles and a vessel of molecular sieve were installed between the chambers for collection the ^{42}K radionuclides directly produced by the $^{40}Ar(\alpha, pn)^{42}K$ reaction. Pure water was firstly filled to remove the ^{42}K radionuclides, the generator chamber was pumped up to vacuum state, then, the ^{42}Ar-gas was transferred to the generator chamber through the two bubbling chambers being up to equal pressure. The water removed from the two bubbling bottles was dried in a filter paper using a hot plate and an infrared lamp. The generator chamber filled by the irradiated Ar-gas was left for

measuring the cross section of $^{40}Ar(\alpha, 2p)^{42}Ar$ in another run. The inside of the target chamber was washed with pure water. The water was also dried in a filter paper. Finally the filter papers were set on a Ge detector to measure the γ-ray of 1524 keV from ^{42}K radionuclides. Fig.2 shows the γ-ray spectrum of the ^{42}K radionuclides collected from the target chamber. It is clearly seen the peak of 1524 keV in the figure.

An amount of the ^{42}K radionuclides on the filter papers was estimated from yields of the γ-ray of 1524 keV assuming the cross section which is the value reported by Tanaka *et. al.* It was found that only a magnitude of 48% to the total amount of ^{42}K radionuclides produced by the irradiation was collected in the filter paper for the target chamber. Even if the KCl solution was used for washing the inside of the target chamber, a magnitude of 54% to the total amount of ^{42}K radionuclides was collected in the filter paper. In the filter paper for the trap, a magnitude of 5.2% to the total amount of ^{42}K radionuclides was collected. A magnitude of several percentage to the total amount remained in the target chamber and beakers used for the concentration procedure. Therefore, further experimental investigations are needed to determine the exact values of the cross sections of the $^{40}Ar(\alpha, pn)^{42}K$ reactions. We are thinking that TPB (tetraphenylborate) can be useful for washing the inside of the chamber and trapping the ^{42}K radionuclides.

References

1) Blann M., Vonach K.H., Phys. Rev. C **28** (1983) 1475.
2) Tanaka S, Furukawa M., Mikumo T., Iwata S., Yagi M., Amano H., J. Phys. Soc. Jpn **15** (1960) 952.

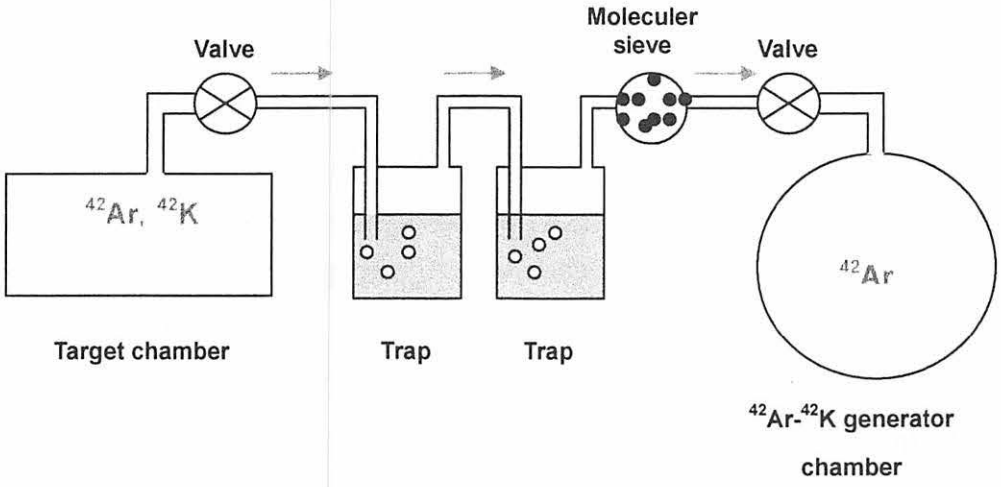

Fig. 1. A schematic view of the target chamber, the bubbling bottles, vessel of molecular sieve and the ^{42}Ar-^{42}K generator chamber.

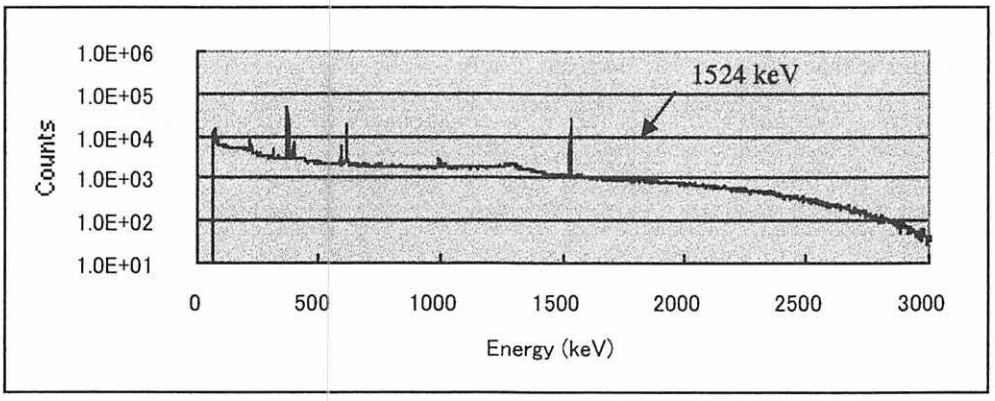

Fig. 2. A typical γ-ray spectrum of ^{42}K radionuclides collecting from the target chamber.

VI. 3. Target Preparation by the Precipitation Method for Nuclear Reactions and the Production of Californium Isotopes

Ohtsuki T., Yuki H., Takamiya K.[*], Shibata S.[*], Mitsugashira T.[**], Sato N.[***], Suzuki T.[***], Miyashita Y.[***], Fujita M.[***], Shinozuka T.[***], Kasamatsu Y.[****], Hasegawa H.[****], and Shinohara A.[****],

Laboratory of Nuclear Science, Tohoku University
Research Reactor Institute, Kyoto University, Kumatori-cho, Sennan-gun, Osaka 590-0494, Japan[*]
Institute of Materials Research, Tohoku University, Oarai Branch, Oarai, Ibaraki 311-1313, Japan[**]
Cyclotron Radio-isotope Center, Tohoku University, Aramaki, Aoba, Sendai 980-8578, Japan[***]
Deptartment of Chemistry, Osaka University, Osaka 560-0043, Japan[****]

We applied a simple and an unique method to the target preparation by using a membrane filter (Anodisc 25 which is consisted by Al_2O_3, pore size; 0.1 μm , diameter; 20 mm, an effective thickness; 25 μm) distributed commercially by Whatman Co Ltd[1]. It can be useful for the method with a precipitation after filtrating the target material. We found that the deposition efficiency is almost 100 % for obtainable thickness. The ^{238}U deposited on the Anodisc disk was irradiated with ^{12}C ions in order to produce the ^{245}Cf and ^{244}Cf with $^{238}U(^{12}C,xn)$ reactions.

An amount of 1g ^{238}U (^{nat}U) in 6 N 100 m*l* of nitric acid (HNO_3) solution was diluted by pure water to concentrate ^{238}U as 9.6 mg(^{238}U)/6.2 m*l*. The diluted HNO_3 solution was collected and a few drops of phenolphthalein were added to the solution in order to check its pH afterwards. Ammonia water in concentration of 25% (pH~10) was added to the solution with being checked the alkalinity indicated by phenolphthalein. Then, water was added to be its total volume of 9.6 m*l*. (1 mg ^{238}U/ m*l*). The solution was permitted to stand for at least 30 min due to the growth of uranium crystals (uranium hydroxide) in the solution. The solution of 9 m*l* exactly containing the ^{238}U of 900 μg as a hydroxide was partially collected in a separate beaker, and diluted by 2-3 m*l* of water. Finally, the solution was filtrated to deposit ^{238}U hydroxide on the Anodisc. Therefore, the chemical yield of the filtration was estimated to be approximately 100 %.

Recently, a He-gas jet transport system was installed for producing heavy elements

around Z=100 at the CYRIC. The target was mounted in an aluminum holder and placed in a He-jet reaction-chamber placed on the end of a beam course. The reaction-chamber was connected to the He-gas (containing KCl clusters) jet transporting system. He-gas (a flow rate of 5 *l* /min) was applied through a KCl-cluster generator with heating at 660 degree C. The transport efficiency of the system was estimated to be 30-40 %.

The Anodisc deposited ^{238}U (300 $\mu g/cm^2$) was mounted in a target holder and irradiated with 120 MeV ^{12}C ions in order to produce heavy isotopes such as ^{245}Cf and ^{244}Cf by the $^{238}U(^{12}C,xn)$ reactions[2-3]. The beam current was typically 150 particle-nA. The reaction products adsorbed on the cluster were transported with He-gas through a capillary tube (15 m long) to an automated rotating–wheel-chamber placed at the room in the next door. Four α-ray detectors consisted of a PIN-photodiode were installed in the rotating-wheel-chamber in order to measure the α-rays emitted from the nuclides transported. The products transported by He-gas were blown on a polyethylene terephtalate films. The accumulation of the transported products and the measurements of the α-rays from ^{245}Cf and ^{244}Cf was repeated by each 20 min. The data were stored with a PC-CAMAC system.

After the irradiation, the surface of the Anodisc was examined with a SEM image in order to confirm the damage. Typical SEM images are shown in Fig. 1(a)-1(d). The Anodisc before use is shown in Fig. 1(a) with an unit magnification ratio of 10 μm, and here, the ^{238}U hydroxide was seen on the surface though observing the local cracks. The Anodisc irradiated by ^{12}C ions are shown in Fig. 1(b)-1(d) by the different magnification ratios, 1(b) for 100 μm, 1(c) for 10 μm and 1(d) for 1 μm (the reverse side). It was found that no damage was seen though some faintly brown-colored at the area irradiated. The SEM image is almost similar to that of the Anodisc before use.

The α-ray spectrum of ^{245}Cf and ^{244}Cf produced by the ^{238}U (^{12}C,5n) and $^{238}U(^{12}C,6n)$ reaction is shown in Fig. 2. It was found that clear peaks of the α-rays of ^{245}Cf and ^{244}Cf were observed at 7.13 and 7.21 MeV with the $^{245}Cm(\alpha,5n)$ and $^{24}{}^{4}Cm(\alpha,6n)$ reactions. Therefore, it seems that the Anodisc is useful for the target-backing irradiated by several ion beams. The α (γ)-ray spectra and/or the excitation functions for producing such heavy elements, not only ^{245}Cf, ^{244}Cf but also heavier nuclides, can be obtained by means of the Anodisc target. This utilization may lead a new method for target preparations, simple procedures and high yields for depositing source materials.

References

1) Mitsugashira, T. et al., private communication.
2) Magara M., Shinohara N., Hatsukara Y., Tsukada K., Iimura H., Usuda S., Ichikawa S.I., Suzuki T., Nagame Y., Kobayashi Y., Oshima M., Radiochim. Acta **72** (1996) 39.
3) Sikkeland T., Maly J., Lebeck D., Phys. Rev. **169** (1968)1000.

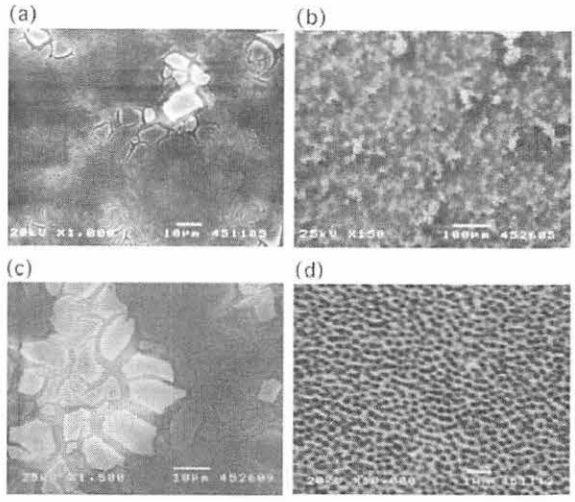

Fig. 1. SEM images; (a) for the Anodisc deposited ^{238}U before use, (b)-1(d) for the different magnification ratios, 100 μm for 1(b), 10 μm for 1(c) and 1 μm for 1(d) (the reverse side).

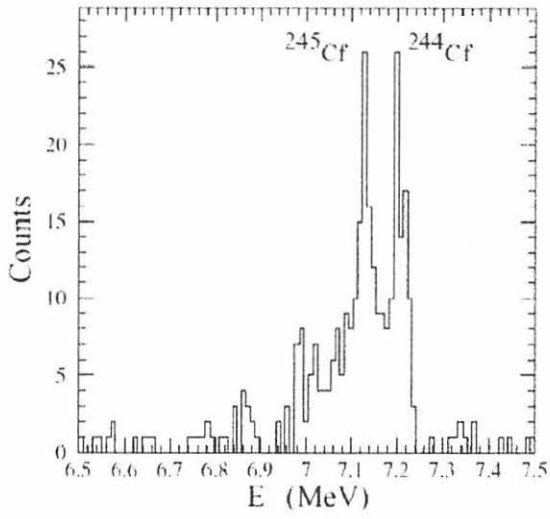

Fig. 2. The α-ray spectrum of ^{245}Cf and ^{244}Cf produced by the $^{238}U(^{12}C,5n)$ and $^{238}U(^{12}C,6n)$ reactions.

VI. 4. Analysis of Technetium-99 in Marshall Islands Soil Samples by ICP-MS

*Tagami K., Uchida S., and Sekine T.**

Environmental and Toxicological Sciences Research Group, National Institute of Radiological Sciences
*Department of Chemistry, Graduate School of Science, Tohoku University**

Introduction

Technetium-99 (^{99}Tc) is an important fission product which has been widely distributed in the environment as a result of fallout from nuclear weapons testing[1-4] and discharges from nuclear facilities[5,6]. Measurements of ^{99}Tc are of special interest because of the high mobility of Tc in the environment, its long half-life ($T_{1/2}$ = 2.11 x 10^5 y) and potential long-term radiological consequences.

In order to improve our understanding of the behavior of ^{99}Tc in the environment and to develop appropriate radioactive waste storage/disposal options, it is essential that we obtain more reliable information on the levels, distributions and fate of ^{99}Tc in the environment. It is known that there are several sources of ^{99}Tc in the environment, mainly, reprocessing plants and nuclear weapons test sites. One of the sites is the northern Marshall Islands where the United States carried out over 60 nuclear test detonations during the 1950's. Total carbonate contents of the soil samples are higher than those of normal terrestrial soils. Thus, a separation method for Tc which suits the characteristics of these samples is necessary.

In this study, soil samples collected from various sites in the Marshall Islands were used to evaluate different techniques for the extraction of ^{99}Tc from soil matrices for the determination of ^{99}Tc by inductively coupled plasma mass spectrometry (ICP-MS).

Experimental

Sample and reagents.

Soil samples used in this study were collected from the Marshall Islands between 1992 and 1996 by the Lawrence Livermore National Laboratory (LLNL). The details of

the soil preparation were reported elsewhere[7]. Nitric acid was ultrapure-analytical grade (Tama Chemicals, AA-100). Deionized water (>18 MΩ) was obtained from Milli-Q water system (Millipore Co.). Pre-packed columns of Tc-selective chromatographic resin, TEVA (Ehchrom Industries, Inc.) were used for separations of Tc. A standard ^{99}Tc solution available from Amersham (solution TCZ.44) was used for calibrating the ICP-MS. Technetium-95m ($T_{1/2}$ = 61 d) was prepared by irradiation of Nb in a cyclotron to be used as a yield monitor[8].

Chemical separations

Three Tc extraction techniques were examined as shown in Fig. 1. Each solution obtained by the extraction procedures was adjusted to 0.1 M HNO_3 and passed through a TEVA resin column to purify and concentrate Tc isotopes[9]. Because ICP-MS cannot differentiate between ^{99}Ru and ^{99}Tc, it is necessary to remove all Ru from the final sample solution prior to ICP-MS measurement. Ruthenium present in the sample solution is not effectively retained on the TEVA resin. More than 95% of Ru passes directly through the column with the solution. The column was then washed with 2 M HNO_3 to remove any remaining trace Ru. Technetium was eluted with 5 mL of 8 M HNO_3. By the separation steps, Ru was completely; only < 0.1% of the element was found in the 8 M HNO_3 eluate. The strip solution containing Tc was evaporated to dryness, and the residue dissolved in 5 mL of 2% HNO_3.

Measurement

The chemical recovery was measured by counting ^{95m}Tc in the sample on an NaI (Tl) scintillation counter (Aloka, ARC-380) and comparing the results with standard solutions. The ^{99}Tc content of the sample solution was then determined by ICP-MS (Yokogawa, PMS-2000) with 180 s counting time at mass 99. To check levels of potential interference elements (e.g., Ru, Mo), m/z = 98, 101 and 102 were also scanned at the same time.

Results and Discussion

ICP-MS is applicable for the measurement of long-lived radionuclides, if the total elemental concentration in the solution is less than 1000 mg/L due to instrumental limitation. A lower total elemental concentration than 300 mg/L is preferable for stable

operation of the instrument. Thus, ranges of element concentrations were measured by ICP-MS in final Tc column eluted solutions from seven separate soil samples using each of the three extraction methods (M1, M2 and M3). The results are shown in Fig. 2. The recovery of matrix elements Na and Al were also very similar between each of the extraction methods. Interestingly, consistently higher concentrations of Ca, Cu, Nb, Mo, I and U were observed in M2 eluates where soils were leached with nitric acid without any prior treatment. It is not clear why we observed consistently higher levels (1-2 orders of magnitude) of matrix elements in the final sample solution using this extraction technique. High levels of dissolved solids in sample solutions may cause matrix induced interferences, and lead to poor instrument stability and suppression of the analyte signal. Thus, M2 extraction technique is less suited for ^{99}Tc measurement by ICP-MS. We therefore suggest that careful attention should be given to the type of extraction procedure used, and the preparation of the sample load solution used for the separation of ^{99}Tc on TEVA columns. For example, the elution characteristics of the TEVA column may have been affected by the presence of small residual quantities of organic material because, unlike M2 soils, the M1 and M3 extracts were both prepared from ashed and/or combusted materials. No interference of ^{98}MoH on the determination of ^{99}Tc by ICP-MS was observed in this study.

Total chemical recoveries of Tc for extraction techniques M1, M2 and M3 were 49.6-98.5%, 39.7-76.4% and 7.6-16.9%, respectively (Fig. 3). M3 extraction method appeared to show that Tc is not very efficiently volatilized from Marshall Islands soils. Probably, due to the high carbonate contents in the samples, Tc was trapped in the molten sample during heating like an alkaline fusion condition. From the results, we judge M1 to be the best method among the studied separation methods. However, we found that the use of a combustion apparatus offers significant advantages over acid dissolution techniques for other soil types/elements. We plan to continue to optimize the technique for routine analyses of ^{99}Tc. Sample volatilization techniques are not critically dependent on sample size, and they help to improve the effectiveness of the following separation by drastically reducing the total dissolved solids content of the sample load solutions.

The concentrations of ^{99}Tc in the seven soil samples collected from the Marshall Islands as determined by M1 and M2 ranged from 0.1 to 1.1 mBq/g dry weight[10]. Using a reference date of 1954 the ^{99}Tc /^{137}Cs activity ratios in Bikini surface soils ranged from 0.7 - 1.1 x 10^{-4} or around 50 - 70% of the theoretical fission yield production ratio of 1.4 x 10^{-4}. The residual levels of radionuclides retained in surface soils of the Marshall Islands will depend on the initial inputs, their half-lives and environmental behaviors of the

radionuclides. However, at this time we have no information on the distribution of ^{99}Tc in soil profiles, on the rates of ^{99}Tc transport into underlying ground waters nor on ^{99}Tc transfer factors into plants or organisms. Based on this initial assessment, we can state that persistent levels of ^{99}Tc are being retained in surface soils of the atoll, and that removal rates of ^{99}Tc and ^{137}Cs in surface soils are occurring on similar time-scales. More studies are required to address any possible long-term radiological issues related to ^{99}Tc -particularly developing an understanding of Tc cycling, rates of transport, and uptake factors into native plants and/or organisms.

References

1) Attrep M., Enochs J.A. and Broz L.D., Environ. Sci. Technol. **5** (1971) 344.
2) Holm E., Rioseco J., Ballestra S. and Walton,A., J. Radioanal. Nucl. Chem. **123** (1988) 167.
3) García-León M., Manjón G. and Sanchez-Angulo C.I., Radioact. **20** (1993) 49.
4) Tagami K. and Uchida S., J. Nucl. Radiochim. Sci. **3** (2002) 1.
5) Aarkrog A., Chen Q.J., Dahlgaard H., Nielsen S.P., Trapeznikov A. and Pozolotina V., J. Environ. Radioact. **37** (1997) 201.
6) Dahlgaard H., J. Environ. Radioact. **25** (1994) 37.
7) Stuart M.L., Collection and processing of plant, animal and soil samples from Bikini, Enewetak and Rongelap Atolls, US DOE Rep. (1995), UCRL-ID-120427, 33pp.
8) Sekine T., Konishi M., Kudo H., Tagami K. and Uchida S., J. Radioanal. Nucl. Chem. **239** (1999) 483.
9) Uchida S. and Tagami K., Radioact. Radiochem. **10** (1999) 23.
10) Tagami K., Uchida S., Hamilton T. and Robison W., Appl. Radiat. Isot. **53** (2000) 75.

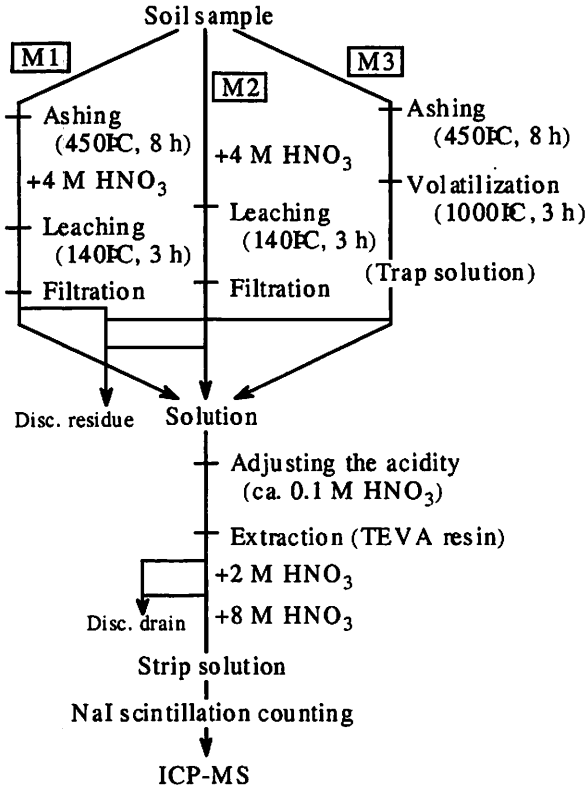

Fig. 1. Schematic diagram of separation methods, M1, M2 and M3, for Marshall Island soil samples.

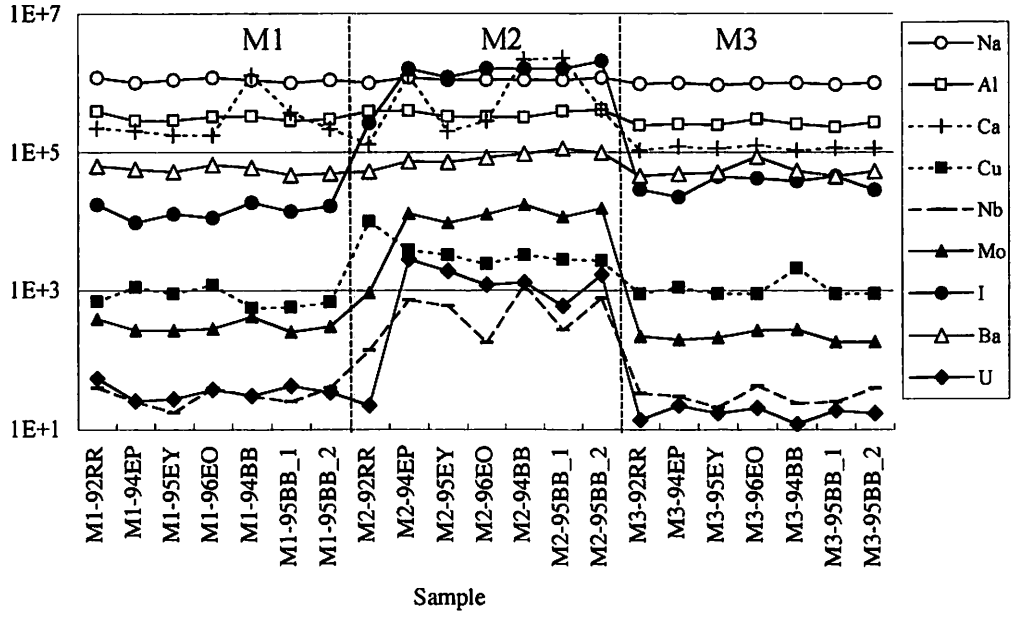

Fig. 2. Concentrations of Na, Al, Ca, Cu, Nb, Mo, I, Ba and U in final solutions for ICP-MS analyzed by M1, M2 and M3.

VII. RADIOPHARMACEUTICAL CHEMISTRY AND BIOLOGY

VII. 1. Automated Preparation of [^{18}F]FRP-170 as a Hypoxic Cell Marker for Clinical PET Studies

Ishikawa Y., Morita M.[*], *Furumoto S.*[**], *Takai Y.*[***], *and Iwata R.*

Cyclotron and Radioisotope center, Tohoku University
Graduate School of Engineering, Tohoku University[*]
Institute of Development, Aging and Cancer, Tohoku University[**]
University Hospital, Tohoku University[***]

2-Nitoroimidazoles have high reduction potential and radiosensitizing activity. Since reduction of the nitro group in the molecule leads to selective binding and retention in hypoxic cells, F-18 labeled 2-nitroimiodazole analogs such as [^{18}F]FMISO[1,2], [^{18}F]fluoroetanidazole[3], [^{18}F]EF1[4] and [^{18}F]EF5[5] are expected to be a good candidate for imaging tumor hypoxia by positron emission tomography (PET). Fluorine-18 labeled FRP-170 ([^{18}F]FRP-170) was developed by modification of RP-170[6], a radiosensitizer of POLA Chem.[7], and evaluated as a new imaging agent for hypoxia at Tohoku University[8]. For applying this potential radiopharmaceutical to routine clinical diagnosis by PET an automated system was developed in this study.

The synthetic procedure (see Fig. 1) consisted of (1) separation of [^{18}F]fluoride from the target water, (2) drying the aqueous mixture of Kryptofix 222 and [^{18}F]KF by evaporation, (3) reaction with the precursor in DMF, (4) purification of the intermediate product by solid-phase extraction, (5) deprotection of the purified product by base hydrolysis and (6) final purification by high performance liquid chromatography (HPLC). They were modified or simplified to adapt to automation as follows:

Frequently used procedures of addition of liquid reagents, transfer of reaction solutions and evaporation of solvents were automated by sensing the change in He flow[9]. As seen in Fig. 2 the He flow was markedly changed according to the vapor pressure in the reaction vessel during evaporation or the presence of liquid in the tube and thus completion of each process could be detected without requiring a manual interruption.

An original glass reaction vessel was substituted for a small round bottom flask with thin walls (10 mL, Wheaton) to reduce the time for azeotopic distillation of

water-acetonitrile. This was also useful for preventing the contamination of carrier fluoride derived from the plastic cap and sealing O-ring used for the original vessel.

On-column hydrolysis using a Sep-Pak C18 cartridge was introduced to simplify the procedure. The protected intermediate product retained by the cartridge was hydrolyzed on-column by filling with the NaOH solution and thus second vessel for this reaction could be omitted. It can be seen from Fig. 3 that the on-column method requires a much higher concentration of NaOH whereas it is efficiently hydrolyzed even with 0.1 M NaOH by the conventional vessel method. A 0.5 M concentration of NaOH was adopted. After hydrolysis the cartridge was first washed with water and then the deprotected product was eluted with an appropriate solvent.

Elution of [^{18}F]FRP-170 from the C18 cartridge was optimized. In order to simplify the procedure the solvent used for the elution was directed to an HPLC column. In general, a product retained by the C18 cartridge is more efficiently eluted with a lower polar solvent. However, this lower solvent, if injected onto an HPLC column for subsequent separation, may spoil the separation by leading compounds together. This is clearly demonstrated in Fig. 4. Only the solvent of <15% MeCN contents provides a satisfactory separation between [^{18}F]FRP-170 and an undesired non-radioactive by-product. Using a 2 mL portion of this solvent system, the [^{18}F]FRP-170 was eluted only in 30% efficiencies from the Sep-Pak. The elution efficiency was twice improved with a 1 ml portion of the solvent system of water-MeCN (70:30) followed by a 1 mL portion of water.

A commercial automated synthesis system, F121 (Sumitomo Heavy Industries), was adapted to the automated preparation of [^{18}F]FRP-170 (see Figs. 5 and 6). Using the automated system [^{18}F]FRP-170 was prepared in decay-corrected radiochemical yields of 15-20% within 50 min. The method developed in the present study was also demonstrated to be simple and reliable enough to carry out the reproducible production of [^{18}F]FRP-170 for routine use.

References

1) Jerabek P.A., Patrick T.B., Kilbourn M.R., Dischino D.D., Welch M.J., Appl. Radiat. Isot. **37** (1986) 599.
2) Grierson J.R., Link J.M., Mathis C.A., Rasey J.S., Krohn K.A., J. Nucl. Med. **30** (1989) 343.
3) Tewson T.J., Nucl. Med. Biol. **24** (1997) 755.
4) Kachur A.V., Dolbier W.R., Evans S.M., Shuie C.-Y., Shuie G.G., Skov K.A., Baird I.R., James B.R., Li A.-R., Roche A., Koch C.J., Appl. Radiat. Isot. **51** (1999) 643.
5) Dolbier W., Jr., Li A.-R., Koch C.J., Shiue C.-Y., Kachur A.V., Appl. Radiat. Isot. **54** (2001) 73.
6) Wada H., Iwata R., Ido T., Takai Y., J. Label. Compd. Radiopharm. **43** (2000) 785.

7) Murayama C., Suzuki A., Suzuki T., Miyata Y., Sakaguchi M., Tanabe Y., Tanaka N., Mori T., J. Radiation Oncology Biol. Phys. **17** (1989) 575.
8) Kaneta T., Takai Y., Kagaya Y., Yamane Y., Wada H., Yuki M., Iwata R., Tsujitani M., Takahashi S., Yamada S. J. Nucl. Med. **43** (2002) 109.
9) Iwata R., Yamazaki S., Ido T., Appl. Radiat. Isot. **41** (1990) 509.

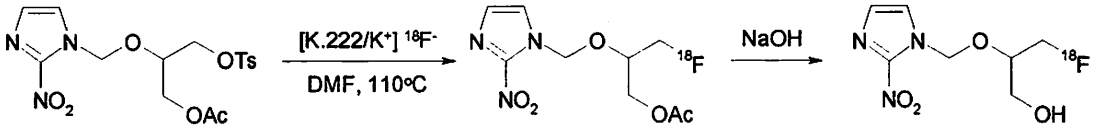

Fig. 1. A synthetic scheme of [^{18}F]FRP-170 from [^{18}F]fluoride.

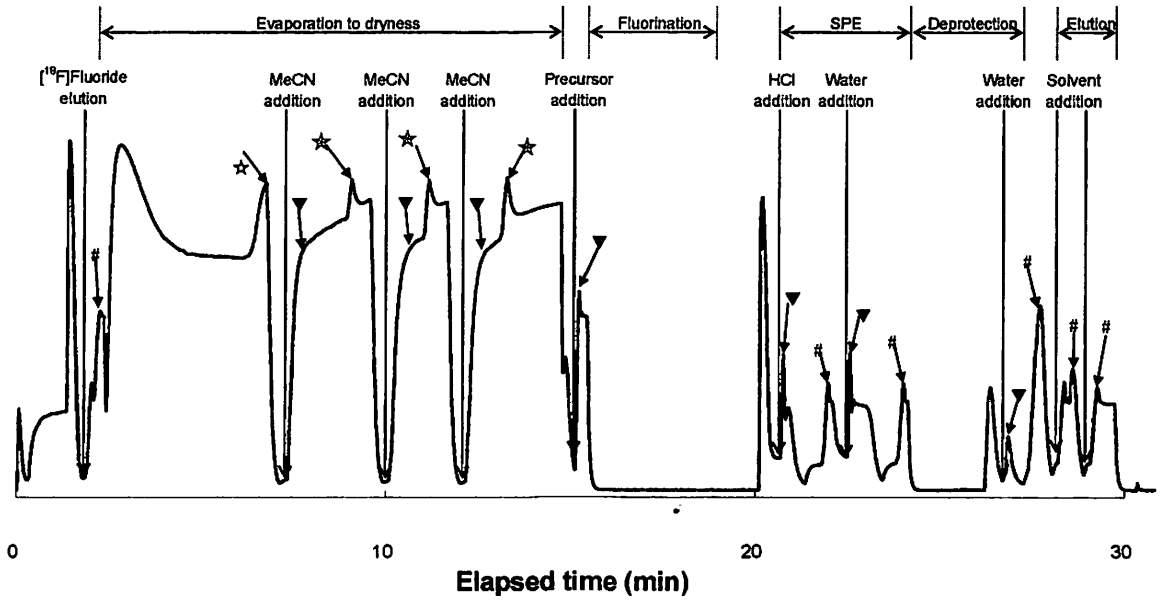

Fig. 2. A typical He flow change during the automated preparation.

★: completion of evaporation
▼: completion of addition
#: completion of passage

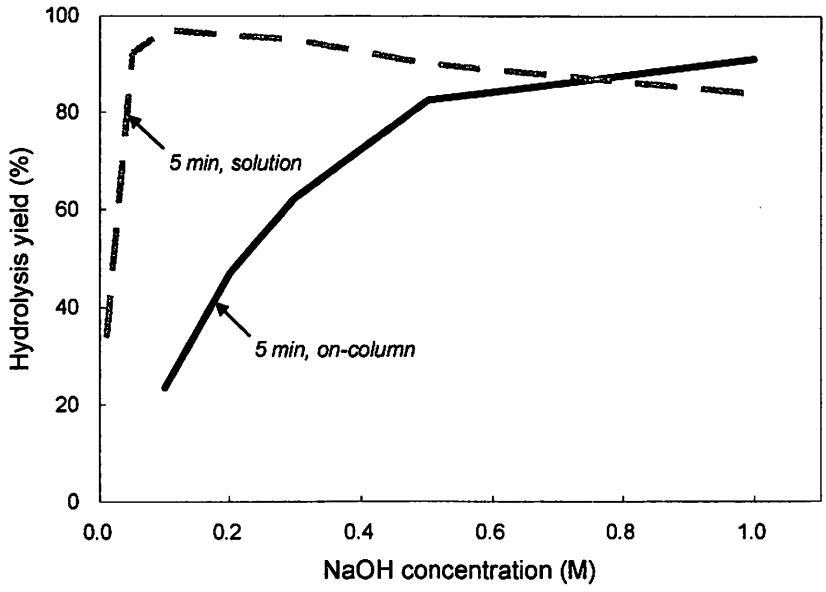

Fig. 3. Dependence of base hydrolysis on NaOH concentration.

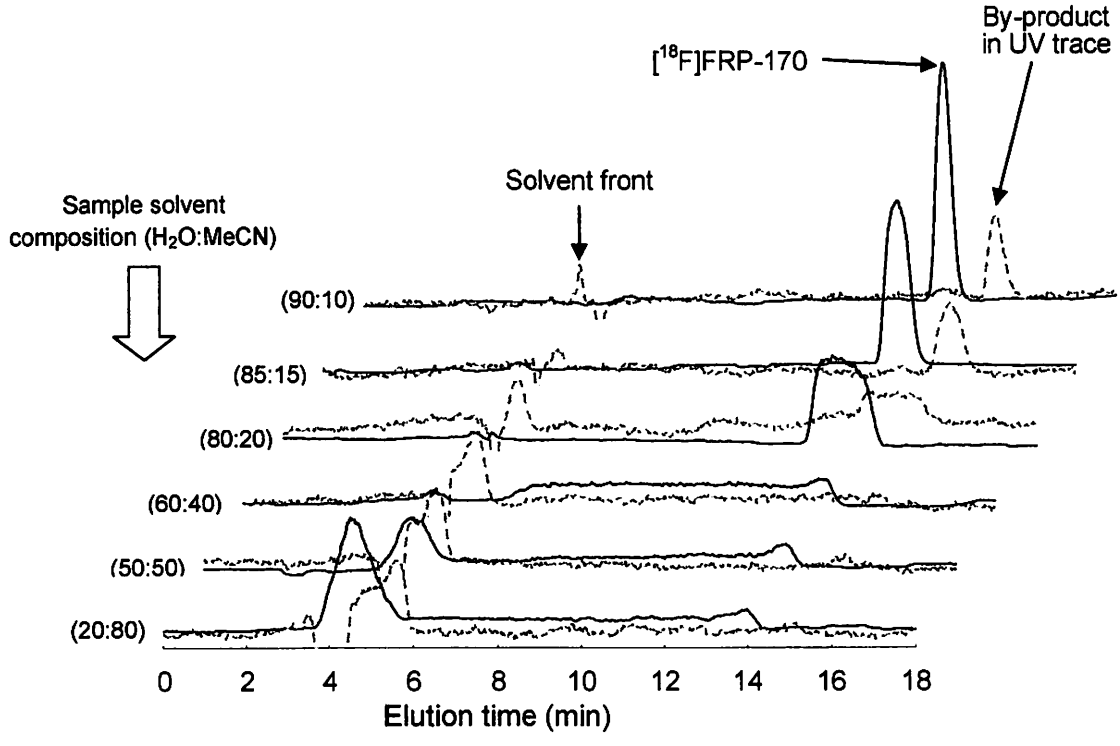

Fig. 4. Effects of polarity of sample solvent on separation profiles of [^{18}F]FRP-170 from the by-product.

- Column: YMC ODS-A-324
- Solvent: MeCN-H2O (12:88), 4.0 mL/min
- UV: 280 nm

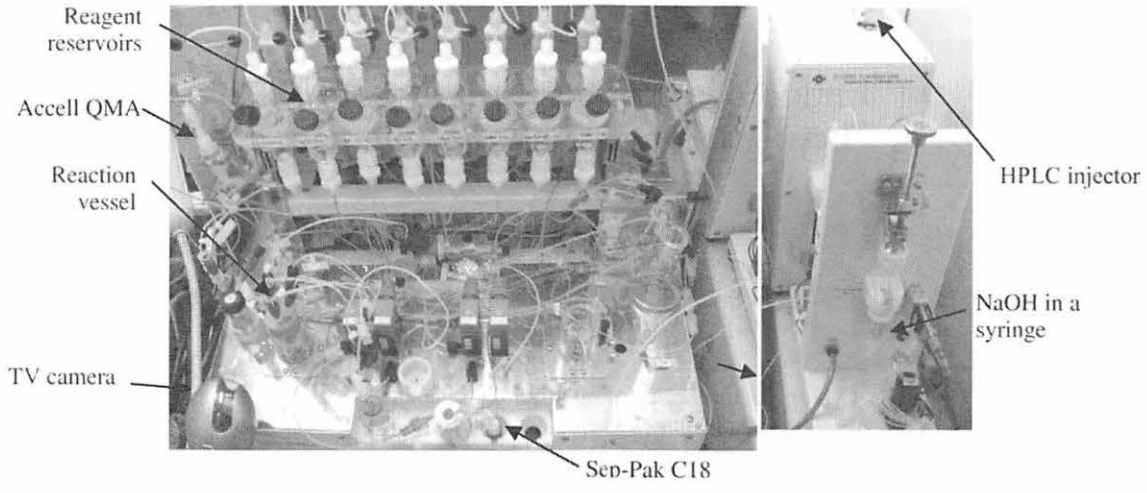

Fig. 5. An automated system (F121).

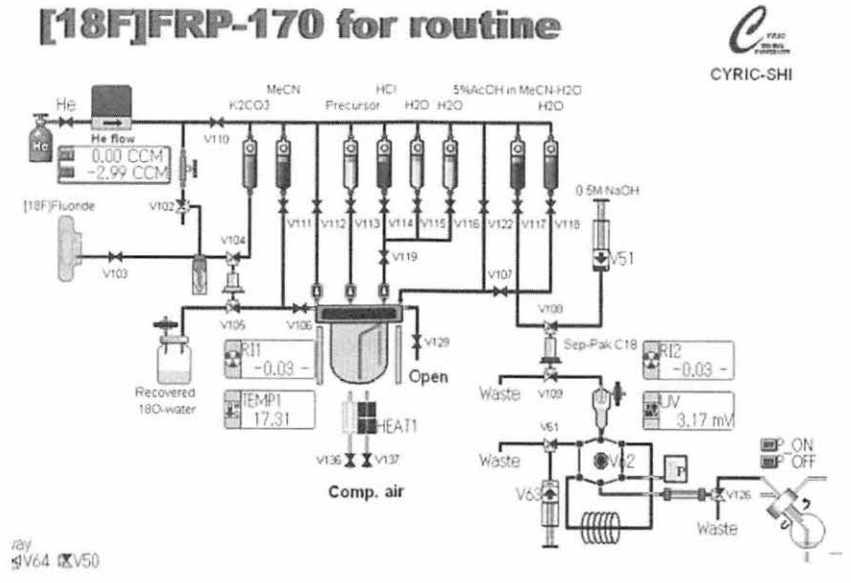

Fig. 6. A flow diagram of an automated system for [^{18}F]FRP-170

VII. 2. *O*-[^{18}F]Fluoromethyl-L-Tyrosine for the Differentiation Between Tumor and Inflammation

Suzuki M., Yamaguchi K., Honda G., Iwata R., Furumoto S., Jeong MG., and Itoh M.*

Cyclotron and Radioisotope Center, Tohoku University
*Tohoku University Biomedical Engineering Research Organization**

Introduction

^{18}F-2-deoxy-2-fluoro-D-glucose (^{18}F-FDG) is useful as a tumor-detecting agent in clinical positron emission tomography (PET) studies[1]. However, ^{18}F-FDG accumulates highly not only in tumors but also in inflamed tissues[2]. This nonspecific accumulation of ^{18}F-FDG leads to false-positive results and reduces the diagnostic accuracy[3].

In tumor cells, amino acid metabolism is enhanced and amino acid transport and the rate of protein synthesis increase[4]. On the other hand, inflammatory cells did not take amino acids much compared with ^{18}F-FDG[5,6]. These properties suggest the specificity in tumor imaging. Various amino acids have been labeled for the tumor detection and investigated for their clinical application in oncology[7].

Recently, the synthesis of *O*-[^{18}F]fluoromethyl-L-tyrosine (^{18}F-FMT), has been reported as a new tumor-detecting agent by Iwata et al.[8]. The ^{18}F-FMT preparation was simple with high radiochemical yields and consequently suitable for routine production.

The aim of this study was to evaluate the potency of ^{18}F-FMT for the differentiation between tumor and inflammation using animal models with experimentally induced inflammation and implanted tumor.

Materials and methods

The animal study was carried out according to the protocol approved by the Animal Care Committees of Cyclotron and Radioisotope Center, Tohoku University.

The methods of ^{18}F-FMT labeling with ^{18}F were reported elsewhere[8].

Male Donryu rats weighing 150 to 180 g (Japan SLC, Japan) were used. They

were fed food and water ad lib. Tumor cell suspension of ascites hepatoma, AH109A (Cell Resource Center for Biomedical Research, Tohoku University, Japan), was inoculated subcutaneously into the right thigh of the rats 7 days before the experiment. Ten microliters of turpentine oil (Wako Pure Chemical Industries Co., Ltd., Japan) was injected subcutaneously into the rats' back twice in different positions 12 and 4 days respectively before the experiment to induce inflammation foci. These inflammation foci were assumed to represent chronic and acute inflammations, respectively.

Rats were injected intravenously with 1.85 MBq of ^{18}F-FMT via the tail vein, and sacrificed at five time points (5, 10, 30, 60 and 120 min after injection). Blood and the tissues of interest (tumor, acute inflammation, chronic inflammation, brain, heart, pancreas, liver, kidney, small intestine, muscle and bone) were partially or wholly removed immediately. The samples were weighed and ^{18}F radioactivity was measured by a gamma counter (PerkinElmer, Inc., USA). The amount of radioactivity was expressed as a percentage of the injected dose per gram of tissue (%ID/g).

One-way ANOVA with Scheffé's F correction was used to analyze all the results. Statistical significance was considered at $P < 0.05$.

Results and discussion

Table 1 shows the results of biodistribution studies with ^{18}F-FMT in tumor and inflammation bearing rats. Tissue radioactivities, in general, showed a steady decline in the course of the experiment, while tumor, the pancreas and the bone showed either retention or build-up patterns. ^{18}F-FMT accumulations in tumors at 30 and 60 min after injection were significantly higher than those of the other tissues ($P < 0.01$), except for the pancreas. The peak uptake time in the tumor was found to be around 60 min after injection, and the %ID/g in tumor at this time point was 3.2 times higher than in the other tissues, except for the pancreas. The accumulations of ^{18}F-FMT in acute and chronic inflammations were similar and showed no statistical difference from the background tissues at all time points.

In conclusion, although this study is still preliminary, ^{18}F-FMT seems promising tracer for the differentiation between tumors and inflammation with higher specificity to tumors. The simplicity in radiolabeling supports ^{18}F-FMT as a potential amino acid tracer in oncological imaging.

Referances

1) Rigo P., Paulus P., Kaschten B.J., Hustinx R., Bury T., Jerusalem G., Benoit T. and Foidart-Willems J., Eur. J. Nucl. Med. **23** (1996) 1641.
2) Kubota R., Yamada S., Kubota K., Ishiwata K., Tamahashi N. and Ido T., J. Nucl. Med. **33** (1992) 1972.
3) Strauss L.G., Eur. J. Nucl. Med. **23** (1996) 1409.
4) Isselbacher K.J., N. Engl. J. Med. **286** (1972) 929.
5) Kubota R., Kubota K., Yamada S., Tada M., Takahashi T., Iwata R. and Tamahashi N., J. Nucl. Med. **36** (1995) 484.
6) Kubota K., Matsuzawa T., Fujiwara T., Sato T., Tada M., Ido T. and Ishiwata K., Jpn. J. Cancer Res. **80** (1989) 778.
7) Jager P.L., Vaalburg W., Pruim J., de Vries E.G., Langen K.J. and Piers D.A., J. Nucl. Med. **42** (2001) 432.
8) Iwata R., Furumoto S., Pascali C., Bogni A. and Ishiwata K., J. Label. Compd. Radiopharm. **46** (2003) 555.

Table 1. Tissue distributions of ^{18}F-FMT in rats with AH109A tumor, acute and chronic inflammations.

Tissue	Time after injection				
	5 min	10 min	30 min	60 min	120 min
Tumor	0.64 ± 0.31	0.78 ± 0.41	1.27 ± 0.35	1.43 ± 0.43	1.06 ± 0.37
Acute inflammation	0.49 ± 0.07	0.43 ± 0.10	0.50 ± 0.08	0.50 ± 0.13	0.59 ± 0.11
Chronic inflammation	0.46 ± 0.21	0.41 ± 0.11	0.53 ± 0.14	0.50 ± 0.14	0.64 ± 0.22
Blood	0.63 ± 0.10	0.51 ± 0.10	0.51 ± 0.09	0.46 ± 0.09	0.48 ± 0.08
Brain	0.36 ± 0.12	0.37 ± 0.11	0.52 ± 0.12	0.47 ± 0.12	0.46 ± 0.11
Heart	0.56 ± 0.08	0.48 ± 0.11	0.46 ± 0.07	0.41 ± 0.09	0.44 ± 0.06
Pancreas	3.68 ± 1.15	3.15 ± 0.74	3.16 ± 0.52	3.48 ± 0.55	3.42 ± 0.47
Liver	0.59 ± 0.13	0.53 ± 0.15	0.45 ± 0.08	0.43 ± 0.08	0.43 ± 0.05
Kidney	0.65 ± 0.19	0.53 ± 0.12	0.48 ± 0.08	0.42 ± 0.07	0.42 ± 0.06
Small intestine	0.51 ± 0.19	0.42 ± 0.13	0.38 ± 0.09	0.41 ± 0.09	0.40 ± 0.08
Muscle	0.52 ± 0.17	0.45 ± 0.14	0.44 ± 0.09	0.43 ± 0.07	0.43 ± 0.09
Bone	0.38 ± 0.13	0.39 ± 0.11	0.39 ± 0.07	0.51 ± 0.11	0.62 ± 0.11

Values are expressed as mean ± standard deviation of %ID/g. (n=8)

VIII. NUCLEAR MEDICINE

VIII. 1. Central Itching Modulation : A Human PET Study

Mochizuki. H, Tashiro M., Kano M., Sakurada Y., Itoh M., and Yanai K.*

Department of Pharmacology, Tohoku University School of Medicine
*Cyclotron and Radioisotope Center, Tohoku University**

Introduction

Itching can be defined as "an unpleasant sensation associated with the desire to scratch"[1]. Scratching behavior in atopic dermatitis can become just as unbearable and debilitating as chronic pain, leading to depression and suicidal thoughts. Generally, antihistamines are prescribed for patients with allergic diseases to suppress itching symptoms through the blockade of histamine H1 receptors (H1R)[2]. However, administration of antihistamines, especially of the first generation, interfere with the activities of daily living and with work that requires full alertness, since they elicit sedation and impair various cognitive functions such as psychomotor speed and learning[3]. The unpleasant sensation caused by itching can also be reduced by cooling. Skin cooling can reduce itch sensation without aggravation while scratching tends to aggravate the symptom and while antihistamines often cause sedation. Interestingly, Murray reported that the itching sensation, when itch and pain stimuli were applied to different parts of the body, was lower than the itching alone. They predicted the presence of the central itch modulation system, though details of the system were not understood[4]. However, as far as the authors know, little has been reported focusing on the itch inhibitory mechanism by cooling in the brain. Even it is still unclear whether such mechanism exists in human brains or not.

Therefore, in the present study, we investigated the mechanism of itch modulation by cooling in human brains using PET and $H_2{}^{15}O$.

Methods

Fifteen healthy male volunteers (mean ± SD of age, 22 ± 2.3 years old) were included in the present study. Subjects with a history of allergy, atopic eczema or other dermatological diseases were excluded from the study. Written informed consent was obtained from each subject and the study was performed in compliance with the relevant laws and institutional guidelines.

In the present study, PET measurement was conducted under 6 different conditions as follows: Condition 1) saline stimulus, Condition 2) mild itching stimulus with 0.001 % histamine solution, Condition 3) intense itching stimulus with 0.01% histamine solution, Condition 4) dual stimulations of intense itching (0.01 % histamine) and cold pain (5°C) (dual stimuli), Condition 5) cold pain stimulus (5°C), and the resting condition (condition 6).

Two different concentrations of histamine solution were used in the present study to verify the dose-dependency. The histamine solutions (0.01% and 0.001%) were prepared by dissolving histamine to saline. Two ml of the histamine solution was infiltrated into a square electrode pad (2 cm x 2 cm), which was attached to the back of the right foot. Itch sensation was elicited by the electrical subcutaneous penetration of the histamine solution with iontophoresis system (UI-2060, Uniflows, Japan). In the present study, the electrical current given by the iontophoresis was 1 mA. The duration of the iontophoretic stimuli was 2 min (total charge: 120 mC, 1 mA x 120 sec). A saline condition served as a control for the itching stimuli where the saline solution (2 ml) was applied to the subjects in the same way as itching stimulus conditions using iontophoresis. No stimulus was given to the left foot in the following three conditions: 1) saline, 2) mild and 3) intense itching stimulus conditions. In the dual stimuli condition, the intense itching and cold pain stimuli were simultaneously applied to the right and left feet, respectively. For cold pain stimulus, thermocooler (Thermal cycler, Japan) was used to keep the skin temperature of the back of the left foot at 5°C, where the areas to be stimulated by iontophoresis and cold pain were controlled to be equal (2 cm x 2 cm). The cold pain stimulus was given to the left foot for 2 min simultaneously with the intense itching stimulus. The sequence of conditions 3 (intense itching stimulus) and 4 (dual stimuli) were randomized among the subjects. We employed the cold pain stimulus condition in order to examine whether the regional cerebral blood flow (rCBF) changes observed in the dual stimuli was attributable to the cold

pain stimulus to the left foot or not. A control for the cold pain stimulus condition was the resting condition.

All subjects closed their eyes during PET scanning. Time intervals between scans were more than 10 min in order to eliminate the effect of previous itch and/or cold pain sensations. After each scanning, intensity and unpleasantness of subject's itch sensation was scaled with visual analog scales ranging from 0 to 10. When subjects feel no itch sensation on their right foot, the scale will be "0". When the itch intensity and unpleasantness is the worst in their past experience, the score will be "10".

The cerebral blood flow (CBF) images were obtained at whole brain level using a PET scanner (Shimadzu SET-2400W, Japan). PET measurement was performed for 70 sec. Subjects were injected with approximately 5.4 mCi (200 MBq) of [^{15}O]-H_2O through antecubital vein for each scan.

The CBF images obtained were processed and analyzed by Statistical Parametric Mapping (SPM) software (SPM99; Welcome Department of Cognitive Neurology, London, U.K.). After realignment for intra-subject motion correction, all images were stereotaxially normalized, using linear and non-linear transformations into a standard space of Talairach and Tournoux. The normalized images were then smoothed using a 16 x 16 x 16 mm Gaussian filter. The values of rCBF were expressed as ml 100 g^{-1} min^{-1}, adjusted using ANCOVA and scaled to a mean of 50 ml / 100 g / min. The significant increase or decrease in rCBF was evaluated according to the general linear model at each voxel.

To test the hypotheses on specific rCBF changes, the estimates were compared using linear contrasts. The resulting set of voxel values for each contrast constitutes a statistical parametric map of the *t*-statistics. To discover brain regions related to the histamine stimulus, CBF images during the intense itching stimulus were compared to those during the saline stimulus. CBF images during the intense itching stimulus were compared to those during the dual stimuli to detect any rCBF difference between the conditions. The effect of cold pain stimulus on the brain activity was investigated by comparing CBF images in the cold pain stimulus condition to those in the rest. The *t*-value of each voxel was transformed into normally distributed Z-statistics. For each comparison, voxels with a Z-value higher than 2.99, corresponding to $p<0.001$ (uncorrected), were considered to represent regions with significant change in rCBF.

The changes of subjective feelings of itch intensity and unpleasantness were compared among the mild itching, the intense itching and the dual stimuli conditions with ANOVA and multiple comparison (Tukey). A probability of less than 0.05 was

considered to be statistically significant.

We performed volume of interests (VOI) analysis with SPM to compare the brain activity related to itching among the conditions such as the mild itching, the intense itching and the dual stimuli conditions. We determined the localization of the peak activation related to the intense itching stimulus as compared to the saline stimulus condition. Mean voxel values were calculated among the voxels including the peak and also exceeding a threshold of $Z > 2.99$. Mean of these voxel values reflected rCBF since all voxel values in the CBF images were scaled to a mean of 50 ml / 100 g / min. The rCBF changes in the mild itching, the intense itching and the dual stimuli conditions in comparison to the saline stimulus condition were examined by ANOVA and multiple comparison (Tukey). A probability of less than 0.05 was considered to be statistically significant.

Results

Itch sensation induced by histamine increased in a dose-dependent fashion and decreased when the cold pain stimulus was given on the right foot (Fig.1). The significant increases of regional cerebral blood flow (rCBF) caused by histamine stimuli using iontophoresis were observed in the left anterior cingulate cortex (BA24), the left thalamus, the right anterior parietal cortex (BA40), the right posterior parietal cortex (BA7), the bilateral dorsolateral prefrontal cortex (BA46) and the right premotor cortex (BA6) (Fig.2). Activations in the itching-related brain regions were decreased by cold pain stimulus simultaneously given to the opposite side of the itching stimulus, as compared to itching alone (Fig.2). In addition, the midbrain including periaqueductal gray matter (PAG) was activated only during the simultaneous stimulation of itching and cold pain (Fig.3).

Discussion

Several investigators have proposed hypotheses to account for the inhibitory mechanism of itch sensation by cooling in the central nervous system (CNS). However, it has been still unclear whether such a system exists in the human brain or not.

Subjective feelings of itch intensity and unpleasantness increased with the increment of histamine concentration, and the itch intensity during the dual stimuli was significantly lower than that during the intense itching stimulus (Fig.1). These results suggested that itch sensation was suppressed by the cold pain stimulus simultaneously given to the contralateral side of the itching stimulus. These results supported the presence of the itch modulation mechanism in the human brain[4].

The rCBF in the anterior cingulate cortex (ACC), the dorsolateral prefrontal cortex (DLPFC), the posterior parietal cortex and the premotor cortex increased with the increment of histamine concentration and decreased in the dual stimuli of itching and pain (Fig.2). Interestingly, midbrain including the periaqueductal gray matter (PAG) was activated during the dual stimuli as compared to the intense itching stimulus alone as shown in Fig.3. The midbrain did not show even any tendency toward increased rCBF in the cold pain stimulus condition or in the intense itching stimulus condition. PAG is known as the central pain modulation system. PAG neurons project axons down to the dorsal horns of the spinal cord via medulla and raphe nuclei, where they suppress the activity of nociceptive neurons[5]. Furthermore, in the animal study, it was demonstrated that spinal neuronal responses to histamine were markedly suppressed by electrical stimulation to the midbrain PAG[6]. In views of the previous reports, it was suggested that the activation of PAG was associated with the attenuation of the itch intensity and of the itch related-brain activity during the dual stimulations of itching and cold pain. Our results supported the hypothesis that the descending inhibitory mechanism of PAG for pain would also work for itch modulation.

References

1) Rothman S., Physiology of itching. Physiol. Rev. **21** (1941) 357.
2) Mochizuki H., Tashiro M., Tagawa M. et al. Hum. Psychopharmacol **17** (2002) 413.
3) Murray F.S., Weaver M.M., J. Comp. Physiol. Psychol. **89** (1975) 819.
4) Mayer D.J., Prog. Neuropsychopharmacol Biol. Psychiatry **8** (1984) 557.
5) Carstens E., J. Neurophysiol. **77** (1997) 2499.
6) Mochizuki H., Tashiro M., Kano M. et al., Pain. **105** (2003) 339.

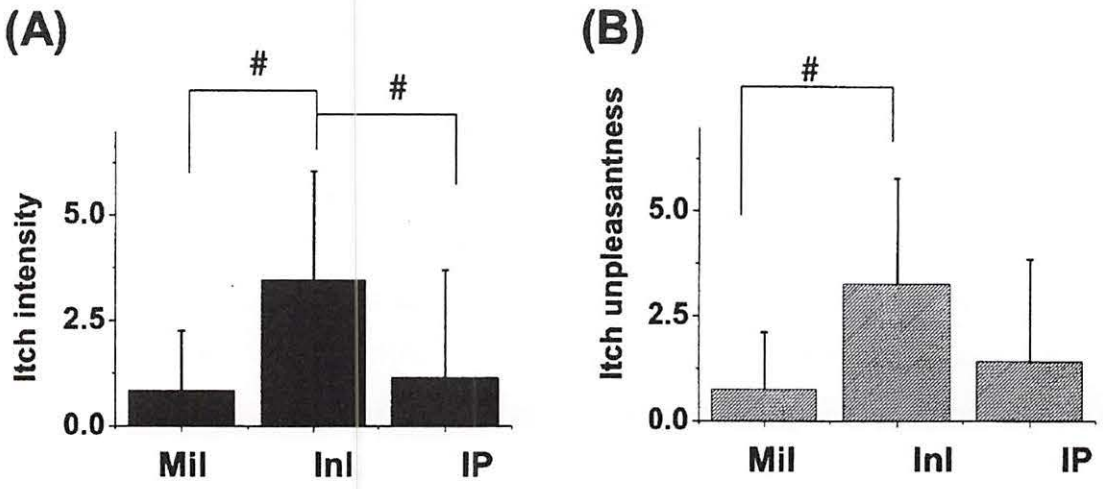

Fig. 1. The increases in subjective feelings of itch intensity (A) and unpleasantness (B) (mean and SD) in the mild itching stimulus (MiI), the intense itching stimulus (InI) and the dual stimulations of intense itching and cold pain (IP) conditions in comparison to the saline stimulus condition are shown. #: $p < 0.05$ by ANOVA and post-hoc multiple comparison (Tukey).

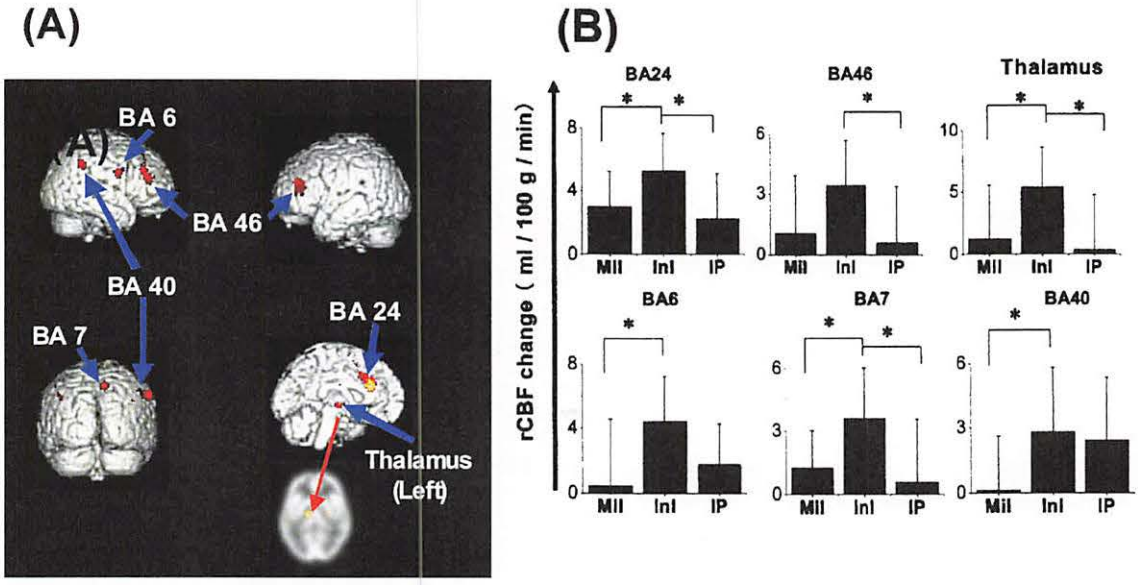

Fig. 2. (A) Areas of significant rCBF increase during the intense itching stimulus as compared to the saline stimulus (uncorrected p value < 0.001). Red arrow shows the left thalamus on a transaxial slice of the PET template. (B) The change in rCBF (mean and SD) from the baseline (saline stimulus) in each brain region related to itching. Abbreviations: MiI = mild itching stimulus, InI = intense itching stimulus, IP = dual stimulations of intense itching and cold pain, L = left hemisphere and R = right hemisphere. *: $p < 0.05$ by ANOVA and post-hoc multiple comparison (Tukey).

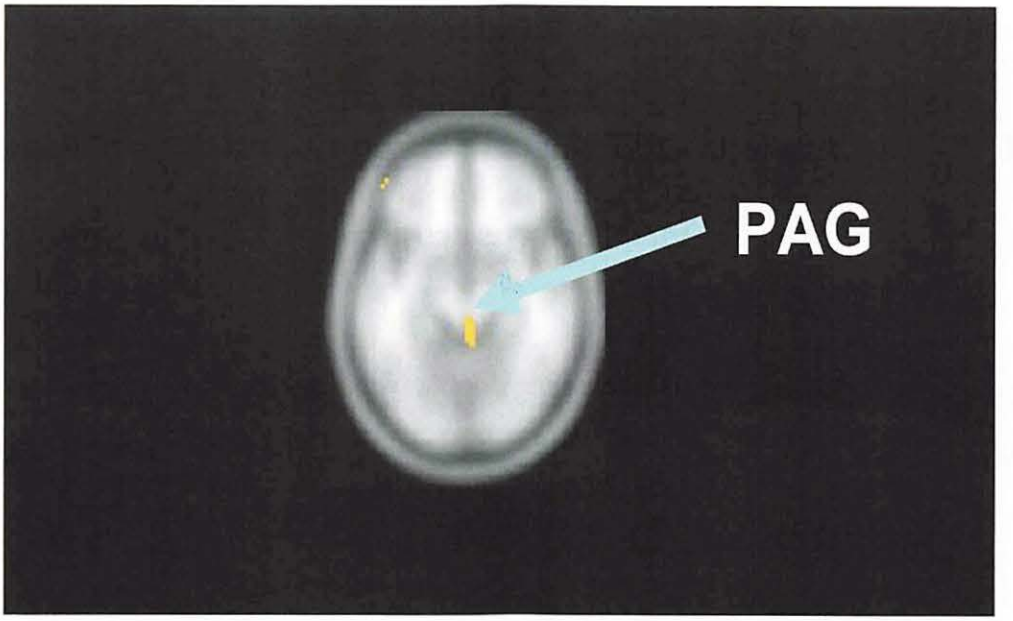

Fig. 3. Areas of rCBF increase during the dual stimuli as compared to the intense itching stimulus (uncorrected p value < 0.005). Blue arrow shows PAG on a transaxial slice of the MRI template.

VIII. 2. Exercise Induced Changes in Whole-body Energy Metabolism Evaluated by Positron Emission Tomography and ^{18}F-fluorodeoxyglucose (FDG-PET)

Mehedi M., Itoh M., Fujimoto T.[*], *Yamaguchi K., Miyake M., Watanuki S., and Sabina K.*

Division of Nuclear Medicine, Cyclotron and Radioisotope Center, Department of Medicine and Science in Sports and Exercise Tohoku University[*].

ABSTRACT

Purpose: Our purpose was to evaluate workloads induced changes in whole-body glucose metabolism using two analytical methods.

Subjects & Methods: Eleven healthy normal males [exercise group; n(5) & controls; n(6)] were assigned for this investigation. The exercise group were investigated with 3D FDG-PET technique after different workloads (40% and 70% of $\dot{V}O_2$max). Autoradiographic method (Phelps et al.) was applied to measure rMRGlc of skeletal muscles and viscera. Two analytical methods (quantitative & semiquantitative), were compared using Pearson's correlation coefficient analysis. The controls were investigated using similar study protocol as exercise group.

Results: Quantitative analysis revealed that rMRGlc was increased ($p<0.05$) in the skeletal muscles of thigh, lumbar/gluteal region and upper-limb, and decreased in the brain ($p<0.05$) at mild and/or moderate exercise loads. A correlation was found between MRGlc and SUR at thigh, brain and heart that not suggestive at lumbar/gluteal muscles.

Discussion & Conclusion: In spite of complexity of energy metabolic controls, exercise loads induced organ glucose metabolism were successfully visualized using FDG-PET technique. Linear increases and/or decreases in glucose uptake supports that FDG-PET technique can be used as an index of *in vivo* organ energy metabolism inducing different exercise loads. However, some discrepancy between two methods (SUR and rMRGlc) in the organ glucose metabolism suggests the complexity of *in vivo* energy metabolism. However, it is suggested that semiquantitative approach needs a great care when metabolic rate of glucose utilization changes at whole-body level.

Keywords: FDG-PET, Exercise, Glucose-Metabolism, Semiquantification, Quantification.

INTRODUCTION

Upto recent, it had not been possible to measure muscle glucose metabolism noninvasively in humans in vivo. Recently, the nuclear medicine technique such as positron emission tomography (PET) after administration of certain tracer (^{18}F-FDG) are useful to measure workloads induced energy metabolic changes. Fujimoto et al. (1996), first reported the feasibility of metabolic mapping of working muscles in runners investigated by FDG-PET method[1]. Tashiro et al.[2] (1999) and Iemitsu et al.[3] evaluated the running induced glucose metabolic changes of lower limb skeletal muscles and whole-body organs by applying ^{18}F-FDG and PET. However, the previous investigators demonstrated the glucose metabolic alterations in the lower leg muscles, visceral organs with semiquantitative analytical method at fixed exercise loads. Recently, Kemppainen J. and co-workers (2002), investigated different workloads induced changes of glucose metabolism in the skeletal muscle and myocardium[4].

In their investigations, they applied the absolute quantification method to assess regional metabolic rate of glucose in the thigh muscle and myocardium applying ^{18}F-FDG-PET technique. Quantification of individual organ glucose metabolism was not performed in the previous investigation.

The purpose of present investigation was to evaluate the dynamic control of energy metabolism (quantification and semiquantification) both in the skeletal muscles and visceral organs induced by mild and/or moderate exercise intensities (40% and 70% $\dot{V}O_2$max workloads respectively) by using ^{18}F-FDG and PET technique. The ergometer cycling was chosen as a mean for exercise loads.

Subjects & Methods

Five subjects, aged mean 21.80 ± 0.84 y, were studied as exercise group. The type of exercise was ergometer bicycling at 40and 70% $\dot{V}O_2$max workloads. Each subject of the exercise group was studied in two separate days within 3 weeks period with minimal 2 days separation. To evaluate $\dot{V}O_2$max, subjects performed intermittent exercise on an ergometer bicycle (Monark 818E, Sweden), and the oxygen consumption rate was determined by an automated metabolic unit machine (AE280-S, Minato Co. Ltd. Osaka, Japan). $\dot{V}O_2$max was measured by the discontinuous method inducing intermittent

bicycling at 60 revolution/min for 10 min/bout with 5 min intervals for 3 or 4 times (60W, 120W, 180W and 240W respectively). Subjects' O_2 consumption was measured at mild and moderate workloads (40% and 70% $\dot{V}O_2max$) as 17.77±1.49 ml/kg/min and 31.10±2.60 ml/kg/min (mean±S.D) respectively.

Before the experiment, they were instructed to take rest for 20 minutes in a dim lit quiet room. One teflon catheter was inserted to their antecubital veins of the left hand for blood sampling to measure plasma glucose, lactate, insulin and FDG concentrations. Another teflon catheter was inserted to subject's antecubital vein of the opposite hand for FDG administration. Then, they started ergometer bicycle riding at the speed of 60 revolution/min (Monark 818E, Sweden) at 40% and 70% $\dot{V}O_2max$ workloads. FDG was injected through a catheter at 10 minutes later following exercise task. After the injection, the subjects continued to pedal the bicycle for another 30 minutes to complete the total exercise task of 40 minutes.

Blood sampling protocol

Immediately after FDG administration, heated (arterialized) venous blood was sampled from cubital vein opposite to the injection site. Plasma glucose, lactate and insulin concentrations were measured at two points such as pre and post-exercise conditions using glucose analyzer (Gluco card GT-1630, KDK corporation, Kyoto, Japan), enzymatic lactate analyzer (Lactate Pro, KDK Corporation, Kyoto, Japan) and double antibody radio-immunoassay (Riabead 2, Dynabot Co, Ltd., Tokyo, Japan and coat cortisol, Incstar Co, Ltd. Stillwater, USA) respectively. The plasma FDG concentrations were measured during exercise; every 6 sec interval for 10 times, 1 min interval for twice, 2.5 min interval for twice, 5 min interval for twice, and at the end of exercise. During PET scan, the blood samples were taken for 7 times as follows; once at the onset of PET scan, and after 5 min interval, then every 10 min interval for 4 times, and once at the end of PET scan (Figure-1).

PET scan protocol

The subjects lay down in supine position on the PET table with eyes open in a dimmed and quiet room. The scan protocol was as follows; a 3 dimensional (3D) whole-body emission scan (3 min × 9 positions) was performed from the knee joint to the vertex followed by transmission scan (3 min × 9 frame). The transmission scan (post-injection mode) was performed with a $^{68}Ge/^{68}Ga$ external rotating line source (370

MBq at purchase) (Figure-1). All the subjects were abstained from eating and drinking atleast 5 h before the experiment, and they were requested for written fully informed consent. The clinical committee for the radioisotope use of Tohoku University approved this investigation.

In another, 6 subjects, aged mean 23.17 ± 5.1 y, were studied as the resting control maintaining the similar study protocol without exercise.

Quantitative approach (Calculation of glucose metabolic rate)

To evaluate the rate of glucose utilization, the autoradiographic method (3 compartment model method) was applied which was developed by Sokoloff et al.[5] and modified by Phelps et al[6]. rMRGlc images (regional metabolic rate of glucose images) were calculated using the equation shown below;

$$rMRGlc = \frac{Cp}{LC}\left[\frac{K^*_1 k^*_3}{k^*_2 + k^*_3}\right]\left[\frac{C^*i(T) - C^*e(T)}{C^*m(T)}\right]$$

Here, Cp and LC denote the native glucose concentration in plasma and lumped constant respectively. K*1, k^*_2, and k^*_3 are denoted as first order kinetic rate constants for FDG. [C*i(T)-C*e(T)]/C*m(T) is a correction factor which represents the estimations of the ratio between the true and the average metabolic rates. C*i(T) is the actual PET count at time (T), and C*e(T) and C*m(T) are calculated using population average rate constants. The rate constants and the lumped constants were decided separately for each organ[7-14].

Semiquantitative approach

Organ glucose uptake was evaluated by applying semiquantitative analytical approach. To determine semiquantification, standardized uptake ratio (SUR) was measured by using the equation mentioned below

$$SUR = \frac{MeanROIcts\ (cps/pxls) \times Body\,weight\,(g)}{Injected\,dose(\mu Ci) \times Calibration\,factor(cps/\mu Ci)}$$

where cps and pxls denote counts per second and pixels respectively. Shimadzu software (Shimadzu Co. Kyoto, Japan) was used for the analytical measurements (Quantification and Semiquantification).

Regions of Interest Analysis

Data analysis was performed based on the regions of interest analysis (ROIs) for measurements of rMRGlc and SUR. ROIs were drawn on selected organs by using Shimadzu software program (Shimadzu Co, Kyoto Japan). First, the coronal whole-body images were generated from the transverse whole-body images. ROIs were set on the skeletal muscles of thigh, lumbar/gluteal regions, upper-limb, and visceral organs such as liver, heart, brain etc. using coronal whole-body images. The anatomical locations were determined from the succeeding radioactivity distributions. The definition of anatomic locations of the organs were determined as following; the leg/foot; from knee joint down to the foot covering the extensor muscles, posterior part of the leg including gastrocnemius and soleus muscles, and the muscles of foot consisting flexors and adductors, the thigh; from anterior superior iliac spine down to the patella covering the quadriceps femoris muscle (QF), posterior part of the thigh including adductors and hamstrings muscles, the lumbar and gluteal region; a line between the posterior iliac crest and ischial tuberosity to the adjoin to the gluteal and lumbar muscles, the upper-limb; from the shoulder joint to the tip of the fingers covering biceps and triceps muscles of upper-arm, extensor and flexor muscles of forearm, and palmar and dorsal muscles of the hand. The visceral organs such as liver, heart and brain were identified from their anatomical locations and succeeding radioactivity distributions.

To minimize the partial volume effects, ROIs were set atleast 5 mm from the border of each slice. The average glucose uptake values of these ROIs counts were used for calculation.

Statistical analysis

Group comparisons were made for rMRGlc data using one way analysis of variance (Anova), and significant differences were determined by Scheffe's test (post-hoc analysis). The significant differences were set at $p<0.05$ for all the data. Group comparisons between pre- and post-exercise values of plasma glucose, lactate and insulin concentrations for exercise group subjects (40% and 70% $\dot{V}O_2max$) were made by using non-parametric test (WilcoxonSigned Rank test), and the significant differences were set at $p<0.05$. To evaluate relationship between quantitative and semiquantitative analytical methods, Pearson's correlation coefficient analysis was performed between SUR [(rest; n=2) and (exercise group; 40%$\dot{V}O_2max$; n=5, 70%$\dot{V}O_2$ max n=5)] and rMRGlc [(rest; n=6) and

(exercise group; 40% $\dot{V}O_2$max; n=5, 70%$\dot{V}O_2$ max=5)] data at thigh, brain, heart and lumbar/gluteal muscles.

Results

The present investigation demonstrated that glucose metabolism (rMRGlc) was increased in the working skeletal muscles, and decreased in the brain at mild and/or moderate exercise loads (Table-1). In the thigh muscles, glucose metabolic rate (mg/100g tissue/min) was increased ($p<0.05$) 8 times at 40% $\dot{V}O_2$max (1.76±0.21) and 10 times at 70% $\dot{V}O_2$max workloads (2.31±0.30) when compared with resting subjects (0.21±0.08). rMRGlc was significantly increased ($p<0.05$) in the skeletal muscles of lumbar/gluteal region at 70% $\dot{V}O_2$max (1.07±0.28) when compared with the resting controls (0.48± 0.26) (TABLE-1). The myocardial and abdominal organ such as hepatic glucose metabolic reductions (rMRGlc) were suggestive but not significant. Cerebral metabolic rate for glucose (CMRGlc) revealed significant decline ($p<0.05$) at moderate exercise load (70% $\dot{V}O_2$max) (3.19±0.81) when compared with rest (4.73±1.03). The biochemical measurement of plasma glucose was relatively stable with exercise loads. However, the plasma lactate was increased 6 times ($p<0.05$) at moderate workloads (5.3±2.4) when compared with pre-exercise condition (0.9±0.2). The plasma insulin concentration was shown significantly ($p<0.05$) decreased at moderate exercise loads (2.0±0.7) when compared with the pre-exercise condition (4.6±1.5).

The correlation analysis between rMRGlc and SUR suggested that metabolic glucose uptake in the brain, liver and heart were correlated [Figure-3(A) & 3(B) and Figure-4(A)] aside from lumbar/gluteal region [Figure-4(B)].

Discussions

We attempted to map the glucose metabolic changes in the skeletal muscles and visceral organs induced by mild to moderate exercise intensities using FDG and PET comparing two analytical methods such as semiquantitative and quantitative. Quantification approach showed that glucose metabolism (rMRGlc) was increased in the skeletal muscles of lower limb (i.e., thigh) ($p<0.05$), and decreased in the abdominal organ (i.e., liver), myocardium and brain ($p<0.05$) at mild and/or moderate workloads.

There are some crucial factors that might disrupt in the quantification of glucose metabolism in the current FDG-PET method. Quantification of glucose metabolism needs a steady condition. Therefore, it is essential to keep fasting of the volunteers before

investigation for maintaining steady plasma glucose concentration. Present investigation demonstrated that plasma glucose concentration was relatively stable at post-exercise condition of different exercise loads that suggesting glucose metabolic rate changes would not have to be affected. It is argued that glycogenolysis and gluconeogenesis would be pronounced under different workloads. Considering complexity of energy metabolism, FDG uptake probably underestimates overall energy production both at mild and/or moderate exercise loads. However, linear increases of FDG uptake with changes in the workloads found in the present experiment support the usefulness of FDG imaging in measuring tissue energy consumption.

Energy consumption in the skeletal muscles are mostly dependent upon fiber composition. Considering increases in the metabolic rate of glucose in the skeletal muscles of thigh, suggests aerobic and anerobic energy generation in the present study. It is argued that thigh muscles are composed of type-IIa and type-IIb fibers those are used up both at aerobic and anerobic exercise states. Workloads induced glucose metabolic rate changes in the liver was shown decreased without statistical implication. The interpretation of FDG metabolism in the liver is not simple because this endocrine organ has a small amount of hexokinase and used glucokinase to phosphorylase glucose. Since FDG is a poor substrate for glucokinase, its uptake in the liver is small. Nevertheless, the patterned FDG uptake by the liver at rest and different exercise loads were indicative. The absolute quantification method revealed the decreases in the myocardial glucose metabolism at moderate workloads without statistical significance. In normal physiologic state, myocardium consumes energy from glucose-fatty acid cycle. Kemppainen J et al. (2002) found that at rest and during low intensity exercise condition, myocardial glucose uptake correlated inversely with circulating FFA concentrations. In our present investigation, changes in the rMRGlc was not dependent upon exercise loads probably due to this glucose-FFA interactions. However, decline in the FDG uptake at moderate workload suggested that in this state myocardial energy was compensated by other metabolic substrate than glucose. Plasma lactate might be reasonable metabolic substrate for this compensation because at moderate workloads this lactate concentration was shown elevated. Finally, we focused on the brain glucose uptake inducing different exercise loads. Glucose is consumed as a principal energy susbstrate for the brain tissue. Until now, a few studies were organized to evaluate brain energy metabolic changes inducing various exercise loads. We found that CMRGlc was decreased significantly ($p<0.05$) at moderate workload. The possibilities for this metabolic reductions are reductions in either

gluts or hexokinase or both because changes of blood flow in the brain is unlikely from the concept of autoregulation. However, this reduction does not mean reduction in the total energy metabolic rate of the brain because other fuels may be burned out. Recently, Ide et al., (2000), reported that lactate was the metabolic substrate for the brain at graded exercise and recovery phase (15). In our present investigation of 70% $\dot{V}O_2$max exercise load, 6 fold increases in the plasma lactate concentration, susggested that this metabolite might fulfill energy demand for the brain tissue at this stage. However, further investigations are required for this evaluation.

From the present investigation, we could confirm that the functional levels of all the body organs are under dynamic homeostatic control, and it is argued that when exercise is initiated up to moderate level, energy resources such as glucose in predominant are recruited to the working skeletal muscles from other visceral organs including brain. This homeostatic control is said to be also carried out through adrenal hormone, catecholamine[16].

In the concluding section, the methodological validation of the quantitative approach would have to be assumed. In this experiment, autoradiographic method (Phelps et al.) demonstrated the concurrent validity to evaluate metabolic rate of glucose in the FDG-PET technique in the following points; (i) In the 3 compartment model of autoradiographic method, time related behavior of FDG was explored among plasma, non-metabolite and metabolic tissue compartments enabling absolute values, (ii) PET measurement was obtained 45 min after FDG injection that maintained the steady-state condition, (iii) In the steady state condition of 45 min after FDG injection, the error in the MRGlc would be minimum. In the scanning technique, single scan procedure was employed in which population average FDG kinetic rate constants were used instead of individual rate constants. Measurements of individual rate constants were difficult because dynamic PET measurement was not possible for all the organs due to limited axial field of view. The actual rate constants are not extremely different from the reported values incase of ARG method where dynamics of tissue radioactivities are not measured. Considering the above mentioned points, quantification approach in determining organ glucose metabolism would be satisfactory in the present FDG-PET technique.

Conclusion

In the present investigation, quantification method was applied to measure workloads induced organ glucose metabolism. We validated semiquantitative approach

(SUR) taking the absolute quantification method of glucose metabolic rate as a standard. However, some organ discrepancies between SUR and rMRGlc suggested the complexity in the energy metabolic control. Further investigations are necessary for this evaluation.

ACKNOWLEDGMENTS

This work was supported in part by a grant-in-aid (No. T Fujimoto) from the ministry of Education, Science, Sports and Culture, Japan. This work was also supported by the 13th Research-Aid Report in Medical Health Science of Meiji Life Foundation and Welfare, and by the Tohoku University 21COE Program "Future Medical Engineering Based on Bio-nanotechnology".

References

1) Fujimoto T., Itoh M., Kumano H. et al., Lancet. **48** (1996) 266.
2) Tashiro M., Fujimoto T., Itoh M. et al., J. Nucl. Med. **40** (1999) 70.
3) Iemitsu M., Itoh M., Fujimoto T. et al., Medicine & Science in Sports & Exercise**32** (2000) 2067.
4) Kemppainen J., Fujimoto T., Kari K.K., Viljanen T., Nuutila P. and Knuuti J., J. Physiol. **542** (2002) 403.
5) Sokoloff L., Reivich M., Kennedy C. et al., J. Neurochem. **28** (1977) 897.
6) Phelps M.E., Huang S.C., Hoffman E.J., Selin C., Sokoloff L., Kuhl D.E., Ann. Neurol. **6** (1979) 371.
7) Kelley D.E., Williams K.V., Price J.C., Amer. J. Physiol. **277** (1999) E361.
8) Kelley D.E., Williams K.V., Price J.C., Goodpaster B., J. Nucl. Med. **40** (1999) 1798.
9) Choi Y., Randall A.H., Huang S.C. et al., J. Nucl. Med. **35** (1994) 818.
10) Meszaros K., Lang C.H., Hargrove D.M. and Spitzer J.J., J. Appl. Physiol. **67** (1989) 1770.
11) Schwaiger M., Huang S.C., Krivokapich J., Phelps M.E. and Schelbert H.R., J. Amer. College Cardiol. **1** (1983)688 (abstract).
12) Ng C.K., Soufer R. and McNulty P.H., J. Nucl. Med. **39** (1998) 379.
13) Reivich M., Alavi A., Wolf A. et al., J. Cerebral Blood Flow & Metab. **5** (1985) 179.
14) Romijn J.A., Coyle E.F., Sidossis L.S., Gastaldelli A., Horowitz J.F., Wolfe R.R., Amer. J. Physiol. **265** (Endocrinology Metabolism 28) (1993) E380.
15) Ide K., Schmalbruch I.K., Quistorff B., Horn A. and Secher N.H., J. Physiol. **522** (2000) 159.
16) Exton J.H. et al., Diabetes Metabol. Rev. **3** (1987) 163.

TABLE-1: rMRGlc values in different organs at rest and 40% and 70% $\dot{V}O_2$max workloads.

	Thigh	Upper limb	Lumb/gluteal	Liver	Heart	Brain
Rest (n=6)						
1.	0.36	0.28	0.75	2.04	1.72	4.01
2.	0.28	0.31	0.87	2.19	1.52	4.11
3.	0.16	0.11	0.30	1.02	0.8	5.90
4.	0.16	0.09	0.36	1.05	1.56	3.81
5.	0.16	0.11	0.32	0.68	0.68	6.18
6.	0.15	0.11	0.27	0.86	0.51	4.40
Mean	**0.21**	**0.17**	**0.48**	**1.31**	**1.15**	**4.73**
S.D.	**0.08**	**0.09**	**0.26**	**0.64**	**0.50**	**1.03**
Exercise (n=5)						
40%$\dot{V}O_2$max						
1.	1.50	0.56	1.10	0.83	1.61	4.24
2.	2.07	0.69	0.66	1.33	1.68	5.38
3.	1.86	0.60	0.53	0.97	1.10	3.37
4.	1.67	0.91	0.64	1.09	0.83	4.19
5.	1.71	0.57	0.51	0.86	0.44	3.50
Mean	***1.76**	***0.66**	**0.69**	**1.02**	**1.13**	**4.14**
S.D.	**0.21**	**0.14**	**0.23**	**0.20**	**0.52**	**0.79**
70%$\dot{V}O_2$max						
1.	2.64	1.07	1.35	0.72	0.92	2.40
2.	2.56	1.12	1.25	0.59	0.94	3.68
3.	2.06	0.28	1.09	0.73	0.77	4.36
4.	2.35	0.23	1.02	0.71	0.89	2.73
5.	1.93	0.49	0.62	0.78	0.69	2.75
Mean	**§#2.31**	**#0.64**	**#1.07**	**0.71**	**0.84**	**#3.19**
S.D.	**0.30**	**0.43**	**0.28**	**0.07**	**0.11**	**0.81**

* P<0.05 (statistically significant; rest V.S. 40% $\dot{V}O_2$max)
\# P<0.05 (statistically significant; rest V.S. 70% $\dot{V}O_2$max)
§P<0.05 (statistically significant; 40% $\dot{V}O_2$max V.S. 70% $\dot{V}O_2$max).

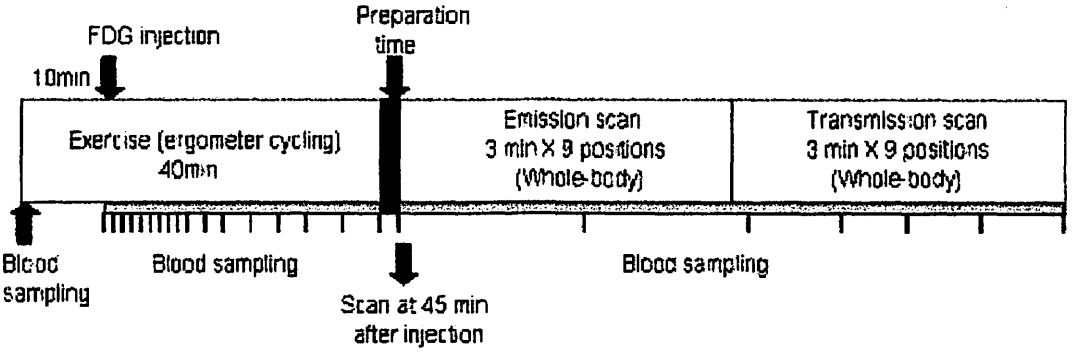

Fig. 1. Study design is illustrated schematically.

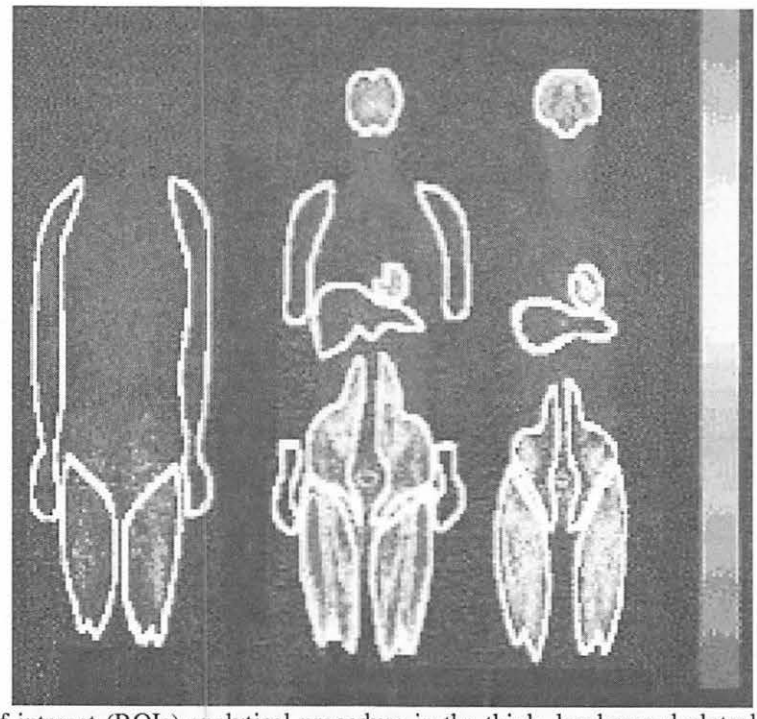

Fig. 2. Regions of interest (ROIs) analytical procedure in the thigh, lumbar and gluteal region, upperlimb, liver, heart, and brain are shown based on their anatomical locations and succeeding radioactivity distributions.

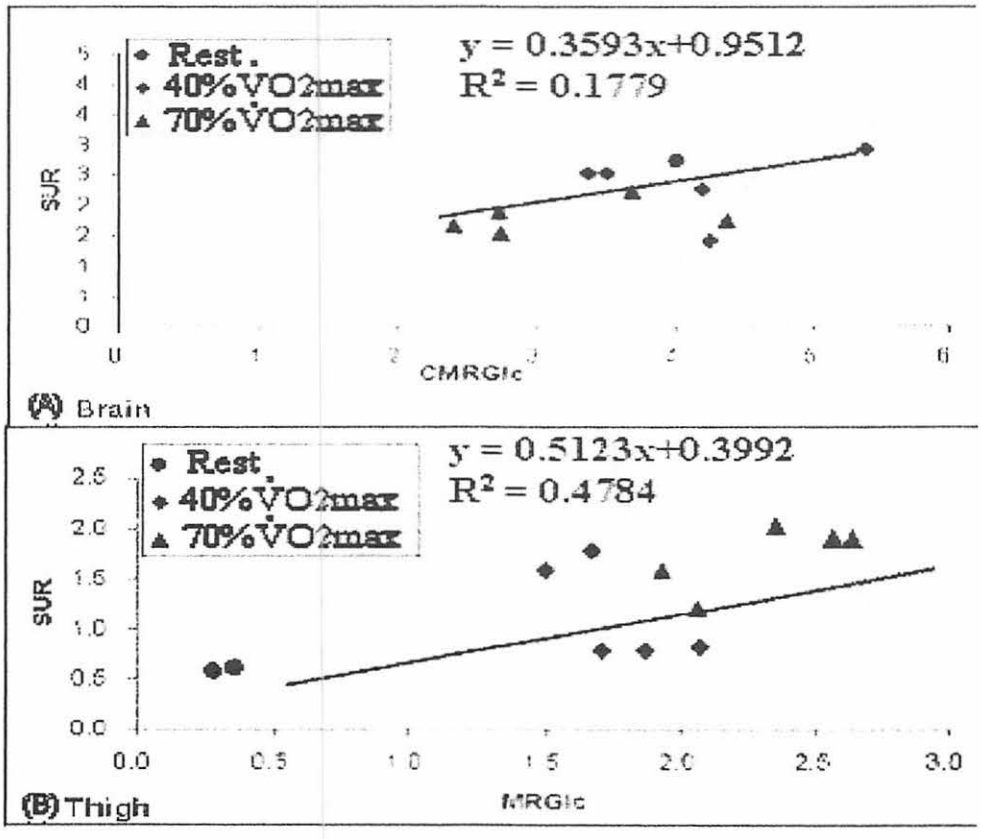

Fig. 3. The upper (A) and lower (B) figures demonstrated the correlation between SUR and MRGlc in the brain and thigh respectively.

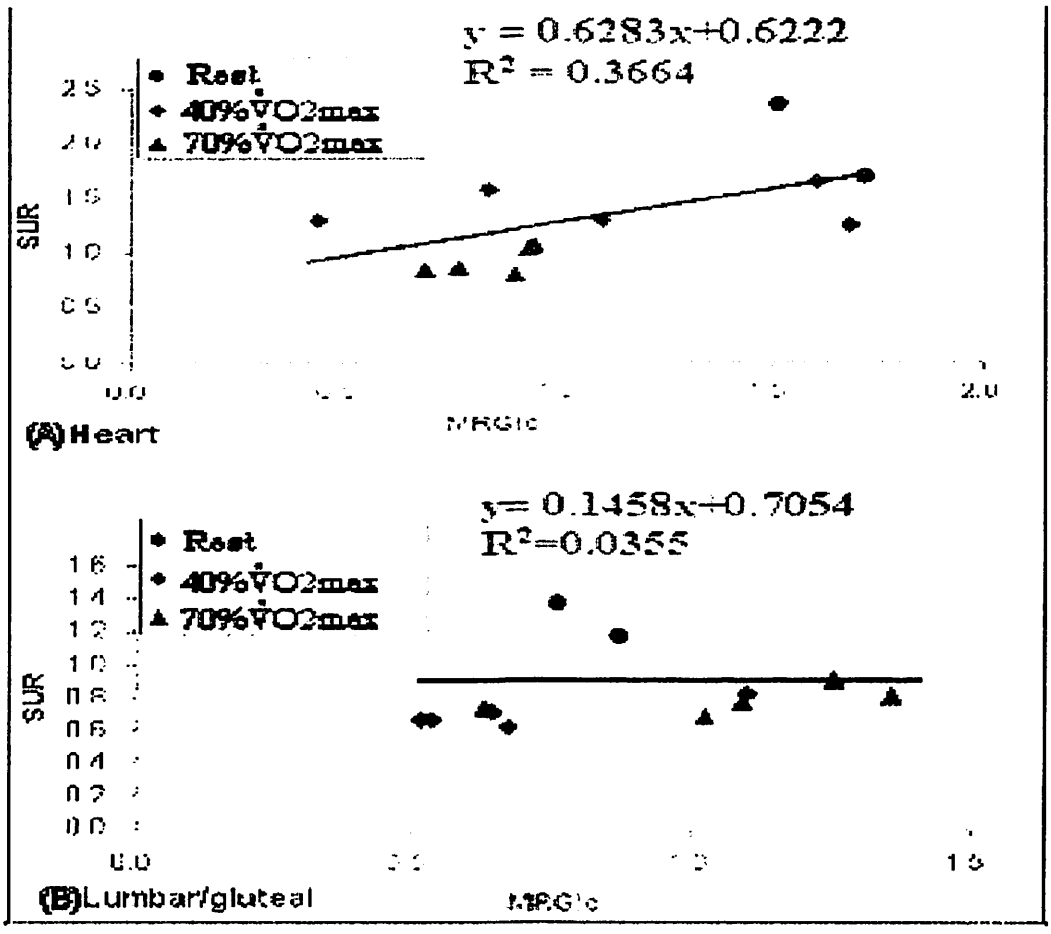

Fig. 4. The upper (A) and lower (B) figures demonstrated the correlation between SUR and MRGlc in the heart whether correlation was not suggestive in the lumbar/gluteal muscles.

VIII. 3. Functional Brain Mapping During Actual Car Driving: A FDG-PET Study

*Jeong M., Singh L.N., Yamaguchi K., Horikawa E.**, Tashiro M., Miyake M., Fukuda H.***, Iwata R.**, and Itoh M.*

Division of Nuclear Medicine, Cyclotron and Radioisotope Center, Tohoku University
Division of Radiopharmaceutical Chemistry, Cyclotron and Radioisotope Center, Tohoku University;*
*College of Medical Sciences, Tohoku University ***
*Institute of Development Aging and Cancer, Tohoku University****

INTRODUCTION

The invention of automobiles has provided high-speed travel on the ground, which requires processing of multimodal perceptions of sensory, visual, auditory, balance, and proprioceptive information. All of the information is constantly changing and needs to be revised in real time. In addition to sensory information processing, control of muscles is needed as well as referring to a space-map in memory. Despite this overwhelming amount of information to be processed and risks of car accidents, few people decide to abandon driving. This is because driving is not only convenient, but also a pleasure. All of these physical and psychological factors imply that the brain's role in driving is complicated but important.

Modern technology is being used to understand brain functions. Nuclear medicine techniques provide functional brain imaging using regional cerebral blood flow or metabolism as markers. However, imaging of brain function during car driving has been restricted due to technical limitations. Using an electroencephalogram (EEG) has been the only choice to record brain function on the road[1]. However, the low spatial resolution of EEG is not sufficient to localize brain activations related to driving.

Recently, Walter et al. employed functional MRI (fMRI) technique to map brain substrates engaged in driving simulations[2,3]. They found broad activations in occipital and parietal brain regions bilaterally. However, manipulating a driving simulator is not totally the same as actual car driving.

^{18}F-labeled-fluoro-deoxy-glucose (FDG) has been used for measurement of glucose

metabolism in the brain. FDG, which is trapped in the cells after conversion to FDG-6-phosphate by hexokinase, works as a molecular memory of cellular energy metabolism. The trapping phase lasts around 45 minutes after intravenous injection of FDG. Using this advantage, functional brain imaging is possible outside of laboratories. In this experimental design, we employed FDG-PET to visualize the roles of the brain during car driving.

MATERIALS AND METHODS

Thirty healthy male volunteers, all right-handed, aged 20 to 56 years, participated in this study. A written informed consent was obtained from each subject after full-explanations of the protocol. The study was approved by the Clinical Review Committee on Radioisotope Studies at Tohoku University Postgraduate Medical School. The volunteers were divided into three groups: (A) driving group; 10 subjects with mean age of 35.8 years (SD ±12.2) who drove on an ordinary road; (B) passenger group, 10 volunteers (34.8±13.1 years) participated as a passenger in the front passenger seat; and (C) control group, 10 volunteers (32.7±9.6 years), remained in a comfortable seat inside an experiment room.

The driving group drove a car with automatic transmission for 30 minutes around a university campus immediately after intravenous injection of ^{18}F-FDG, average 40.7 MBq (1.1 mCi). After micturition and preparation for a PET scan they were scanned with PET as described below. The same procedure was used for the passenger group, except that they sat silently facing forward beside the driver during driving. The control group were injected with FDG, average 40.7 MBq (1.1 mCi), and remained in a lit PET waiting room with their eyes open and without earplugs for the same period of time as the task groups. The driving route was in hilly suburbs with limited moving vehicles and a few traffic signals. The car speed was kept fairly constant at 40-km per hour. The driving route was not explained to the drivers beforehand but directed to the drivers on sites by an instructor sitting in the rear seat. Both the passengers and drivers were requested not to converse throughout the car ride.

Data Analyses

Driving-related brain activations were evaluated using the Statistical Parametric Mapping technique (SPM2, Wellcome Department of Cognitive Neurology, London, UK)[4,5]. Brain images were anatomically normalized to a standard brain template

(FDG-PET version adapted to the MNI-MRI template by Montreal Neurological Institute[6] by linear (Affine) and non-linear transformations to minimize inter-subject anatomical variations using a SPM routine. The brain images were then smoothed using a 11 mm isotropic 3D Gaussian filter to increase the signal to noise ratio. Indices of global activity were modeled as a confounding covariate (after normalization of the brain global value to 50 ml/100ml/min) using ANCOVA[7]. Linear contrasts were used to test for regionally specific condition-related effects, producing *t*-statistic maps in the Talairach standard space[8]. These *t*-statistics were transformed to corresponding Z maps, which constituted the statistical map (SPM {Z}). The peak voxel-based significance of statistics was chosen at $p < 0.001$ ($Z > 3.18$) without corrections for multiple comparisons.

RESULTS

The plasma glucose level of all subjects taken before FDG injection was within the normal range (101.2±9.4 mg/dl, mean±SD). When brain images in the driving group were compared with the resting group, significant activations were found in the primary and secondary visual areas, primary sensorimotor areas, parietal association areas (precuneus) and in the cerebellum (Table 1, Fig. 1A and 2). Activations were almost symmetrical between hemispheres. The comparisons between the passengers and the control groups identified similar brain areas as drivers in the motor, visual, and parietal areas but with little cerebellar activation (Table 2, Fig. 1B and 3). The direct comparison between the driver and the passenger groups identified only a part of the cerebellum, which was more active in the driver group than the passenger group.

DISCUSSION

As far as we know, no report has been published on the details of regional brain physiology during car driving or being a passenger on actual roads. Our results have confirmed activations of the visual and sensorimotor areas and parietal lobe by a car-driving task.

De Jong et al[9]. using a $H_2{}^{15}O$ activation study, reported areas of activation in the dorsal cuneus (area V_3), the latero-posterior precuneus (or superior parietal lobe), the occipito-temporal ventral surface, and fusiform gyrus during perception of forward motion. Similar brain areas were detected when subjects watched complex scenes on a monitor screen[10]. These brain areas were strongly activated in our study in both the drivers and

passengers. These remarkable activations in the visual areas supported our belief that perception and processing of visual information are essential components for car driving.

The posterior parietal cortex is thought to play a crucial role in the integration of limb (body) and field (visual) coordinates[11]. These areas were activated in our study. Sensory inputs from visual, somatosensory and vestibular systems need to be integrated before appropriate actions are made. The parietal cortex is regarded as an area for multimodal sensory integrations as seen in studies that showed a retina adjusting to visual inputs, both environmental world coordinates and body-oriented inner coordinates[12,13]. During driving the brain needs to calibrate and match visual images of the environmental space to the driver's egocentric coordinate continuously in real time. This collaboration is reportedly carried out in the posterior parietal cortex (BA 7)[14]. Previous brain mapping studies on limbs' movements disclosed that the primary somatosensory area and primary motor cortex were mostly responsible, but the premotor, supplementary motor areas and the parietal cortex aided them[15]. Therefore, the extensive brain activation in the parietal regions observed in our study reflects highly demanding data processing including the integrations and calibrations of multi-modal information, which is crucial for car driving.

Tashiro et al.[16] reported that activations of sensory brain areas including visual areas were more pronounced than those of motor areas in a running task using similar FDG brain mapping protocol. This agrees with previous observation that the sensory component of the neural processing circuitry was more energy demanding than the motor component in an ergometer task[17]. This sensory overload was confirmed during car driving also in this study.

Calhoun et al.[3] and Walter et al.[2], using simulated driving experiments, found similar activation sites as in this study; namely sensorimotor cortex and cerebellar regions. However, the visual cortices (BA 17/18) activation were not remarkable or found only by Calhoun et al.[3]. This suggests that visual stimulations were more pronounced in actual driving than simulated driving and that brain mapping by virtual driving experiments should be confirmed by an actual driving study.

In this experiment, regional brain metabolism was compared between conditions as a driver and a passenger. We could find similar brain activations in the visual areas because the subjects in both conditions saw exactly the same scenery. However, unexpectedly, the passengers showed similar brain activations in the motor areas despite the fact that they did not engage in any motor tasks. Activations in the parietal lobule were similarly active in the passenger group. These findings support the fact that the passengers

were not at rest during car driving but were engaged in virtual car driving beside the driver. In the case of drivers, the pattern of regional brain metabolism was clearly contrasted, e.g., activations in the motor and parietooccipital brain areas with deactivations in the prefrontal and temporal brain. This contrast was similar but less in the passenger group. A possible explanation for this difference between drivers and passengers is the level of concentration between the two groups.

CONCLUSION

This study demonstrated how the brain works while driving or being a passenger. The results suggested that visual perception and its integration with motor control were the main brain functions while driving. FDG technique is useful for brain mapping while subjects are performing daily activities.

REFERENCES

1) Miller J.C., Biomed Sci. Instrum. **34** (1997) 93.
2) Walter H., Vetter S.C., Grothe J., Wunderlich A.P., Hahn S., Spitzer M., Neuroreport **13** (2001) 1763.
3) Calhoun V.D., Pekar J.J., McGinty V.B., Adali T., Watson T.D., Pearlson G.D., Hum Brain Mapp. **16** (2002)158.
4) Friston K.J., Frith C.D., Liddle P.F., Frackowiak R.S., J. Cereb. Blood Flow Metab. **11** (1991) 690.
5) Friston K.J., Ashburner J., Frith C.D., Poline J.B., Heather J.D., Frackowiak R.S. J., Hum Brain Mapp. **3** (1995) 165.
6) Evans A.C., Collins D.L., Milner B., J. Soc. Neurosci. (Abstr) **18** (1992) 408.
7) Friston K.J., Frith C.D., Liddle P.F., Dolan R.J., Lammertsma A.A., Frackowiak R.S., J. Cereb. Blood Flow Metab. **10** (1990) 458.
8) Talairach J., Tournoux P., Co-Planar Stereotaxic Atlas of the Human Brain. 3-Dimenstional Proportional System: An Approach to Cerebral Imaging (Translated by M. Rayport). Thieme, New York. 1988:1-122.
9) De Jong B.M., Shipp S., Skidmore B., Frackowiak R.S., Zeki S., Brain **117** (1994) 1039.
10) Menon V., White C.D., Eliz S., Glover G.H., Reiss A.L., Hum Brain Mapping **11** (2000) 117.
11) Kertzman C., Schwarz U., Zeffiro T.A., Hallett M., Exp. Brain Res. **114** (1997) 170.
12) Kawashima R., Roland P.E., O'Sullivan B.T., Cereb. Cortex. **5** (1995) 111.
13) Hasselbach-Heitzeg MM, Reuter-Lorenz PA., Neuropsychologia. **40** (2002) 1822-33.
14) Duhamel JR, Colby CL, Goldberg ME., Science. **255** (1992) 90-92.
15) Colebatch JG, Deiber MP, Passingham RE, Friston KJ, Frackowiak RS. J Neurophysiol. **65** (1991) 1392-401.
16) Tashiro M., Itoh M., Fujimoto T., Fujiwara T., Ota H., Kubota K., Higuchi M., Okamura N., Ishii K., Bereczki D., Sasaki H., J Sports Med Phys Fitness. **41** (2001) 11.
17) Herholz K., Buskies W., Rist M., Pawlik G., Hollmann W., Heiss W.D., J Neuro 234 (1987) 9.

Table 1. Brain areas activated by driving.
The main effect of driving was tested by inter-group comparison between the driving group (n = 10) and a resting control group (n = 10).

Region	Brodmann's area	side	Talairach coordinates at peak activation x	y	z	Z-score
Cuneus	18	left	-2	-77	8	5.51
Cuneus	17	left	-12	-98	-2	5.01
Cerebellum		right	22	-51	-24	4.71
Gyrus fusiformis	18	left	-18	-91	-12	4.69
Gyrus postcentralis	4	right	38	-27	57	4.20
Gyrus occipitalis medius	18	right	32	-90	1	4.19
Gyrus fusiformis	19	right	30	-48	-8	4.02
Gyrus occipitalis inferior	18	right	22	-89	-9	3.97
Gyrus temporalis medius	39	right	36	-68	20	3.81
Precuneus	7	left	-10	-49	63	3.67
Precuneus	18	right	24	-78	28	3.57
Gyrus occipitalis medius	18	right	38	-90	-16	3.54
Gyrus precentralis	4	left	-10	-22	64	3.40
Gyrus postcentralis	3	left	-44	-18	52	3.40
Thalamus		right	16	-17	1	3.36
Gyri occipitales	18	left	-28	-77	1	3.31
Gyrus cinguli	24	right	10	-7	41	3.27
Gyrus parahippocampi	35	left	-18	-36	-2	3.18

The statistical threshold is $P < 0.001$ (uncorrected)

Table 2. Brain areas activated by being a passenger.
The main effect of passenger was tested by inter-group comparison between the passenger group (n = 10) and a resting control group (n = 10).

Region	Brodmann's area	side	at peak activation x	y	z	Z-score
Gyrus lingualis	18	right	8	-76	4	4.84
Gyrus occipitalis medius	18	right	34	-93	-1	4.61
Gyrus fusiformis	18	left	-20	-90	-12	4.43
Cuneus	17	left	-8	81	7	4.43
Gyrus occipitalis inferior	18	right	30	-88	-12	4.42
Gyrus fusiformis	19	left	-22	-58	-12	3.98
Cerebellum		left	-24	-59	-12	3.90
Gyrus lingualis	19	left	-14	-43	-1	3.83
Precuneus	7	left	-4	-54	51	3.79
Gyrus temporalis medius	19	right	38	-73	22	3.58
Cuneus	18	right	16	-98	20	3.51
Gyrus precentralis	4	right	36	-28	64	3.47
Gyrus fusiformis	37	right	30	-48	-8	3.31
Gyrus postcentralis	3	right	42	-15	62	3.23

The statistical threshold is $P < 0.001$ (uncorrected)

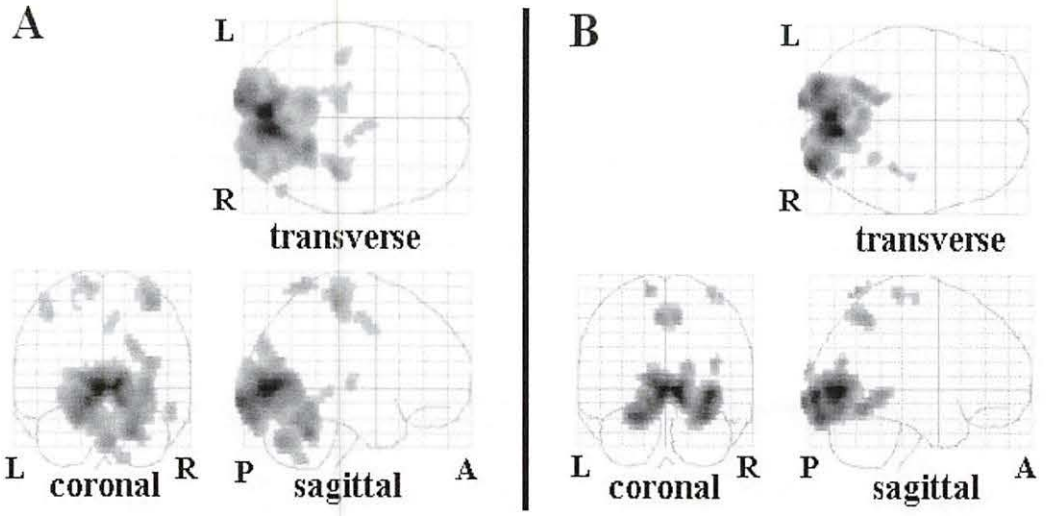

Fig. 1. The main effects of driving(A) and passenger groups(B) with resting control group as a reference tested using SPM2. Activations in the bilateral primary and secondary visual areas were most notable in the both conditions. Cerebeller activations were found in the driving condition only. The activation sites are displayed in three orthogonal directions, sagittal (top left), coronal (top right), and transverse (bottom), thresholded at $Z > 3.18$, $k > 20$ pixels (160 mm^3), $p < 0.001$ (uncorrected).

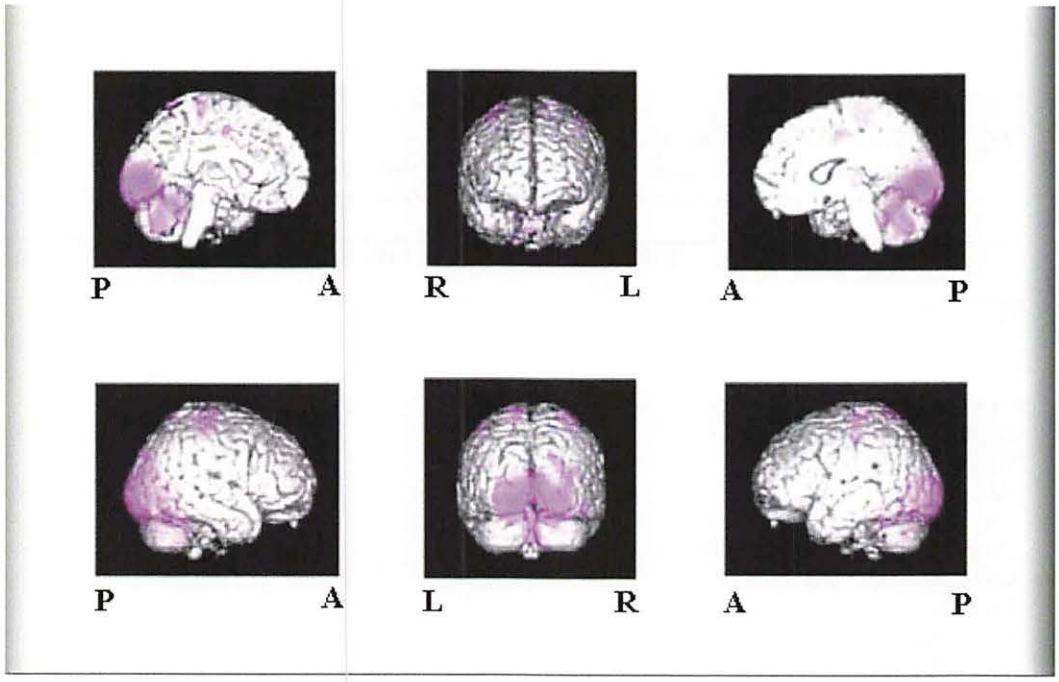

Fig. 2. Brain images for the main effects of driving which is the contrast between driving and resting conditions ($Z > 3.18$, $k > 20$, $p < 0.001$ uncorrected) rendered on a standard brain template. The data are same as in Fig.1A. From the left top to the right bottom panel, left medial, frontal, right medial, right lateral, occipital, and left lateral surface.

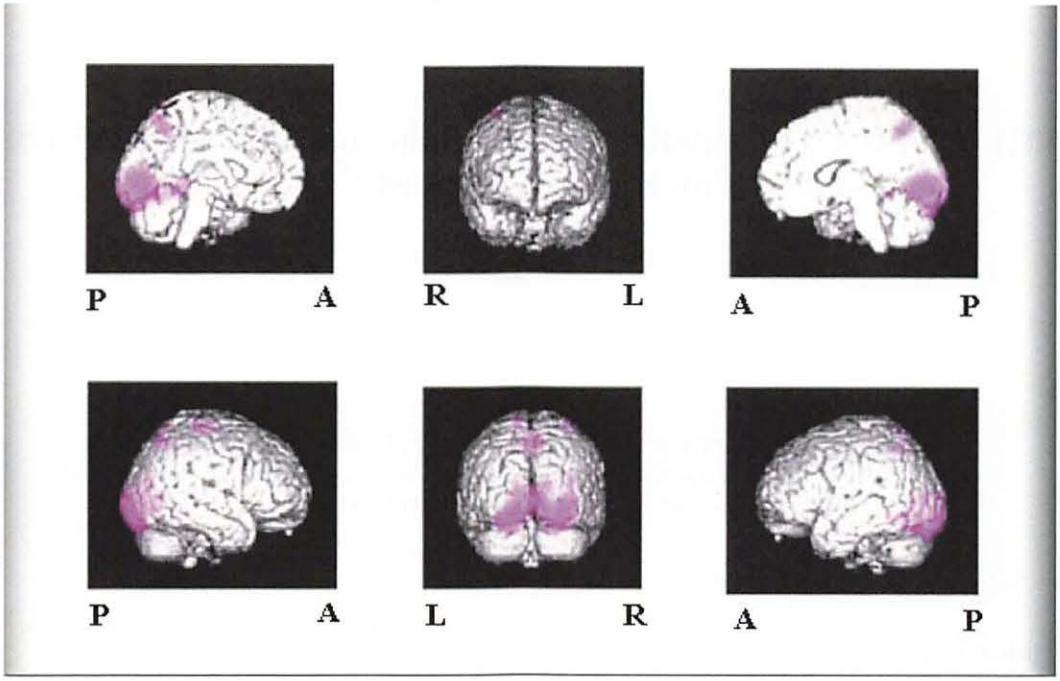

Fig. 3. Brain images for the main effects of being a passenger ($Z > 3.18$, $k > 20$, $p < 0.001$ uncorrected) rendered on a standard brain template. The data are same as in Fig.1B.

VIII. 4. Effects of Sedative Antihistamines on the Regional Cerebral Blood Flow During Simulated Car Driving

Sakurada Y., Tashiro M., Mochizuki H., Horikawa E.[*], *Okamura N., Itoh M.*[**], *and Yanai K.*

Departments of Pharmacology, Tohoku University Graduate School of Medicine
Center for Comprehensive and Community Medicine, Faculty of Medicine, Saga University [*]
Division of Nuclear Medicine, Cyclotron and Radioisotope Center [**]

Introduction

Histamine H_1 receptor antagonists (antihistamines) are widely used for treatment of allergic disorders and are well-known for central nervous system (CNS) side effects such as drowsiness, sleepiness and impaired psychomotor performance[1]. Car driving is closely connected with our everyday life. There are so many reports about the effects of antihistamines on car driving performance but its mechanism has not been demonstrated yet. Recently, some functional MRI (fMRI) studies have been published on brain activities during simulated car driving[2,3,4]. Walter and colleagues revealed that the regional cerebral blood flow (rCBF) increased in the sensorimotor cortex and the cerebellum, by comparing active and passive driving conditions. Calhoun and colleagues demonstrated that car driving was able to be divided into several basic componentsand that fMRI was useful to investigate the neural correlates of car driving. However, there was no functional neuroimaging study on the drug-induced sedation during car driving. So we investigated the rCBF changes during simulated car driving after oral administration of d-chlorpheniramine, a sedative antihistamine, by positron emission tomography (PET) with $H_2{}^{15}O$.

Materials and Methods

Subjects

Fourteen healthy male volunteers, ranging 20-25 years old (mean +/- SD: 21.9 +/- 1.8), participated in the present study. All subjects were evaluated as right-handed based on the Edinburgh inventory and Chapman test. Mean driving history of all the subjects

was 17 months. Written informed consent was obtained from each subject and the study was performed in compliance with the relevant laws and institutional guidelines.

Study design

The present study was conducted as a single-blind crossover study. The subject was given one of a d-chlorpheniramine 6 mg repetab (Polaramin) or a placebo in each study. According to the previous report, it was estimated that the peak plasma drug concentration of orally-administered d-chlorpheniramine was achieved at 2 hours post-administration. Then, the PET investigation started approximately 2 hours after oral administration of d-chlorpheniramine 6 mg and so did it for placebo.

PET scans were performed for the following three conditions: 1) resting condition with the eyes closed, 2) active driving condition where the subjects had to drive by their own, using a steering wheel and accelerating pedal, and 3) passive driving condition where the subjects were requested to watch the changing landscape that had been videotaped, with the both hands fixed on the handle and with the right leg kept on the accelerating pedal.

Driving simulation

Commercially available software (Gekisoh 99, Twilight Express Co., Tokyo, Japan) was used for simulated driving task. The subjects were positioned in a PET scanner, wearing a head mount display (HMD: Glasstron PLM-A35, SONY, Tokyo, Japan) in a comfortable manner. They were able to operate the steering wheel and press the accelerating pedal quickly while watching landscape of driving course projected onto the HMD.

PET measurements and data analysis

The rCBF images were obtained using a 3D-acquisition PET scanner (SET 2400W, Shimadzu Co. Ltd., Japan), with an average spatial resolution of 4.5 mm the full-width half-maximum and with a sensitivity of a 20 cm cylindrical phantom of 48.6 k.c.p.s. $KBq^{-1}ml^{-1}$. PET acquisition was performed for the duration of 70 sec. The subject was injected with $H_2{}^{15}O$ of 157.8 ± 25.6 MBq (5.8 ± 0.9mCi) through the antecubital vein for each scan.

The rCBF images obtained were realigned, normalized and smoothed by Statistical Parametric Mapping (SPM) software (SPM99; Welcome Department of Cognitive Neurology, London, U.K.). T-Statistics were computed for each voxel for the

comparisons: 1) active driving condition or passive driving condition scan minus resting condition scan after oral administration of placebo or d-chlorpheniramine, 2) after oral d-chlorpheniramine minus placebo in condition of active driving scan. For each comparison, each voxel difference with Z-value higher than 3.01, corresponding to $p < 0.001$ (uncorrected), was considered as significant changes in rCBF.

Results

After oral administration of placebo, the significant increase of rCBF was found in the sensorimotor (Brodman Area: BA 4), premotor (BA6), parietal (BA 7, 40), temporal (BA 37), occipital (BA17-19) cortices and in the cerebellum, midbrain, pulvinar, globus pallidus medialis and cingulated gyrus during active driving compared with the resting condition (Fig. 1). And the regions of increased CBF during active driving in comparison to the passive driving condition were nearly the same. Compared to placebo, d-chlorpheniramine produced significant increase of rCBF in the cerebellar vermis and decrease of parietal (BA 7), temporal (BA 37), occipital (BA 19) cortices and cerebellum hemisphere during active driving.

Discussion

Car driving is closely connected with our everyday life and needs integration of various brain functions such as attention to other vehicles and walkers, circumstantial judgment, motor programming and output, working memory, etc. It is well-known that antihistamines, especially first generation antihistamines, have sedative side effects. These side effects are dangerous especially during operating a machine or driving a car. The sedative antihistamines are available more easily as over-the-counter drugs than newer less sedating antihistamines. There are various methods to evaluate driving performance after administrating sedative drugs such as subjective sleepiness, reaction time, EEG changes, vehicle maintenance capability, during both actual and simulated driving.

Walter and colleagues first measured the regional brain activity in healthy volunteers during simulated driving using fMRI[2]. They detected the brain activation mainly in the visual and somatosensory cortices and in the cerebellum by contrasting active and passive driving conditions. It has been demonstrated functional neuroimaging is a very useful tool to elucidate neural correlates of driving. In the present study, the contrast between active and resting conditions and that between active and passive conditions both

demonstrated similar results to the previous fMRI study by Walter and colleagues[2]. Taking all these findings together, it could be concluded that $H_2{}^{15}O$-PET gives basically the same results as those obtained with fMRI.

On the other hand, rCBF responses were reduced after administration of d-chlorpheniramine in the parietal (BA 7), temporal (BA 37), occipital regions, that are considered to be the visuo-spatial pathway. The results might suggest that d-chlorpheniramine tends to suppress mainly visuo-spatial function during simulated driving.

References

1) Adelsberg B.R., Arch. Int. Med. **157** (1997) 494.
2) Walter H., Vetter S.C. and Wunderlich A.P., Hahn S., Spitzer M., Neuroreport **12** (2001) 1763.
3) Calhoun V.D., Pekar J.J., McGinty V.B., Adali T., Watson T.D. and Pearlson G.D., Hum. Brain Mapping **16** (2002) 158.
4) Uchiyama Y., Ebe K., Kazato A., Okada T. and Sadato N., Neurosci. Lett. **352** (2003) 1999.

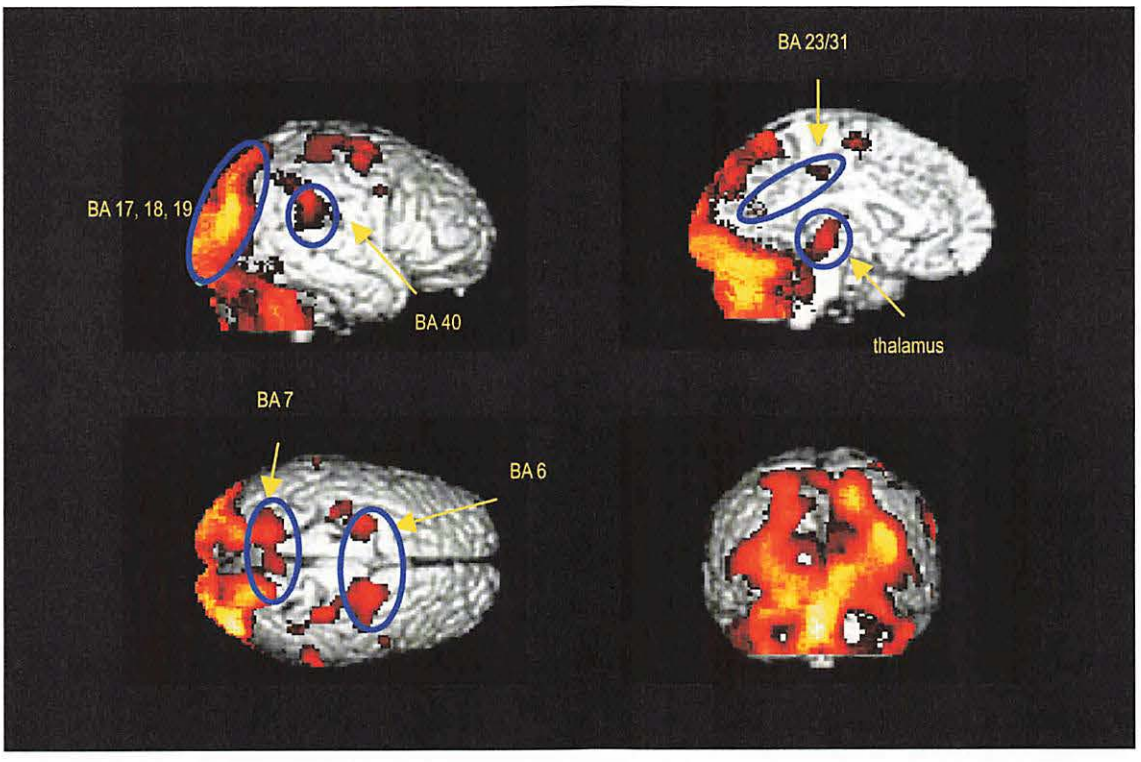

Fig. 1. The significant increase of rCBF during active driving compared with resting condition after oral administration of placebo.

VIII. 5. Metabolic Correlations Between Muscle and Brain at Exercise

Sabina K., Fujimoto T., Ishii K.*, Yamaguchi K., Watanuki S., Miyake M., and Itoh M.*

Division Of Nuclear Medicine, Cyclotron and Radioisotope center, Tohoku University,
Department Of Medicine And Science In Sports And Exercise, Postgraduate School Of Medicine,
*Tohoku University**

Introduction

In recent days, functional neuroimaging in vivo has increasingly become a focus of interest in brain science. Central motor controls have been extensively studied using animals as well as human. Conversely, exercise itself is an important factor that can alter the brain functions not only related to the movement control but also due to neuropsychological consequence such as fatigue. Therefore regional brain activities related to intensive exercise are the main topics of this study. The ergometer cycling (stationary cycling) in contrast to the other forms of locomotion can be performed by forward pedaling with only minor dislocation of the body and head in space. We chose this exercise as a tool to map exercise related brain activities because the measurement of the work force is quantitatively available. Previously, Mishina et al.[1] measured cerebellar glucose uptake before and after walking in patients with neurological disorders while regional metabolic changes in the brain were investigated for outside running by Tashiro et al[2]. In the present study FDG-PET study was conducted to clarify the functional metabolic changes in local brain induced by ergometer movements at three loads of intensities. FDG-PET technique is particularly useful for metabolic studies during exercise. Using trapping nature of the tracer substrate, exercise could be loaded outside of PET examining room. However, the motive of this study was to identify global value corrected glucose metabolic changes in cerebral regions induced by different loads of ergometer exercise.

Subjects and methods

Seventeen healthy volunteers were divided into two groups, task group were participated in ergometer cycling at 40%, 70%, 80% VO2max on separate days and the resting control group who sat on an ergometer without pedaling in a lit room. A total of 35 minute ergometer cycling was done after FDG administration followed by emission and transmission scans with a multi-ring tomography, SET-2400 (Shimadzu, Japan) in three-dimensional data acquisition mode. PET scanner. The overall time for study was 110minutes from the tracer injection. To explore the regional changes between exercise task and resting control, voxel based statistical parametric technique was applied using the SPM 2[3,4] software for both analyses. A custom made FDG template was used for the anatomical normalizations applying smoothing using a 12-mm isotropic Gaussian filter kernel to increase the signal to noise ratio. Statistical analysis was performed by choosing the (1) covariate only analysis to find out the linearly increased metabolic regions with loads and (2) multiple conditions analysis to discriminate the variation with loads of SPM 2 applying the significant threshold at $p<0.001$ (extended voxel threshold was 20) without correction for multiple comparisons. Location of each statistical peak was identified based on a co-planar stereotaxic atlas of the human brain[5].

Results

The voxel based covariate search between FDG uptake and the loads of exercise (from rest to mild, moderate and severe intensity) showed a strong and highly significant activated linearly increased metabolism as shown in Figure 1. Maximum peak of activations with loads was found in precental gyrus (BA 4) bilaterally. Other regions were found in superior parietal lobe (BA 5), cerebellum, medial frontal gyrus (BA 9) and insula. All areas were statistically significant only in left hemisphere, except precenal gyrus and insula. Inferior parietal gyrus (BA 40) and Post central gyrus of occipital cortices (BA 3) were also significant but the activations clusters were relatively small (< 20voxels). Linear decrease or non-linear changes in response to the increasing movement loads were found mostly in posterior part of the brain. Discriminations between three load effects.

When mild task compared with control, maximum intensity was found in superior parietotemporal cortex (BA 7 and 22). Other regions were activated in precentral gyrus (BA 4) and inferior frontal gyrus (BA 46). Cingulated cortex was also activated but cluster was too small.

Moderate task induced brain regions activated were in cerebellum, middle frontal gyrus (BA 6 and 8), precental gyrus (BA 4), angular gyrus (BA 39), supramarginal gyrus (BA 40), lingual gyrus (BA 18) and postcentral gyrus (BA 5). Primary motor region and limbic lobe are significant only in right hemisphere where as parietal activations were prominent in left side.

When severe exercise group compared with the resting control, the maximum activations were found in frontal gyrus (BA 6, 8, 9). Other regions activated for this loads were cerebellum, cingulated gyrus (BA 32), angular gyrus (BA 39), postcentral gyrus (BA 5). Medial and superior part of frontal gyrus and cingulate gyrus activated bilaterally. Precentral gyrus, middle frontal gyrus and lingual gyrus activated only in right hemisphere.

Discussions

We confirmed that using an imaging approach brain activations associated with exercise were identified in the motor, premotor and sensory areas when the task group was compared with the resting control group. The highest activity was noted in the superior temporoparietal association cortex for the mild task condition while moderate load induced peak activation in the cerebellum. Intensive task induced extended and strong activations in the primary motor, sensory and association motor cortex as well as in the cerebellum with the maximum activation in the frontal gyrus. The supplementary motor area was active for all loads. Other regions such as inferior frontal gyrus was activated only by light load while medial frontal activation was noted for severe task condition only. These results clearly showed that regional brain activations were dependent on the exercise loads.

Activations in the primary motor cortex were observed during rhythmic cycling movement of all intensities. Previously it has been demonstrated with oxygen 15-labelled H_2O PET study for active and passive bicycling that M1 activation was positively correlated with the rate of active bicycling[6]. Williamson et al[7] made a similar observation using single photon emission computed tomography (SPECT). Although these authors focused on the insular cortex, they also noted activations in the leg area of the primary motor cortex. Our findings and those of other groups demonstrate that there is a significant cerebral involvement in the control of rhythmic movements in man. Linear relationships between the ergometer task loads and activations in the primary motor cortex suggest that the intensity of the movement may be coded here that was established by the previous study with bicycle movement by Christensen et al.

Primary motor and premotor areas of the frontal lobe of the primate brain most directly associated with planning and executing voluntary movements. Parietal cortex is richly interconnected with these two regions through which it receives information about the status of joints and muscles. For example, the parietal cortex is selectively activated under certain experimental conditions as the subjects must always refer to visual inputs to an internal spatial map in body-oriented co-ordinates[8]. We noted peak activation in superior part of parietal cortex for mild load only. However, higher loads also significantly activated in parietal cortices but did not show maximum accumulation. The increased high glucose metabolism with rising loads and variation within regions with loads may be well explained by earlier study related with different movements. Previously it was demonstrated that parietal regions showed peak activation for a running case (supposed to be mild load) by Tashiro et al. Additionally, prefrontal activation found alone by mild exercise suggested that cognitive participation could be come to mind during easy task but hard task demand concentrate only to work.

Thus the present study successfully visualized the state of brain engaged at different exercise loads by the FDG method. Global corrections revealed stronger activations in cerebral regions associated with movement compared to control. The precise role of the cerebeller activation in relation to muscle movements, however, still needs to be resolved.

References

1) Mishina M., Senda M., Ohayama M., Ishii K., Kitamura S. and Terashi A., Rinsho Shinkeigaku **35** (1995) 199 (in Japanese).
2) Tashiro M., Itoh M., Fujimoto T., Fujiwara T., Ota H., Kubota K., Higuchi M., Okumura N., Ishii K., Berezeki D. and Sasaki H., J. Sports Med. Phys. Fitness **41** (2001) 11.
3) Friston K.J., Holmes A.P., Worsley K.J., Poline J.P., Frith C.D. and Frackowiak R.S.J., Human Brain Mapping **3** (1995) 189.
4) Friston K.J., Ashburner J., Holmes A. and Poline J., (2002) Statistical Parameteric Mapping [http://www.fil.ion.ucl.ac.uk/spm/].
5) Talairach J.and Tournoux P., Co-planar Stereotaxic atlas of the human brain. Stuttgart: George Thieme Verlag (1988).
6) Christensen L.O., Johannsen P., Sinkjaer T., Petersen N., Pyndt H.S. and Nielsen J.B., Exp. Brain Res. **135** (2000) 66.
7) Williamson J.W., Nobrega A.C., McColl R., Mathews D., Winchester P., Friberg L. and Mitchell J.H., J. Physiol. **503** (1997) 277.
8) Kawashima R., Roland P.E. and O'Sullivan B.T., Cerebral Cortex **5** (1995) 111.

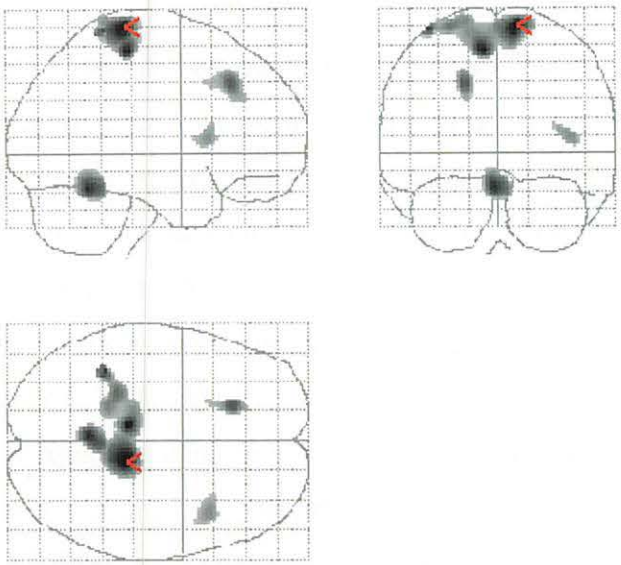

Figure 1. Linearly increased activations with the task load at $p<0.001$ with extended voxel threshold 20.

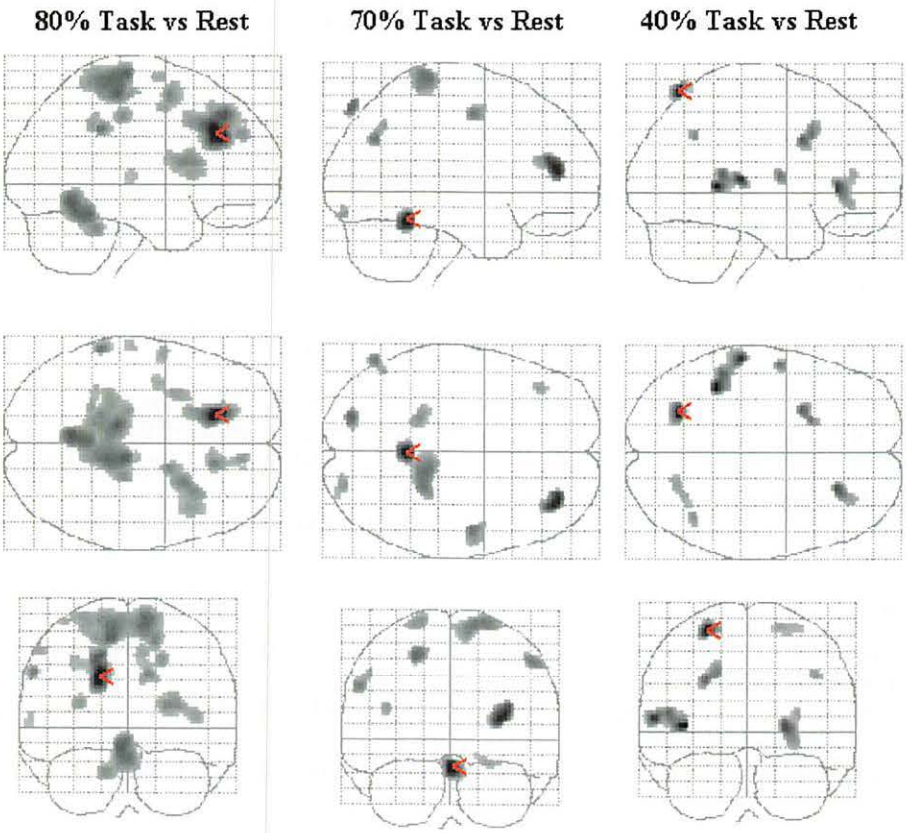

Figure 2. Regional brain activations by three loads of exercise comparing with the control at $p<0.001$ with extended threshold voxel 20.

VIII. 6. Sedative Profiles of Second-generation Antihistamines

Tashiro M.[*], *Iwabuchi.*[*], *Sakurada Y.*[*], *Mochizuki H.*[*], *Kato M.*[*], *Horikawa E.*[**], *Funaki Y.*[**], *Iwata R.*[**], *Itoh M.*[**], *and Yanai K.*[*]

Dept. Pharmacology, Tohoku Univ. School of Medicine, Sendai,
Cyclotron and Radioisotope Centre, Tohoku Univ., Sendai,
Centre for Comprehensive and Community Medicine, Saga Univ.,
School of Medicine, Saga, Japan

Introduction

Effective and safe treatments are required to relieve symptoms and improve the health-related quality of life of the millions of individuals who suffer from allergic symptoms[1]. Oral antihistamines represent a mainstay of treatment because of their potent inhibition of the allergic response. However, many antihistamines are associated with central nervous system (CNS) effects because of their lack of exclusive selectivity for the H_1-receptor and their capacity to penetrate the blood-brain barrier (BBB)[2]. Sedation and psychomotor impairment associated with antihistamines can have serious safety implications. The performance of everyday activities, such as car driving, in addition to tasks that require high levels of concentration, can be impaired after the administration of some antihistamines, with subsequent potentially serious, even fatal, consequences[3]. It is accepted that older-generation antihistamines have sedative and impairing effects at recommended doses, which prompted the development of newer agents devoid of such effects. However, newer-generation antihistamines are associated with divergent sedative profiles, so there remains a need to establish reliable and sensitive tests to evaluate this property[2].

This study was once reported as a work in progress and this time the complete results are reported here. This study employed a variety of tests to examine their relative sensitivity and to establish the sedative profiles of three antihistamines – hydroxyzine (HYD; verum control), cetirizine (CET) and fexofenadine (FEX) – compared with placebo. Written informed consent was obtained from all study participants. Study subjects were assessed in terms of: How sleepy they felt and how their performance was objectively

impaired using a series of laboratory tests (Study 1). How their performance was impaired in a 'real-life' scenario, using a car driving test (Study 2). The extent to which antihistamines bound to cerebral H_1 - receptors using positron emission tomography (PET) (Study 3). Studies 1 and 2 were conducted at CYRIC, Tohoku University.

Materials and Methods

Study 1: A total of 20 healthy adults males (mean age 23.1 ± 2.8 years) were recruited into this double-blind, placebo- and verum-controlled study. Subjects were randomized to receive FEX 120 mg, CET 20 mg, HYD 30 mg and placebo in a crossover fashion. Subjective sleepiness was assessed using the Stanford Sleepiness Scale (SSS). This test was performed before and at 90 minutes after study drugs were administered, at which point visual cognitive function tests were also performed. The visual cognitive function tests were analyzed using two variables: (1) reaction time (RT) and (2) correct answer rate (AR). Both RT and AR were obtained for each subject who each performed a series of six tests.

In the first test (choice reaction time: CRT), subjects were presented with an image to the left or right of a screen and were asked to respond by pressing the left-hand button if the image was on the right, and vice versa. Similar to the CRT, the simple reaction time test (SRT) involved the random presentation of images on the screen, to which the subject was asked respond by pressing the right-hand button as quickly as possible. The third test, comprising four different subtests, was a visual discrimination task (VDT). A total of 120 images were presented with different exposure durations such as 3, 5, 7 or 20 msec and subjects were asked to respond only when figures, not letters were presented.

Study 2: A total of 18 healthy adults males (mean age 23.4 ± 1.6 years) were recruited into this double-blind, placebo- and verum-controlled crossover study. Each subject was administered FEX 120 mg, HYD 30 mg (verum control) and placebo and asked to perform a series of car braking tests using a system provided by Prof. Hindmarch (Human Psychopharmacology Research Unit, Surrey Univ., UK) with agreement of his group. Subjects were asked to press a brake pedal when a light on the bonnet was lit, a process which occurred 25 times at random intervals during each test. The brake reaction time (BRT) and subjective sleepiness were measured for each individual during each test. Tests were performed before and at 90 and 240 minutes after administration. During each test, subjects inserted an earphone to enable them to talk on a mobile phone. The four test

driving conditions for BRT were when:

1) Not talking on mobile phone while driving,

2) Driving and answering simple arithmetic questions on the mobile phone,

3) Driving and answering complex arithmetic questions on the mobile phone,

4) Driving and answering questions on a specific theme (such as a favorite movie).

Study 3: Eleven healthy males (mean age 23.1 ± 2.8 years) underwent brain positron emission tomography (PET) after randomization to receive either FEX 120 mg or CET 20 mg. Dynamic scanning of each subject was performed for 90 minutes, starting at 90 minutes after drug administration (corresponding to the Tmax of the agents), at which point subjects were also administered intravenous ^{11}C-doxepin, a selective radioligand for the H_1-receptor. To calculate the H_1-receptor occupancy (H_1RO) of each drug, the binding potential (BP; Bmax/KD) of each agent in each region of interest (ROI) in the brain was calculated, as described elsewhere[4,5]. BP images were created, from which H_1RO was calculated for the frontal cortex, anterior cingulate gyrus, temporal cortex, parietal cortex and occipital cortex, using the mean BP values of placebo condition obtained in other additional subjects. The H_1ROs of FEX and CET were calculated using the following equation:

H_1RO = [(mean BP of control – mean BP with each drug)/mean BP of control] x 100.

Results

Study 1: As for the change in mean RT before and after medication (Figure 1), in five of six cognitive tasks, HYD was significantly more impairing than placebo. FEX did not differ significantly from placebo in terms of impairment. CET was significantly more impairing than FEX in CRT test (p=0.008). The results of AR showed similar tendency. As for subjective sleepiness, FEX resulted in indistinguishable sleepiness compared with placebo. Trends towards increased sleepiness with HYD and CET compared with placebo and FEX were observed, although these did not reach statistical significance. In addition, increased sedation was reported with CET compared with FEX in one task.

Study 2: Significant sedation was observed with HYD at 90 and 240 minutes after administration, as assessed by the SSS (p=0.017 and p=0.003 versus placebo, respectively). No significant subjective sedation was observed with FEX compared with placebo (Figure 2) (p>0.05). At 240 minutes, HYD significantly prolonged BRT compared with

placebo under all test conditions except when driving but not talking on the mobile phone ($p<0.05$). At 240 minutes, HYD prolonged BRT significantly compared with FEX when driving and performing simple arithmetic, and when driving and talking on a mobile phone ($p<0.05$). Interestingly, prolongation in BRT seems more influenced by a dual task situation caused by cellular phone talks during driving than an administration of HYD, a sedative drug (Figure 2).

Study 3: Sample PET scans of an individual subject are shown (Figure 3). The brighter the region, the greater the concentration of free H_1-receptors to which ^{11}C-doxepin molecules bind, or the lower the concentration of antihistamine penetrating BBB. CET binds more readily to cerebral H_1-receptors than either FEX or placebo, as evidenced both from the PET images and the H_1RO calculations. CET was observed to occupy H_1-receptors in the cerebral cortex (20 to 30%). In contrast, FEX occupied receptors in the cerebral cortex to lesser extent (0 to 5.6%).

Discussion

The twin purposes of performing and comparing the three different studies were to evaluate the relative sensitivities of each test to detect impairment by antihistamines and to explore the impairment profiles of FEX, CET and HYD. The results of Study 1 demonstrate that evaluation of subjective sleepiness using the SSS sometimes cannot distinguish clearly between the known sedative effects of the positive control, HYD, and placebo. Although the results of the SSS suggest a trend in increasing sleepiness: FEX=placebo< CET< HYD, these differences were not statistically significant. However, this relationship was confirmed by the results of the objective psychomotor tests performed in the laboratory in Study 1. Then, it seems that objective psychomotor tests are more sensitive than measurement of subjecitve sleepiness.

Study 2 was conducted to determine if the results of an objective 'real-life' test of impairment could "mirror" the results obtained in the laboratory and to assess patients' reactions to performing dual tasks of varying difficulty. An additive impairing effect was observed when subjects performed dual tasks simultaneously following administration of HYD, which was not observed after administration of FEX. Since the dorsolateral prefrontal cortex, which is postulated to be involved when performing the multiple tasks demanded of the driving study (Study 2) simultaneously, is relatively abundant in histamine H_1-receptors, this brain region is likely to be affected strongly by antihistamines that can penetrate the BBB[6]. The results suggest that an experiment in real-life situation is less

sensitive than that done in laboratory situation.

The results of Studies 1 and 2 imply that HYD crosses the BBB, binds to receptors in the cerebral cortex, thus resulting in impairment, whereas FEX does not. Study 3 confirmed that FEX does not penetrate the BBB, in contrast to CET, which had an H_1RO rate of around 20 to 30% depending on the ROI. The PET results suggest that the impairing properties of CET demonstrated in some psychomotor tests in Study 1 could be attributed to the binding of the antihistamine to cerebral H_1-receptors.

Conclusions

These studies suggest that sensitivities of the methods are as follows: [BRT study in real-life situation]= [subjective sleepiness]< [psychomotor study in a laboratory]< [H_1RO measurement with PET]. These studies also suggest that antihistamines increase in their impairing potential in the following order: FEX< CET< HYD. Further, FEX has a similar sedative profile to placebo. A multidimensional testing system is required to establish the relative impairment profiles of antihistamines, since a single test cannot reveal H_1RO, how sedated patients feel and how well they perform a diverse range of tasks. Further testing is required of all newer-generation agents to confirm their relative propensity to cross the BBB and cause impairment.

References

1) Bousquet J. et al., J. Allergy Clin. Immunol. **108** (2001) S147.
2) Casale T.B. et al., J. Allergy Clin. Immunol. **111** (2003) S835.
3) Cookson J., Use of drugs in psychiatry. 5th ed. London, UK: Gaskell (2002).
4) Logan J. et al., J. Cereb. Blood Flow Metab. **10** (1990) 740.
5) Yanai K. et al., Neurosci. Lett. **137** (1992) 145.
6) Mochizuki H. et al., Human Psychopharmacol. **17** (2002) 413.
7) Tashiro M. et al., J. Clin. Pharmacol. **44** (2004) 890.

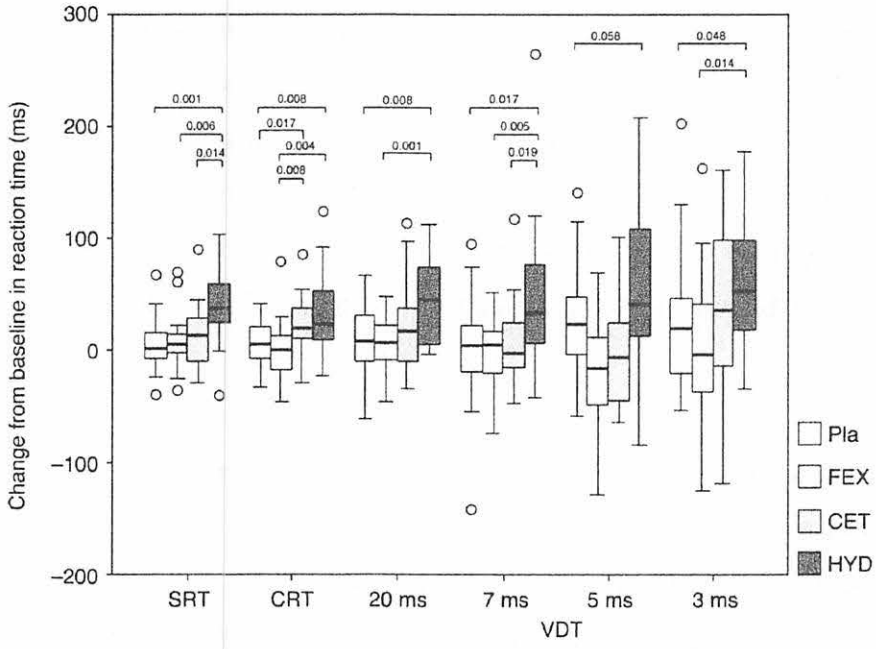

Figure 1. Change in the mean reaction time before and after medication.
Statistical examination was done by Friedman's test followed by post-hoc Bonferroni test (ref.7).

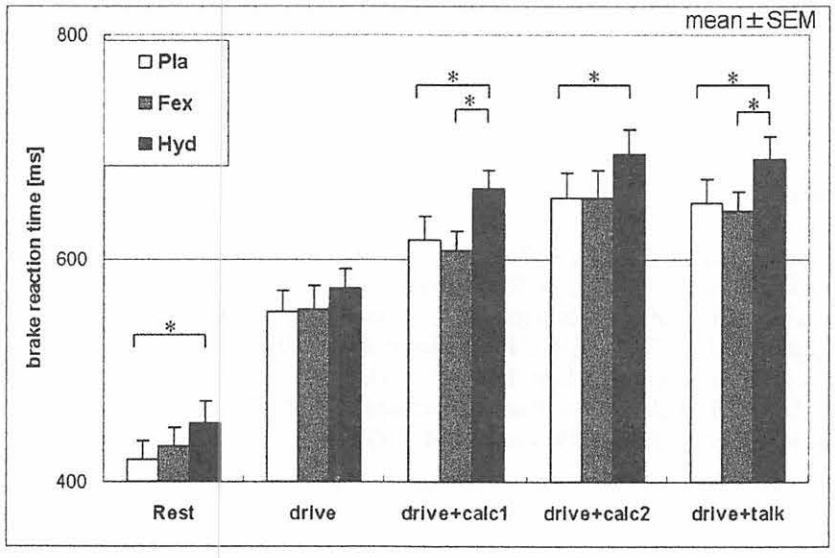

Figure 2. Results of BRT measurement in car driving study. *statistically significant examined by Friedman's test followed by post-hoc Bonferroni test ($p < 0.05$).

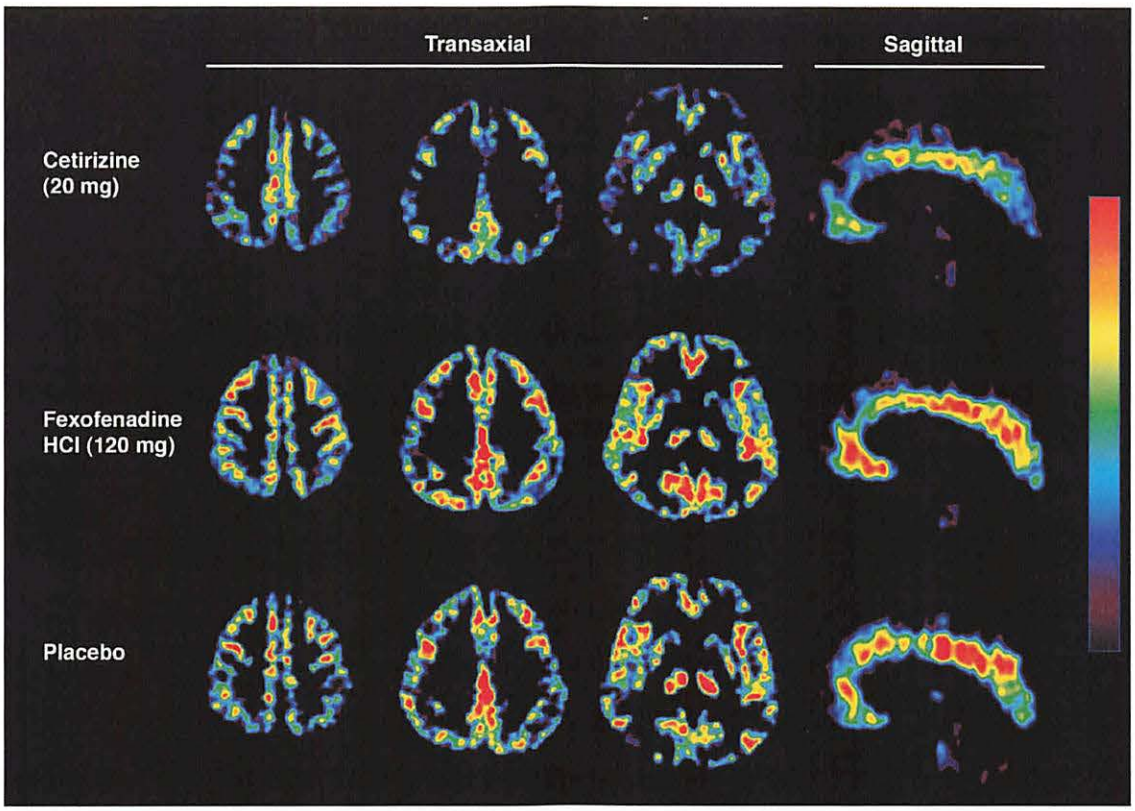

Figure 3. PET scans of brain regions after administration of CET, FEX and placebo. Images after administration of CET show lower binding of ^{11}C-doxepin compared to tother conditions (FEX and placebo) (ref.7).

VIII. 7. Imaging of Histamine H_1 Receptors in Schizophrenic Patients

Iwabuchi K.[*,**], *Ito C.*[*], *Tashiro M.*[**], *Kato M.*[**],
Itoh M.[***], *Iwata R.*[***], *Matsuoka H.*[*], *Sato M.*[****], *and Yanai K.*[**]

Departments of Psychiatry and Pharmacology[*], *Tohoku University School of Medicine*[**],
Cyclotron Radioisotope Center, Tohoku University[***], *and*
Department of Psychiatry, Tohoku Fukushi University Graduate School[****]

Introduction

There is some evidence that the histaminergic neuron system is implicated in the pathophysiology of schizophrenia[1, 2]. Indeed, a significant increase in the level of N^{τ}-methylhistamine was found in the cerebrospinal fluid of schizophrenics when compared to controls[3]. In addition, in postmortem binding studies using ^{3}H-mepyramine as a ligand, Nakai et al. found that the number of histamine H_1 receptors in the frontal cortex of schizophrenics was reduced[4]. Although previous findings have suggested that the high activity of brain histamine synthesis or release could be related to schizophrenia, no report has investigated the measurement of brain H_1 receptors in schizophrenic patients in vivo.

In this study, the distribution of histamine H_1 receptors in schizophrenics was compared to that in normal subjects. We measured cerebral H_1 receptor binding by PET and [^{11}C] doxepin in 10 patients with schizophrenia and in age-matched 10 normal subjects using the same methods used in the studies of H_1 receptor occupancy.

Methods

Ten male patients with schizophrenia and ten normal male volunteers with no neurological abnormalities were enrolled in this study. The schizophrenic subjects were diagnosed according to the diagnostic and statistical manual of mental disorders (DSM)-IV criteria from the clinical services affiliated with Tohoku University Hospital. Psychopathology was assessed by means of brief psychiatric rating scale (BPRS) as shown in Table 1. Healthy control subjects were recruited through advertisement. Based on unstructured psychiatric screening interviews, the control subjects were free of and never

had any psychiatric or major medical diseases, had no relatives with neuropsychiatric disorders, and showed no anatomical abnormalities according to MRI images. All schizophrenic patients were treated with haloperidol. Nine patients were treated for akathisia with biperiden, and five patients were treated for insomnia or anxiety with benzodiazepines [flunitrazepam (2 patients), brotizolam, cloxazolam, and quazepam (1 patient each)].

PET measurements were performed at Tohoku University Cyclotron Radioisotope Center using SET2400W scanner in three-dimensional mode. Binding potential (BP = Bmax / Kd) values of [^{11}C] doxepin for available brain histamine H_1-receptors in the schizophrenics and control subjects were calculated using a previously-reported method of H1 receptor occupancy[5-7].

Results

Averaged PET images obtained 45-90 min after intravenous injection of [^{11}C] doxepin are shown in Fig. 1. High radioactivity was observed in the frontal, temporal and occipital cortices, the cingulate gyrus, striatum and thalamus in the normal subjects. On the other hand, the distribution patterns of radioactivity in the cortical areas of schizophrenic patients were apparently lower than those of the control subjects.

Parametric neuroimages of BP of [^{11}C] doxepin in the schizophrenic patients and in the control subjects were constructed by graphical analysis and statistically compared using SPM99 on a voxel-by-voxel basis (Fig. 2) (Table 2). The colored areas show areas where BP values in the schizophrenic patients were significantly lower than those in the control subjects. In addition, histamine H_1 receptors density was significantly low in the cortices, especially the frontal and prefrontal, and the cingulate gyrus, which are known to be H_1-receptor rich regions. In contrast, SPM99 analysis could not detect any area where BP values were significantly higher in the schizophrenic patients than in the control subjects.

BP values in the prefrontal cortex, anterior cingulate cortex, posterior cingulate cortex, and thalamus were evaluated using ROI-based analysis (Fig. 3). BP values in the schizophrenic patients were significantly lower than those in the controls in the prefrontal cortex and cingulated cortex.

Discussion

H_1 receptors estimated on a voxel-by-voxel basis using SPM99 were significantly lower in several brain areas of the schizophrenic patients than in the normal subjects.

Similarly, H1 receptor bindings evaluated using ROIs placed on the prefrontal cortex and the anterior and posterior cingulate gyrus were significantly lower in the schizophrenic patients than in the normal subjects. These results are generally consistent with those of histamine H_1 receptor binding assays in post-mortem schizophrenic patients brain[4]. The present study demonstrates for the first time the decrease of histamine H_1 receptor density in the brain of schizophrenic patients in vivo by PET, though a careful interpretation of our results is needed.

The PET findings of this study are preliminary and require replication because of the relatively small number of subjects and the problem of patients medication. However, the present study clealy demonstrates a decrease of histamine H_1 receptors in chronic schizophrenics by PET. It is speculated that neuronal histamine functions as a bio-protective system against various noxious and unfavorable stimuli such as convulsion, nociception, drug sensitization, ischemic lesions, and stress[8]. There is evidence that implicates brain histamine in animal model of psychosis[9, 10]. The decrease of H_1 receptors observed in the schizophrenic patients in this study would be a consequence of downregulation caused by excessive histamine release from histamine neurons. Here we propose that histamine neurons have an inhibitory role on the development of stress-vulnerability or schizophrenic symptoms. To confirm this, further studies, particularly studies of drug-naïve patients, are needed.

Recently, Pillot et al. reported that acute administration of ciproxifan, a histamine H_3 receptor antagonist/inverse agonist, potentiates the neurochemical and behavioral effects of haloperidol in the rat[11]. These results suggest that histaminergic neurotransmission may be involved in the pathophysiology of schizophrenia and that dysfunction of the histaminergic neuron system might be important as one of the extra-dopaminergic functional abnormalities in the schizophrenic brain. Therefore, activation of the histaminergic neuron system might be useful for the treatment of schizophrenia.

References

1) Usdin E., Hamburg D.A., Barchas J.D. et al., Stripling JS. Proceedings of a conference on neuroregulators and hypotheses of psychiatric disorders held at the asilomar conference center, pacific grove, california, january 13-16, 1976. New York: Oxford University Press, 1977.
2) Rauscher F.P., Nasrallah H.A., Wyatt R.J. et al., J. Clin. Psychiatry **41** (1980) 44.
3) Prell G.D., Green J.P. and Kaufmann C.A., Schizophr. Res. **14** (1995) 93.
4) Nakai T., Kitamura N., Hashimoto T. et al., Biol. Psychiatry **30** (1991) 349.
5) Logan J., Fowler J.S., Volkow N.D. et al., J. Cereb. Blood. Flow. Metab. **110** (990) 740.
6) Okamura N., Yanai K., Higuchi M. et al., Br. J. Pharmacol. **129** (2000) 115.
7) Tagawa M., Kano M., Okamura N. et al., Br. J. Clin. Pharmacol. **52** (2001) 501.

8) Watanabe T. and Yanai K., Tohoku J. Exp. Med. **195** (2001) 197.
9) Ito C., Sato M., Onodera K. et al., Ann. N. Y. Acad. Sci. **801** (1996) 353.
10) Morisset S., Pilon C., Tardivel-Lacombe J. et al., J. Pharmacol. Exp. Ther. **300** (2002) 621.
11) Pillot C., Ortiz J., Heron A. et al., J. Neurosci. **22** (2002) 7272.

Table 1. Clinical features of the ten schizophrenic patients. Age at PET scan, morbidity periods, daily dose of antipsychotics / anticholinergics / benzodiazepines, BPRS scores for each patient are listed.

Patient No.	age	Morbidity period	Antipsychotics (Haloperidol/day)	Anticholinergics (Biperidenl/day)	Benzodiazepines	BPRS score
1	38	16y	1.5mg	1mg	Brotizolam0.25mg	10
2	21	2y	3mg	2mg		15
3	29	3.5y	1.5mg	1mg		20
4	30	3y	6mg	2mg	Cloxazolam 2mg	24
5	36	10y	5mg	8mg		11
6	26	9y	15mg	4mg		26
7	31	1y	9mg	3mg	Quazepam 15mg	27
8	29	12y	4.5mg	3mg	Flunitrazepam 2mg	14
9	36	19y	2.5mg			29
10	20	2.5y	9mg	6mg	Flunitrazepam 1mg	17

Table 2. Regional maxima showing significant differences in BP values estimated by SPM99 between schizophrenic patients and the controls ($p<0.001$, uncorrected).

Area	(Brodmann area)	Side	Z-score	Talairach coordinates		
				x	y	z
Gyrus frontalis medialis	(8)	L	4.37	-10	32	44
Gyrus frontalis inferior	(47)	L	4.33	-28	30	-12
Gyrus frontalis medius	(9)	L	4.05	-28	42	36
Gyrus frontalis medius	(6)	L	3.95	-46	4	46
Gyrus frontalis inferior	(47)	R	3.87	46	26	-2
Gyrus occipitalis medius	(19)	L	3.69	-50	-60	-4
Gyrus lingualis	(18)	R	3.54	16	-82	0
Precuneus	(7)	R	3.53	16	-34	50
Gyrus frontalis medialis	(6)	L	3.46	-12	-8	48
Precuneus	(7)	L	3.43	-14	-36	48

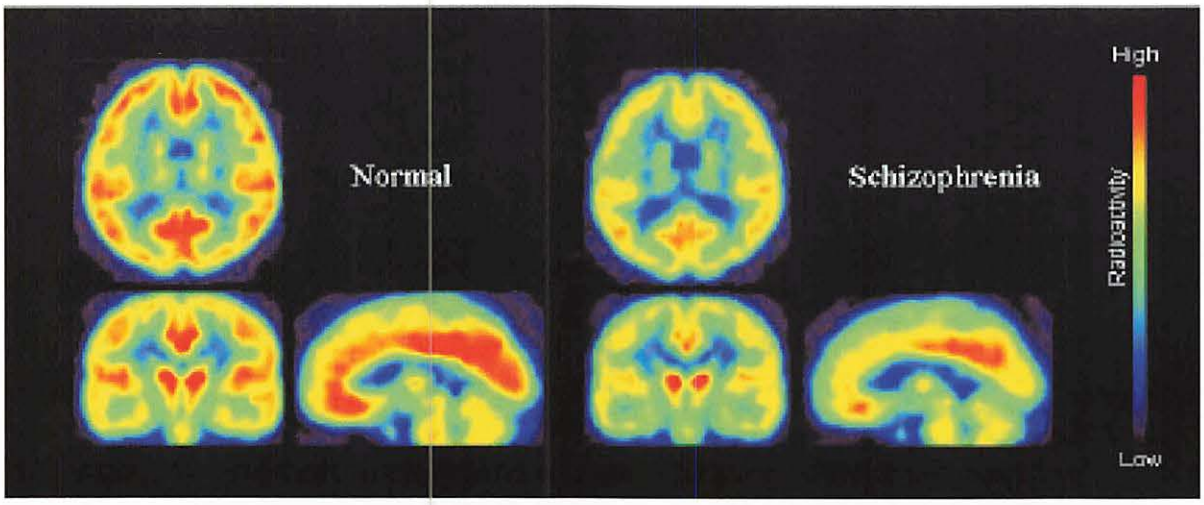

Fig. 1. Brain distribution of [^{11}C]-doxepin radioactivity in schizophrenic patients and healthy control subjects. Averaged PET images are shown at the corresponding levels. The images were obtained 45-90 min after intravenous injection of [^{11}C]-doxepin.

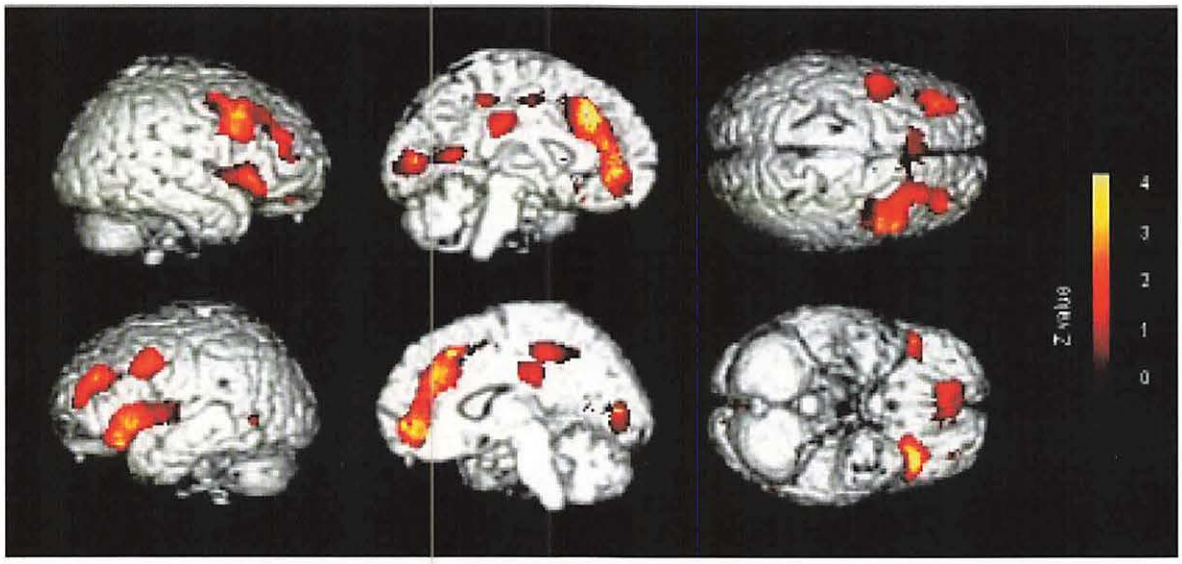

Fig. 2. Brain distribution of [11C]-doxepin radioactivity in schizophrenic patients and healthy control subjects using SPM99. The colored areas show areas where BP values of [11C]-doxepin in schizophrenic patients were significantly lower than those in the control subjects ($p<0.001$, uncorrected).

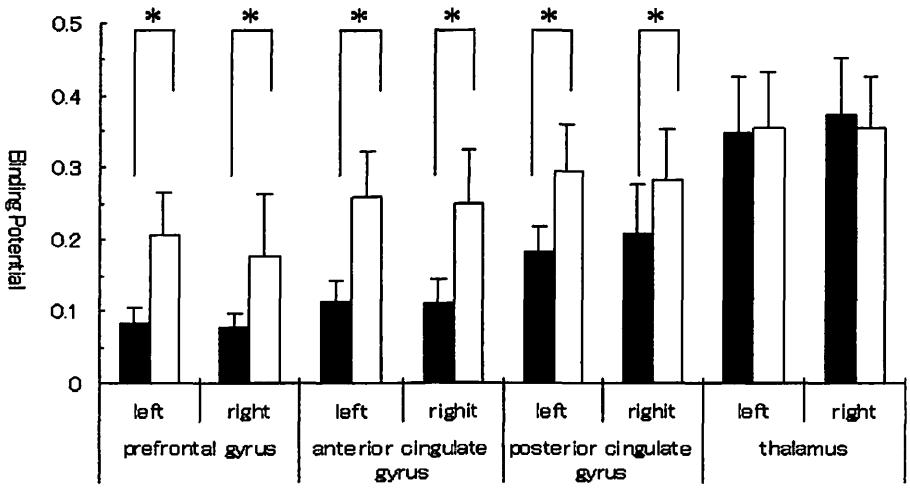

Fig. 3. ROI-based analysis of histamine H1 receptors in the prefrontal cortex, anterior cingulated cortex, posterior cingulated cortex and thalamus. BP values (means+/-SD) for the schizophrenic patients (■) and the controls (□) are shown. *$p<0.05$ Statistically analyzed by non paired t-test.

VIII. 8. Visceral Perception and Emotion are Correlated to Brain Activity during Colonic Distention in Human

Hamaguchi T.[*], *Kano M.*[*], *Rikimaru H.*[**], *Kanazawa M.*[*], *Itoh M.*[**], *Yanai K.*[***], *and Fukudo S.*[*]

Department of Behavioral Medicine, Tohoku University Graduate School of Medicine[*]
Division of Nuclear Medicine, Tohoku University, Cyclotron Radio Isotope Center[**]
Department of Pharmacology, Tohoku University Graduate School of Medicine[***]

Introduction

Psychological stress induces symptoms in the lower digestive tract of humans such as abdominal pain, diarrhea or constipation[1]. These phenomena are explained by stress-induced colonic motility[2] and visceral perception abhorred by the stress[3]. Irritable bowel syndrome (IBS) is a functional gastrointestinal disorder characterized with chronic abdominal pain and abdominal bowel habituation. Recently, research of IBS has been given much attention because of high prevalence and the great influence on the medical economy. However, the cause and the pathophysiology are uncertain. The functional relation between the central nervous system and the gastrointestinal tract is beginning to be clarified[2] and the brain-gut interaction is considered to be a major pathophysiology of IBS.

The functional module of the brain in response to colorectal distention has not been completely determined yet. Whether the visceral perception is actually projected to the somatosensory area is doubtful. Silverman et al., reported that rectal distention induced activation of the anterior cingulate cortex in healthy persons but not in IBS patients[4]. In contrast, Mertz et al., reported that in IBS patients, but not in healthy persons, painful stimuli to the rectum led to greater activation of the anterior cingulate cortex than did non-painful stimuli[5]. Therefore, greater detailed information about the gastrointestinal tract to the brain is needed. Moreover, the stimulated part in earlier studies was the rectum but the pain-producing part in IBS patients is thought to be the colon. In addition, there are a lot of uncertain points in the brain area which relate to emotion provoked by visceral perception.

This study aims to verify the following hypotheses: there are regions of the brain

which relate to visceral perception and emotion provoked by visceral stimulation.

Method

Subjects

Fifteen volunteers participated in this study. They were all male, right-handed, and aged 22±1 (mean±SE). All subjects were free from gastrointestinal symptoms or signs. Each underwent a basic evaluation to exclude organic diseases including medical history and were given a physical examination and colonoscopy. All subjects gave informed consent as approved by the Ethics Committee in Tohoku University School of Medicine.

Distention Protocol

On the day before examination, the subjects took a low residue diet. At 21: 00 before the examination, they ingested 17g (13.6%) of magnesium citrate, 75mg of sodium picosulfate, and 24mg of sennoside A & B to cleanse the colon. Subjects were tested in the fasted state at 8: 15. A colonoscope was inserted into the splenic flexure and a splinting device was inserted along the scope. After the removal of the scope, a plastic tube with a thin polyethylene bag (Synectics Medical, Stockholm) was inserted into the descending colon. The maximal volume of the bag was 700 ml and the maximal diameter of the bag at full inflation was 10 cm. The location of the bag was confirmed with X-ray fluoroscopy. The splinting device was removed and the bag was taped in place. Subjects rested in bed from 9: 15.

The colonic distention stimuli were provided with a computerized barostat pump (Medtronics Synectics, Shoreview, MN). The sham stimulation with 0 mmHg was given at first. The colon was then stimulated with the bag pressure of 0 mmHg, 20 mmHg, and 40 mmHg for 80 seconds. The intensity of stimulus was randomly given to avoid the order effect of the stimulation.

After the stimulation, subjects were asked the following 7 items of visceral sensation or emotion: abdominal discomfort, abdominal distention, abdominal pain, urgency, perceived stress, sleepiness, and anxiety. They judged the sensation from 0 ("not sensed") to 10 ("maximally sensed") on the ordinate scale, which was previously validated [6].

Positron emission tomography (PET) scanning

[^{15}O] labeled water which was synthesized by the cyclotron was injected into the right arm vein at the beginning of colonic distention. Ten seconds later, both radioactivity and peak pressure of the bag reached plateau. The PET scan was then started and continued for 70 seconds. We measured rCBF during 4 scans (70 seconds each) using a PET scanner in three-dimension sampling mode (HEADTOME V SET-2400W, Shimadzu, Japan). To ensure that the radioactivity levels in the subjects returned to background before starting a new scan, a 10 min interval was given between successive scans.

Analysis

The PET image analyzed for brain image analysis software (Statistical Parametric Mapping; SPM99, The Wellcome Department of Cognitive Neurology, London) according to the Friston method[7-9]. The PET images were realigned, spatially normalized and transformed into an approximate Talairach-Tournoux stereotactic space[10], 3D Gaussian filtered (FWHM = 13 mm), and proportionally scaled to account for global confounders. The size of each voxel was set at $2 \times 2 \times 2$ mm. The individual specificity of the whole brain blood flow between subjects was corrected in analysis of covariance (ANCOVA).

The multiple regression analysis was done on each voxel of each ordinate scale and the whole brain in each stimulation in order to clarify the region where the rCBF fluctuated by correlating with visceral perception and emotion. We set 0.1 % level of significance or less (uncorrected, $Z > 3.60$) at the region of significant correlation.

Results

Numerous brain regions correlate significantly and positively to visceral perception and emotion in results of multiple regression analysis of threshold set at Z value > 3.60, uncorrected $p < 0.001$. They were the cortical and limbic area, e.g., superior frontal gyrus (BA 10), middle frontal gyrus (BA 9 and 10), inferior frontal gyrus (BA 39, 40, and 44), precentral gyrus (BA 6), postcentral gyrus (BA40), cingulate gyrus (BA 24 and 32), hippocampal gyrus (BA35), parahippocampal gyrus (BA 20), insula, and thalamus.

Abdominal discomfort showed a significant positive correlation to rCBF in the right inferior parietal lobe (BA 40) contained in the inferior frontal gyrus (BA 44)(Fig. 1-a). Abdominal distention showed a significant positive correlation to rCBF in the right inferior frontal gyrus (BA 44) and the inferior parietal lobe (BA 40) (Fig. 1-b).

Abdominal pain showed a significant positive correlation to rCBF in the right inferior parietal lobe (BA40) and the left cerebellum. Perceived stress showed a significant positive correlation to rCBF in the right inferior parietal lobe (BA40). Urgency, anxiety and sleepiness showed no significant positive or negative relation to rCBF at analysis with the corrected p value.

Discussion

Our data revealed a positive relation between abdominal distention and rCBF of the left inferior parietal somatosensory cortex, which is consistent with an earlier report[11]. Hobday et al., reported that rectal balloon distention induced activation of the inferior comatosensory (S1) cortex[11]. The signal from the visceral organ is projected to the prefrontal cortex from the lateral thalamic nucleus group[12]. This might be related to recognition of orientation of the stimulated body. The earlier reports[4),5),11)] stimulated the rectum, which integrates visceral information. However, in this study, pure visceral viscas were stimulated. Therefore, the results of this study strongly suggest co-activation of the somatosensory cortex with the prefrontal cortex and the anterior cingulate cortex.

Several reports have indicated that the anterior cingulate cortex is activated with the stimulation of the colorectum[4),5),13)]. The results of this study are consistent with those earlier reports. Moreover, increased rCBF in the anterior cingulate cortex is proportional to visceral perception, suggesting that this limbic cortex plays a major role in gastrointestinal symptoms in humans. The supplementary motor cortex which between the limbic cortex and the primary motor cortex was also activated in this study. The supplementary motor area is mutually being coupled with the anterior cingulate cortex, the primary motor cortex, and the prefrontal cortex[14]. Goldberg et al., has advocated the idea of an intermediary role of the supplementary motor cortex[15]. The supplementary motor area may choose order and strategy of dealing with motion for a realization of the stimuli to humans. The relation between perceived stress and rCBF of the right prefrontal cortex in this study may indicate the preparation of motion against stress and avoidant behavior at the sensation of unease.

References

1) Drossman D.A., Sandler R.S., McKee D.C. and Lovitz A.J., Gastroenterology **83** (1982) 529.
2) Fukudo S., Nomura T., Murakawa M. and Taguchi F., J. Clin. Gastroenteol. **16** (1993) 133.
3) Accarino A.M., Azpiroz F. and Malagelada J.R., Gastroenterology **113** (1997) 415.

4) Silverman D.H., Munakata J.A., Ennes H., Mandelkern M.A., Hoh C.K. and Mayer E.A., Gastroenterology **112** (1997) 64.
5) Mertz H., Morgan V., Tanner G., Pickens D., Price R., Shyr Y. et al., Gastroenterology **118** (2000) 842.
6) Drossman D.A., The functional gastrointestinal disorders -diagnosis, pathophysiology, and treatment- A multinational consensus. In: Talley NJ. Optimal design of treatment trials. Boston/New York/Toronto/London: Little, Brown and Company; 1994. p. 265-310.
7) Friston K.J., Worsley K.J., Frackowiak R.S.J., Mazziotta J.C. and Evans A.C.., Hum. Brain Mapp. **1** (1994) 210.
8) Friston K.J., Holmes A., Worsley K.J., Poline J.P., Frith C.D. and Frackowiak R.S.J., Hum .Brain Mapp. **1** (1995) 189.
9) Friston K.J., Ashbuner J., Poline J.B., Frith C.D. and Frackowiak R.S.J., Hum. Brain. Mapp **2** (1995) 165.
10) Talairach J. and Tournoux P., Co-Planar stereotaxic atlas of the human brain. New York: Thieme Medical Publishers; 1988; p. 37-110.
11) Hobday D.I., Aziz Q., Thacker N., Hollander I., Jackson A. and Thompson D.G., Brain **124** (2001) 361.
12) Resenkilde C.E., Behav. Neural. Biol. **25** (1979) 301.
13) Kern K.M. and Shaker R., Gastroenterology **122** (2002) 290.
14) Damasio A.R. and Van Hoesen G.W., Neulorogy **30** (1980) 359.
15) Goldberg G., Behav. Brain Sci. **8** (1985) 567.

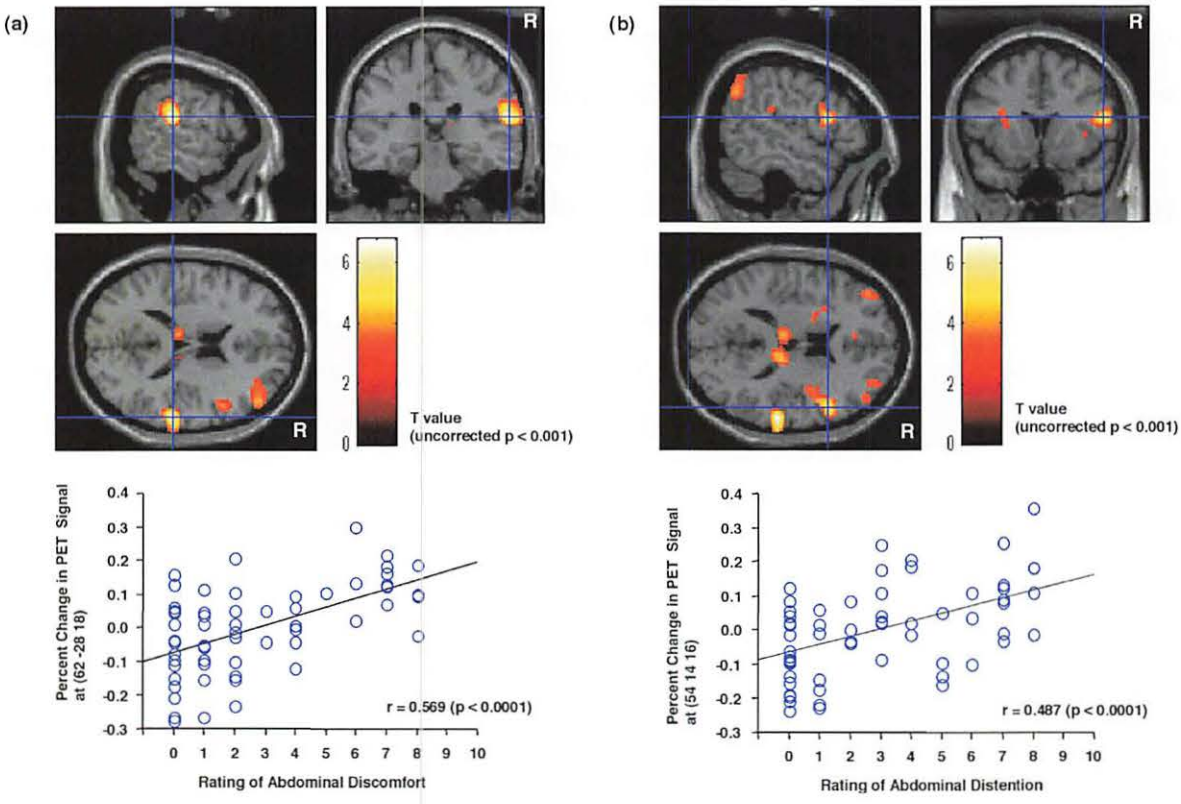

Fig. 1. Brain regions of positive correlation to visceral perception and emotion. Results from the multiple regression analysis. (a) shows demonstrating voxels in the right inferior parietal lobule, (x y z), (62 -28 18), contained the postcentral gyrus and the inferior frontal gyrus that correlated significantly to abdominal discomfort. There were superimposed on the structural MRI scan of a single subject. (b) shows demonstrating voxels in the right inferior frontal gyrus, (x y z), (54 14 16) that correlated significantly to abdominal distention. The bottom shows the median percent change in PET signal from baseline across subjects (with the value for each subject in the ordinate scale) for rating of visceral perception and emotion. Results are from the single regression analysis.

VIII. 9. FDG-PET for Diagnosis of an Advanced Jejunal Adenocarcinoma with Distant Metastases, Compared with Gallium Scintigraphy

Yamaura G., Yoshioka T., Yamaguchi K., Fukuda H.**, and Ishioka C.*

Department of Clinical Oncology, Institute of Development, Aging and Cancer, Tohoku University
*Cyclotron and Radioisotope center, Tohoku University**
*Department of Nuclear medicine and Radiology, Institute of Development, Aging and Cancer, Tohoku University***

Introduction

Patients with primary adenocarcinoma of the jejunum are very rare[1)], and there has been no report to our knowledge showing how nuclear medicine techniques may play a role in diagnosis. We have experienced a case of an advanced adenocarcinoma of the jejunum with distant metastatases, for which positron emission tomography (PET) with fluorine-18 2-deoxy-2-fluoro-D-glucose (FDG) and gallium-67 citrate scintigraphy were compared.

A Case Report

A 70-year-old woman was referred to our institute because of an adenocarcinoma metastasis to cervical lymph node with unknown primary lesion.

She had found painlessly swelling in her left cervical lymph nodes three months previously and visited her local hospital. Biopsy revealed metastases from an adenocarcinoma and a series of investigations were carried out to find the primary site but failed.

When she visited our institute, she presented no symptoms except for swollen cervical lymph nodes and her laboratory data were unremarkable. Gastroduodenal and colonic endoscopies were carried out but the original site was undetected. Computed tomography (CT) scanned the whole body and revealed the right cervical lymph nodes and para-abdominal aortic lymph nodes and retro-pancreatic lymph node to be swollen (Fig 1). Gallium scintigraphy was carried out and abnormal accumulations in the left cervix, left axillary and the center of the abdomen could be visualized (Fig. 2b). When CT scan

images were checked retrospectively, the lymph nodes in the left axillary were found to be swollen (Fig. 1).

As the next step for diagnosis, FDG PET was carried out and showed accumulation corresponding to all of the swollen lymph nodes and the small intestine (Fig 3). According to these findings, the barium meal fluoroscopy of the small intestine was carried out and showed a defective image near the angle of Treitz (Fig.4). From these findings, the horizontal portion of the duodenum or the jejunum was suspected as the primary site. A gastroduodenal endoscope was therefore introduced into the deep horizontal portion of the duodenum, and a Bormann type II tumor were found. A biopsy was carried out and the histological examination revealed an adenocarcinoma.

Two weeks thereafter, partial resection of jejunum was performed due to the risk of the obstruction and bleeding, and clarified the existence of a Bormann type II tumor, a moderately differentiated adenocarcinoma of the jejunum, 5 cm to the anal side of the Treiz ligament.

Discussion

Small intestinal adenocarcinomas are very rare, accounting for only 2% of gastrointestinal tumors[1]. In 4995 cases reported to the National Cancer Data Base between 1985 and 1995, 55% of them occurred in the duodenum, 18% in the jejunum, 13% in the ileum and 14% in nonspecified sites[2]. There are no specific symptoms and diagnosis is frequently very late at an advanced stage. Most common symptoms are pain due to obstruction, weight loss and massive and occult hemorrhage[3]. In our case, cervical lymph nodes were found to be swollen at first and in the search for the primary site, a jejunal adenocarcinoma was diagnosed.

FDG PET is a noninvasive approach for determination of glycolytic status. PET is able to make an image that shows the tissue distribution of FDG, a structural analog of glucose labeled with the short-lived positron-emitting ^{18}F[4]. FDG is transported into the cell via a glucose-transporter, then is converted to FDG-6-phosphate by hexokinase in cells, but it is not a substrate for further metabolism, nor permeable to the cell membrane, and therefore accumulates within the cell[5]. Enhanced glycolysis is one of the most important characteristics of cancer cells[6], and FDG PET has proved successful for imaging various malignant neoplasms[7]. In our case, FDG PET could detect the primary lesion and apparently all of the metastastic lesions. Koles et al.[8] and Bohuslavizki et al.[9] reported that FDG PET is a valuable diagnostic tool in patients with cancer of unknown primary.

In our case, FDG PET is also helpful to find the primary lesion. This is the first report of FDG PET imaging of a jejunal adenocarcinoma, providing support for the conclusion that this approach can greatly contribute to the differential diagnosis of primary lesions in patients with metastatic lymph node deposits. The final diagnosis can then be made on histological examination after endoscopic sampling, advised here.

Gallium scintigraphy was also carried out in our case and succeeded in detecting another lymph node metastasis in the upper body. However, it failed to detect lesions in the abdomen, presumably due to the physiological accumulation of gallium in the liver and the excretion with bile juice into the bowel[10].

In conclusion, FDG PET should prove helpful in the diagnosis of the small intestinal adenocarcinomas with metastases.

Acknowledgment

The authors thank Mr. Syouichi Watanuki and Mr. Masayasu Miyake for PET operation and the other staffs of the Cyclotron Radioisotope Center, Tohoku University. This work was supported by grants-in-aid for scientific research (No. 13670910 and No. 10670820) from the Ministry of Education, Science, Sport, Culture and Technology, and for Cancer Research (14S-3) from the Ministry of Health, Labour and Welfare, Japan.

References

1) Martin R.G., Surg. Clin. North. Am. **66** (1986) 779.
2) Howe J.R., Karnell L.H., Menck H.R. et al., Cancer **86** (1999) 2693.
3) Ashley S.W. and Wells S.A., Semin. Oncol. **15** (1988) 116.
4) Reivich M., Kuhl D., Wolf A. et al., Circ. Res. **44** (1979) 127.
5) Gallagher B.M., Fowler J.S., Gutterson N.I., MacGregor R.R., Wan C.N. and Wolf A.P., J. Nucl. Med. **19** (1978) 1154.
6) Warburg O., Science **123** (1956) 309.
7) Gambhir S.S., Czernin J., Schwimmer J., Silverman D.H.S., Coleman R.E. and Phelps M.E., J. Nucl. Med. **42** (2001) 1S.
8) Kole A.C., Nieweg O.E., Prium J. et al., Cancer **82** (1998) 1160.
9) Bohuslavizki K.H., Klutmann S., Kroger S. et al., J. Nucl. Med. **41** (2000) 816.
10) Togawa T., Tokyo: Kanehara Press, (1999) 518.

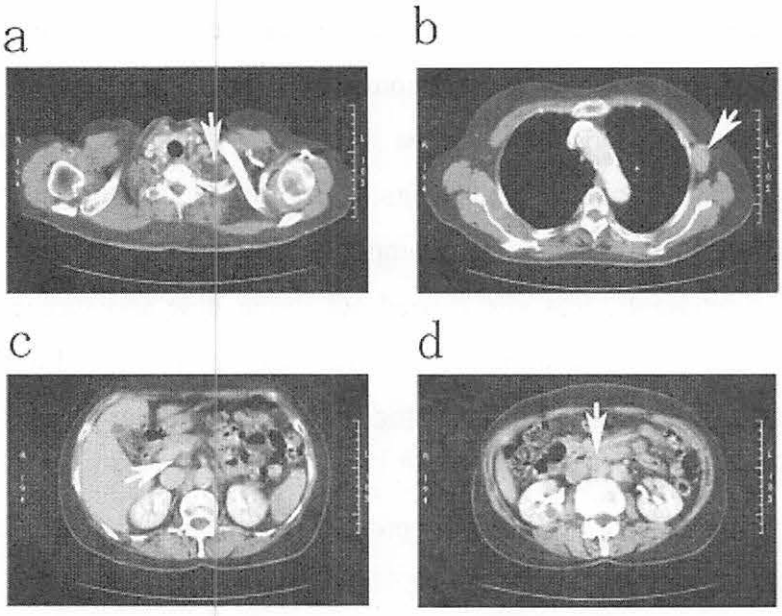

Fig. 1. CT images show lymph nodes swelling in; a: left cervical lymph nodes. b: the left axillary lymph node. c: the retropancreatic lymph node. d: para-aortic lymph nodes.

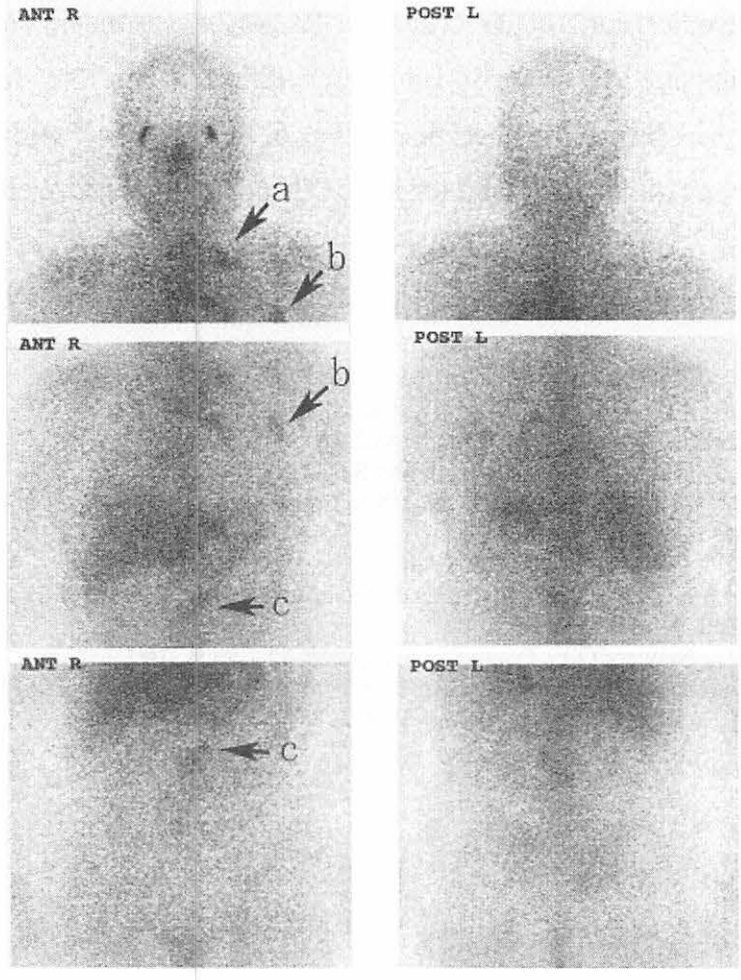

Fig. 2. Gallium scintigraphy shows abnormal accumulations in the left cervix (arrow (a)), left axillary (arrow (b)), and the center of the abdomen (arrow (c)).

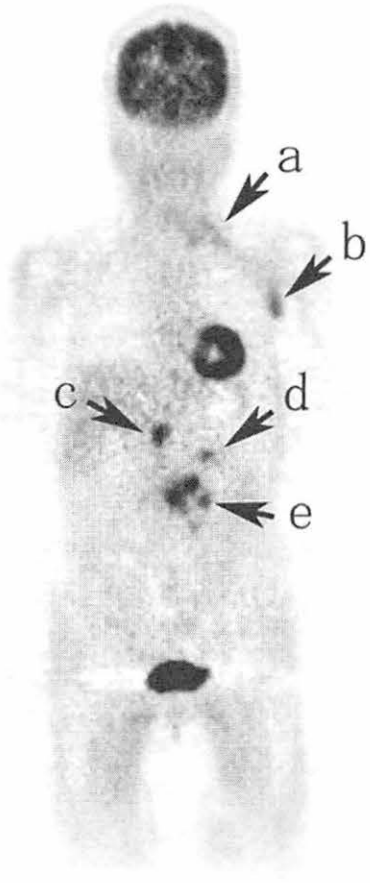

Fig. 3. The image of FDG PET has accumulations corresponding to all lesions. The arrow (d) indicates the slightly high accumulation of FDG that is thought to be corresponding to the primary lesion. All other high accumulations of FDG are corresponding to the metastatic lesions in; a: the cervical lymph nodes. b: the axillary lymph node. c: the retropancreatic lymph node. e: the para-aortic lymph nodes.

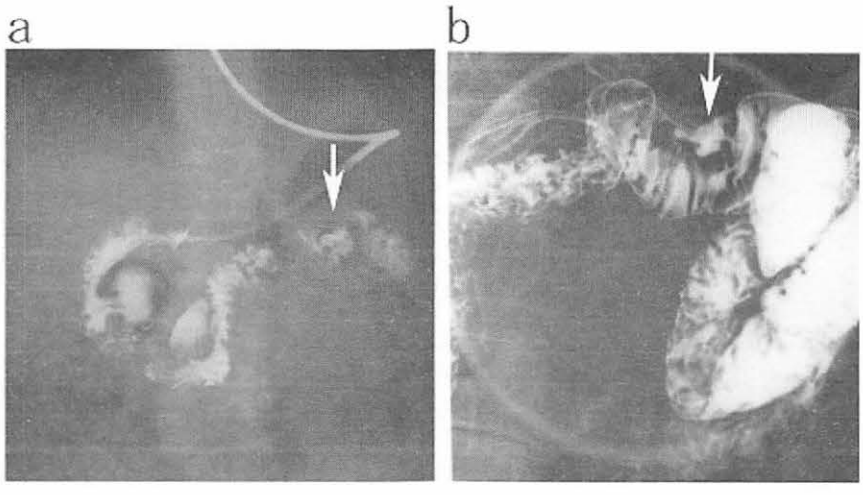

Fig. 4. The barium meal fluoroscopy of the small intestine shows a defective image near the angle of Treitz. a: the image of the whole. B: the enlarged and pressured image of the lesion suspected as a primary lesion. Arrows indicate the lesion.

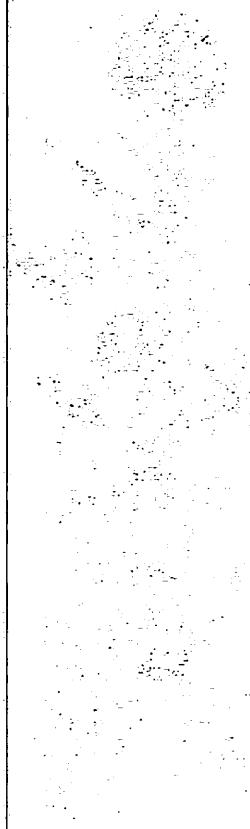

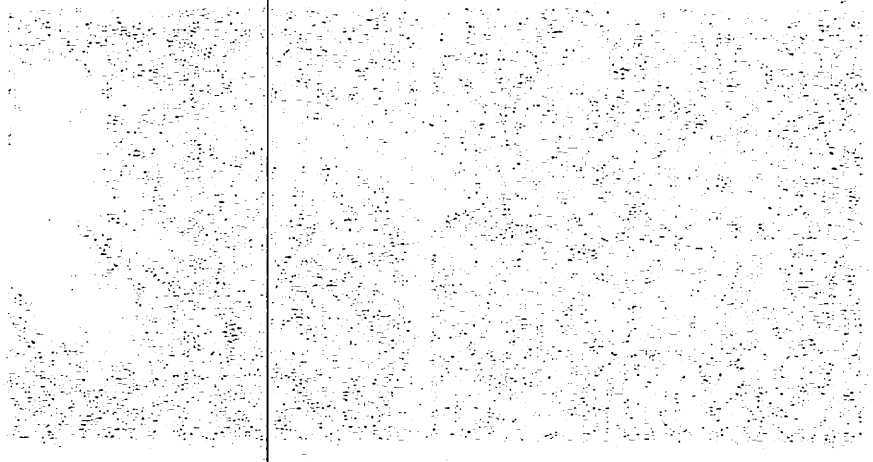

IX. RADIATION PROTECTION AND TRAINING OF SAFETY HANDLING

IX. 1. Beginners Training for Safe Handling of Radiation and Radioisotopes in Tohoku University

Baba M., Miyata T., Iwata R., and Nakamura T.

Cyclotron and Radioisotope Center, Tohoku University

During 2003, the beginners training for safe handling of radiation and radioisotopes in Tohoku University was conducted in three courses as usual; 1) Radiation and Isotopes, 2) X-ray Machines and Electron Microscope, and 3) Synchrotron Radiation (SOR). The training was held twice a year, May and November, under the help for lectures and practice from various departments and research institutes of the university.

Lectures in English which were started in November of 2002 were continued for students and/or researchers who are not so familiar with Japanese language, by using PC projector and text of copies of view graphs (English class). The number of English class increased significantly.

The training for "Radiation and Radioisotopes" is for persons who use unshielded radioisotopes and accelerators, and has been conducted from 1977. The contents of lectures and practices are shown in Table 1. In the fiscal year of 2003, the training was performed for 597 persons (35 persons in the English class). The departments or institutes to which they belong are given in Table 2.

The training for "X-ray machines and electron microscopes" started at the end of 1983. The training is scheduled twice a year at the same time as that for "Radiation and Radioisotopes". In this course, only lectures are given with no practice. The contents of the lectures and the distributions of trainees are shown in Table 3 and Table 4, respectively. The number of trainees was 318 (40 in the English class).

The training for the "Synchrotron Radiation" began at the end of 1995. The contents of the lectures are the same as those of the radiation and radioisotopes but no practice. In 2003, the number of trainees of the SOR course was 98 (1 in the English class).

Table 1. Contents of the lectures and practices for safe handling of radiation and radioisotopes in 2003.

Lectures (one day)	Hours
Radiation physics and measurements	1.5
Chemistry of radioisotopes	1.0
Radiological protection ordinance	1.5
Effects of radiation on human	1.0
Safe handling of radioisotopes	1.5

Lectures (one day)	Hours
Treatment of unsealed radioactive solution	4.0
Measurements of surface contamination and decontamination	1.0
Measurements of gamma rays and beta rays	2.0

Table 2. Distribution of trainees for "radiation and radioisotopes" in 2003.

Department	Staff	Student	Total	English class
Medicine	9	111	120	7
Dentistry	2	18	20	
Pharmacy	1	63	64	4
Science	1	61	62	1
Engineering	4	75	79	6
Agriculture	1	107	108	8
Research Institutes	5	78	83	9
The others	1	60	61	
Total	24	573	597	35

Table 3. Contents of the lectures for "X-ray machines and electron microscopes" in 2003 (same for both Japanese and English class)

Lectures (one day)	Hours
Safe handling of X-ray machines	1.5
Radiological protection ordinance	0.5
VTR for safe handling of radiation and radioisotopes	0.5

Table 4. Distribution of trainees for "X-ray machines and electron microscopes" in 2003

Department	Staff	Student	Total	English class
Medicine	0	1	1	
Dentistry	0	1	1	
Science	0	16	16	1
Engineering	2	110	112	5
Research Institutes	11	154	165	31
The others	6	17	23	3
Total	19	299	318	40

Table 5. Distribution of trainees for "synchrotron radiation" in 2003.

Department	Staff	Student	Total	English class
Medicine	3	0	3	
Pharmacy	0	3	3	
Science	0	15	15	
Engineering	0	38	38	
Research Institutes	5	33	38	1
The others	0	1	1	
Total	8	90	98	1

IX. 2. Radiation Protection and Management

Miyata T., Baba M., and Watanabe N.[*]

Cyclotron and Radioisotope Center, Tohoku University
Japan Radiation Protection Co., Ltd.[*]

(1) Overview

During the fiscal year of 2003, research and education in the center were conducted as active as usual.

During the year, the new online radiation protection and management system of CYRIC was installed under the auspice of Monbu-kagakusho (the Ministry of Education and Culture, Sports, Science and Technology). The system performed reliably except for slowing down of the system response when the data transfer rate is so high and the response of the system becomes much quicker than old one. The radiation detectors were not replaced because of limited fund, but performed stably except for one failure of neutron monitor.

From the fiscal year of 2004, the organization of Tohoku University changes to from a national university to a university cooperation. Along with the change of organization, measurement of radioactivity concentration is required. To carry out the measurement, devices for radioactivity concentration measurement (samplers, αβ automatic counters) were purchased and setup under the financial support by Tohoku University. These counters will be used commonly by radiation facilities in Tohoku University.

(2) Unsealed radio nuclides used in CYRIC

The species and amounts of unsealed radio nuclides handled in CYRIC during the fiscal year of 2003 are summarized in Table 1. The table includes the isotopes produced by the cyclotron as well as those purchased from the Japan Radio Isotope Association or taken over from other radioisotope institutes.

(3) Radiation exposure dose of individual worker

The exposure doses of the workers in CYRIC during 2003 are given in Table 2.

The doses were sufficiently lower than the legal dose limits.

(4) Radiation monitoring of the workplace

Radiation dose rates inside and outside of the controlled areas in CYRIC were monitored periodically and occasionally when needed. They were generally below the legal dose limits. Surface contamination levels of the floors inside the controlled areas were also measured with a smear method and a survey meter method. They were under the legal regulation levels.

(5) Wastes management

The radioactive wastes were delivered to the Japan Radio Isotope Association twice in the fiscal year of 2002. For the reason, no wastes were delivered in 2003.

The concentration of radioisotopes in the air released from the stack after filtration was monitored with stack gas monitors. The values on concentration were lower than the legal regulation levels. The radioactive water was stocked in the tanks at least for 3 days and then released to the sewerage after confirming that the concentration was lower than the legal regulation levels.

Radioactive organic scintillator waste of 800 litter was treated by incinerator provided by Fuji-kogyo Co.Ltd.

Table 1. Unsealed radioisotopes used in each building of CYRIC during 2003.

(a) Cyclotron Building (kBq)

Group1,2		Group3		Group4	
^{42}Ar	3.000	^{11}C	311,832,800.000	^{18}F	900,417,400.000
				^{3}H	257,165.300
Total	0	Total	311,832,800.000	Total	900,674,565.300

(b) Radio-isotope Building (kBq)

Group1,2		Group3		Group4	
^{90}Sr	180.000	^{11}C	481,000.000	^{14}C	79,026.300
^{109}Cd	4,200.000	^{90}Mo	9,885,100.000	^{18}F	34,549,100.000
^{137}Cs	1,001.000	^{24}Na	1.000	^{3}H	300,266.120
^{55}Fe	16,100.000	^{32}P	1,587,887.177		
^{68}Ge	134,554.000	^{99m}Tc*	9,701,800.000		
^{125}I	40,135.690				
Total	61,616.690	Total	21,655,788.177	Total	34,928,392.420

* Including the use in the "β -ray analysis" room

(c) Research Building (kBq)

Group1,2		Group3		Group4	
		^{15}O	12,765,000.000	^{18}F	4,329,000.000
Total	0	Total	12,765,000.000	Total	4,329,000.000

Table 2. Occupational radiation exposures at CYRIC during the fiscal year of 2003.

Dose range (mSv)	Number of individuals
No measurable exposure	35
Less than 1.0	15
1.0 to 2.0	1
2.0 to 3.2	1
Total number of persons monitored	52

X. PUBLICATIONS

X. PUBLICATIONS

(January 2003 ~ December 2003)

[571] Evaluation of the Binding Characteristics of [5-^{11}C-*methoxy*]Donepezil in the Rat Brain for In Vivo Visualization of Acetylcholinesterase.
Yoshihito Funaki, Motohisa Kato, Ren Iwata, Eiko Sakurai, Eiichi Sakurai, Manabu Tashiro, Tatsuo Ido, Kazuhiko Yanai.
J. Pharmacol. Sci., **91** (2003) 105-112.

[572] Tumor detection using ^{18}F-labeled matrix metalloproteinase-2 inhibitor.
Shozo Furumoto, Kyoka Takashima, Kazuo Kubota, Tatsuo Ido, Ren Iwata, Hiroshi Fukuda.
Nucl. Med. Biol., **30** (2003) 119-125.

[573] Stability of L-[*S*-methyl-^{11}C]methionine solutions.
A. Bogni, E. Bombardieri, R. Iwata, L. Cadini, C. Pascali.
J. Radioanal. Nucl. Chem., **256** (2003) 199-203.

[574] Radiosynthesis of *O*-[^{11}C]methyl-L-tyrosine and *O*-[^{18}F]Fluoromethyl-L-tyrosine as potential PET tracers for imaging amino acid transport.
Ren Iwata, Shozo Furumoto, Claudio Pascali, Anna Bogni and Kiichi Ishiwata.
J. Label. Compd. Radiopharm., **46** (2003) 555-566.

[575] Characterization of the interactions of □-amyloid peptides with glycolipid receptors by surface plasmon resonance.
Tania Valdes-Gonzalez, Junichi Inagawa and Tatsuo Ido.
Spectroscopy, **17** (2003) 241-254.

[576] Evaluation of ^{18}F-FDG PET in Patients with Advanced, Metastatic, or Recurrent Gastric Cancer.
Takashi Yoshioka, Keiichirou Yamaguchi, Kazuo Kubota, Toshiyuki Saginoya, Tetsuro Yamazaki, Tatuo Ido, Gengo Yamaura, Hiromu Takahashi, Hiroshi Fukuda and Ryunosuke Kanamaru.
J. Nucl. Med., **44** (2003) 690-699.

[577] Improved synthesis of pure[^{18}F]fluoro-compounds for **PET** studies from bromo-compounds.
Toshihiro Takahashi, Takashi Mizuno, Tatsuo Ido, Ren Iwata, Ken-ichi Watanabe.
Appl. Radiat. Isot., **58** (2003) 557-566.

[578] Thinking of the future and past: The roles of the frontal pole and the medial temporal lobes.
Jiro Okuda, Toshikatsu Fujii, Hiroya Ohtake, Takashi Tsukiura, Kazuyo Tanji, Kyoko Suzuki, Ryuta Kawashima, Hiroshi Fukuda, Masatoshi Itoh and Atsushi Yamadori.
NeuroImage, **19** (2003) 1369-1380.

[579] Decreased striatal D_2 receptor density associated with severe behavioral abnormality in Alzheimer's disease.
Yasuhiro Tanaka, Kenichi Meguro, Satoshi Yamaguchi, Hiroshi Ishii Shoichi Watanuki, Yoshihito Funaki, Keiichiro Yamaguchi, Atsushi Yamadori, Ren Iwata and Masatoshi Itoh.
Ann. Nucl. Med., **17** (2003) 567-573.

[580] Effect of Anoxia on Choline Uptake and Release of Acetylcholine in Brain Slices Estimated With a Bioradiographic Technique Using [^{11}C]Choline.
Toru Sasaki, Yoshihito Funaki, Masanori Shozushima and Kazunori Terasaki.
Radioisotopes, **52** (2003) 677-685.

[581] Polarization Transfer Mrasurement for ***d-p*** Scattering and Three Nucleon Force Effects.
K. Sekiguchi, H. Sakai, H. Okamura, A. Tamii, T. Uesaka, K. Suda, N. Sakamoto, T. Wakasa, Y. Satou, T. Ohnishi, K. Yako, S. Sakoda, K. Suda, H. Kato, Y. Maeda, M. Hatano, J. Nishikawa, T. Saito, N. Uchigashima, N. Kalantar-Nayestanaki and K. Ermisch.
Nucl. Phys. A, **721** (2003) 637c-640c.

[582] Polarization Transfer Measurement for *d-p* Elastic Scattering: to Search for Three Nucleon Force Effects.
K. Sekiguchi, H. Sakai, H. Okamura, A. Tamii, T. Uesaka, K. Suda, N. Sakamoto, T. Wakasa, Y. Satoh, T. Ohnishi, K. Yako, S. Sakoda, H. Kato, Y. Maeda, M. Hatano, J. Nishikaea, T. Saito, N. Uchigashima, N. Kalantar-Nayestanaki, and K. Ermisch.
Modern Phys. Lett. A, **18** (2003) 327-329.

[583] Measurement of *p+d* Elastic Scattering at *Ep*=392 MeV.
A. Tamii, N. Uchigashima, H. Sakai, M. Hatano, Y. Maeda, T. Saito, T. Ishida, H. Kuboki, K. Hatanaka, T. Wakasa, J. Kamiya, Y. Sshimizu, Y. Kitamura, H. Okamura, K.Suda, K. Yako, K. Sekiguchi, Y. Satou.
Modern Phys. Lett. A, **18** (2003) 440-443.

[584] Measurement of the Analyzing Powers for the $\vec{d}d$ → ^{3}H*en* and $\vec{d}d$→ ^{3}H*p* Reactions at Intermediate Energies.
T. Saito, M. Hatano, H. Kato, Y. Maeda, H. Sakai, S. Sakoda, A. Tamii, N. Uchigashima, V. P. Ladygin, A. Yu. Isupov, N. B. Ladygina, A. I. Malakhov, S. G. Reznikov, T. Uesaka, K. Yako, T. Ohnishi, N. Sakamoto, K. Sekiguchi, H. Kumasaka, J. Nishikawa, H. Okamura, K. Suda, R. Suzuki.
Modern Phys. Lett. A, **18** (2003) 294-297.

[585] Measurement of Differential Cross Sections and Vector Analyzing Powers for the $\vec{n}d$ Reaction at 250MeV.
Y. Maeda, H. Sakai, A. Tamii, S. Sakoda, H. Kato, M. Hatano, T. Saito, N. Uchigashima, H. Kuboki, K. Hatanaka, D. Hirooka, Y. Shimizu, Y. Kitamura, K. Fujita, N. Sasamoto, H. Okamura, K. Suda, T. Ikeda, K. Itoh, Y. Sakemi, T. Wawasa, J. Kamiya, K. Yako, K. Sekiguchi, Y. Sato, M. B. Greenfield, J. Rapaport, H. Kamada.
Modern Phys. Lett. A, **18** (2003) 298-301.

[586] Feasibility Study on Epithermal Neutron Field for Cyclotron-Based Boron Neutron Capture Therapy.
Shunsuke Yonai, Takao Aoki, Takashi Nakamura, Hiroshi Yashima, Mamoru Baba, Hitoshi Yokobori and Yoshihisa Tahara.
Medical Physics, **30** (2003) 2021-2030.

[587] Shielding experiment of heavy-ion produced neutrons using a Tissue Equivalent Proportional Counter.
Tomoya Nunomiya, Shunsuke Yonai, Masashi Takada, Akifumi Fukumura, Takashi Nakamura.
Radiat. Protection Dosimetry, **106** (2003) 207-218.

[588] Neutron Energy and Time-Of-Flight Spectra behind the Lateral Shield of a High Energy

Electron Accelerator Beam Dump. Part I: Measurements.
Shingo Taniguchi, Takashi Nakamura, Tomoya Nunomiya, Hiroshi Iwase, Shunsuke Yonai, Michiya Sasaki, Sayed H. Rokni, James C. Liu, Ken R. Kase, Stefan Resler.
Nucl. Instrum. Methods, **A503** (2003) 595-605.

[589] Measurement of neutrons from thick Fe target bombarded by 210 MeV protons.
Shunsuke Yonai, Tadahiro Kurosawa, Hiroshi Iwase, Hiroshi Yashima, Yoshitomo Uwamino, Takashi Nakamura.
Nuclear Instruments and Methods, **A515** (2003) 733-744.

[590] Evaluation of resolved and unresolved resonance range of ^{232}U.
V. M. Maslov, Yu. V. Porodzinskij, N.A.Tetereva, M.Baba, A.Hasegawa.
Annals of Nucl. Energy, **30** (2003) 1155-1179.

[591] Neutron Capture Cross Section of ^{232}Th.
V. M. Maslov, Yu. V. Porodzinskij, M.Baba, A.Hasegawa.
Nucl. Science and Eng., **143** (2003) 177-187.

[592] Development of a new passive integral dosemeter for gamma ray monitoring using an imaging plate.
H. Ohuchi, A. Yamadera, and M. Baba.
Radiation Protection Dosimetry, **107** (2003) 239-246.

[593] 3D imaging of elemental distributions using multi-angle RBS 2D-data.
Y. Oishi, K. Hotta, K. Ishii, Y. Komori, S. Matsuyama, H. Yamazaki, T. Amartivan, M. Rodriguez, K. Katoh, D. Izukawa, K. Mizuma, T. Satoh, T. Kamiya, T. Sakai, K. Arakawa, M. Saidoh, M. Oikawa.
Nucl. Instrumen. Methods in Physics Research, **B210** (2003) 117-122.

[594] Preliminary Results of Microbeam at Tohoku University.
Yamazaki, R. Sakamoto, M. Fujisawa, Ts. Amartaivan, Y. Oishi, M. Rodriguez, A. Suzuki, T. Kamiya, M. Oikawa, K. Arakawa and N. Matsumoto.
Nucl. Instrum. Methods in Physics Research, **B210** (2003) 59-64.

[595] Summary of the Workshop on Practical Problems in Biological Applications of Micro-PIXE Analysis.
H. Yamazaki, K. Ishii, S. Matsuyama, Y. Komori, K. Mizuma and T. Izukawa.
In. J. PIXE, **13** (2003) 89-96.

[596] Multi-site Aerosol Monitoring Using Mini Step Sampler.
S. Matsuyama, K. Katoh, S. Sugihara, K. Ishii, H. Yamazaki, T. Satoh, Ts. Amartaivan, A. Tanaka, H. Komori, K. Hotta, D. Izukawa, K. Mizuma, H. Orihara, E. Nakamura, N. Satoh, S. Futatsukawa and K. Sera.
Int. J. PIXE, **13** (2003) 65-80.

XI. MEMBERS OF COMMITTEE

XI. MEMBERS OF COMMITTEE (as of Jan. 1, 2004)

General

(Chairman)	Keizo	Ishii	(Graduate School of Engineering)
	Katsuto	Nakatsuka	(Vise President)
	Osamu	Hashimoto	(Graduate School of Science)
	Hiroshi	Kudo	(Graduate School of Science)
	Akira	Takahashi	(Graduate School of Medicine)
	Nobuhiro	Takahashi	(Graduate School of Dentistry)
	Yasushi	Ohizumi	(Faculty of Pharmaceutical Sciences)
	Katsunori	Abe	(Graduate School of Engineering)
	Teruo	Miyazawa	(Graduate School of Agricultural Science)
	Kazuhiko	Nishitani	(Graduate School of Life Science)
	Isamu	Sato	(Institute for Materials Research)
	Hiroshi	Fukuda	(Institute for Development, Aging and Cancer)
	Yukio	Noda	(Institute of Multidisciplinary Research for advanced Materials)
	Syogo	Yamada	(University Hospital)
	Jirohta	Kasagi	(Laboratory of Nuclear Science)
	Tatsuo	Ido	(CYRIC)
	Masatoshi	Itoh	(CYRIC)
	Mamoru	Baba	(CYRIC)
	Ren	Iwata	(CYRIC)
	Hiroyuki	Okamura	(CYRIC)
	Tsutomu	Shinozuka	(CYRIC)
	Toshio	Kobayashi	(Graduate School of Science)
	Kazuhiko	Yanai	(Graduate School of Medicine)
	Tetsuya	Ono	(Radiation Safety Committee, Research Promotion Council)

	Hiroyasu	Hasegawa	(Director-General, Administration Bureau)
	Makoto	Sugawara	(Head of Administration Office, Graduate School of Information Science: Observer)

Research Program

(Chairman)	Mamoru	Baba	(CYRIC)
	Tatsuo	Ido	(CYRIC)
	Masatoshi	Itoh	(CYRIC)
	Mamoru	Baba	(CYRIC)
	Ren	Iwata	(CYRIC)
	Hiroyuki	Okamura	(CYRIC)
	Tsutomu	Shinozuka	(CYRIC)
	Osamu	Hashimoto	(Graduate School of Science)
	Tsutomu	Sekine	(Graduate School of Science)
	Kazuhiko	Yanai	(Graduate School of Medicine)
	Akira	Takahashi	(Graduate School of Medicine)
	Katsunori	Abe	(Graduate School of Engineering)
	Hiromichi	Yamazaki	(Graduate School of Engineering)
	Isamu	Sato	(Institute for Materials Research)
	Hiroshi	Fukuda	(Institute for Development, Aging and Cancer)
	Syoki	Takahashi	(University Hospital)
	Jirohta	Kasagi	(Laboratory of Nuclear Science)

Cyclotron

(Chairman)	Osamu	Hashimoto	(Graduate School of Science)
	Toshio	Kobayashi	(Graduate School of Science)
	Naoki	Toyota	(Graduate School of Science)
	Tsutomu	Sekine	(Graduate School of Science)
	Kazushige	Maeda	(Graduate School of Science)
	Hirokazu	Tamura	(Graduate School of Science)
	Keizo	Ishii	(Graduate School of Engineering)
	Akira	Hasegawa	(Graduate School of Engineering)

Isamu	Sato	(Institute for Materials Research)
Masao	Saitoh	(Institute of Multidisciplinary Research for advanced Materials)
Tsutomu	Otsuki	(Laboratory of Nuclear Science)
Tatsuo	Ido	(CYRIC)
Masatoshi	Itoh	(CYRIC)
Mamoru	Baba	(CYRIC)
Ren	Iwata	(CYRIC)
Hiroyuki	Okamura	(CYRIC)
Tsutomu	Shinozuka	(CYRIC)
Atsuki	Terakawa	(CYRIC)
Mashiro	Fijita	(CYRIC)

Radiation Protection and Training of Safe Handling

(Chairman)	Mamoru	Baba	(CYRIC)
	Hiroshi	Kudo	(Graduate School of Science)
	Yoshihiko	Uehara	(Graduate School of Medicine)
	Tsutomu	Araki	(Graduate School of Pharmaceutical Sciences)
	Keizo	Ishii	(Graduate School of Engineering)
	Toshiyasu	Yamaguchi	(Graduate School of Agricultural Science)
	Kazuhiro	Togawa	(Graduate School of Agricultural Science)
	Masayuki	Hasegawa	(Institute for Materials Research)
	Hiroshi	Fukuda	(Institute for Development, Aging and Cancer)
	Yoshihiro	Takai	(University Hospital)
	Tatsuo	Ido	(CYRIC)
	Tsutomu	Shinozuka	(CYRIC))

Life Science

(Chairman)	Tatsuo	Ido	(CYRIC)
	Yasuhito	Itoyama	(Graduate School of Medicine)
	Kazuie	Iinuma	(Graduate School of Medicine)
	Syoki	Takahashi	(Graduate School of Medicine)
	Reizo	Shirane	(Graduate School of Medicine)
	Masahiko	Yamamoto	(Graduate School of Medicine)
	Makoto	Watanabe	(Graduate School of Dentistry)
	Sumio	Ohtuki	(Graduate School, Division of Pharmaceutical Sciences)
	Keizo	Ishii	(Graduate School of Engineering)
	Satoshi	Yokota	(Graduate School of Agricultural Science)
	Kazuo	Yamamoto	(Graduate School of Life Science)
	Hiroshi	Fukuda	(Institute for Development, Aging and Cancer)
	Junichi	Gotoh	(University Hospital)
	Shin	Maruoka	(College of Medical Sciences)
	Ren	Iwata	(CYRIC)
	Masatoshi	Itoh	(CYRIC)
	Kei-ichiro	Yamaguchi	(CYRIC)
	Yoshihito	Funaki	(CYRIC)

Prevention of Radiation Hazards

(Chairman)	Mamoru	Baba	(CYRIC)
	Osamu	Hashimoto	(Graduate School of Science)
	Tsutomu	Sekine	(Graduate School of Science)
	Keizo	Ishii	(Graduate School of Engineering)
	Tatsuo	Ido	(CYRIC)
	Mamoru	Baba	(CYRIC)
	Tsutomu	Shinozuka	(CYRIC)
	Katsuyuki	Takada	(CYRIC)
	Takamoto	Miyata	(CYRIC)

XII. STAFF

XII. STAFF (as of Jan. 1, 2004)

Director Keizo Ishii

Division of Accelerator

Osamu	Hashimoto[1)]
Tsutomu	Shinozuka
Masahiro	Fujita
Takuya	Endo
Toru	Miyake
Akiyoshi	Yamazaki
Eiji	Tanaka
Shizuo	Kan[4)]
Shizuo	Chiba[4)]
Yasuaki	Ohmiya[4)]
Naoto	Takahashi[4)]
Shigenaga	Yokokawa[4)]

Division of Instrumentations

Hiroyuki	Okamura
Toshio	Kobayashi[1)]
Hikonojo	Orihara[3)]
Atsuki	Terakawa
Hiroshi	Suzuki
Sho-ichi	Watanuki
Ryuuji	Maruyama

Division of Radiopharmaceutical Chemistry

Tatsuo	Ido
Ren	Iwata
Yoshihito	Funaki
Yo-ichi	Ishikawa

Tania	Valdes-Gonzales
Hideo	Takahashi

Division of Cyclotron Nuclear Medicine

Masatoshi	Itoh
Kazuhiko	Yanai[2)]
Keiichiro	Yamaguchi
Takehisa	Sasaki
Masayasu	Miyake

Division of Radiation Protection and Safety Control

Mamoru	Baba
Takashi	Nakamura[3)]
Takamoto	Miyata
Noboru	Watanabe[5)]

Graduate Student and Researcher

Tetsu	Sonoda	(Graduate School of Science)
Tomokazu	Suzuki	(Graduate School of Science)
Atsushi	Gotoh	(Graduate School of Science)
Yu-ji	Miyashita	(Graduate School of Science)
Naoya	Sugimoto	(Graduate School of Science)
Hideo	Shinozaki	(Graduate School of Science)
Takashi	Hasegawa	(Graduate School of Science)
Aiko	Ono	(Graduate School, Division of Pharmaceutical Sciences)
Megumi	Maeda	(Graduate School, Division of Pharmaceutical Sciences)
Laxmi N.	Singh	(Graduate School, Division of Medicine)
Sabina Khond	Kar	(Graduate School, Division of Medicine)
Manami	Suzuki	(Graduate School, Division of Medicine)
Honda	Goh	(Graduate School, Division of Medicine)
Targino RodriguesDosSantos		(Graduate School, Division of Medicine)
Tetushi	Yamaguchi	(Graduate School, Division of Medicine)
Hiroshi	Yashima	(Graduate School of Engineering)

Syunsuke	Yonai	(Graduate School of Engineering)
Md Shuza	Uddin	(Graduate School of Engineering)
Masayuki	Hagiwara	(Graduate School of Engineering)
Naoya	Hirabayashi	(Graduate School of Engineering)
Toshiro	Itoga	(Graduate School of Engineering)
Hirabayashi	Naoya	(Graduate School of Engineering)
Takeshi	Yamauchi	(Graduate School of Engineering)
Takuji	Oishi	(Graduate School of Engineering)

Office Staff

Makoto	Sugawara
Katuyuki	Takada
Akihiro	Matsuya
Kyoko	Fujisawa
Junko	Matsuno
Fumiko	Mayama
Mitsuko	Endo
Yu-ko	Yamashita
Keietsu	Aizawa
Kietu	Takahashi
Yuri	Okumura
Noriko	Suzuki
Kimiko	Abe

1) Graduate School of Science
2) Graduate School of Medicine
3) Visiting Professor
4) SUMI-JU Accelerator Service Ltd.
5) Japan Radiation Protection Co., Ltd.